Improving Prediction of Traversability for Planetary Rovers Using Thermal Imaging

Christopher Cunningham

CMU-RI-TR-17-28

April 6, 2017

The Robotics Institute
Carnegie Mellon University
Pittsburgh, PA 15213

Thesis Committee:
William "Red" Whittaker, Chair
David Wettergreen
Stephen Nuske
Issa A. Nesnas, *Jet Propulsion Laboratory*

Submitted in partial fulfillment of the requirements for the degree of Doctor of Philosophy.

Abstract

The most significant mobility challenges that planetary rovers encounter are compounded by loose, granular materials that cause slippage and sinkage on slopes or are deep enough to entrap a vehicle. The inability of current technology to detect loose terrain hazards has caused significant delays for rovers on both the Moon and Mars and, most notably, contributed to Spirit's permanent entrapment in soft sand on Mars. Classical, vision-based traversability prediction methods are inherently limited by only measuring surface appearance, which is not necessarily correlated to subsurface bulk mechanical properties that influence mobility, such as bulk density and particle size distribution. The inherent difficulty of estimating traversability is compounded by the conservative nature of planetary rover operations. Mission operators actively avoid potentially hazardous regions. Hence there is little intentional driving in weak soil and limited data from which to train a feature-intensive, vision-based algorithm.

Instead, this thesis leverages thermal physics to improve traversability prediction for rovers operating in planetary terrain. Unlike visual appearance, the thermal inertia of a granular material is directly influenced by its bulk physical properties both at and below the surface. A robot can use a thermal camera to observe the surface temperatures of terrain, which are then fit to an analytical model to find thermal inertia. These measurements can then be used to distinguish between safe and hazardous granular materials on Mars and to a lesser extent on the Moon.

This research investigates how to use thermal inertia to improve traversability prediction as well as when and where it applies. Both natural fluxes and laser heating are leveraged to produce a transient temperature response, from which a robot can estimate the thermal properties of terrain. Natural heat sources (i.e. solar and atmospheric fluxes) are shown to be more effective because they are uniform and have longer illumination periods, which results in measurements over the whole surface that are influenced by materials at depths of several centimeters. Terrestrial experiments show that the ability of this approach to predict traversability depends both on time of day and length of observation, with longer, nighttime measurements resulting in the fewest errors.

Experimental results using in-situ data from the Curiosity rover demonstrate the ability of thermal inertia measurements to improve slip prediction accuracy on Mars by reducing cross-validation slip prediction error by 26%. Simulations show that at most times of day, thermal imaging could also identify hazards caused by thin duricrust over deep sand, which was the situation that trapped Spirit on Mars. Results also show that there is a measurable difference in temperature between nominal and loose regolith samples on the Moon, even in permanently shadowed polar craters. This effect is most consistent at night in the absence of solar radiation and generally causes temperature differences between 2 and 3 K. Though it certainly does not account for all of the intricacies of a rover's interaction with terrain, thermal inertia represents a single measurement that can improve traversability prediction, especially at night when visual approaches fail.

Acknowledgments

I would like to thank my advisor, Red Whittaker, who has guided me through my graduate career and my thesis while allowing me the freedom to pursue interesting research. Thanks to my committee members, Stephen Nuske and David Wettergreen, who gave me valuable perspectives and advice throughout my thesis. A special thanks goes to my external committee member, Issa Nesnas, who was a second advisor to me, providing context and motivation for this research.

I would like to thank the members of the lunar group at CMU for the invaluable collaboration and moral support, including Heather Jones, Chuck Whittaker, Kevin Peterson, Uland Wong, Joe Bartels, Eugene Fang, Dan Arnett, Tom Carlone, Joe Amato, Wennie Tabib, Neal Bhasin, Curtis Boirum, Chris Skonieczny, and Nate Otten. Special thanks goes to Kevin, Uland, and Heather for all of the guidance they gave me at the beginning and to Chuck for his help in every experiment despite his other numerous commitments. I'm also very thankful for our extended lunar family at Astrobotic, including Fraser Kitchell, Kerry Snyder, Eric Amaroso, Steven Huber, Aaron Acton, Steve McGuire, and Andrew Horchler. I'm especially grateful to Fraser and Kerry for all of their effort in designing and executing the field testing in this thesis. Thanks also goes to my friends in the RI soccer group for giving me a weekly outlet that I've throughly enjoyed.

After spending nearly a year of my graduate career at JPL, it has felt like a second home. Many thanks go to the many I've met through those experiences who have helped me along the way, including Mark Maimone, Masahiro Ono, Jeng Yen, Ryan Kennedy, Jeremie Papon, Scott Moreland, Garret Meirion-Griffith, Arturo Rankin, Rob Reid, Ian Baldwin, Heather Justice, Ashwin Vasavada, Sylvain Piqueux, Amanda Steffy, Feng Zhou, and Raymond Arvidson. A big thanks also goes to the NSTRF program for enabling this. This thesis would not have been possible without the help and perspectives from the people working actively on rover missions. I am also very grateful to the MSL and MER teams as well as the PDS Geosciences Node for providing me with data from the Mars rovers.

The whole PhD process was streamlined by the fantastic support staff at CMU. A specific thanks to Suzanne Lyons Muth, Nora Kazour, and Victoria Homitsky, who have helped me with proposals, budgets, reimbursements, and everything else.

Thanks to Lafarge's Duquesne Processing Plant for providing a fantastic test site and operational support that enabled the field testing in this work. I'm also grateful to Colin Creager at NASA's Glenn Research Center for lending me the bevameter, and Nate Melaro at Geotechnics for graciously performing soil testing.

I'd like to thank my family for all of their support throughout this process. Finally, thanks go to my wife, Lindsey. Thank you for moving with me to Pittsburgh and for dealing with all of my trips to JPL and late nights of work. I would not have gotten through this without your love and encouragement.

Contents

List of Figures

List of Tables

Chapter 1

Introduction

Robotic hazard avoidance classically detects and negotiates geometric obstacles and steep slopes. However, in natural and planetary terrain, soil weakness is a significant, more subtle hazard that such techniques do not address. Loose, granular materials have entrapped robots and often cause wheels to slip and sink. Contact measurements of wheel slip and sinkage can detect when a rover has encountered hazardous terrain. However, by the time it is detected, the rover could already be in an inescapable situation. This is a significant problem for rovers operating in planetary environments, as soft sand and regolith cover much of both the lunar and Martian surfaces (see example in Figure 1.1).

Classical visual and geometric perception techniques are superficial and have difficulty detecting the subtle differences in terrain properties that affect soil strength. They are unable to directly measure differences in terrain properties beneath the surface layer. Vision-based approaches also require complex feature representations to evaluate terrain and risk significant overfitting in planetary applications where data is scarce.

Vision and depth sensing have difficulty measuring bulk mechanical properties like bulk density and particle size distribution that govern a wheel's interaction with granular terrain. While they help to estimate these parameters at the surface, the subsurface cannot be directly measured. These physical characteristics are, however, directly related to the surface temperatures and thermal inertia of terrain. Temperatures can be observed with robotic cameras to measure thermal inertia using estimates of albedo and surface heat fluxes. The capability to measure temperatures, estimate thermal inertia, and infer mechanical properties is the basis for innovative methodology to predict traversability during robotic exploration. In contrast to feature-heavy, visual techniques, thermal inertia represents a single measurement that can provide significant insight into the mechanical properties of terrain both at and below the surface. This thesis evaluates the ability of thermal inertia to improve mobility prediction in planetary environments. It demonstrates experimentally on Earth, with Curiosity data on Mars, and in simulation on the Moon, that thermal imaging differentiates between hazardous and safe granular materials.

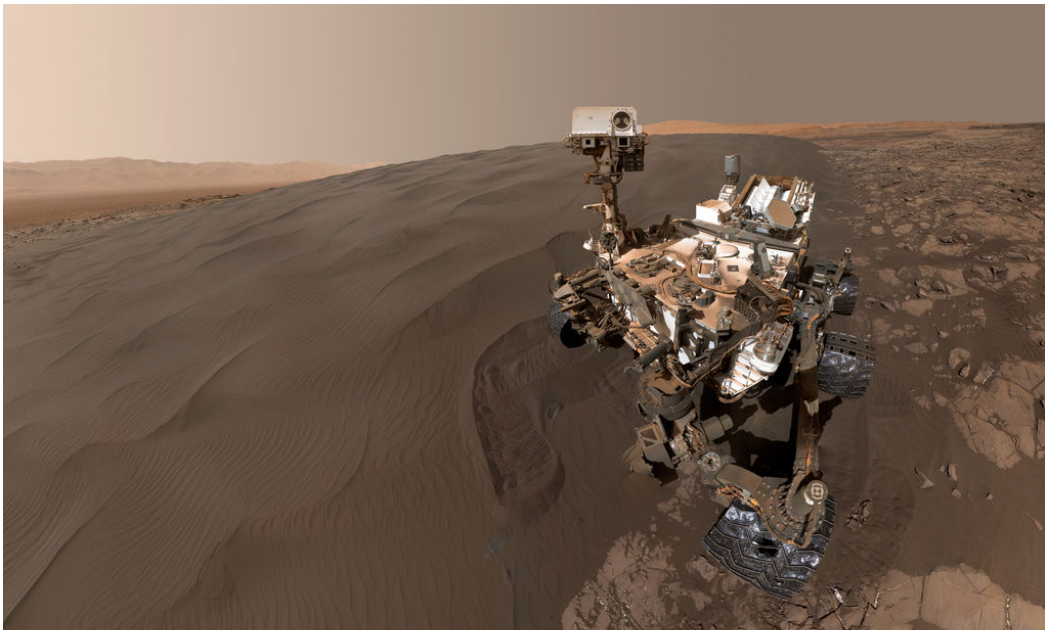

Figure 1.1: Curiosity “selfie” on Mars in front of Namib Dune. Image credit: NASA/JPL

1.1 Motivation

The motivation of this research is to increase the safety and efficiency of planetary rover operations. Safe, reliable robotic mobility in the presence hazardous terrain is critical to both current and future planetary missions. Some of these missions cost billions of dollars. Unforeseen terrain hazards can be mission ending as was the case with the Spirit rover on Mars [6]. Any delays caused by slipping and sinking into loose regolith reduce the overall science return of the mission and increase the cost. Traversability predictions that are too conservative might cause a rover to circumvent an area that is perceived as an obstacle but would not impede driving. This could potentially delay a mission just as much as an unidentified hazard. The following two sections give context for this research by describing the environments on the Moon and Mars as well as relevant experiences of rovers on those bodies.

1.1.1 Mars

The terrain on Mars is surprisingly heterogeneous. The surface contains jagged rocks, exposed bedrock, windblown sand, and fine dust. The characteristics of these regions and relative frequency with which they occur in an area varies greatly across Mars. Mobility on bedrock or areas with only thin layers of dust is relatively easy to predict. The exception to this are the regions of embedded rocks that recently damaged Curiosity’s wheels [159]. Detecting and avoiding these hazards will not be addressed in this thesis. The primary mobility hazards that rovers face on Mars are regions of deep sand that can cause wheels to slip and sink. In some areas surface sand is uniformly sloped. Other aeolian deposits, for example, exhibit ripple geometries [8].

The most serious mobility problem encountered by a planetary rover was Spirit’s entrapment

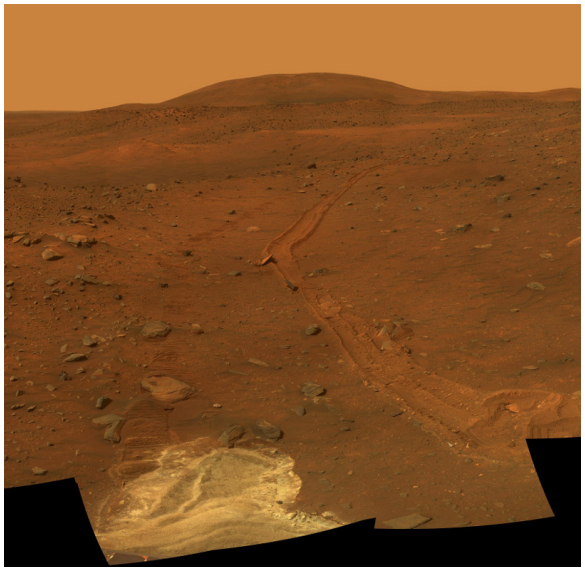

(a) Spirit's tracks leading up to it's entrapment.

(b) Spirit's wheel embedded in sand.

(c) Purgatory Dune where Opportunity was embedded for 5 weeks.

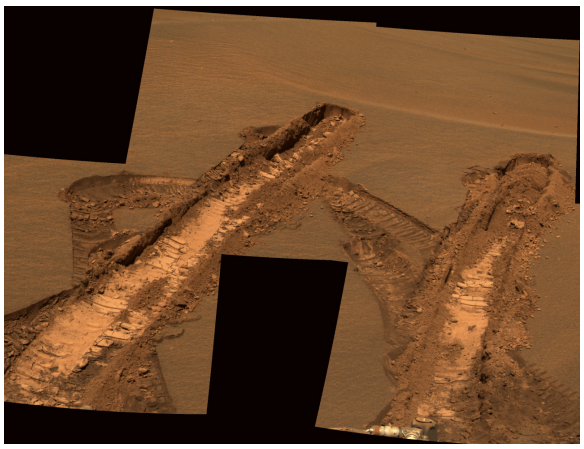

(d) Jammerbugt Dune where Opportunity was embedded for 6 days.

(e) Dingo Gap dune after Curiosity traverse.

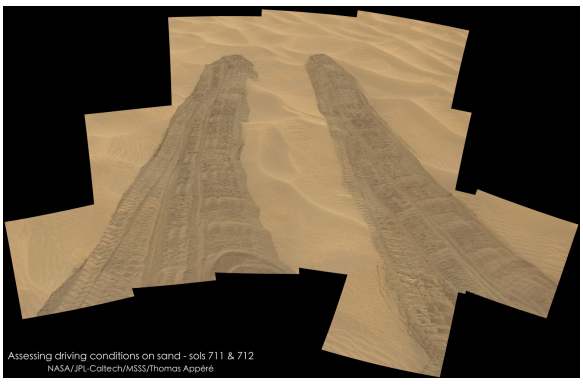

(f) Curiousity's tracks in Hidden Valley, 80% slip.

Figure 1.2: Mars rovers stuck in or delayed by loose terrain hazards. Image credits: NASA/JPL

at Troy. Spirit was driving over what appeared to be relatively benign terrain. However, it was actually skirting the edge of Scamander Crater, a barely visible 8 m wide and 0.25 m deep crater. The crater contained loose, deep sand that was not visible due to a thin, 1 cm duricrust layer on the surface. Three of Spirit's wheels broke the surface and became embedded in the loose material underneath. Despite managing to move 34 cm, Spirit did not reach its goal before permanently losing power due to its angle with respect to the Sun and accumulated dust on its solar panels [6]. Figure 1.2a shows a view of Spirit's tracks leading up to its entrapment. The lighter terrain in the lower-left of the image shows the sand that was uncovered by Spirit. Figure 1.2b shows Spirit's wheel buried in sand. Despite more than five years of driving experience, the sub-surface material was not detected by orbital data or any of Spirit's instruments [94]. However, sub-surface sand does affect apparent surface thermal inertia [129] and could potentially be used in the future to identify hazardous regions.

Even when visible, loose sand has caused several delays for rovers on Mars. The first major delay for Opportunity was at the Purgatory Dunes (Figure 1.2c), where the rover experienced 100% slip while it was embedded in a ripple 30 cm high. It took about 5 weeks to extricate [146]. Shortly afterwards Opportunity became stuck again in the Jammerbugt ripple (Figure 1.2d), requiring six sols for extraction. It was observed that there are generally problems when the ripple wavelength is larger than the wheel base. After these delays, drivers actively avoided rippled sand regions that appeared dangerous. However, despite these precautions, Opportunity still occasionally has problems with high slip [5].

Curiosity had avoided driving on sand until wheel wear from rocks mandated avoidance of sharp rocks. Since then, Curiosity has had several delays due to sandy ripples. The first was at Dingo Gap, a single large ripple (Figure 1.2e). There was a delay of about one week for planning and mobility tests before the ripple was finally surmounted. There was no significant mobility hazard, but the delay cause by uncertainty was nonetheless costly [8].

The two most dangerous areas followed in Moosilauke Valley and Hidden Valley (Figure 1.2f). These contained deep, loose sand that formed ripples in polygonal patterns. In both cases slip of up to 80% was detected and the rover had to back out and find another route. Simulations have estimated that the sand at Dingo Gap was significantly more cohesive than Hidden Valley. Furthermore, if the sand in Hidden Valley kept the same polygonal geometry but had Dingo Gap's sand, it is likely that the rover would have successfully traversed [8].

After those two scares, it was decided to avoid polygonal ripples. However, not even a year later more trouble was encountered in Logan's Pass. A route was taken directly adjacent to a ripple field in what appeared to be rockier, more consolidated material. However, once again high slip caused a detour [161]. The failure here along with the difference in sand properties between Hidden Valley and Dingo Gap suggests that it is important to estimate not only the geometry of sand but the strength as well.

Curiosity and Opportunity continue to operate on Mars and still risk these hazards. In fact, in late 2015, Curiosity began a test campaign at Bagnold dunes, the first actively moving dunes visited on another planet (Figure 1.1) [160]. Mars 2020 and potential future missions aspire to drive faster, more autonomously, and visit more challenging terrain. Accurate and reliable prediction of terrain hazards is necessary to achieve these goals.

1.1.2 The Moon

The lunar surface is far more homogeneous than Mars. Nearly all of the surface is covered by several meters of regolith due to near-continuous meteoroid impacts and the lack of the hydrological and aeolian processes that have helped shape the terrain on Mars [64]. Much of this regolith, at least in equatorial areas, has been shown to be fairly homogeneous in thickness, particle size distribution, and most other properties [64, 151]. It is, however, far from smooth with craters as small as 0.3 m scattered across the surface. The primary cause of variations in the mechanical behavior lunar regolith are differences in bulk density. Higher bulk and relative densities make stronger granular materials that are more easily traversed by a wheeled vehicle. The average bulk density in the top 15 cm of lunar regolith is believed to be 1500 kg/m^3 [64]. However, estimated bulk density values have ranged from 800 kg/m^3 (reported by Luna 13) [29] to 2000 kg/m^3 (reported by Apollo 17) [25]. The surface of the soil may also have a thin, coherent duricrust layer on surface [56].

The average relative densities in intercrater areas were estimated to be between 48-71% compressed with sharply increasing density even at shallow depths of 10-15 cm. There were very few mobility problems with any of the rovers in these areas. However, around fresh craters and on slopes, the relative density is much lower around 30-38% compressed [64]. One example of loose lunar regolith is shown in Figure 1.3a. In the image of regolith temperatures, the bluer, colder areas indicate very loose regolith caused by a fresh meteorite impact. Note that no evidence of this is seen in the visible imagery [15, 16]. Figure 1.3b shows bootprints from Apollo astronauts around a very small crater. The deep bootprints are indicative of very loose regolith around the crater rim.

In equatorial and mid-latitude regions of the Moon, rovers have struggled with loose regolith. The depth of Apollo Lunar Roving Vehicle (LRV) tracks ranged from imperceptible to 13 cm [64]. The Apollo 15 LRV even got stuck in loose regolith, requiring the astronauts to dislodge it [37]. Both of the Soviet Lunokohd rovers also experienced wheel sinkage up to 20 cm during their missions [86].

Future robotic missions to the Moon target permanently shadowed polar regions to prospect for ice. While permanently cold craters are havens for solid volatiles [35], the slopes and loose regolith they exhibit may prove treacherous for rovers. Regolith in polar craters is hypothesized to be finer and looser than in other regions of the Moon and could pose a significant threat to rover mobility [149]. This may be caused by the fact that these permanently shadowed regions do not experience the daily hot-cold swings of sunlit locations, which help settle regolith [52]. This hypothesis is supported by orbital thermal imaging data, which predicts the thermal conductivity of regolith in these craters to be much lower than in other regions of the Moon, which likely corresponds to less dense regolith [113]. It is also supported by analysis of the LCROSS impact, which predicts a low-density surface layer [135]. Both sets of data support the theory that the regolith in permanently shadowed craters is looser than in other areas of the Moon. Means to predict the traversability of terrain would increase the safety and reliability of a lunar rover mission. This is a particularly difficult problem in dark polar craters where state-of-the-art visual techniques fail due to lack of natural illumination.

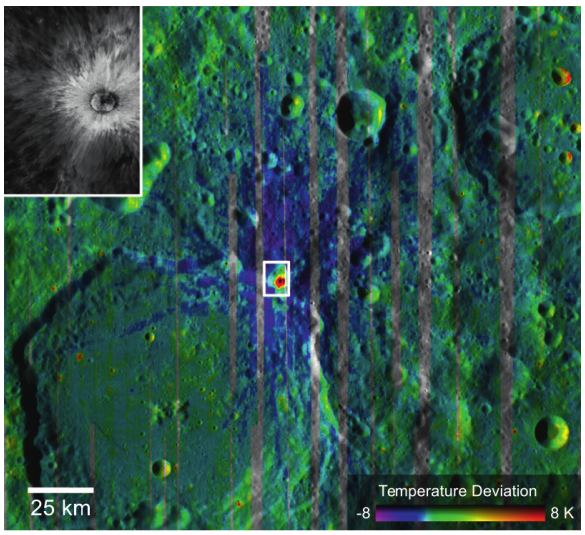

(a) Image of a crater showing a comparison of Lunar regolith nighttime temperature and closeup visual imagery (inset). Colder temperatures show looser regolith. Image credit: [16].

(b) Bootprints in soft regolith surrounding a small crater during Apollo 16. Regolith around craters is much looser than the intercrater regions. Image credit: NASA/JSC

Figure 1.3: Example images of terrain types tested in related work on traversability prediction in granular materials.

1.2 Approach

The ability of a wheeled vehicle to successfully traverse granular terrain is a complex function of the bulk mechanical properties of the material, terrain geometry, and mobility system configuration. Even with perfect information about all of these components, prediction of traversability is difficult. Characteristics of a mobility system are designed and can later be calibrated. In most planetary terrain, terrain geometry can be measured with stereo cameras, though this can be challenging in smooth sand with little texture. Unfortunately, estimating the strength of a granular material before contact is extremely difficult. This thesis addresses the improvement of mobility prediction using thermal measurements.

For a given rover, wheel-terrain interaction in a loose granular material is strongly influenced by particle size distribution and density [24]. Having a less uniform distribution of particle sizes with larger particles increases soil strength [75, 107]. Similarly, denser, more compact sands are more traversable than fine, loose sands [156, 170]. In addition, as particles become cemented together the terrain becomes more cohesive and, thus, easier to traverse [88, 166]. The layering of materials is also important in determining wheel-terrain interaction. A thin layer of windblown sand over bedrock may cause wheels to slip at high slopes but it does not pose the threat of sinkage and embedding that thick sand does [8].

Vision-based techniques have achieved some success in predicting traversability for relatively coarse terrain classes in terrestrial environments. Unfortunately, they are fundamentally limited by only sensing the surface of a material. State-of-the-art, vision-based methods only see surface appearance at macroscopic scale, and can have difficulty detecting subtle differences in material

properties. Traditional sensing methods, such as cameras and LIDAR, measure the color, texture, and geometry of the most superficial surface layer, which is not necessarily correlated to the bulk mechanical properties of a granular material below the surface. For example, two granular materials can have the exact same particle shape and size distribution but vary in the consolidation of individual particles and therefore density. The denser material would be stronger and more traversable than the looser one. However, when viewing the surface of the same two materials at macroscopic scale, the difference would be subtle and difficult to detect.

The inherent difficulty of predicting slip is exacerbated by the risk-averse nature of planetary rover missions that avoid any potentially hazardous sand regions whenever possible. Most terrestrial-based related research uses traversability models that are learned from experiences. With enough experience, a strictly vision-based machine learning approach could be suitable for the planetary domain. However, in practice it is nearly impossible to obtain the necessary training data due to mission constraints. If a terrestrial platform becomes embedded in sand, a human can pull it out. However, if a billion dollar planetary rover is trapped, the mission ends. Consequently, rover planners are very conservative. They avoid traveling through even potentially hazardous areas. This results in few training examples from which to learn a competent prediction model. Consequently feature-intensive, visual approaches that only consider surface appearance risk significant over-fitting.

To overcome the limitations of visual techniques and find an exteroceptive measurement physically correlated to wheel-terrain interaction, this thesis looks to thermal imaging for a physics-based approach. In the visual spectrum, cameras can only measure light reflected from the surface of terrain. In the infrared spectrum, the predominant source of radiation coming from the surface of terrain is not reflection but thermal emission [113]. This emitted thermal radiation is strongly influenced by the temperatures and thermal properties both at and below the surface. In a granular material, the bulk thermal properties are strongly influenced by many of the same physical characteristics that influence wheel-terrain interaction, including particle size distribution, density, layering, and cementation. Thus by estimating the thermal properties of terrain, a rover can gain insight into both its physical properties and wheel-terrain interaction. This relationship has long been used to infer global geologic composition for scientific applications; however, no significant analysis has addressed its applicability to rover traversability prediction. In addition, this analysis has primarily occurred using thermal instruments on orbiting satellites, which do not have fine enough resolution to identify all hazards that a rover could encounter.

Thermal inertia is property of a material that controls its resistance to changes in temperature. Thermal inertia is strongly correlated to the physical properties of granular materials [129] but is independent of the chemical composition and albedo [77]. This thesis uses thermal inertia as a single measurement that is correlated to the underlying granular properties that govern wheel-terrain interaction. In general, more dense, cemented, rockier materials have higher thermal inertia than loose, uncemented, fine materials. A thin layer of a low thermal inertia material (sand) over a higher thermal inertia material (rock) will appear to have higher thermal inertia than the same materials with a far deeper surface layer. These are the same physical properties that control wheel interaction. Thereby thermal inertia could distinguish a harmless scenario from a potentially hazardous scenario for a rover. This thesis develops and analyzes an approach for differentiating between safe and hazardous granular terrain by leveraging estimates of its thermal inertia derived from observations of temperature from a rover-mounted sensor.

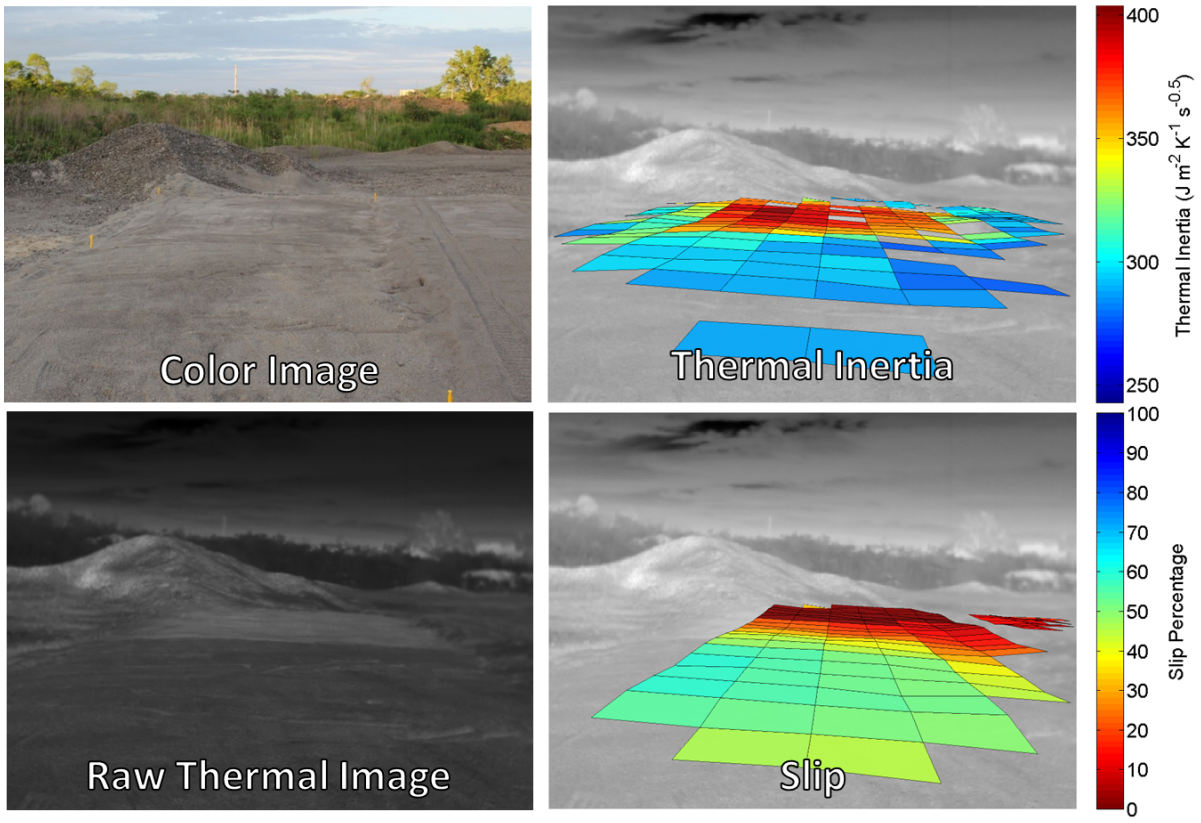

Figure 1.4: A transition from loose to compact sand regions. The loose region was manually loosened with a shovel, and the compact region was compacted with a vibratory compactor. Thermal inertia was estimated by fitting nighttime surface temperatures to an analytical model. A rover was driven across the scene several times with an applied drag force from a sled. Slip was measured by comparing distance from wheel odometry to ground truth distance measured by tracking a survey prism on the rover.

The thermal properties of terrain can be estimated by application of a heat flux to a surface, observing the resulting temperature response, and fitting the result to an analytical model. The heat flux causes the temperature of both the surface and subsurface to change. The resulting surface temperatures are strongly influenced by the thermal properties of the terrain. Estimates of the surface heat fluxes are used to fit of observed temperatures to a physics-based mathematical model to solve for thermal properties. Using an analytical model rather than merely differences in surface temperature enables comparison of thermal properties of terrain for different times of day, seasons, albedos (reflectivities), and heat fluxes. A terrestrial example showing the potential of thermal inertia to improve slip prediction is shown in Figure 1.4.

Two heat flux sources are explored in this thesis for estimating the thermal properties of terrain measured from rover-mounted instruments: (1) existing, natural heat fluxes from the Sun and atmosphere and (2) radiation from a rover-mounted laser. The use of natural fluxes from the environment has the benefit that the entire area around a rover is heated and its thermal properties can be estimated and compared. The long period of illumination (one day on the given body)

allows for the surface temperature to be influenced by terrain further below the surface. When using a laser to heat the terrain as a robot drives, the period of illumination is much shorter, so thermal measurements are influenced by much shallower depths. Measurement is also limited to areas illuminated by the laser rather than the entire environment.

However, using a laser to heat the terrain enables measurement of thermal properties at all times of a day. This is in contrast to the use of environmental fluxes where certain times of day illuminate differences in thermal properties better than others. The other benefit of using a laser is that the amount of radiation incident on the surface is well-known. When relying on environmental fluxes, differences in atmospheric conditions or reflection and emission from the surrounding terrain can make it difficult to know exactly how much heat is applied.

When using thermal inertia to differentiate between loose and compact terrain, either relative comparisons or absolute measurements can be used. Absolute measurements of thermal inertia enable classification of terrain as safe or hazardous. Comparisons can be made across kilometers, days, and seasons. However, errors in radiometric calibration of thermal imagery and surface heat flux estimation introduce error in thermal inertia estimates. Because these errors vary over time but are independent of terrain, relative comparisons between thermal inertia measurements taken at the same time and place have lower relative error. Higher thermal inertia measurement more reliably correspond to more traversable areas. Absolute measurements apply best to environments with even, predictable heat fluxes and warmer temperatures for accurate radiometric calibration (i.e. Mars). Relative, local comparison of thermal inertia can be applied on any planetary body where there are measurable temperature differences between hazardous and loose terrain.

Experiments evaluate the ability of thermal properties to separate loose and compact terrain on Earth. However, one of the primary goals of this research is to determine the efficacy of the proposed approach in predicting traversability on both the Moon and Mars. In particular, it is critical to understand whether thermal inertia improves traversability prediction, how much, and under what conditions. The Moon and Mars are the most relevant planetary exploration environments where these techniques could be used but pose very different problems due to differences in granular materials, atmospheric thermal effects, and availability of data from prior missions. In addition, due to differences caused by geology, gravity, and atmospheric pressure, showing a correlation between thermal inertia and mobility on Earth is not a guarantee that the same correlation exists on Mars or the Moon. For Mars, efficacy is evaluated both empirically using data from the Curiosity rover and in simulation. Unfortunately, significant empirical data is not abundant for the Moon, so applicability is analyzed in simulation.

Results in this thesis will show that thermal inertia has great potential to improve traversability prediction on future Mars missions. Mars has near-ideal conditions that produce large temperature variations between different types of terrain. It also has warm enough surface temperatures and a cloud-less atmosphere that enable accurate thermal inertia measurements. On the Moon and Earth, applicability is more limited. On the Moon, this thesis will show that in permanently shadowed polar craters and at night, hazardous, loose regolith is detectable by thermal sensing. However, during the day due to the long diurnal period and very low thermal inertias, there is no measurable temperature difference between loose and compact regolith. Finally, experiments on Earth demonstrate that, in most cases, vegetation, water content, a thick atmosphere, and clouds preclude the use of thermal imaging for confident traversability prediction. Applicability on Earth is limited to very dry, desert environments.

1.3 Thesis Statement

This thesis asserts that rover-scale measurements of the thermal properties of terrain improve traversability prediction in planetary environments by differentiating between loose and compact granular materials.

- **Planetary Environments**: Dry environments with no vegetation and minimal to no atmosphere, characteristic of the Moon and Mars.
- **Granular Material**: A collection of macroscopic rock particles that can take different sizes, shapes, and packing configurations.
- **Rover-Scale Measurements**: Measurements with high enough resolution to isolate regions of approximately the size of a rover.

1.4 Thesis Outline

The remainder of this thesis profiles background and related work, presents and tests the two approaches for estimation of terrain thermal properties and traversability prediction from a rover, and analyzes how these approaches apply to Mars and the Moon.

Chapter 2 presents an overview of related work in traversability prediction and thermal terrain analysis. The state-of-practice in traversability estimation is exhibited by the Mars rovers but is limited by computational and mission constraints of space missions. The state-of-the-art in traversability prediction on Earth uses both vision-based learning algorithms and physics-based wheel-terrain interaction simulators.

Chapter 3 establishes the physical correlation between the thermal properties of terrain and wheel-terrain interaction. The specific relationships among the most important physical properties of granular materials, thermal inertia, and traversability are presented and analyzed.

The following two chapters present and test two different approaches for traversability prediction using thermal information. Chapter 4 uses a low-power laser to induce a transient temperature response, estimate thermal diffusivity, and distinguish between different densities of the same material. Testing occurred in a laboratory environment using three different lunar regolith simulants. Chapter 5 instead relies on existing solar and atmospheric radiation to produce a thermal response, estimate thermal inertia, and predict traversability. Two different terrestrial experiments demonstrate the ability of thermal inertia to distinguish between loose and compact terrain and analyze how the efficacy of this approach varies throughout the day.

Chapters 6 and 7 analyze how well this approach could apply to rovers operating on Mars and the Moon, respectively. In Chapter 6, data from the Curiosity rover is used to demonstrate that estimates of thermal inertia improves traversability prediction over the state of practice by distinguishing between low- and high-slip sand. Unlike on Mars, there is no significant amount of rover data available. Consequently all of the analysis in Chapter 7 uses simulations with thermal properties measured from returned Apollo samples. This chapter analyzes under what conditions loose and compact regolith can be distinguished by surface temperature. Emphasis is placed on permanently shadowed polar craters where there is minimal incident solar radiation.

Chapter 8 summarizes the results and analysis from previous chapter to discuss how, where, and when thermal inertia can improve traversability prediction. Additional thermal simulations are presented that evaluate how well thermal inertia can distinguish between different terrains on Mars and how instrument resolution affects results.

Finally, Chapter 9 concludes by discussing the contributions of this thesis and directions for future research.

Chapter 2

Related Work

This thesis improves traversability prediction in planetary, granular terrain by using thermal inertia to distinguish between strong and weak granular materials. This chapter contextualizes the research within state-of-the-art approaches for mobility prediction.

Section 2.1 discusses the state of practice for traversability prediction on Mars. Planetary rover autonomy generally lags behind cutting-edge terrestrial research due to limited computation power and risk-averse missions. Consequently, current approaches are generally low-risk and computationally efficient.

Section 2.1.1 presents relevant prior research in the field of physics-based traverse simulation applied to granular, planetary terrain. These approaches use physics-based models of a rover and wheel-terrain interaction to forward-simulate the forces acting upon and resulting dynamics of the rover. They rely on known terrain properties.

Section 2.2 overviews prior work on vision-based traversability prediction in terrestrial and planetary analog environments. These approaches use cameras, LIDAR, or a combination of the two to assess terrain before contact. Most learn traversability models based on prior experiences using either close-range geometric or proprioceptive measurements to inform long-range prediction.

Finally, Section 2.3 discusses related research on using thermal imaging to improve traversability prediction. Thermal inertia has primarily been used from orbit to analyze surface geology both for scientific purposes and for long-range rover planning. It is not currently used for day-to-day hazard avoidance

2.1 State of Practice on Mars

The current state of practice for traversability prediction in planetary environments is exhibited by the Mars Rovers. This occurs at several levels: (1) long-term strategic planning using orbital data products, (2) ground-based slip prediction using rover imagery and Earth-calibrated models, (3) terrain assessment during autonomous drives, and (4) safe-guarding using slip estimates from visual odometry (VO).

The goals of pre-landing and mid-mission strategic planning are to determine the overarching science goals and path for the rover mission [153]. When determining a global-scale path for a

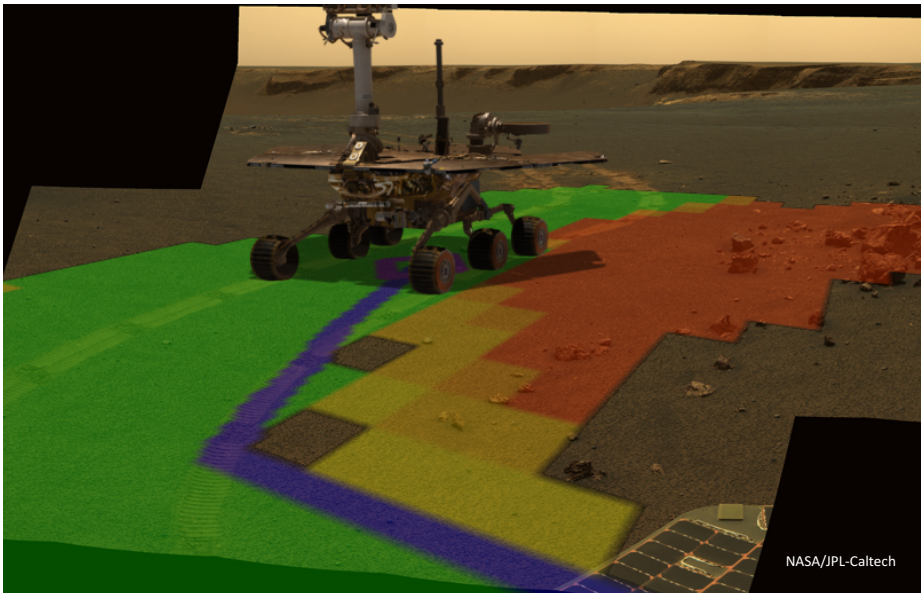

Figure 2.1: Illustration of a scaled terrain goodness map generated by GESTALT. Green indicates good areas and red indicates more hazardous areas. Note how GESTALT identifies the rocky areas as hazardous. Image credit: [96].

rover, traversability is estimated from orbital imagery. Both slope and appearance are considered to predict what drive modes, if any, are possible for different areas on the surface. Slip prediction for daily, tactical planning is done manually on Earth. Rover operators first visually analyze the type of terrain, then estimate slip by checking slope vs. slip curves for a given terrain class. These curves were calculated through extensive Earth-based testing at the JPL Mars Yard and Dumont Dunes for loose sand, consolidated sand, and bedrock classes [67]. The Earth-calibrated curves are surprisingly accurate at predicting slip in relatively benign terrain. However, in loose sand, average terrain slope alone fails to fully account for the slip behavior [40, 132]

When the rovers are driving autonomously, they use the Grid-based Estimation of Surface Traversability Applied to Local Terrain (GESTALT) system [53], which evolved from the Morphin algorithm developed at CMU [140, 141]. GESTALT assesses terrain based on its geometry as inferred from stereo imagery. Slope, roughness, and step height are estimated and then thresholded to estimate the traversability of terrain. GESTALT works well for safeguarding a rover from geometric obstacles, but does not address prediction of slip in hazardous loose sand. An example of output from GESTALT is shown in Figure 2.1.

Due to computational cost, the rover is rarely commanded to navigate autonomously. Instead, most rover traverses are designed by rover operators and drive blindly with the exception of safeguarding by VO-based slip detection [96]. Slip is estimated by comparing distance traveled from VO to no-slip wheel odometry distance. Slip is defined as:

$$s = \begin{cases} 1 - \frac{v}{v_{ref}}, & v < v_{ref} \text{ (driving)} \\ \frac{v_{ref}}{v} - 1, & v > v_{ref} \text{ (braking)} \end{cases} \tag{2.1}$$

where v is the rover's velocity and v_{ref} is the commanded velocity. A positive slip means that the rover is traveling slower than commanded, and a negative slip means the rover is traveling faster than commanded [168]. Slip varies between -1 and 1. In this thesis, all slip values represented as percentages by multiplying s by 100.

For the Mars rovers, when slip exceeds an operator-defined threshold, the rover ceases operations in order to prevent from further entrenchment and waits for instruction from Earth. This approach has a couple drawbacks. First, VO computation slows down driving. This is a greater problem with the MER rovers than Curiosity due to Curiosity's increased processing power, which is why Curiosity calculates VO more often than Opportunity [97]. Second, by the time slip is sensed, it the rover may already be trapped in sand.

Terrain analysis using on-board processing for the Mars rovers has primarily addressed the problem of autonomous targeting for science sampling in rocks. The Autonomous Exploration for Gathering Increased Science (AEGIS) system currently running on the Opportunity rover is being tested for autonomous targeting of the ChemCam spectrometer. AEGIS can use two different methods to detect interesting science targets, Rockster and TextureCam. Rockster detects rocks by looking at enclosed edges in gray scale imagery [44, 45]. TextureCam uses a random forest classifier to differentiate geologic surfaces based on texture in the imagery [155]. Neither of these methods attempt to estimate traversability.

2.1.1 Rover Traverse Simulation

By combining wheel-terrain interaction models with multi-body dynamics simulations, traverses of full vehicles over granular terrain can be simulated. A dynamics simulator iteratively calls a wheel-terrain interaction library to compute forces and torques acting on each wheel of a rover. It then integrates the forces over time to estimate rover motion. Most of these approaches use classical Bekker-Wong semi-analytical equations to model the forces and torques acting on each wheel and then forward-simulate the dynamics of the full rover [168]. Some of the basic ideas behind these models will be described in Section 3.4.1. Such simulations are used for simulation of rover traverses in two ways: (1) estimation of mobility performance in future drives and (2) terrain parameter estimation from prior drives.

Future traverse performance is estimated by forward simulation of rover dynamics and wheel-terrain interaction given known soil properties. Several different groups have implemented such simulations including Krenn and Hirzinger at the German Aerospace Center [85] and Negrut et al. at The University of Wisconsin Madison [102]. The ARTEMIS (Adams-based Rover Terramechanics and Mobility Interaction Simulator) wheel-terrain interaction software developed by Arvidson et al. has recently been used for simulation of drives for the Mars rovers with reasonable accuracy [150, 172]. ARTEMIS currently classical terramechanics models for deformable soils. It takes as input a digital terrain model, soil characteristics, and a vehicle model [172]. Using this information the simulation can provide reasonable estimates of wheel slip and sinkage. ARTEMIS has been validated in single-wheel test beds, terrestrial full vehicle tests, and using Mars data [67, 172].

Rover traverse simulation can also be used to estimate soil properties from completed drives. Estimated values of slip, sinkage, and wheel torques from simulation are compared to rover telemetry to find the best-fit terrain parameters [72]. In this way, a rover is used as a "virtual

instrument" to estimate soil properties while it drives [7]. Unfortunately, these models are have many parameters, which leads to multiple local minima during optimization [72].

More recently particle simulations are becoming more popular for estimating wheel-terrain interaction. Particle simulations (e.g. LIGGGHTS [82]) use discrete element methods to individually model particles and better approximate particle forces and dynamics. This approach has successfully been applied to simulate traverses in both lunar [93, 108] and Martian [78, 83] terrain. Discrete element methods have more parameters and can achieve better results than Bekker-Wong equations. However, they have significantly higher computational cost [143].

The most critical drawback is that all of these approaches require detailed knowledge of the physical characteristics granular material to ensure accuracy. For example, ARTEMIS requires at least 11 parameters to describe the surface of the terrain [172]. These physical properties can be estimated by fitting the simulated to observed telemetry data but are difficult to estimate from non-contact sensor measurements [72]. This research addresses the remote estimation of soil strength using thermal imaging. Detailed estimation of specific physical properties (e.g. density, shear strength, etc.) is not addressed in this thesis but could be explored in future work.

2.2 Visual and Geometric Traversability Prediction

Prior work on non-contact traversability prediction for robots operating in natural environments has primarily focused on appearance- and geometry-based methods. Traversability prediction became the subject of heavy research after the Defense Advanced Research Projects Agency (DARPA) helped advance outdoor autonomous driving through the Learning for Autonomous Ground Robots (LAGR) program [76]. Most research has addressed *near-to-far* architectures that train long-range, appearance-based classification using ground truth traversability measurements. In the context of this thesis, approaches from related research generally fall into two groups whether they learn their ground truth from: (1) direct proprioception or (2) heuristics and expert labeling.

Direct Proprioception

Proprioceptive traversability measurements refer to measurements that require a rover to be in contact with the terrain. These include measurements of wheel torques, terrain roughness from IMU, wheel slip, and wheel sinkage. A popular *near-to-far* traversability prediction approach is to train a long-range classifier to use geometric and/or visual information to predict these proprioceptive measurements. This framework requires robots to collect large amounts of proprioceptive ground truth data and associated exteroceptive measurements.

Groups at MIT and Caltech have explicitly addressed estimating mobility in granular materials. At MIT, Halatci et al. applied a naive Bayes fusion of individual Support Vector Machines (SVMs) that used color, texture, and depth from Mars Exploration Rover stereo imagery to classify terrain into three different traversability classes: rocky, sandy, and mixed [61]. This was later expanded by Brooks and Iagnemma to enable self-supervised learning of traversability prediction by training on proprioceptive data. The lower bound of coefficient of traction was estimated by discretizing the possible range of values and using a multi-class classifier. This research achieved

(a) Sand, soil, gravel, and woodchip terrains tested in Angelova, et al. Image credit: [2].

(b) Beach terrain tested in Brooks and Iagnemma. Image credit: [21].

Figure 2.2: Example images of terrain types tested in related work on traversability prediction in granular materials.

"reasonable results" in a beach environment (shown in Figure 2.2b) but did not have ground truth for quantitative results [21, 22].

At Caltech, Angelova et al. developed a mixture of experts approach for explicitly predicting slip. First, terrain classes are estimated from texture in camera imagery using the majority vote of nearest neighbors a dictionary of textons as features. Then, given a terrain class, a slip predictor is learned from the estimated pitch and roll of a robot on the terrain using a receptive field regression algorithm [134, 145]. These algorithms achieved about 20% RMS error when tested in soil, sand, gravel, asphalt, and wood chips (shown in Figure 2.2a) [2, 3]. This algorithm was later tested in the JPL Mars Yard as part of an integrated path planning and slip prediction architecture, but quantitative results on slip accuracy are not reported [65]. Both groups address slip-prediction in granular materials. However, they only analyze benign sand environments. Planetary environments are much more varied with extremely loose materials and varying surface morphologies (i.e. ripples) that can endanger rovers. The also only considered coarse terrain classes rather than attempting to differentiate between different types of sand as is addressed in this thesis.

Many other researchers have more broadly developed techniques that learn to predict traversability using proprioceptive feedback without specifically tackling the non-geometric hazards posed by granular materials. Stavens and Thrun developed a technique to predict road roughness for the DARPA Grand Challenge. Roughness was measured using IMU feedback on the robot. Long-range evaluation was possible by correlating ground-truth roughness to local elevation differences as measured in the LIDAR point cloud [147]. Ho et al. addressed the problem of estimating control uncertainty in both rigid and deformable terrain by using a Gaussian Process to map from rover control predicted from geometry to a distribution of rover controls learned

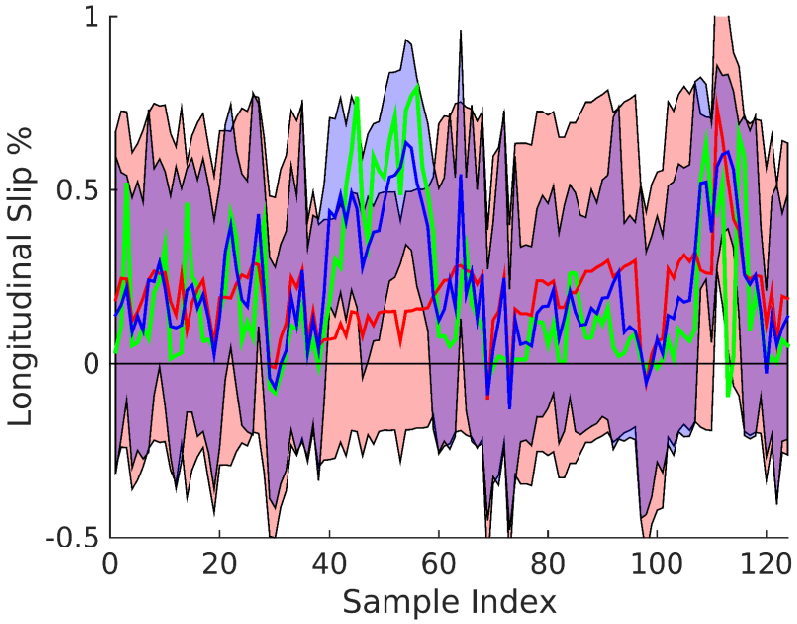

Figure 2.3: Comparison of slip prediction algorithm with and without local adaptation on a subset of Curiosity's drives through sand. Green is ground truth, red does not use local adaptation, and blue includes local adaptation. Shaded areas represent 2.5 standard deviation bounds. Predictions were made for 1 m ahead of the robot [40].

from rover experience. The deformable terrains tested were unstable rock piles and not loose sand [68, 69, 117]. Other groups have also used color and texture features from camera imagery to learn to predict based on onboard sensors, such as IMUs, motor currents, bumpers, and suspension angles [81, 84].

Even with perfect information about the terrain and robot, it is still difficult to predict traversability due to the complexity of the rover-terrain interaction. On a uniformly sloped surface, slip is predicted with relative ease using only slope angle. However, many areas contain complex terrain geometries like dunes and ripples that influence wheel-terrain interaction. Even with no pitch or roll, a rover can still slip significantly due to local slopes caused by sinkage or ripples. Complex, polygonal dune structures have proven particularly problematic for Curiosity [8]. To overcome the inability to identify visual differences in sand properties, Cunningham et al. leverage spatial correlations between slip measurements. A rover learns prediction models using all slip data and adapts to new terrain using data local to the rover. Using this local information improves prediction accuracy for regions several meters ahead of a rover [40]. Figure 2.3 shows an example of this local adaptation. Note how the local model (green) is adapts to high slip regions better than the basic model. However, this approach still requires proprioceptive measurements of slip and cannot detect differences in sand traversability from range.

In some cases, to determine the traversability of terrain, more high fidelity terrain modeling is used. This was pioneered by Wellington et al., who developed algorithms for predicting the load-bearing surface in heavily vegetated areas for agricultural applications. They used a voxel-column representation in a MRF framework to learn obstacle detection and traversability

prediction despite partially the ground being partially occluded by vegetation. Ground truth ground height was measured by the robot driving over the terrain [162, 163, 164].

To learn a mobility model in this way requires many training samples that are drawn from a distribution representing all of the terrain a robot will encounter. However, planetary mission planners are very risk-averse. Very few samples are taken in areas that might be hazardous because these are actively avoided in order to safeguard the mission. This makes it difficult to build a feature-rich, vision-based model based solely on vehicle experience.

Heuristics and Expert Labeling

Instead of direct proprioception, other approaches have used human experts or heuristics to evaluate ground-truth traversability. For example, an obstacle might be detected as a large deviation from the ground plane based on stereo-measured geometry. However, because stereo does not produce high accuracy geometric measurements at long range (e.g. further than 10 m for the LAGR robots) [12], a monocular classifier can be used to mimic its close-range capabilities.

Hadsell et al. used a deep convolutional neural network (CNN) to predict obstacles at up to 40 m range from monocular imagery based on stereo training data. Ground truth obstacles were determined heuristically based on deviation from the ground plane in stereo [59, 60]. Vernaza et al. used a similar close-range obstacle definition but used submodular Markov Random Fields (MRFs) to classify at long range [154].

Many approaches learned their ground truth from human experts. Happold et al. approached this problem by representing the traversability cost of terrain as the sum of geometric features that included height variation, slope, and the percent of points above the ground plane. Ground truth traversability labeling was done by a human expert that labeled terrain as one of four cost classes (low, intermediate, high, or lethal). They then trained a neural network to predict this cost from color in imagery using the geometric features [63]. Bajracharya et al. more simply trained a two-class SVM to predict long-range traversability in color imagery based on training data from a close-range classifier. The close-range, geometric classifier was first trained manually by an operator. However, in one test they also demonstrated the ability for the close-range classifier to be learned through self-supervised proprioceptive feedback [12, 13, 71]. Berczi et al. trained a Gaussian Process Classifier to detect traversable versus untraversable terrain based on roughness from stereo imagery. Ground truth was also from human labeling [19]. *Near–to–far* learning has even been shown to be effective at training an algorithm to predict traversability from orbital imagery. In this case, ground truth traversal costs were learned through imitation learning in which the robot learned a cost function that aimed to mimic the decisions that a human driver would make [10, 144].

Both heuristics and human labeling are insufficient for traversability prediction in granular planetary terrain. The main problem is that humans are not always good at intuitively determining what is and what isn't traversable by a robot on another planetary body as evidenced by the troubles the Mars rovers have encountered to date.

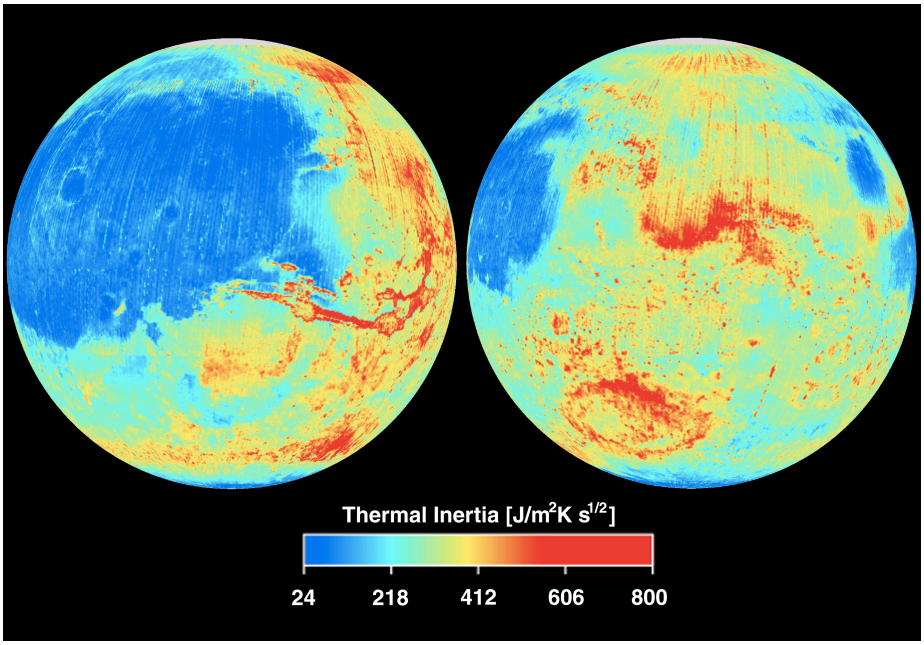

Figure 2.4: Mars global thermal inertia maps generated using orbital Thermal Emission Spectrometer (TES) data. Image credit: NASA/JPL

Limitations of Vision-Based Methods

The downfall of prior approaches is that they learn mobility models only from imagery and/or geometry. They have shown success in outdoor domains with macro-scale, rigid obstacles like trees or rocks. However, detecting hazardous, loose terrain in planetary environments is more difficult. The visible differences between consolidated and loose sand are much more subtle. Appearance can be used to associate similar terrain but cannot measure important characteristics such as compaction. As a result, terrain patches with similar appearance, but dissimilar compositions and traversability, can have an ambiguous classification when using only geometry and appearance data. This research seeks to overcome this problem by incorporating thermal inertia, which is directly influenced by physical properties of the terrain that influence wheel-terrain interaction.

2.3 Thermal Terrain Analysis

In contrast to visual imagery, thermal measurements provide information about the bulk mechanical properties both at and below the surface [127]. Thermal imaging has been used for terrain in analysis primarily for scientific applications. The relationship between thermal inertia and the physical properties of terrain has been used to infer geological composition at global scale on Earth [125], the Moon [16, 151], and Mars [48, 103] using data from orbital instruments. An example showing global thermal inertia for Mars is shown in Figure 2.4.

The analysis of orbital infrared imagery was used to help select landing sites for the Mars rover missions that were both safe and scientifically interesting [47, 54]. Orbital thermal data is also used by mission planners when selecting long-term routes for the rovers. However, orbital data

has low resolution and cannot be used to detect all rover-scale hazards. For example, THEMIS only has a resolution of 100 m per pixel, which is the highest thermal resolution available on Mars [32]. This is not high enough resolution to detect all hazards facing a 2 m scale rover. Analysis in Section 8.5 will demonstrate that orbital imagery resolution is not fine enough to detect rover-scale hazards.

Measurements from rover-board sensors provide the ability to get much higher resolution data. The Miniature Thermal Emission Spectrometer (Mini-TES) instruments aboard the Mars Exploration Rovers and the Ground Temperature Sensor (GTS) aboard Curiosity have been used to estimate the thermophysical properties of the Martian surface primarily for scientific investigation [46, 62, 98]. These instruments, however, only give very sparse spatial coverage and are not used to inform day-to-day rover operations. This thesis will investigate the extent to which high-resolution thermal inertia measured from on-board instruments can be used to detect loose terrain hazards in planetary environments. Certain times of day are better for sensing differences in thermal inertia. This research will explore both how to use thermal inertia as well as limitations caused by times of day and lengths of observations.

Some terrestrial research has applied thermal imaging for obstacle detection as well. Caillas estimated thermal inertia and showed that it could be used to distinguish rock from sand for planetary robotic applications [23]. Matthies and Rankin used thermal imagery to detect negative obstacles (e.g. ditches and potholes) by observing that the interiors of potholes remain warmer than the surrounding terrain [101]. Recent work by González et al. applied thermal inertia estimation to identify terrain for terrestrial applications. They showed that thermal inertia can distinguish between wet and dry sand as well as identify vegetation [55]. These papers, however, did not address differences in particle size distribution and density that are critical in planetary rover applications.

Chapter 3

Relating Thermal Inertia to Mobility

The key idea of this thesis is that measurements of the thermal properties of terrain improve traversability predictions in granular materials by providing insight into wheel-terrain interaction. This chapter provides background on granular materials, thermal properties, and terramechanics. Then a correlation between traversability and thermal inertia is established by observing that they are both dependent on bulk density, particle size distribution, and cementation.

First, Section 3.1 provides an overview of the most important physical characteristics of granular materials considered in this work. Section 3.2 presents an overview of the thermal model that relates heat fluxes and surface temperatures to the thermal properties of a material. Section 3.3 discusses thermal inertia and how different granular properties affect it. Similarly, Section 3.4 presents background information about wheel-terrain interaction and how it relates to the physical properties of terrain. Finally, 3.5 summarizes the analysis and clearly defines the correlation between thermal inertia and mobility.

3.1 Physical Properties of Granular Materials

Carrier identifies the most important properties of lunar soil to be: particle size distribution, particle shape, and density (both absolute and relative) [24]. These properties are determined by the mineralogy of the material, how the particles were formed, and how the particles are sorted. This thesis also considers cementation of particles and layering of multiple heterogeneous materials as both are very important in mobility and thermal response, especially on Mars. This section outlines the most important physical properties of granular materials that relate to both the geotechnical and thermal properties.

Particle Size Distribution The particle size distribution of a granular material describes the relative abundance of different sizes of particles. In geology literature, a well-sorted material contains all grains of approximately the same size. A poorly-sorted material contains a much wider mixture of grain sizes. A poorly-sorted material generally has lower porosity than a well sorted material as the voids between the larger particles become filled by smaller particles. Figure 3.1 illustrates the differences between well- and poorly-sorted particle size distributions. In

engineering literature, grading is used instead of sorting to describe particle size distributions. Poorly-graded materials are well-sorted, and well-graded materials are poorly-sorted.

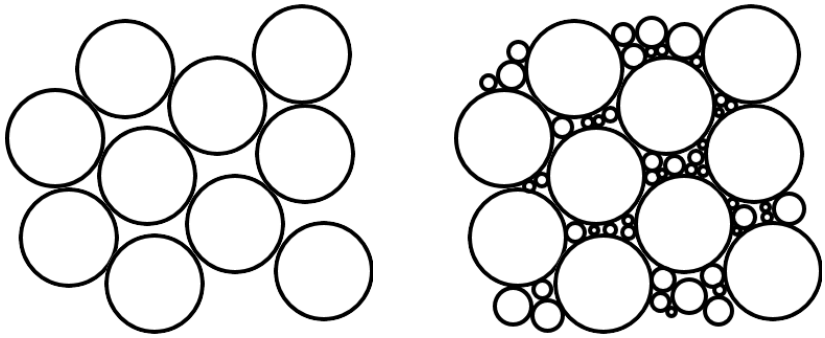

Figure 3.1: Illustration of differences between particle size distributions. The left image shows a well sorted granular material composed of spherical particles. The right image shows a poorly sorted material consisting of the same large particles with smaller grains added in the voids.

Particle Shape The shape of particles in a granular material are artifacts from the formation history of the material. A particle's shape is described by its: (1) eccentricity, (2) angularity, and (3) roughness. Eccentricity describes how much a particle deviates from a perfect sphere. Angularity describes how sharp the corners of the particle are. Roughness describes the smaller-scale texture of the surface [30].

Density Bulk density (ρ) is defined as the mass of a material divided by the volume. Density is related to and controlled by several other physical properties. For example, more irregular particle shapes enable a material to obtain a wider range of packing densities [30]. Sorting also has a significant affect on density. A sample with uniform large particles has a lower bulk density than the same sample with added small particles to fill the interstitial voids. When holding all other parameters (e.g. particle sizes and shapes) constant, changing density corresponds to a change in the packing configuration of a material.

Both the absolute density of a material and the relative density of a material are important in both thermal and mobility analysis. The relative density of a granular material is defined as [26]:

$$D_r = \frac{\rho_{max}}{\rho} \frac{\rho - \rho_{min}}{\rho_{max} - \rho_{min}} \times 100 \tag{3.1}$$

where ρ_{max} and ρ_{min} are the maximum and minimum achievable densities of the material. Intuitively, relative density represents where the current bulk density, ρ, falls in the range between ρ_{min} and ρ_{max}. Although relative density is extremely important [24], it is very difficult to measure outside of a laboratory. Compacting a material increases both its relative and bulk density. Similarly, loosening a material decreases both its relative and bulk density. In this thesis, changing "density" will primarily refer to changing relative density while holding all other parameters constant.

Cementation As a granular material becomes more cemented, its particles become more bonded. The process responsible for the deposition of bonding materials varies. The most common process is through the precipitation of soluble minerals resulting from evaporation of water [115]. The term duricrust refers to the crust resulting from the cementing of a granular material. Duricrust is abundant on Mars [77]. There is some evidence of a thin duricrust on the surface of the Moon. However, the origin of this lunar duricrust and whether it exists at all is debated in the scientific community [64].

Layering Most planetary terrain is not a homogeneous mixtures of a single type of material but rather a combination of different materials. Examples include wind-blown sand covering a surface of bedrock and the density of lunar regolith continuously increasing with depth below the surface. For simplicity, quantitative analysis in this thesis will consider vertical layering with a discrete number of materials rather than continuous distributions of densities and particle sizes.

3.2 Thermal Model

The surface temperatures of terrain are governed by a balance of heat fluxes at the surface, including heat radiated from the surface, conducted into the surface, and absorbed from both the Sun and the atmosphere. This section outlines the analytical temperature model and how it relates to the thermal properties of a material.

3.2.1 Analytical Model

A thermal model is presented here following the derivation in Putzig [129]. Both the surface and subsurface temperature of homogeneous terrain is governed by the well-known, semi-infinite one-dimensional heat diffusion equation.

$$\frac{\partial T}{\partial t} = \frac{k}{\rho c} \frac{\partial^2 T}{\partial Z^2} \tag{3.2}$$

where k is thermal conductivity, ρ is bulk density, c is specific heat capacity, Z is the distance into the terrain, and t is time. The lower boundary condition is usually assumed to be either insulating or a constant geothermal heat flux.

Let $Z' = Z/\delta$. At $Z = \delta$ the temperature wave is attenuated by a factor of e^{-1} [129]. δ is known as the thermal skin depth defined by:

$$\delta^2 = \frac{k}{\rho c} \frac{P}{\pi} \tag{3.3}$$

The surface boundary condition at $Z' = 0$ is balance of heat fluxes from the Sun, the atmosphere, and the ground.

$$(1 - A)R_{sw} + \epsilon R_{lw} - \epsilon \sigma T_s^4 = -I \sqrt{\frac{\pi}{P}} \left. \frac{\partial T}{\partial Z'} \right|_{Z'=0} \tag{3.4}$$

where A is albedo, ϵ is emissivity, σ is the Stefan–Boltzmann constant, P is the period of a diurnal cycle, R_{sw} is shortwave radiation from the Sun, R_{lw} is longwave radiation emitted by the atmosphere, T_s is the surface temperature, and $\frac{\partial T}{\partial Z'}\Big|_{Z'=0}$ is the temperature gradient at the surface.

The most important term in Equation 3.4 is I, which represents the thermal inertia. Thermal inertia is defined as:

$$I = \sqrt{k\rho c} \tag{3.5}$$

with units of $Jm^{-2}K^{-1}s^{-\frac{1}{2}}$ [129]. A change of variables in Equation 3.2 from Z to Z' results in:

$$\frac{\partial T}{\partial t} = \frac{\pi}{P}\frac{\partial^2 T}{\partial Z'^2} \tag{3.6}$$

This isolates all of the influences of terrain properties on surface temperatures in I. Hence under periodic illumination, with known surface heat fluxes, emissivity, and albedo, thermal inertia controls the surface temperature. Thermal inertia can be estimated by fitting observed surface temperatures to an analytical model [103]. For more detailed derivations see [129] and [80].

3.2.2 Parameter Effects

Numerous parameters affect surface temperatures in varying degrees. To provide an understanding of the effect of the major variables, several figures are presented that vary these parameters. These examples are evaluated in the context of Mars using the KRC analytical model [80]. More details about this model will be presented in Section 6.1.1. Figure 3.2 shows R_s and R_lw over the course of a day. Solar radiation is much more significant than atmospheric radiation. However, this is not always the case as will be discussed in the context of permanently shadowed craters in Chapter 7.

Figure 3.3 shows the effect of varying thermal inertia. Higher thermal inertia leads to a smaller temperature swing over the course of a day and vice-versa. High thermal inertia materials have higher temperatures at night and lower temperatures during the day than lower thermal inertia materials.

Figure 3.4 shows the effect of varying albedo. Albedo controls the fraction of the total the amount of incident solar radiation reflected by the terrain's surface. Albedo values range between 0 and 1. Higher albedo materials reflect more radiation than lower albedo materials. Albedo has a higher effect on surface temperature during the day than it does at night. However, a higher albedo material will have a higher temperature at all times during the day than a lower albedo material with all other parameters held constant.

Figure 3.5 shows the effect of varying emissivity. Emissivity controls how much radiation is emitted from the surface through blackbody emission at a given temperature. Emissivity values vary between 0 and 1. Higher emissivity materials emit more radiation and thus are cooler at all times during the day than lower emissivity materials. Emissivity does not have a very large effect on surface temperatures. Emissivity also does not vary significantly on planetary surfaces [62] and at times is assumed to be unity [48].

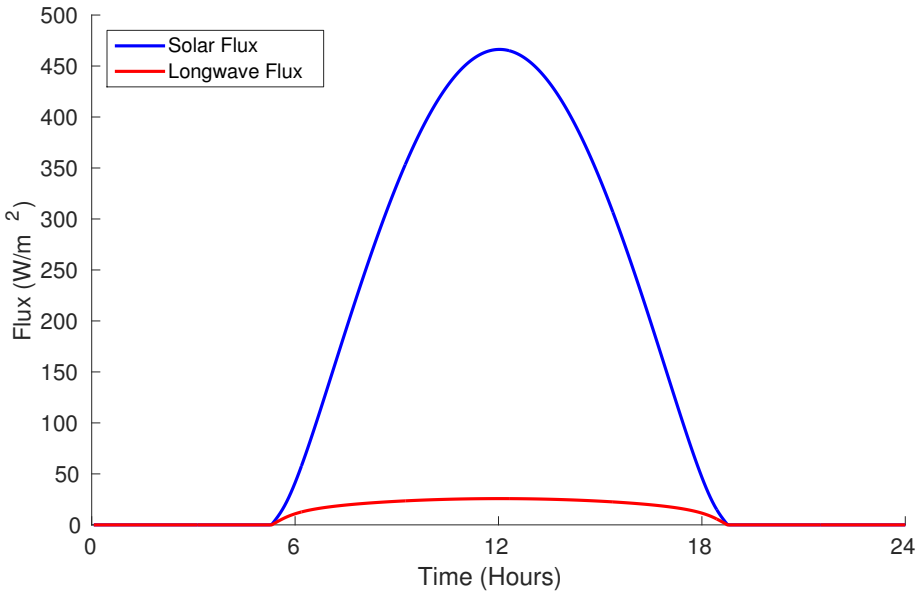

Figure 3.2: Comparison between solar and atmospheric heat fluxes on Mars plotted over the course of a sol.

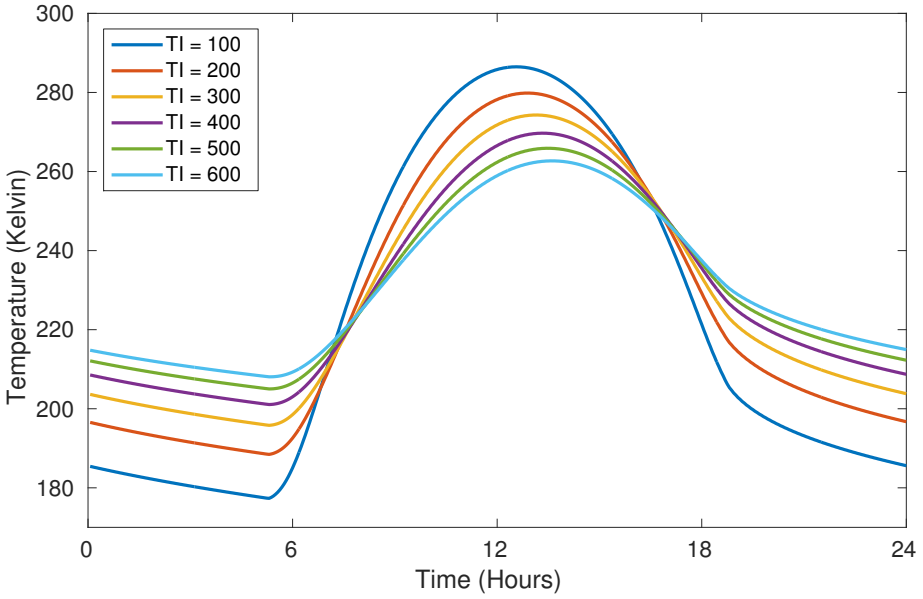

Figure 3.3: Surface temperatures for terrain with varying thermal inertia on Mars plotted over the course of a sol. Units of thermal inertia are $Jm^{-2}K^{-1}s^{-\frac{1}{2}}$.

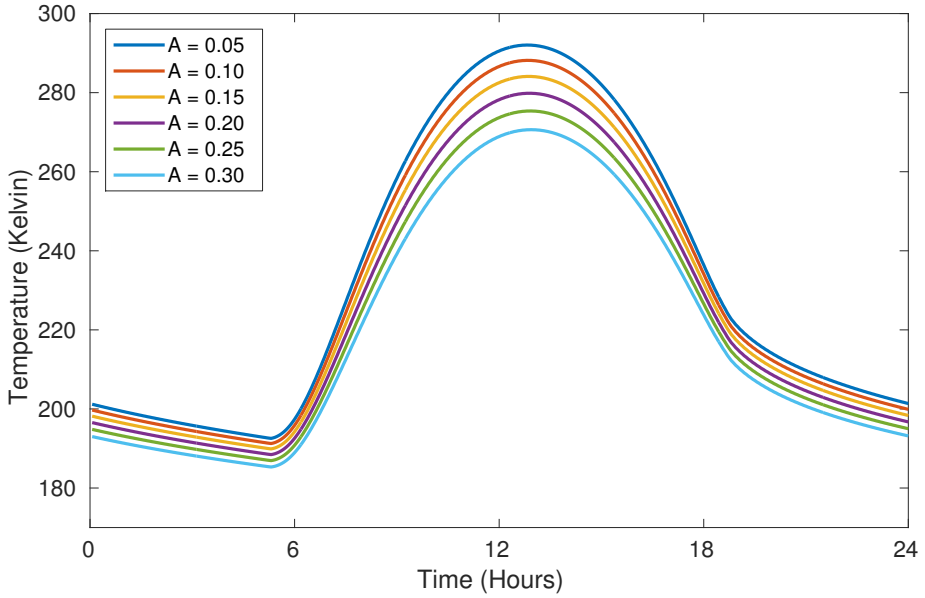

Figure 3.4: Surface temperatures for terrain with varying albedo on Mars plotted over the course of a sol.

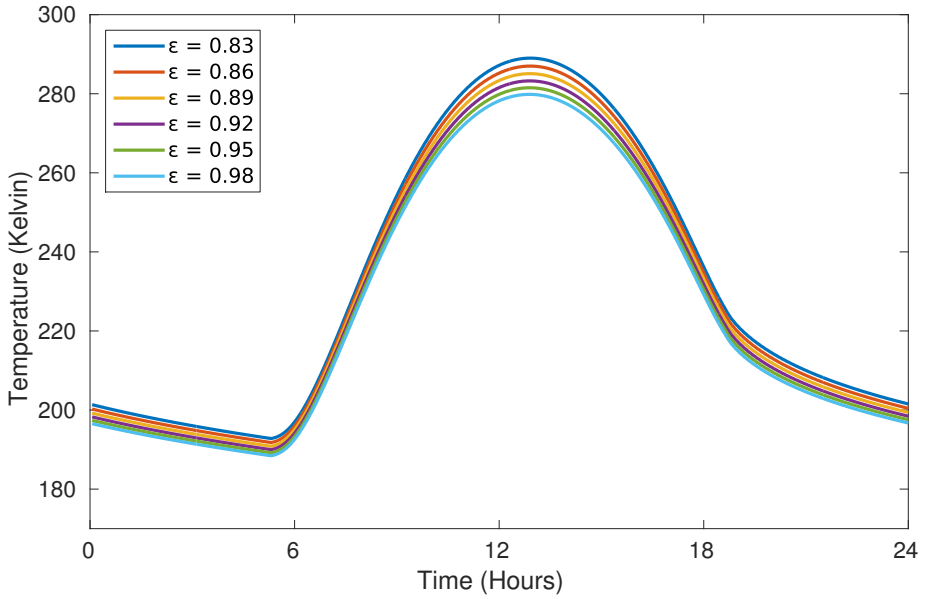

Figure 3.5: Surface temperatures for terrain with varying emissivity on Mars plotted over the course of a sol.

3.3 Thermal Inertia

Thermal inertia isolates the influence of the physical properties of terrain on diurnal surface temperature variations. It represents the resistance of a material to changes in temperature. This section discusses the factors that influence thermal inertia, including the granular properties of terrain.

3.3.1 Thermal Properties Controlling Thermal Inertia

A prerequisite for understanding the effects that physical properties have on thermal inertia is understanding the individual thermal properties and heat transfer mechanisms that control it. From Equation 3.5, thermal inertia is a function of the thermal conductivity, heat capacity, and density of a material. In a granular material, heat capacity is not strongly affected by density or particle size and varies by factors of no greater than 2 or 3 on a planetary surface. Variations in density directly affect thermal inertia as defined in Equation 3.5. However density varies by less than a factor of 2 in sandy materials [118].

The most significant factor affecting thermal inertia in granular materials is thermal conductivity [129]. In most cases, variations in thermal inertia should be directly interpreted as variations in conductivity [110]. In granular materials, bulk thermal conductivity is determined by three different heat transfer mechanisms: (1) heat conducted through gas in the void space (k_{gas}), (2) radiative heat transfer(k_{rad}), and (3) solid path heat conduction(k_{solid}) [118].

On planetary surfaces with an atmosphere, the most significant heat transfer path is by gas conduction. However, this is strongly affected by atmospheric pressure [122]. The thermal conductivity of a granular material is primarily a function of the ratio between the mean free path (λ) and effective size of pores between grains (L), where the mean free path is the average distance traveled by a gas particle before it collides with another particle [11]. This can be expressed as the Knudsen number Kn:

$$Kn = \frac{\lambda}{L} \propto \frac{T}{L\,P} \tag{3.7}$$

where P is atmospheric pressure and T is temperature [118].

When Kn is large, the mean free path is much larger than the average pore size, and the resulting gas conductivity will be low. This is the case either with small particles that have small pore sizes or when atmospheric pressure is very low. Conversely, when Kn is small, the mean free path is much smaller than the pore size. This results in a high gas conductivity, corresponding to large particles or high atmospheric pressure.

In a vacuum, $k_{gas} = 0$ and is obviously not dependent on pore size. At very high pressures, when the mean free path is significantly higher than the pore size, k_{gas} is also relatively independent of pore size thus particle size. However, in the intermediate pressure range, pore size (and consequently particle size) strongly influences gas conductivity [129, 138]. Piqueux and Christensen [118] suggest that the relationship can be captured by:

$$k_{gas} \propto \frac{1}{1 + e^{-\xi\left(Kn^{-1}\right)}} \tag{3.8}$$

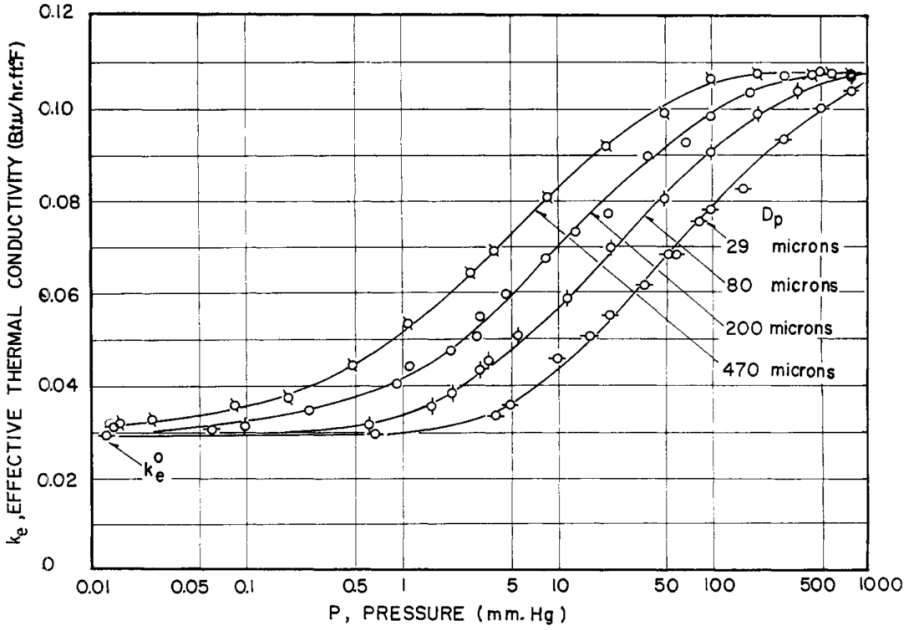

Figure 3.6: Thermal conductivities of glass beads of different sizes measured over a range of gas pressures. Image reproduced from: [99].

where ξ is some function of Kn. This can be seen experimentally through the experiments of Masamune and Smith [99] shown in Figure 3.6. At both low and high pressures, the conductivities of different sized glass beads are very similar. However, in the intermediate pressure range, particle size has a strong affect on conductivity.

Consequently, the dependence of thermal conductivity (and thermal inertia) on particle size varies based on atmospheric pressure. On the Moon, pressure 2×10^{-12} Torr[1], so thermal conductivity is minimally dependent on particle size. On Earth, average pressure is 760 Torr, so particle size is also not a significant effect. However, on Mars, average pressure is 4.5 Torr, which falls in the intermediate range. Thus, on Mars, thermal conductivity is strongly affected by particle size.

Radiative heat transfer is affected by the temperature of a material and the size of the grains. Kasparek and Vortmeyer [79] present a model that encompasses this relationship:

$$k_{rad} \propto D\sigma T^3 \tag{3.9}$$

where D is the particle diameter. Clearly larger particles with higher temperatures result in higher conductivity. However, the effect of radiative heat transfer on overall bulk thermal conductivity is much smaller than that of gas conductivity. As a result, thermal inertias on Mars and Earth are not affected by radiative heat transfer. The effect becomes more significant in a vacuum for bodies like the Moon [118, 129].

Solid path heat conduction between grains is somewhat more significant but is still dwarfed by gas conduction. Unintuitively, solid path conduction is not strongly affected by the specific

[1] 1 Torr $\approx$ 1 mmHg

properties of the solid composing the granular material but is instead limited by the small grain contacts. This is because heat travels significantly faster through a solid than through the small contacts or the gases between contacts [77]. On planetary surfaces, the amount of heat conducted through inter-grain contacts is generally small [118]. The amount of heat conducted through the solid path is primarily a function of the grain-to-grain interface [158]. More densely packed materials with more contacts between particles will have higher k_{solid} than loosely packed particles.

Because of the heat transfer limitation caused by grain contacts, *thermal inertia is not a strong function of the mineralogical composition of a granular material but rather the physical properties of its grains*. This is critical for this work since wheel-terrain interaction is also primarily dependent on physical properties rather than mineralogy.

3.3.2 Affects of Grain Properties on Thermal Inertia

The main mechanisms through which the physical properties of a granular material control heat transfer are summarized above. This section outlines the affects of the important physical characteristics of granular terrain that affect thermal inertia.

Particle Size Distribution As particle size increases, density and heat capacity tend to increase. As shown in Figure 3.6 [99], particle size has a significant affect on thermal conductivity and consequently thermal inertia. However, as explained above, k_{gas} is also strongly influenced by pressure. At Mars pressure, particle sizes strongly affect thermal inertia [122]. On the Moon, there is no atmosphere, so $k_{gas} = 0$. In this case, the radiative term becomes more important, and an increase in particle size still increases thermal inertia as evident in Equation 3.9.

Unlike in many laboratory studies, particle size distributions are not uniform on planetary surfaces. Nonuniform particle sizes result in competing affects of heat transfer mechanisms. Poorly sorted materials with a wide range of grain sizes result in higher k_{solid} by providing more contacts between particles [38]. Poorly sorted materials have higher thermal inertias than a uniform material containing only small particles [77]. Based on Equation 3.8, one might expect that, in the presence of an atmosphere, a uniform granular material's thermal inertia would go down when adding smaller particles between in the pores between the larger particles, since this would reduce the average pore size. However, for Martian pressures, this does not happen. In fact, the thermal conductivity of poorly sorted materials appear to be primarily controlled by the largest particles [121]. Thus, as density increases by adding smaller particles to a well-worted material consisting of only larger particles, thermal inertia also increases.

Density Intuitively, as particles become more packed together, heat capacity, bulk density, and thermal conductivity all increase. Consequently, thermal inertia increases as well. This relationship has been shown to hold at both Martian [121, 123] and lunar [49] pressures. At Martian pressure, the effect has been found to be particle size dependent. The thermal inertia of neither large ($> 70\mu m$) nor small ($< 25\mu m$) particle sizes were found to be strongly affected by density. However, for intermediately-sized particles, there is a near-linear relationship between packing density and thermal conductivity. Presley and Christensen found that a decrease in porosity from 72% to 40% corresponded to an increase in thermal conductivity of $\sim 30\%$ [123].

Particle Shape Particle shape, like particle size, can affect the effective heat transfer distance through the interstitial gases [123]. Experimentally, particle shape appears to primarily influence conductivity by affecting the density. More irregularly shaped particles result in a wider range of achievable densities. When comparing similarly deposited materials, angular particles form less dense states than spherical particles resulting in lower thermal conductivity and lower thermal inertia [121]. This relationship holds at both Martian and lunar pressures.

Cementation Tensity, heat capacity, and conductivity all increase as particles become cemented together [119, 127]. Piqueux and Christensen reported cementation causes increases in thermal conductivity of between a factor of 3 and 8 [119]. This is confirmed by Presley et al. who found that thermal conductivities of cemented samples increased by at least a factor of 3 over their uncemented counterparts [124]. This effect is abundant on Mars [77] due to the atmosphere and presence of water [70]. This effect is less significant on the Moon.

Layering Until this point, analysis of thermal inertia has assumed a vertically homogeneous material. However, this is rarely the case. Vertical heterogeneity has a significant impact on the temperature of a material over the course of a day. Layering obviously does not affect the thermal properties of the individual materials but effects estimated thermal inertia if layering is not explicitly taken into account [127]. Several examples of diurnal temperature curves for vertically layered materials are shown in Figure 3.7. In this example, varying depths of sand are deposited on top of bedrock. Thin layers of sand behave more like high thermal inertia materials than thicker layers. As depth increases, the effect of the bedrock on surface temperature becomes less significant. The effective depth that influences diurnal surface temperatures is controlled by the thermal skin depth of the material.

3.4 Mobility in Granular Materials

Terramechanics is a field of research that studies the interaction between wheeled vehicles and terrain, with specific focus on granular materials. The wheel-terrain interaction is difficult to model because of the complexity of particle interactions. Classical approaches use analytical Bekker-Wong equations to model relationships between wheels and deformable granular terrain in order to estimate the forces and torques on acting on a wheel [5, 18, 167, 168]. Classical terramechanics models make assumptions to enable tractable solutions, including that ground is homogeneous and that the contact area between the soil and wheel can be modeled as a flat plane. Classical approaches do not directly model physical properties like particle shapes, particle sizes, and density. Instead they model empirically derived relationships between ground contacts and forces [72]. First, Section 3.4.1 summarizes basic terramechanics principles relevant to rover mobility. Then, Section 3.4.2 discusses the relationship between traversability and the physical properties of granular materials.

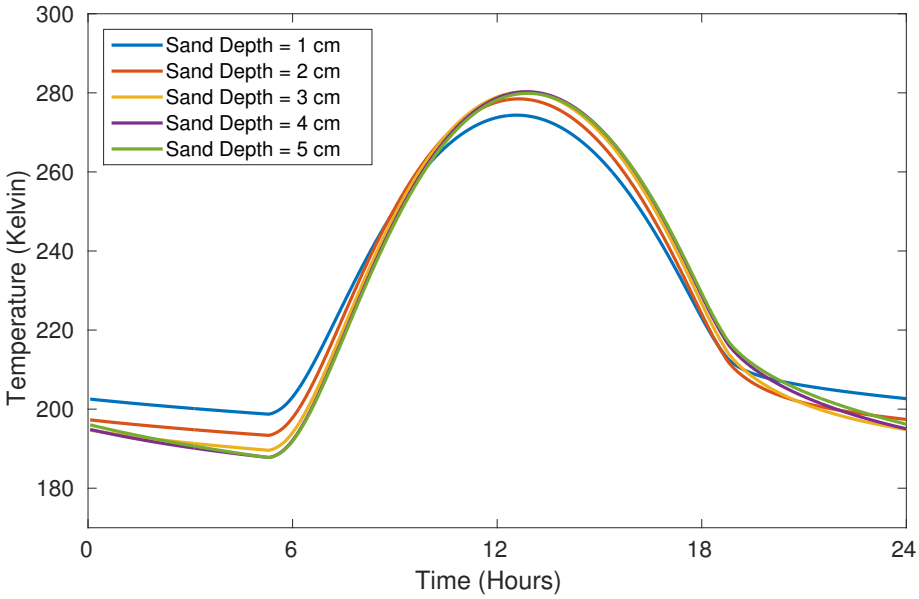

Figure 3.7: Surface temperatures for a layer of surface sand on top of bedrock for varying sand depths.

3.4.1 Terramechanics Principles

There are two fundamental principles in terramechanics, the pressure-sinkage relationship and the Mohr-Coulomb failure criterion. The pressure-sinkage relationship is a semi-empirical model that governs the depth that a wheel sinks into the terrain and, consequently, the motion resistance it experiences while driving [1]. The Mohr-Coulomb failure criterion represents the shear strength of a material as a function of normal stress [87]. The shear strength of a material governs how much traction a wheel can generate when driven [1].

The pressure-sinkage relationship is given by:

$$p = k_p z^n \tag{3.10}$$

where p is the pressure under a plate, k a proportionality constant, n is the sinkage exponent, and z is the sinkage into the surface. n and k are properties of the soil. k is also dependent on the size of the wheel or plate [106]. The pressure-sinkage relationship is important because: (1) shear stress is a function of the normal stress (i.e. pressure) and (2) motion resistance increases with increased sinkage [137].

Motion resistance is caused by components of the normal force acting against the direction of motion. Intuitively, it is the resistance caused by a wheel compacting the terrain in front of it. This is given by [168]:

$$R = \int_0^{z_0} pb\, dz \tag{3.11}$$

where R is motion resistance, z_0 is the sinkage of the wheel, and b is the width of the wheel. This is an approximation that is more accurate in wet, cohesive soils than it is in dry sand [18]. It does

not take into account soil flow present for planetary rovers [106]. However, at first order, it gives a baseline understanding that greater sinkage corresponds to greater motion resistance and thus makes terrain more difficult to traverse.

The Mohr-Coulomb failure criterion is given by:

$$\tau = c + \sigma \tan \phi \tag{3.12}$$

where c is cohesion, ϕ is the angle of internal friction, and σ is the shear stress [87]. Cohesion represents the strength of the bond holding particles together. Angle of internal friction represents the ability of a material to resist sheer stress. Both angle of internal friction and cohesion are properties of a granular material. As both parameters increase, the shear strength of a material increases, consequently, increasing terrain traversability.

In summary, increases in n and k correspond to higher sinkage for a given pressure, which generates higher motion resistance and reduces traversability. Increases in c and ϕ result in higher shear strength, which therefore increases traversability. These relationship will be referred to in the following section to tie the granular properties of a material back to traversability.

The above representations of the equations for forces acting on wheels are simplifications useful for illuminating the importance of various terms and bulk mechanical properties. When actually implementing terramechanics equations, one must take into account other factors including wheel-terrain contact angles, slip, grousers, and forces acting perpendicular to the direction of vehicle travel. More in-depth descriptions of these parameters and equations can be found in [168, 169, 172].

3.4.2 Physical Properties and Wheel-Terrain Interaction

This section outlines how physical properties affect traversability through the shear strength and compaction resistance of a granular material.

Particle Size Distribution Morgan [107] defined a power law relationship for the particle size distribution of a granular material:

$$N_i = N_{max} \left(\frac{R_{max}}{R_i} \right)^D \tag{3.13}$$

where R_{max} and R_i represent the maximum and incremental particle sizes, respectively. N_{max} and N_i represent the relative abundances of the maximum and incremental particle sizes, respectively. The particle size distribution is controlled by D. Higher values of D result in higher abundance of smaller particles in the distribution. Results showed increases in shear strength with increasing values of D [107]. This implies that the more non-uniform the material, the higher the shear strength. Igwe et al. confirm these results to show that poorly-sorted materials have higher peak shear strength than well-sorted specimens [74, 75]. Thus, in a well-sorted, fine material, traversability increases as larger particles are added. Similarly, in a well-sorted, coarse material, traversability increases as smaller particles are added.

Density Compacted materials are stronger than looser materials. As the relative density of a granular material increases, its density approaches the maximum achievable density. This subsequently reduces the amount that a load on the surface could compress it, resulting in less wheel sinkage. An increase in relative density also corresponds to an increase in both angle of internal friction and cohesion [156, 170]. Igwe et al. furthered this result to show that over a series of particle size distributions to find that increasing relative density increases strength regardless of the particle size distribution fo the material [74]. In summary, an increase in the density of a material increases its traversability.

Particle Shape It is more difficult for less spherical, rougher particles to attain dense packing configurations [4]. Consequently, both the minimum and maximum achievable densities increase as the angularity and roughness of particles increase. It follows that the range of achievable densities increases as well. Friction angle also exhibits a strong dependence on particle shapes. Rounder, more regular particles result in lower angles of internal friction. Thus, shear strength and traversability increase as particle smoothness and sphericity decrease [30, 139].

Cementation Granular material become significantly stronger as particles become more cemented together [157]. Increasing strength of the bonds between particles corresponds to increases in both the cohesion and the internal friction angle of a soil [89, 166]. It also reduces the amount that a soil compresses for a given pressure [88]. Cementation increases compaction resistance and shear strength, which makes it easier for rovers to traverse.

Layering As with the thermal properties, inhomogeneous materials complicate models that primarily assume homogeneity. Terramechanics models are not designed for either vertically or horizontally heterogeneous materials [72]. However, in many cases, the affect that layering of materials has on mobility is somewhat intuitive. For a surface layer of sand on top of bedrock, the thicker the sand the further it can sink in. On the other hand, just a dusting of sand may make the surface of bedrock slippery for a rover. Another example of critical importance is a layer of duricrust over sand. A thin layer of duricrust can make the surface more traversable; however, if it is too thin, a rovers wheels can fall through into the sand underneath.

3.5 Relating Traversability and Thermal Inertia

Sections 3.3.2 and 3.4.2 described the effects that the granular properties of a material have on the thermal inertia and traversability, respectively. This section summarizes those contributions to show that thermal inertia is strongly related to the strength of terrain.

Particle Size Distribution Thermal inertia is generally controlled by the largest particles in a material [121]. Higher thermal inertia values correspond to larger particles [122]. Mobility is affected by the particle size distribution as well. Poorly-sorted materials are stronger than well-sorted materials [75, 107]. Consider two situations:

1. Coarse particles are added to a well-sorted, fine material - Thermal inertia and traversability both increase.
2. Fine particles are removed from a poorly-sorted material - Traversability decreases. However, thermal inertia will decrease as well, but not as significantly.

In situation (1), the change in traversability corresponds to a change in thermal inertia. In situation (2), the correlation exists but is not as strong. Clearly, particle size distribution affects both thermal inertia and traversability. Generally, the presence of larger particles results in both higher traversability and thermal inertia.

Density For given particle sizes and shapes, increases in density increase both the thermal inertia [49, 121, 123] and traversability [74, 156]. Higher density materials have more contacts in between individual particles. This increases the amount of heat that can pass through the solid conduction path. Increased contacts between particles also result in a higher of internal friction and greater resistance to wheel sinkage.

Particle Shape Particle shape primarily influences thermal inertia indirectly through its explicit effect on density [123]. Traversability is also affected indirectly by the affect that particle shape has on the range of achievable densities [4]. However, particle shape also has an explicit affect on traversability, with more angular particles resulting in higher shear strength [30, 139]. Unlike other parameters discussed here, there is not an obvious, explicit correlation between traversability and thermal inertia for differences in particle shape.

Cementation For given particle sizes and shapes, increases in cementation increase both the thermal inertia [119, 124, 127] and traversability [89, 157, 166]. As bonds between particles become stronger, it is intuitive that the bulk strength of the material increases as well. The bonds also enable increased solid-path heat flow between particles, which increases thermal conductivity and inertia.

Layering Layering is more complicated and situation-dependent. Consider two situations common on Mars:

1. Sand over bedrock - Apparent thermal inertia and traversability both increase as the surface sand layer becomes more shallow.
2. Duricrust over sand - Apparent thermal inertia and traversability both decrease as the surface duricrust layer becomes more shallow.

Both of these examples illustrate the general idea that as the percentage high thermal inertia materials near the surface increases, generally so does traversability. This relationship varies based on the particular materials involved. This thesis will primarily consider the two examples presented above in the context of mobility on Mars.

3.5.1 Summary

Though there is certainly not a one-to-one correlation between traversability and thermal inertia, in general higher thermal inertia terrain indicates higher traversability. The degree to which this relationship holds depends on many factors including: materials properties, the planetary body considered, and rover characteristics. The effect that pressure has on gas conductivity makes it difficult to ensure that correlations between mobility and thermal inertia on one planetary body will translate to another. Additional difficulties arise when evaluating traversability because of differences in gravity between planetary bodies [170].

Chapter 4

Detecting Differences in Density using Laser-Induced Thermal Transients

Differences in thermal properties influence surface temperatures but require input heat flux to illuminate differences. When leveraging natural, diurnal heat fluxes, certain times of day produce ambiguous results. In order to detect differences in surface density independent of time of day, this research developed a technique that uses a laser to actively heat terrain, inducing a change in temperature. That temperature change is measured by a thermal camera and fit to a thermal model to estimate the thermal diffusivity of a granular material. This could be useful for estimating terrain properties immediately ahead of a rover to safeguard against slippage and sinkage. This chapter presents the technique, a series of laboratory tests, experimental correlations to soil strength measurements, and tests of effective measurement depth.

In this technique, thermal diffusivity is estimated instead of thermal inertia because of the ability to develop an analytical expression, which enables faster computation. It assumes that for the time scales, temperatures, and heat fluxes resulting from the use of a laser, blackbody radiation from the surface can be neglected. Diffusivity is defined as:

$$\alpha = \frac{k}{\rho c} \tag{4.1}$$

Due to the direct relationship between thermal conductivity (k) and thermal diffusivity (α), most of the same trends discussed in Chapter 3 for thermal inertia apply to diffusivity as well.

In the applied physics community, the problem of estimating the thermal diffusivity of a thin, monolithic material by inducing a thermal transient with a laser is well researched. No priors were discovered for application to granular media. Photothermal radiometry is a widely used technique for non-contact estimation of the thermal properties of thin films using an infrared detector and a single laser flash [92, 114]. This method is most effective with a thin film but has been applied to layered materials as well as powders where it can detect a difference in density [148]. Though these methods are effective in a laboratory environment, they require precisely-calibrated, sensitive instruments that are not feasible to implement on mobile robots. This research is distinct from the methods above because this method does not require the highly calibrated experimental setups used in photothermal radiometry for thin films.

Most of this chapter is published in [42].

4.1 Thermal Diffusivity Estimation

Thermal diffusivity is estimated using macroscopic measurements of the transient temperature response caused by a low-power, continuous-wave laser. The laser is pointed at the soil while a thermal camera measures the temperature response of the terrain to laser excitation. The camera and the laser are driven over the soil, at a modest height and constant velocity. The thermal diffusivity of the soil is estimated by fitting parameters of a known model to the transient thermal response of the material to the laser. Differences in density are detected through differences in estimated diffusivity.

4.1.1 Model Derivation

The mathematical model of the thermal response is derived from the three-dimensional heat diffusion equation, which governs heat flow.

$$\frac{\partial T}{\partial t} = \alpha \left(\frac{\partial^2 T}{\partial x^2} + \frac{\partial^2 T}{\partial y^2} + \frac{\partial^2 T}{\partial z^2} \right) \tag{4.2}$$

T is the temperature at a point (x, y, z) in a Cartesian coordinate system, and α is the thermal diffusivity of the material. The material under test is modeled as a semi-infinite plane extending from $z = 0$ in the negative z direction. The diffusion equation is subject to a Neumann boundary condition at $z = 0$.

$$\frac{\partial T}{\partial z} = 0, z = 0 \tag{4.3}$$

This boundary condition makes the assumption that there is no heat lost at the sample surface [92]. The incident heat from the laser is modeled as a Gaussian instead of a uniform distribution, which is more physically accurate and allows for some helpful mathematical simplifications [34].

$$L(x', y', z', t') = \frac{Q}{2\pi r^2} exp \left(-\frac{(x' - vt')^2 + y'^2}{2r^2} \right) \delta(z') \tag{4.4}$$

L represents a Gaussian laser in the plane $z = 0$ moving along the x-axis at $y = 0$. Q is the total power from the laser absorbed by the material, v is the velocity of the laser in the x direction, and r is the radius of the laser spot. Because this problem is addressed macroscopically and the absorption depth of the laser is very shallow, it is assumed that all of the power from the laser is absorbed at the surface of the material [28]. The Green's function for a point source in three-dimensions subject to the boundary condition given above is used to find the equation for the temperature at a point (x, y, z). This Green's function is given by Carslaw and Jaeger [27] and represents the temperature of a point (x, y, z, t) in response to a unit point source at (x', y', z', t').

$$G(x, y, z, t, x', y', z', t') = \frac{1}{4\left(\pi\alpha(t - t')\right)^{\frac{3}{2}}} exp \left(-\frac{(x - x')^2 + (y - y')^2 + (z - z')^2}{4\alpha(t - t')} \right) \tag{4.5}$$

The equation for the heat flow from the laser is used in conjunction with the Green's function to find the temperature at any (x, y, z, t) due to the laser excitation. An offset T_0 is added to represent the initial temperature before laser excitation.

$$T(x,y,z,t) = \int_{-\infty}^{t}\int_{-\infty}^{\infty}\int_{-\infty}^{\infty}\int_{-\infty}^{\infty} L(x',y',z',t')G(x,y,z,t,x',y',z',t')\,dz'dy'dx'dt' + T_0 \tag{4.6}$$

This solution is simplified using the recipricocity and translation properties of Green's functions and the fact that the integrals over $x\prime$ and $y\prime$ can be simplified to gaussian forms, which result in known solutions. The final result is a formula for the temperature at $(x, y, z, 0)$ [58].

$$T(x,y,z,0) = Q\int_0^{\infty} \frac{exp\left(-\frac{(x+vt')^2+y^2}{2r^2+4\alpha t'} - \frac{z^2}{4\alpha t'}\right)}{\sqrt{\pi^3\alpha t'}(2r^2+4\alpha t')}\,dt' + T_0 \tag{4.7}$$

Thus, the temperature at $(x, y, z, 0)$ is only a function of a few variables. T_0 can be easily measured from a thermal camera before the laser excitation. In this paper, v is experimentally controlled. r is estimated by calibrating the laser. The two unknown variables are the thermal diffusivity of the material under test, α, and the amount of power absorbed by the material, Q, which is a function of both the laser and the material.

4.1.2 Diffusivity Estimation

To estimate the thermal diffusivity constant of a material, data is extracted from a thermal image to directly correspond to T_x, which is the model (4.7) evaluated at $y = 0$, $z = 0$, and $t = 0$.

$$T_x(x\,;\,x_{off},Q,\alpha) = Q\int_0^{\infty} \frac{exp\left(-\frac{(x+x_{off}+vt')^2}{2r^2+4\alpha t'}\right)}{\sqrt{\pi^3\alpha t'}(2r^2+4\alpha t')}\,dt' + T_0 \tag{4.8}$$

An example thermal image is shown in Figure 4.1. The maximum temperature in the y direction occurs along the x-axis at $y = 0$, so it is straightforward to extract the maximum temperature in the y direction for every pixel column. These are $(x, T_x(x))$ data points, where translational alignment of the x values with the model is still ambiguous. To align the data points with the model, all x values are translated so that $x = 0$ corresponds to the maximum T_x value. Pixel distances are scaled to the equivalent linear distance on the material.

The approximation that the maximum temperature occurs at $x = 0$ is not always true. With low velocity, high diffusivity, and a small laser spot radius, the temperature response is nearly symmetric about the y-axis with a maximum at $x = 0$. However, as the quantity vr/α increases, the response becomes less symmetric, and the maximum of the curve shifts towards more negative values of x. Thus the maximum value in the x-direction is not easily predicted as it is dependent on the velocity and radius of the laser as well as the diffusivity of the material under test [34, 105, 133]. For the velocities, diffusivities, and radii considered in this paper, the maximum occurs close enough to make the approximation that it is at $x = 0$. In (4.8), x_{off} is an offset value used to compensate for errors in x-alignment. First is the error that occurs through the assumption that

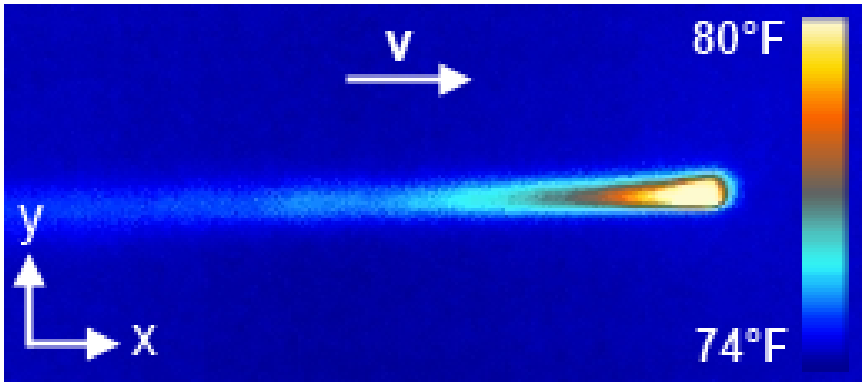

Figure 4.1: Thermal transient produced by a 100mW 532nm laser being translated at a constant velocity on a loose preparation of JSC-1A. $\vec{v}$ shows the direction of the motion of the laser.

the position of the maximum temperature corresponds to $x = 0$, when in fact it does not. Second is error that arises when the resolution of the camera is not high enough to precisely capture the x value of the maximum temperature of the thermal response.

The resulting (position,temperature) data points are used to fit Equation 4.8. The three parameters are x_{off}, Q, and α. T_0 is estimated from the mean temperature of the surrounding material. r is estimated before the experiment through analysis of a static laser pulse [95]. v is known as it is controlled by the experimental setup. An optimization algorithm is used to minimize the squared error between the experimental data and Equation 4.8 evaluated at estimates of x_{off}, Q, and α.

Thermal diffusivity, α, can then be used to detect when the material type or density of the terrain has changed. For a given material, a lower diffusivity corresponds to a lower bulk density and therefore less traction. Likewise, a higher diffusivity corresponds to a higher bulk density and therefore more traction. Thus, if a rover is driving in a safe material and suddenly measures a sharp drop in α in the terrain ahead, it should be cautious or choose another route.

4.2 Experimental Validation

Several experiments were conducted to estimate thermal diffusivity using the method presented in this paper and verify the correlation to density and traversability. A thermal camera is used to capture the transient temperature response caused by a moving laser. Recorded thermal images are then analyzed to produce estimates for thermal diffusivity on both loose and compact granular materials. The experiments evaluated the correlation between density, estimated diffusivity, and pressure-sinkage behavior.

4.2.1 Detecting Density Differences in Lunar Simulants

Three lunar regolith simulants were used in these experiments, JSC-1A, BP-1, and GRC-1. All three simulants were used in both loose and compact preparations. Loose preparation consisted of pouring the material into a sample container, hand agitation with a shovel, and gentle leveling to

Figure 4.2: Three simulants were used for experimental validation. From left to right, JSC-1A, BP-1, and GRC-1.

create a flat surface. Compact preparation utilized a hydraulic press on a flat steel plate top until maximum pressure was achieved.

Data to validate thermal diffusivity estimation was collected using a controlled setup. The experimental setup is shown in Figure 4.3. A thermal camera and a continuous-wave 100 mW 532 nm laser were mounted to a linear mill and pointed down at a sample container containing either a loose or compact simulant. The thermal camera recorded images at 7 Hz. The mill was driven at 2.5 mm/s, 3.8 mm/s, 5.1 mm/s, and 6.4 mm/s. The laser point was translated 0.25 m, from one end of the sample container to the other.

Several example plots for different materials, densities, and velocities are shown in Figure 4.4. The amplitude of the peak of the curves were primarily controlled by the speed of the laser. A slower laser means that more heat can be absorbed. The decay rate of the temperature was primarily controlled by the compaction level. More compact materials absorbed heat into the subsurface much more efficiently than loose materials.

The experimental data was fit to the model (4.8) using the parameters α, Q, and x_{off}. Example best-fit curves are shown in Figure 4.5. The blue points are the measured temperatures and the red line is the analytical model. Four runs at different velocities were averaged together provide estimated values for α and Q for loose and compact preparations of all three simulants. A bar graph showing a comparison between estimated diffusivity values for loose and compact soil is shown in Figure 4.6. This demonstrates that, in all three simulants, this approach distinguishes the difference between loose and compact preparations. This is confirmed by a Mann-Whitney U-test, which tests the hypothesis that a randomly selected compact sample will have higher diffusivity than a randomly selected loose sample. The null hypothesis is that the compact sample would have equal or lower diffusivity. In all three simulants, the hypothesis was confidently confirmed with a p-value of 0.014.

4.3 Validation with Pressure-Sinkage Curves

Connection between diffusivity and traversability is validated with empirical testing using a bevameter instrument to measure soil strength (shown in Figure 4.7). Bevameter measurements are a well-known technique for predicting the response of terrain to a ground vehicle. A bevameter performs two primary functions with high repeatability. Firstly, a sinkage test presses a flat

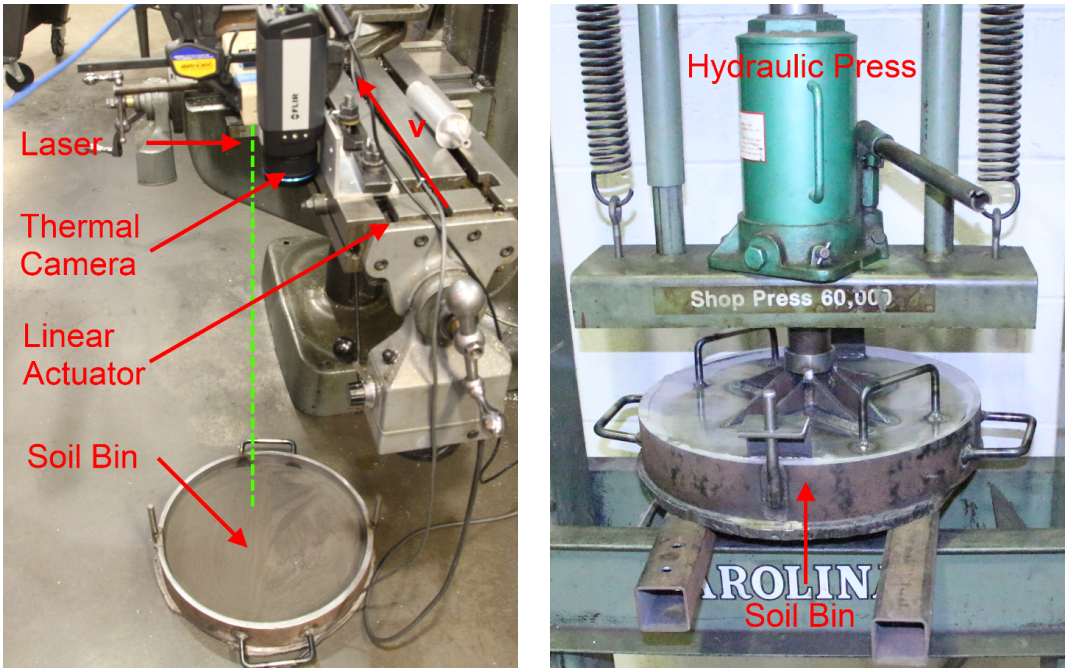

Figure 4.3: Experimental setup for thermal diffusivity experiments (left). A 100mW 532nm continuous-wave laser and a thermal camera are mounted to a linear actuator and translated a constant velocity parallel to a soil sample below. A hyraulic press (left) and compressable soil bin with lid are used to repeatably prepare compressed soil samples.

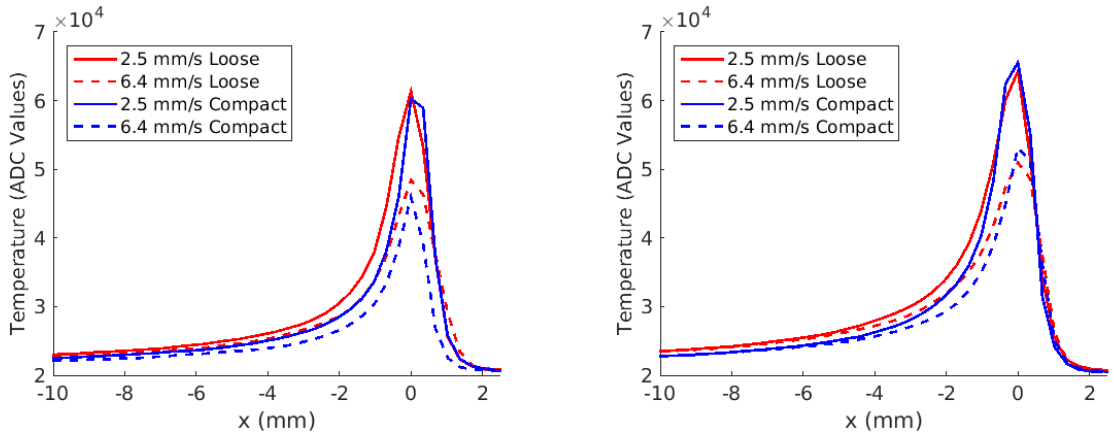

(a) BP-1 (b) JSC-1A

Figure 4.4: Comparison of different laser velocities for loose and compact preparations of both JSC-1A and BP-1. Note that the slower velocity results in a higher amplitude and that decay-time of temperature is a strong function of compaction.

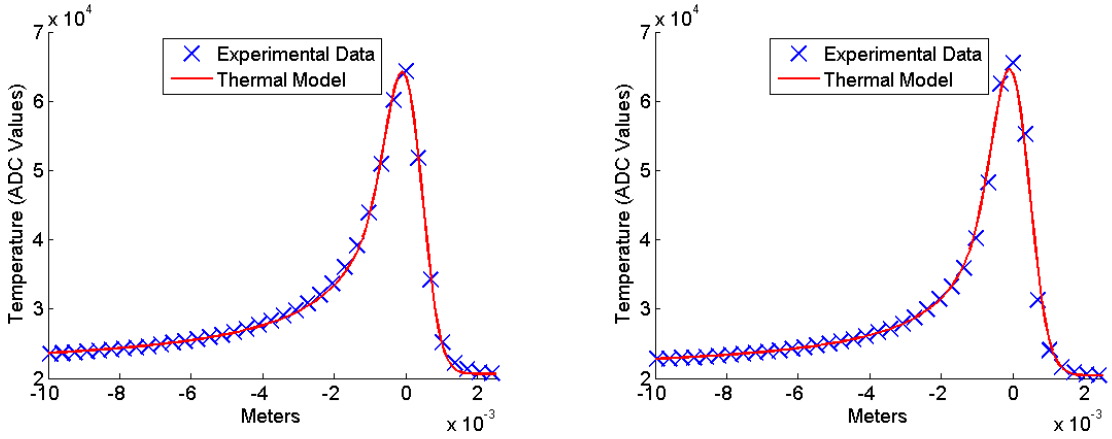

(a) Loose (b) Compact

Figure 4.5: Comparison of experimentally measured temperatures and temperatures estimated from the theoretical model for loose and compact JSC-1A at a laser speed of 2.5 mm/s.

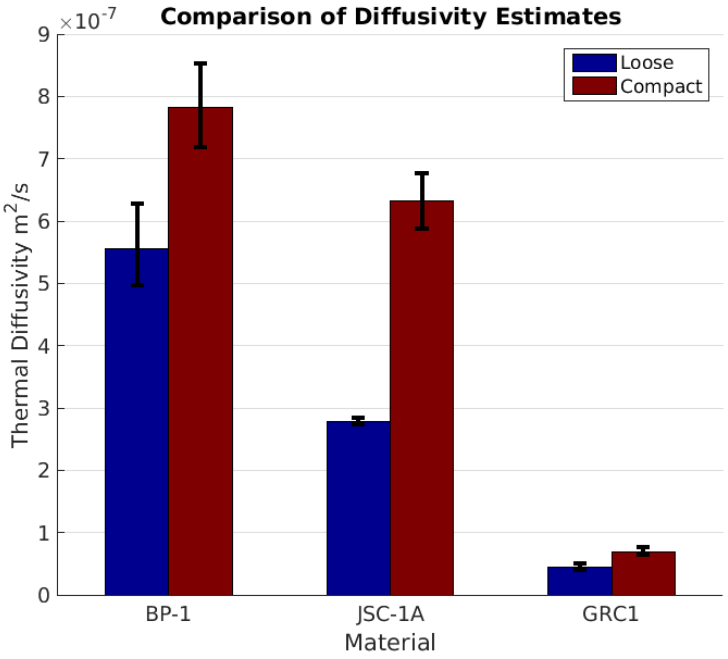

Figure 4.6: Estimated thermal diffusivities (α) of JSC-1A, BP-1, and GRC-1 averaged over four laser velocities. Error bars show maximum and minimum measured diffusivity. Demonstrates a measurable difference between compact and loose granular media.

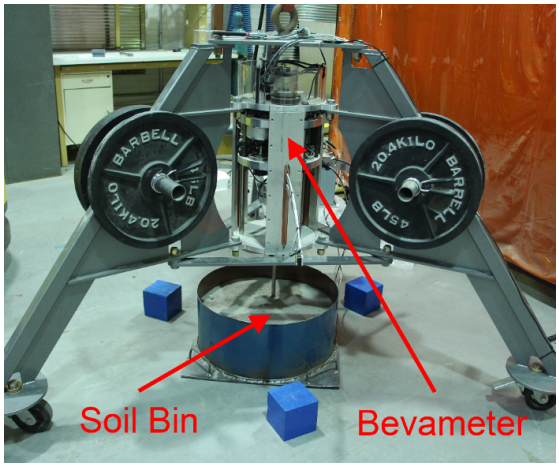

Figure 4.7: A bevameter was used for measuring soil strength.

circular plate into a soil sample while recording ground pressure exerted and linear displacement. Secondly, a shear test presses and rotates a toothed annulus while recording pressure, torque, and displacement. The intent of these functions is to mimic how a robot might sink or slip while negotiating a material [168]. As such, the end effectors are sized to reproduce the ground contact area and traction of a specific wheel (or track) design. The recording of force-displacement data produces a curve that spans robot weights and predicts sink or slip given the wheel design. This work focused on the pressure-sinkage aspect of bevameter testing.

Three to four pressure-sinkage trials were conducted on each of three test materials (BP-1, JSC-1A, GRC-1) under loose and compact preparation. The bevameter measured force-displacement curves by slowly pushing a circular plate with a 5 cm diameter into the material. In all tests, a sample approximately 18 cm deep was utilized; due to edge effects, results for very high ground pressure vehicles ($>$ 400 kPa) may be skewed for some materials. Linear models were fit to each $\{$soil type, compaction level$\}$ sample. This is equivalent to setting the sinkage exponent (n) in Equation 3.10 to 1. Comparisons are then made based on the pressure-sinkage coefficient (k_p). Figure 4.8 shows the individual trials and the best-fit model for each soil type.

Experimental data confirmed that the estimate of thermal diffusivity is can successfully differentiate different densities of granular materials, and that density is directly related to a material's resistance to rover sinkage. Figure 4.9 shows the pressure-sinkage curves for all materials and compaction levels tested. The best-fit pressure-sinkage coefficients are presented in Figure 4.1. Lower sinkages and smaller coefficients indicate a stronger material and easier mobility. Results generally have high certainty for pressures under 400 kPa. In this range, compact BP-1 is empirically the strongest material, while both forms of GRC-1 were the weakest - resulting in greatest sinkage. The strength-order of material combinations here correspond directly to the estimated diffusivity.

This work demonstrates an empirical correlation between measured thermal diffusivity and soil strength. Results measured 56%, 29%, and 35% differences in diffusivity from compact preparations to loose preparations for JSC-1A, BP-1, and GRC-1, respectively. These correspond to percent increases in the pressure-sinkage coefficients from compact to loose material of 56% for JSC-1A, 117% for BP-1, and 22% for GRC-1. The strength-order of material combinations

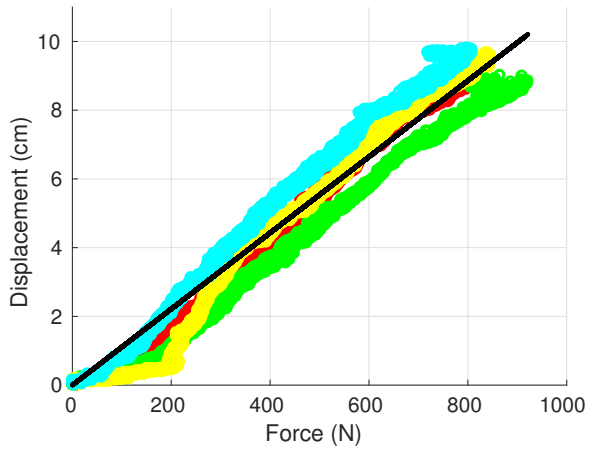

(a) Compact JSC-1A.

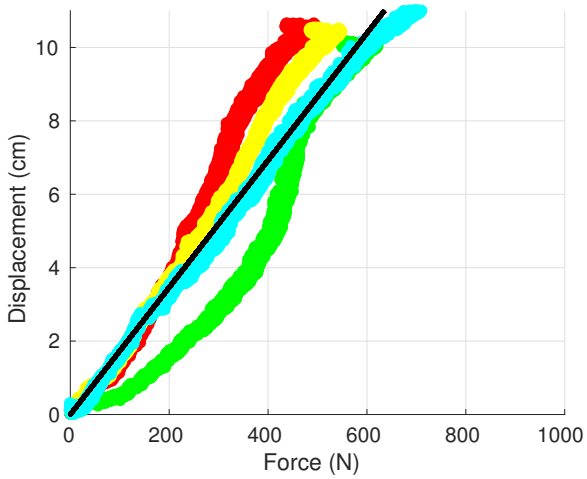

(b) Loose JSC-1A.

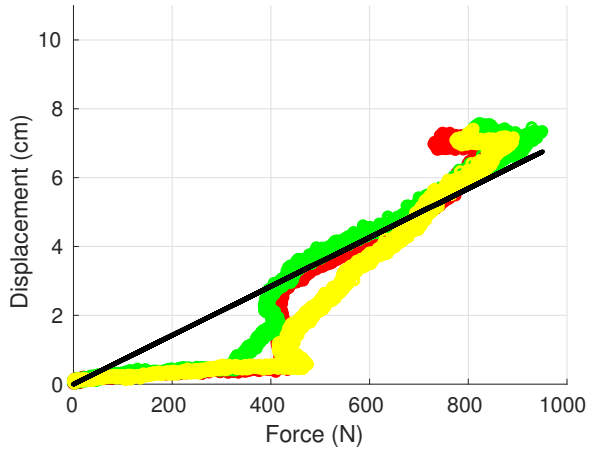

(c) Compact BP-1.

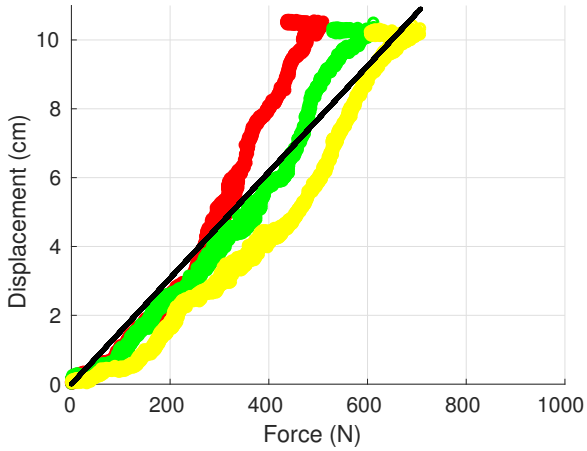

(d) Loose BP-1.

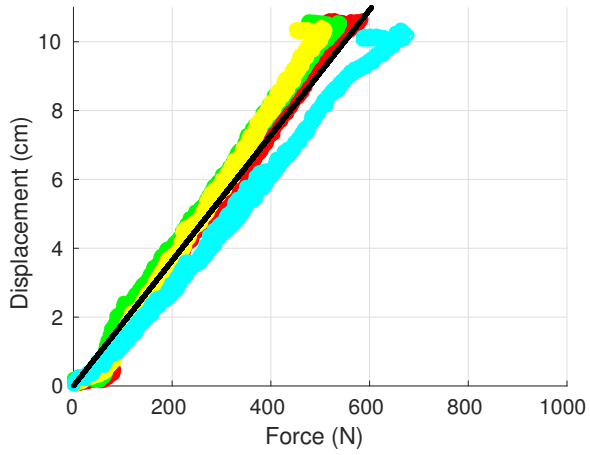

(e) Compact GRC-1.

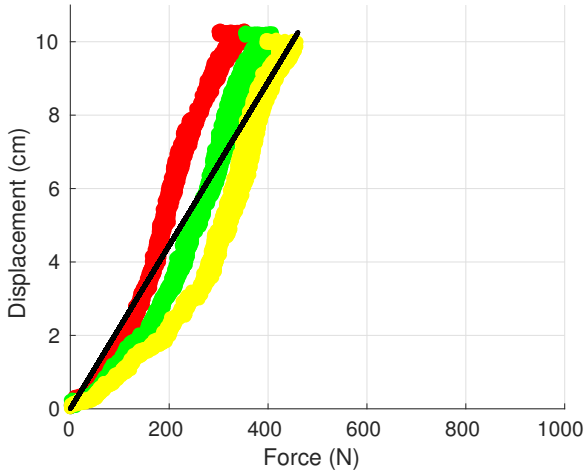

(f) Loose GRC-1.

Figure 4.8: Comparison of bevameter-measured force-displacement curves and best-fit linear models. In each plot the colored lines represent different trials for each soil sample. The black line represents the linear approximation

.

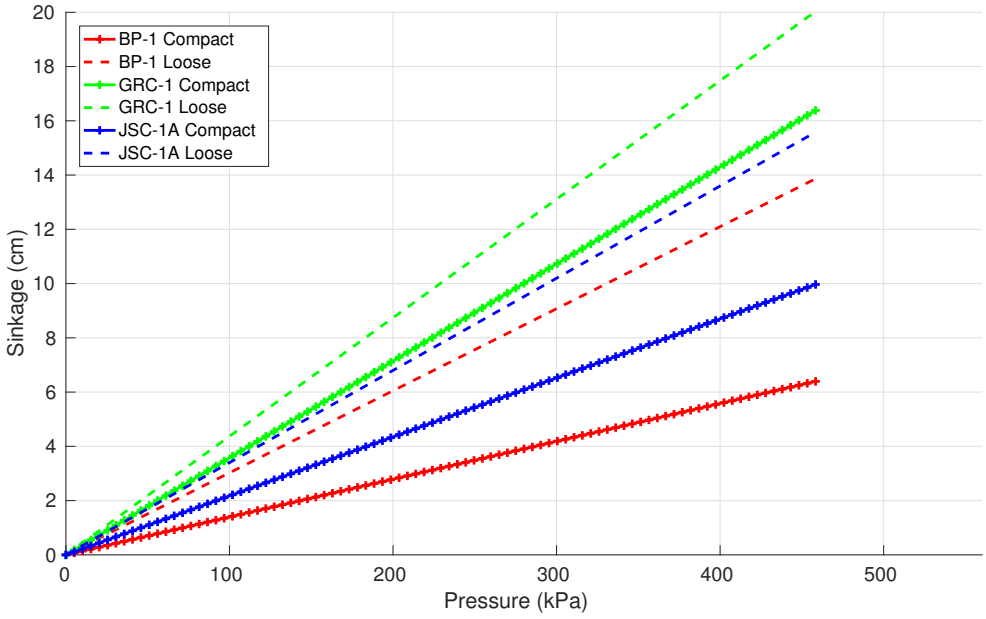

Figure 4.9: Comparison of best-fit linear pressure-sinkage curves. Curves generated for each material type and compaction level are shown. Data for the GRC-1 material is only valid for pressures under 400 kPa; values beyond this are extrapolated for illustrative purposes.

Table 4.1: Pressure-sinkage coefficients for different compaction levels for each simulant. Table also shows the percent change in the coefficient from compact to loose.

Compaction	JSC-1A	BP-1	GRC-1
Compact	0.011	0.007	0.018
Loose	0.017	0.015	0.022
Change	56%	117%	22%

here correspond directly to the estimated diffusivity. However, it is noted that in these experiments that the differences in compaction level is extreme.

For the measurements of the pressure-sinkage relationship, there was significantly more variation between trials in the loose preparations than the compact preparations. This is likely in part due to the more repeatable preparation of the compact materials in comparison to the loose materials. However, it may also be because of more inherent variability in the behavior of loose granular media [142].

4.4 Measurement Depth

The main limitation of this method is the depth of material that it measures. With only a short laser pulse, heat does not always have time to propagate deep into the soil and then back up to produce a measurable surface response that includes information about the soil at depth. In addition, unlike diurnal illumination, heat is uneven throughout the surface. With even surface flux, heat diffuses in approximately one dimension downward. With point illumination, heat diffuses in three dimensions under the surface. This reduces the magnitude of the heat wave at depth.

In order to test the effective measurement depth of this method, simulations were conducted using a thermal model for lunar regolith. The details of the thermal properties on the Moon will be addressed in more depth in Section 7.1. The terrain was treated as a semi-infinite solid, symmetric about the center point. With R as the radius, in cylindrical coordinates, the heat diffusion equation becomes:

$$\frac{\partial T}{\partial t} = \alpha \left(\frac{1}{R} \frac{\partial}{\partial R} \left(R \frac{\partial T}{\partial R} \right) + \frac{\partial^2 T}{\partial z^2} \right) \tag{4.9}$$

Because of radial symmetry, there is no dependence on angle. Hence, this equation can be solved in two dimensions. A laser flash was simulated by applying a heat flux for a set amount of time to the center point of the surface of the solid. In these simulations, the laser has no velocity. A two-dimensional numerical finite difference solution to the heat equation was used to solve for temperature distributions over time. To evaluate the effective measurement depth of this method, simulations were run on several different density distributions. First, a baseline distribution consisted only of 1100 kg/m^3 density regolith. Other samples contained layers of 1100 kg/m^3 regolith on top of the 1800 kg/m^3 base layer. Top layers were tested in increments of 0.2 mm. The goal is to evaluate at which surface layer depths there is a non-negligible temperature difference between the layered example and the homogeneous example. Essentially, under what conditions could a robot detect a difference between: (1) a thin layer of loose regolith on top of compact regolith and (2) homogeneous loose regolith?

For a pulse lengths of 1 and 5 seconds with powers of 2 and 5 kW/m^2, the results are shown in Figure 4.10. Model-predicted surface temperature differences are shown for up to 5 minutes from the end of the illumination pulse. Qualitatively, longer pulse lengths and more applied power result in more significant temperature differences between the layered and homogeneous cases. However, in all cases, the maximum depth that causes a non-negligible difference is small.

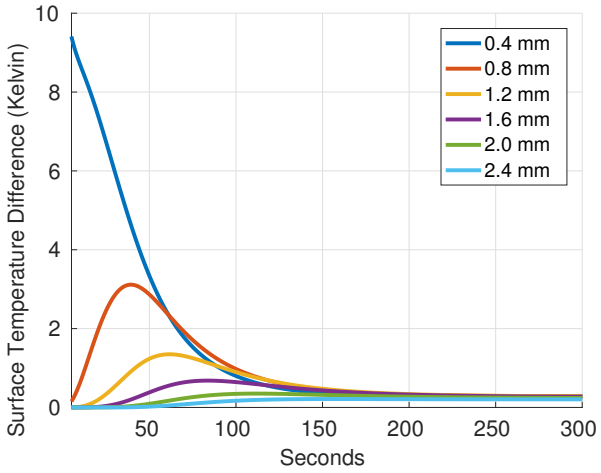

(a) Power = 2 kW/m^2, Pulse time = 1 s

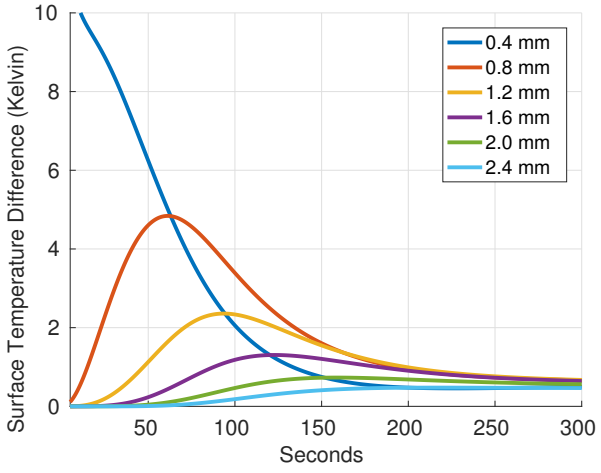

(b) Power = 5 kW/m^2, Pulse time = 1 s

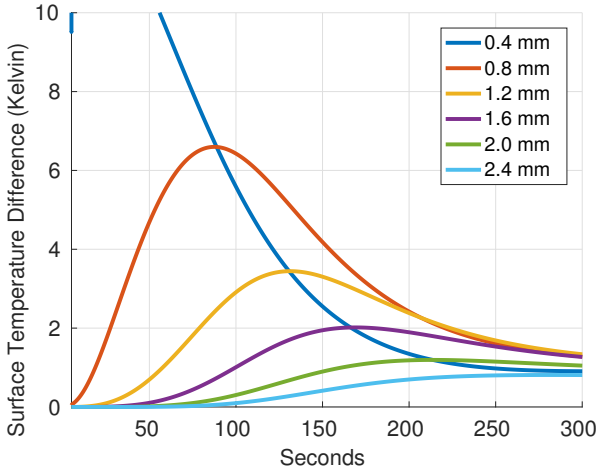

(c) Power = 2 kW/m^2, Pulse time = 5 s

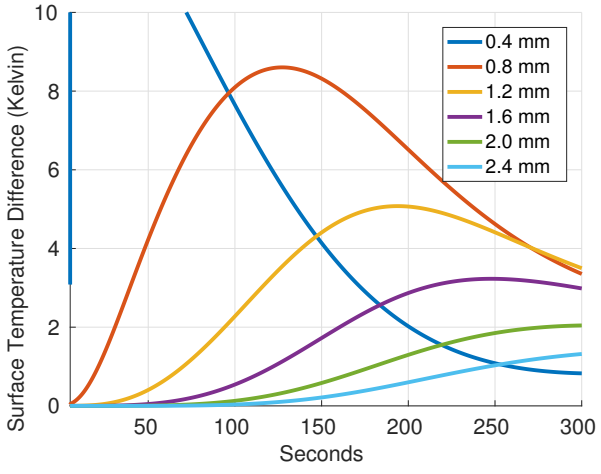

(d) Power = 5 kW/m^2, Pulse time = 5 s

Figure 4.10: Penetration depth test results with varying laser flash powers and pulse times. A baseline distribution consisted of 1100 kg/m^3 density lunar regolith. Other samples contained layers of 1100 kg/m^3 regolith on top of a 1800 kg/m^3 base layer. Each graph gives temperature differences between different surface layer depths and the baseline 1100 kg/m^3 distribution.

Table 4.2: Maximum depth causing a measurable temperature difference on the surface for several noise equivalent temperature differences (NETDs), pulse powers, and pulse lengths

	2 kW/m^2		**5 kW/m^2**	
NETD	**1 s**	**5 s**	**1 s**	**5 s**
0.5 K	1.6 mm	3.0 mm	2.2 mm	3.4 mm
1.0 K	1.2 mm	2.0 mm	1.6 mm	2.8 mm
2.0 K	1.0 mm	1.6 mm	1.2 mm	2.0 mm

To quantify the maximum measurable depth by a thermal sensor, several potential noise equivalent temperature differences (NETDs) are considered. For a given NETD, the maximum measurable depth is estimated to be the case with the thickest loose surface layer that causes a temperature difference equal to or greater than the NETD. Results are shown in Table 4.2. Greater depths can be probed with more sensitive instruments, more heat flux, and longer illumination times (slower rover velocities). In all cases considered in this analysis, the maximum measurable depth is only a few millimeters below the surface.

These results demonstrate a limitation of this method. Despite laser-aided thermal sensing competently determining a difference in surface density, it only measures the top few millimeters of terrain. This means that subsurface properties could be obscured by a thin layer of surface material. For example, sand beneath a thin duricrust layer would go undetected and is the situation that entrapped Spirit. The absolute sensing depth will vary between materials, and longer illumination periods (i.e. slower velocities) will lead to greater depths.

4.5 Summary and Conclusions

This chapter presented an approach to predict the traversability of terrain through non-contact measurements of temperature curves induced by a laser excitation. The method enables differentiation between safe, compact and hazardous, loose preparations of the same soil, which vision-based methods alone cannot reliably achieve. It transits a low-power, continuous-wave laser and thermal camera across a terrain to effect a thermal transient on terrain. The temperature response is then measured fit to an analytical model to solve for an estimate of thermal diffusivity. For each of the three simulants tested (JSC-1A, BP-1, and GRC-1), a higher measured thermal diffusivity correlated to a higher density and a more traversable granular material as validated by measuring the pressure-sinkage relationship with a bevameter. Experimental results measured a 56%, 29%, and 35% average difference in diffusivity from a compact preparation to a loose preparation for JSC-1A, BP-1, and GRC-1, respectively. Corresponding increases in the pressure-sinkage coefficients from compact to loose material of 56% for JSC-1A, 117% for BP-1, and 22% for GRC-1 were also measured. These results demonstrated a correlation between the thermal properties of a material and its strength.

This approach could be applied to detect when a rover encounters hazardous, loose terrain by detecting a drop in diffusivity. However, it has some drawbacks. First, it only measures that top few millimeters of terrain. In many cases this could provide useful information about

traversability. However, in others, it could be misled by a surface layer of dust or duricrust. Second, it is restricted to measuring a single point in front of a robot. This restricts its applicability to safeguarding a rover from entering hazardous terrain rather than analyzing the environment for path planning.

Future work should also analyze the efficacy of this approach on mobile robots. Relative to lab instruments and conditions, robots present new challenges including the fact that the robot's velocity must be estimated in order to use this method to predict traversability. A robot's motion will also not likely be precisely linear as it was in the controlled setup used in this paper. Further work is required to adapt this technique to account for variable velocities and nonlinear trajectories.

Chapter 5

Detecting Relative Differences in Traversability Using Thermal Inertia

This chapter presents a method for evaluating relative differences in the strength of terrain by estimating thermal inertia from observations of surface temperature that change over the course of the day due to solar and atmospheric heat fluxes. Solar irradiance at the equators of the Moon and Mars is $\sim$1370 and $\sim$610 Watts per square meter. These fluxes far exceed any practical possibility of illumination powered from a rover. Moreover, insolation is uniform over a vast area, enabling scene viewing and lookahead by a rover, which is not possible with laser illumination.

The use of a laser to induce a temperature response for measuring the thermal properties of terrain is limited to sensing only the top few millimeters of a single point in front of a robot. These limitations exist because of the single point of illumination and the short illumination period. Fortunately, natural solar and atmospheric heat fluxes overcome these challenges to provide even heat at a significantly longer illumination period. This enables better comparisons between different areas of the environment and measurements that include information from several centimeters below the surface.

In Section 5.1, a method for estimating the thermal inertia of terrain is presented and expected errors are analyzed. The efficacy of this method is highly dependent on the time of day of an observation as well as the length of an observation. Expected errors in thermal inertia estimates are computed as a function of the time and length of an observation to understand the practicality of this method. The efficacy of this approach for predicting traversability as well as the validity of the predicted errors presented are evaluated through two terrestrial experiments.

Section 5.2 discusses the first experiment with periodic data collection in granular slag, which tested the ability of a rover to use thermal camera measurements predict traversability differences at different times of day. Data was collected by driving a rover around a large area with loose and compact terrain with various surface appearances over the course of two days. Terrain strength measurements were conducted using a penetrometer.

Section 5.3 discusses the second experiment with continuous data collection in sand. This experiment tested the effect that time of day and length of time spent observing surface temperatures have on the ability of this approach to predict traversability. In this experiment, a static tripod observed a sand pit prepared in a grid of loose and compact samples over the course of several days. Ground-truth traversability measurements were taken by measuring the slip of a

robot with an applied drag force.

In both experiments, results show that differences in terrain compaction can be detected by thermal measurements despite appearing visually similar. Daytime thermal inertia measurements were more prone to errors caused by inaccurate albedos, surface geometry, or incident heat flux estimates. Nighttime thermal inertias were less affected by such errors and led to better separation of safe and hazardous sand.

Part of this chapter appeared in [39].

5.1 Estimating Traversability with Thermal Inertia

This section outlines how thermal inertia is estimated using observations of diurnal surface temperatures and how these estimates can be affected by errors in albedo and temperature measurement.

5.1.1 Thermal Inertia Estimation

The thermal inertia of terrain can be estimated by observing its temperature with a thermal camera then fitting the observed surface temperatures to an analytical thermal model with estimated values for heat fluxes. The general mathematical model is described in 3.2.1 for planetary environments. Using estimated heat flux values and measured surface temperatures, thermal inertia is found by minimizing the squared error between measured and analytical surface temperatures with thermal inertia as a free variable. If surface temperature measurements are limited to a single point in time, then albedo is estimated by other means and kept as a fixed value in the optimization. However, for longer observation periods, albedo can also be treated as a free variable if albedo is unknown.

Equation 3.4 described the surface energy balance in the context of the Moon and Mars where atmospheric pressures are low enough that sensible and latent heat fluxes are negligible in most cases [98]. Sensible heat flux refers to conductive and convective heat exchange with the atmosphere. Latent heat flux refers to energy gained or lost through a change of state (i.e. energy lost through evaporation). This chapter describes experiments occurring on Earth where these atmospheric affects can be significant. The surface boundary condition for Earth is given by [125]:

$$(1-A)R_{sw} + \epsilon R_{lw} - \epsilon\sigma T_s^4 = H + LE - I\sqrt{\frac{\pi}{P}}\left.\frac{\partial T}{\partial Z'}\right|_{Z'=0} \tag{5.1}$$

where H and LE are the sensible and latent heat fluxes, respectively.

Unfortunately, on Earth, it is difficult to either estimate or measure H and LE. Sensible heat flux can be parameterized as a function of the difference in temperature between the surface and wind speed [120, 126]:

$$H = \rho_a c_a C_T v_w (T_s - T_a) \tag{5.2}$$

where ρ_a is air density, c_a is the heat capacity, v_w is mean wind speed, T_a is air temperature, and C_T is a non-dimensional bulk aerodynamic coefficient. In the experiments in this chapter, wind

speed is was not measured and the C_T constant remains unknown. Instead, a simpler model is learned from the data. Sensible heat flux is approximated as:

$$H = \gamma_H(T_s - T_a) \tag{5.3}$$

γ_H is a scaling parameter that is learned from data. In the experiments to follow, 48 hour data sets are collected. γ_H is learned for the first day by training on the second day and vice versa.

LE is significantly more difficult to estimate from available data. LE can be approximated as [120, 126]:

$$LE = \rho_a L\, C_q v_w (q_s - q_a) \tag{5.4}$$

where L is the latent heat of evaporation, q_a and q_s are the moisture contents of the air and surface, respectively, and C_q is another non-dimensional bulk aerodynamic coefficient. Once again, C_q remains unknown for the environments in this work. It is also unreasonable to require a robot estimate the soil water content to predict mobility. Consequently, this chapter assumes that LE is negligible. This is a better approximation in drier environment than in wetter climates.

Thermal inertia estimates are sensitive to errors in heat fluxes. This can make comparing thermal inertia estimated at different start times and with different observation periods difficult since errors in the model fluctuate with time. However, when comparing temperature curves using the same model over the same period of time, these errors are less important and the relative differences in thermal inertia hold more reliably. This means that if one region's thermal inertia is estimated to be higher than another, its actual thermal inertia is likely to be higher. This can be exploited to maximize traversability over terrain by traveling on materials with higher relative thermal inertia.

5.1.2 Albedo Error Analysis

Effects of different parameters on diurnal temperature variations of terrain are not constant over the course of a day (see Section 3.2.2). For example, during the day, changes in albedo have a larger effect on temperature than at night. Variations in thermal inertia have a slightly lower effect on temperature during the day than at night. Understanding how errors in parameters affect thermal inertia estimates over the course of a day is critical for understanding the reliability of traversability prediction.

The most significant sources of error considered here are in the estimation of albedo and of surface temperature. These are the two largest sources of error identified on the MER Mini-TES instruments. Other errors are caused by the estimation of incident heat fluxes, but these effects are harder to quantify [46]. In order to analyze errors in temperature and albedo, first ground-truth temperature curves were created using the thermal model and reasonable values for all parameters, including a thermal inertia of 800 $Jm^{-2}K^{-1}s^{-\frac{1}{2}}$ and an albedo of 0.3. Then the approach described above was used to estimate the thermal inertia using incorrect values for temperature and albedo to see how those errors would affect the resulting thermal inertia value. The induced errors in albedo and temperature were derived from expected errors for the same values on the Mini-TES instruments in order to understand how well this technique could work on Mars. The maximum albedo error was assumed to be 0.02, and the maximum temperature error

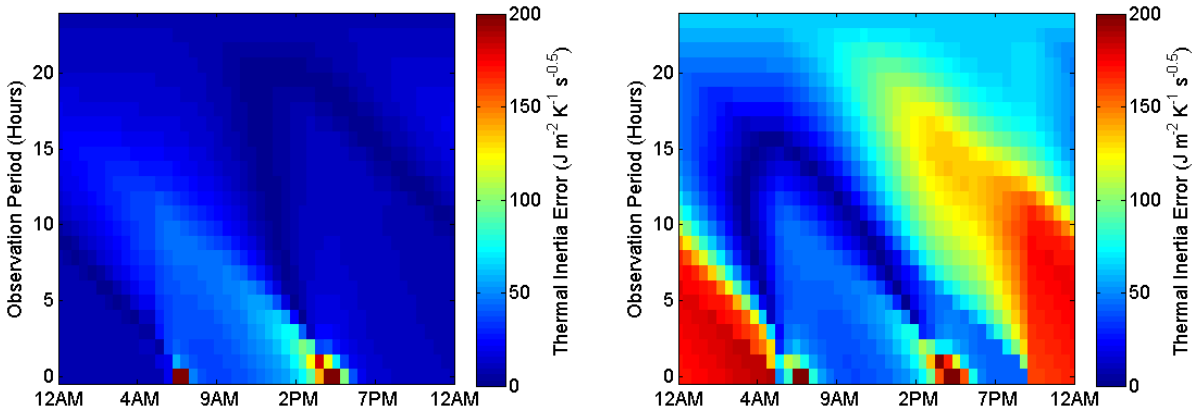

Figure 5.1: The effect of errors in albedo (left) and temperature (right) on resulting thermal inertia estimates as a function of observation start time and observation period. Error is capped at 200 K to prevent saturation of the colormap.

was assumed to be 1 K during the day and 3 K at night. The temperature error was treated as an additive constant because the major source of temperature error is calibration, which results in a bias rather than noise [46]. Albedo error was not a free parameter for either experiment.

The maximum thermal inertia error was computed at evenly spaced start times and observation periods by comparing the ground truth thermal inertia to estimated thermal inertias. Start time is defined as time when the observation of temperatures begins. Observation period is defined as the length of time that temperature curve is observed. Periods ranging between one single observation to a full 24 hour period were considered. The error is plotted in Figure 5.1. In general, observing for longer periods of time produces a better estimate. The highest errors are for short observation periods in the morning when the terrain starts to heat up and in the evening when the terrain starts to cool down. This is supported by the analysis in Section 3.2.2, which show that temperature curves with different thermal inertias intersect at those times. In the albedo analysis, there is higher error during the day and lower error at night, with the lowest error represented by a parabolic shape that occurs when moderate-length observations straddle the morning or the evening. In the temperature analysis, there is higher error at night than during the day, resulting from the higher uncertainty at night.

Based on this analysis and with reasonably accurate estimates of heat fluxes, it is expected that the best time of day to evaluate relative differences in thermal inertia is at night. The best absolute estimates of thermal inertia come from estimates that have both morning and nighttime measurements. Obviously, absolute thermal inertia errors are higher when radiometric calibrations are higher at night. However, errors from a bias in temperature are of less concern in this application because they are independent of terrain. The absolute values of thermal inertia are not expected to be as accurate when radiometric calibration biases are introduced; however, relative differences still hold. Higher thermal inertia will be estimated for higher thermal inertia regions regardless of temperature bias. The temperature biases were taken from a instrument on Mars and are much lower on Earth. Hence, they do not play a significant role in the following experiments.

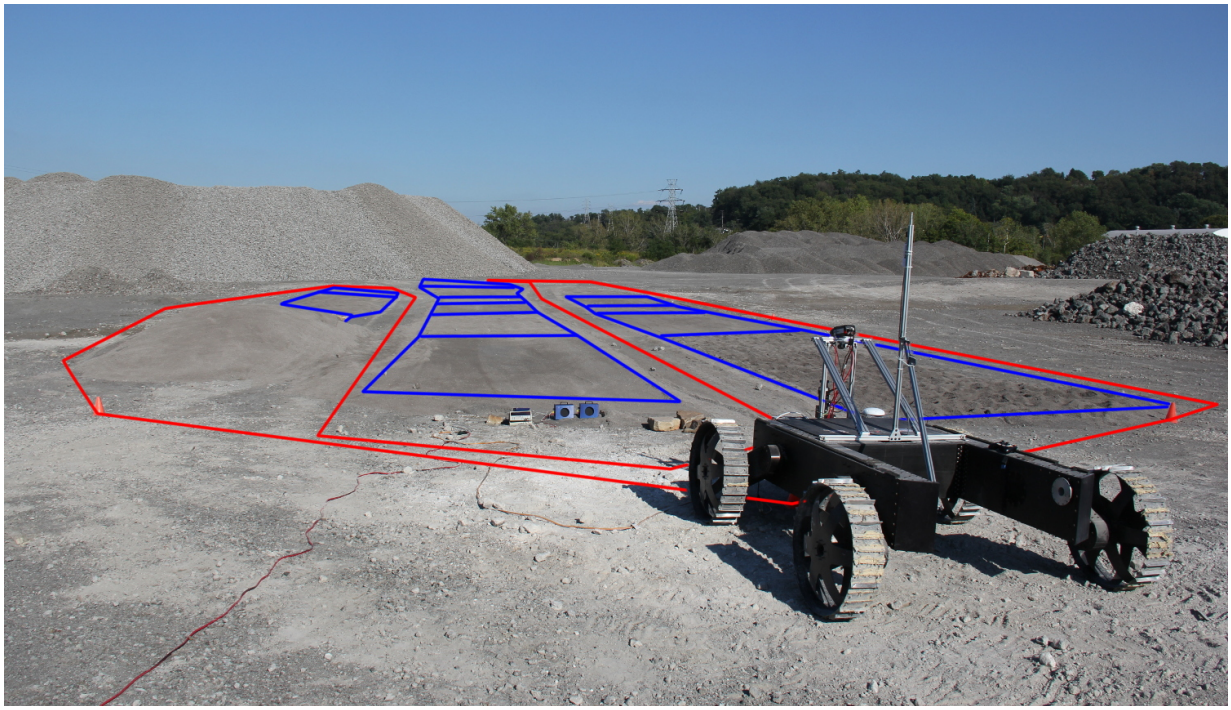

Figure 5.2: Rover and experimental setup for the field experiment with periodic data collection in granular slag. The blue lines show the locations of the prepared granular samples. The red line shows the path taken by the robot during each run. In front of the rover, the blue boxes with black circles in the middle are blackbodies used for temperature calibration.

5.2 Periodic Temperature Measurements of Granular Slag

The goal of the first field experiment was to evaluate the ability of thermal inertia to predict differences in terrain compaction and traversability at different times of day. The test was conducted at a slag processing center in Pittsburgh.

5.2.1 Experimental Setup

For this test, a 30 by 60 m area was covered with coarse, granular slag. With the goal of creating terrain with differing bulk and surface properties, discrete sections of the material were then loosened and compacted manually with a shovel and using a vibratory compactor, respectively. Next, the surfaces of each sample were prepared in several different ways. The surfaces were prepared by either: smoothing with a shovel, smoothing with a broom, depositing a thin layer of loose material on the top, or leaving unchanged after loosening or compacting. There were an additional two regions prepared using flagstone. One was raw stone, the other was covered with a thin layer of granular material. Under all of the rocks and slag was a very hard, compact surface consisting of a range of particle sizes, from gravel to dust. The site was prepared two days before the test. Early preparation ensured the soil had time to go through two complete day/night cycles and allowed the soil to dry out to the greatest extent possible.

Figure 5.3: Image of the rocky region that was occluded in Figure 5.2. Half of the rocks were covered in slag, and the other half were left bare.

An overview of the site is shown in Figure 5.2. The site was separated into three sections that the rover then drove in between. In each section, regions of granular slag were arranged in alternating loose and compact states. Note that in this image, the rocky areas are only barely visible behind a mound on the left. These regions are shown separately in Figure 5.3. The extents of each region were surveyed using a total station for ground truth positions.

The experiment consisted of testing over the course of three days. During the first two days, the rover drove the same predefined course around and through the site approximately every two hours between the 6am (predawn) and 11pm (night). The course is shown in red in Figure 5.2. Each of these "runs" took about 30 minutes.

Data from a thermal camera, a lidar, and a GPS was collected continuously throughout the test. In this way, two near-complete days worth of thermal data were collected for the entire site. The thermal camera was pointing in front of the rover as it drove at a slightly downward pitch. The thermal camera was a FLIR A615. It had a resolution of 640 x 480. The noise equivalent temperature difference (NETD), or sensitivity, was 50 mK. It had an absolute radiometric accuracy of ± 2 K. Figure 5.4 shows example thermal images from approximately the location of the rover in Figure 5.2. Note how the differences between different loose and compact regions ares obvious at certain times of day and more subtle at others. At night, compact regions are warmer than the loose region. The opposite is true during the middle of the day. Processing of rover thermal data will be discussed in Section 5.2.2.

The weather during the test was primarily clear and sunny with some early morning fog. Ground truth measurements of solar and atmospheric irradiance were made with a pyranometer and a pyrgeometer, respectively. Soil samples were taken from the top $\sim$5 cm of slag in each sample region twice per day in the morning and midday. These samples were later weighed, baked, and then reweighed to obtain measurements of soil water content throughout the test.

On the third day after thermal data collection, pressure-sinkage curves and albedo were

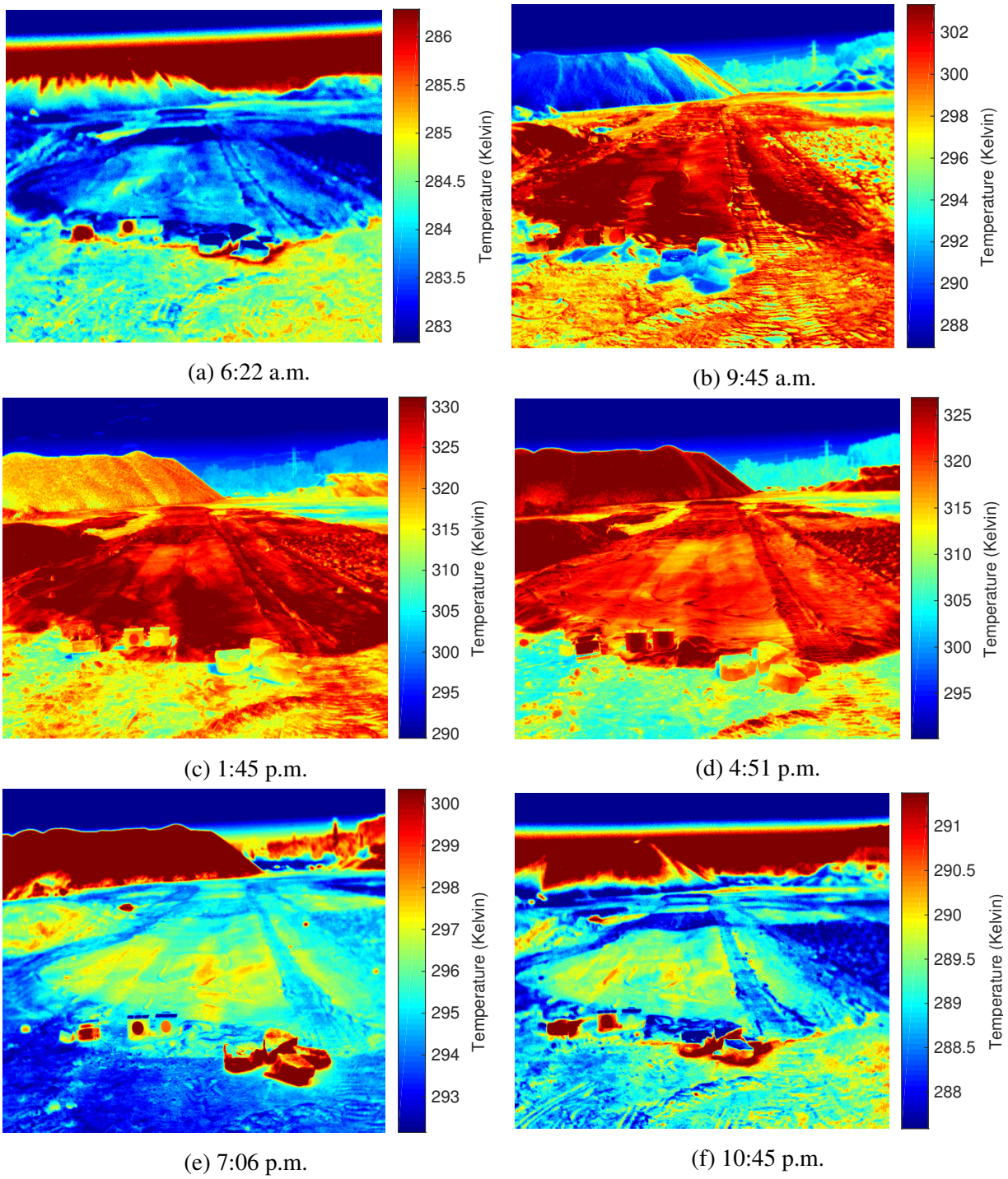

(a) 6:22 a.m.

(b) 9:45 a.m.

(c) 1:45 p.m.

(d) 4:51 p.m.

(e) 7:06 p.m.

(f) 10:45 p.m.

Figure 5.4: Thermal images of the same location at 6 different times of day. The color scale is different for each image. Minimum and maximum values in each colormap correspond to the 10th and 90th percentile of visible temperatures, respectively. Note the temperature difference between loose and compact regions is more visible at some times of the day than others.

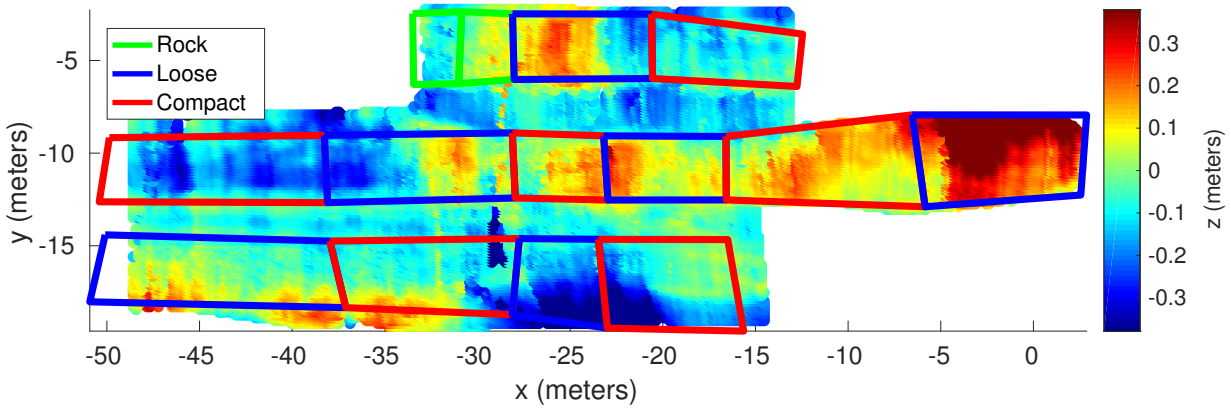

Figure 5.5: Point cloud of the test site. Points are colorized by height. Bluer points are lower and redder points are higher. The outlines show the surveyed sample sites. Outlines are colorized by the type of sample (i.e. rock, loose sand, or compact sand).

measured in each sample. Albedo measurements were collected by measuring the difference between downwelling and upwelling solar radiation over each sample at the site using a solar pyranometer held at approximately 1 m above the surface. Pressure-sinkage measurements and processing will be discussed in Section 5.2.4.

5.2.2 Thermal Data Processing

First, laser and thermal data were combined to create a 3D map of the environment. Data from a single run was used to create a point cloud. The positions of the thermal camera were found using LSD-SLAM [43]. LSD-SLAM was modified slightly to enforce priors on x and y using data from the GPS. This changed helped to constrain scale changes that otherwise occurred when the robot turned in place. Once the camera positions were found, a simple rigid transform was used to find the laser positions. A point cloud was then aggregated from all the laser measurements. The resulting point cloud is given in Figure 5.5. The surveyed positions of each sample region are also shown.

Next, thermal data from each run was projected on to the point cloud. To minimize error caused by localization, mapping, and sensor calibration, data from each thermal image was only projected onto regions up to 18 m away from the rover. The temperature of each point was estimated as a weighted average of all images viewing that point for a given run. Closer images were given higher weight than images further away. Absolute temperature was radiometrically calibrated using the blackbodies shown in Figure 5.2. Finally, a grid was defined over the surface and temperatures were averaged within each grid cell. Each grid cell was a square with 0.8 m sides. The grid is shown in Figure 5.6 where each grid is colorized by temperatures at several times in the day. These figures also shows the clear difference in temperature between loose and compact regions at night and more subtle difference at other times in the day. During some runs, there were areas where the robot did not get a good view of some samples, so no data is shown.

Temperatures were averaged over each of the 14 prepared regions and plotted over the course of the data collection in Figure 5.7. In most cases, the average temperature follow the expected

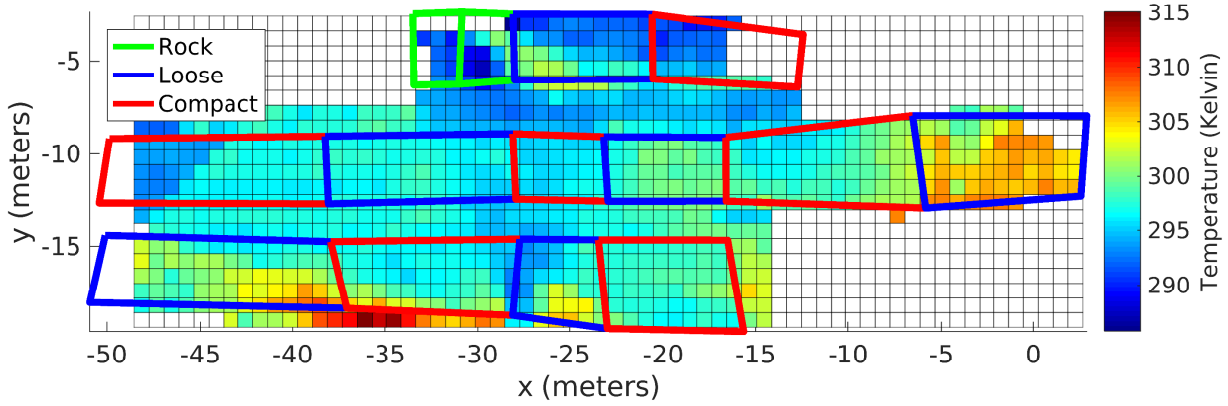

(a) Morning (9 a.m.)

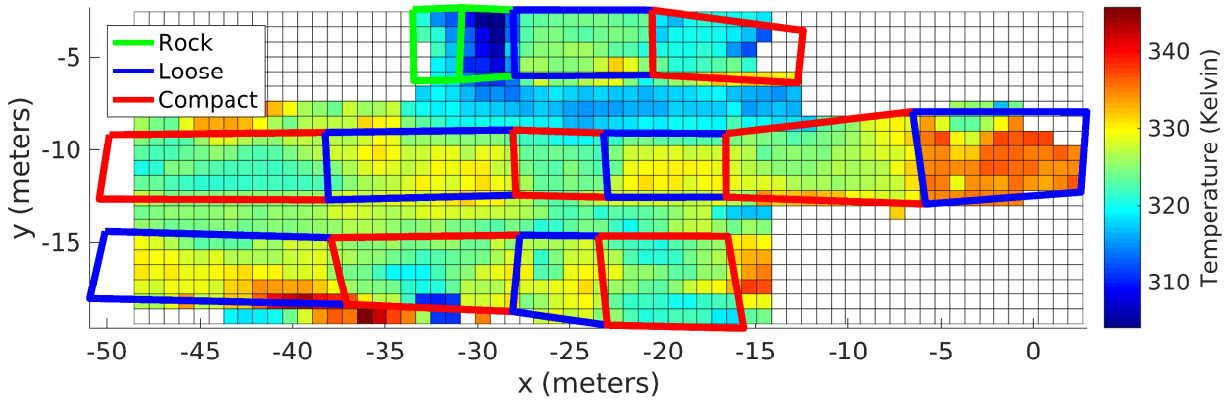

(b) Midday (12 p.m.)

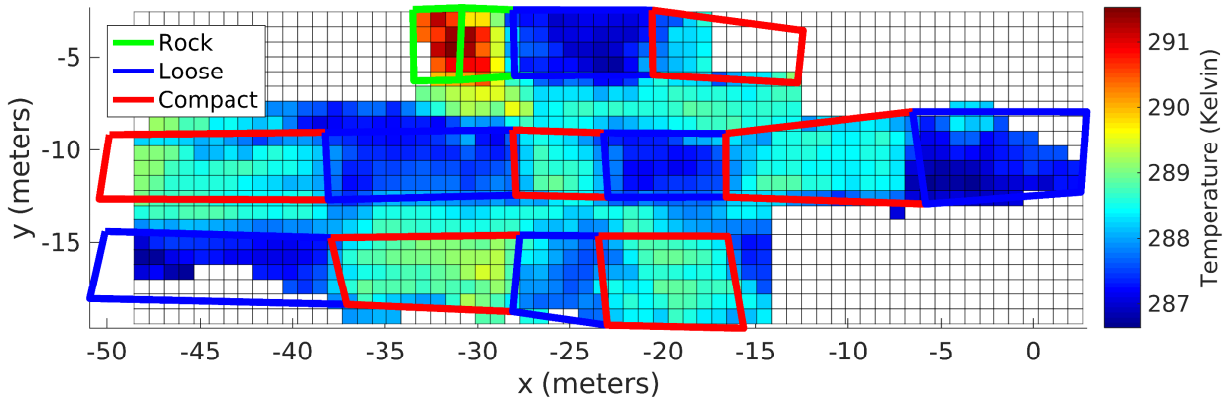

(c) Nighttime (10:30 pm)

Figure 5.6: Temperature measurements plotted for each sample at three times per day.

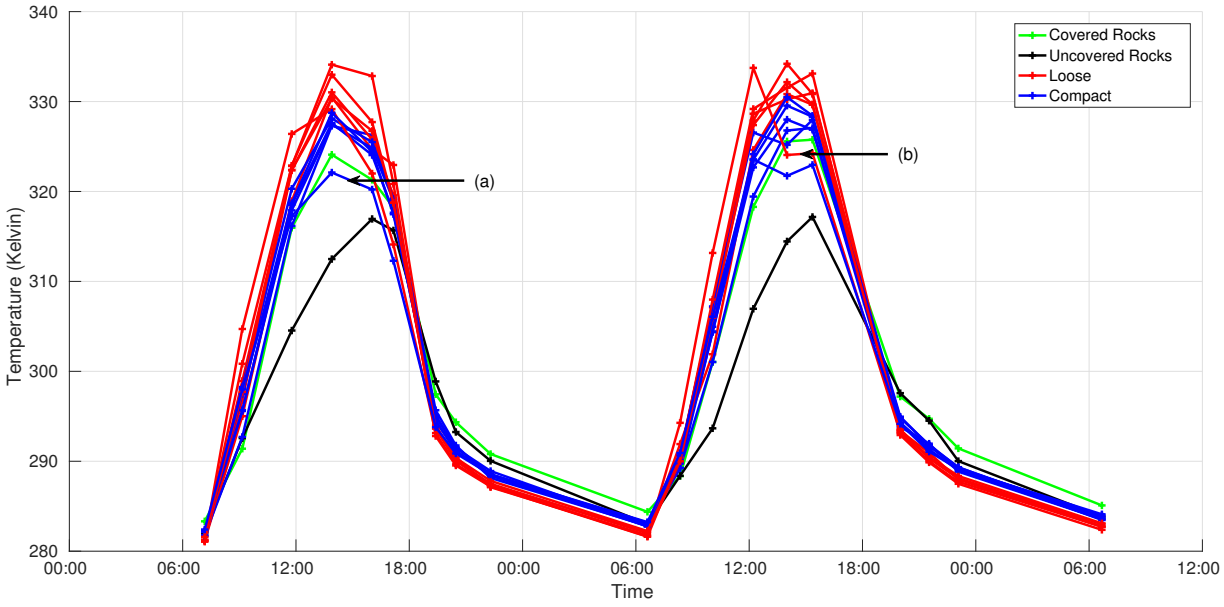

Figure 5.7: Average temperatures in each of the 14 samples plotted over the two day observation period. Two anomalies are labeled (a) and (b).

trend. The loose samples heat up more quickly in the morning to get hotter during the day and cool down more quickly in the evening to stay colder at night. The rocky regions behave as expected as well. They are generally cool during the day and warm at night. The uncovered rock has significantly higher albedo than any other sample, so less energy is absorbed during the day, and thus it doesn't stay warmer than the compact samples all night. The rocks covered by slag get warmer during the day than the uncovered rocks, but the temperature curve is dominated by the subsurface rock at night.

Two anomalies are exhibited in Figure 5.7. The first is labeled as (a). This compact region stays significantly cooler during the day. This is likely caused by the inhomogeneity of this particular region. Some of this region was either barely covered by granular slag or not covered at all. This left visible the hard, compacted surface underneath, which remained very cool during the day. The other anomaly is shown by (b). This is a loose region that appeared to cool down very rapidly in the middle of the day. This region had a very rough surface with significant local slopes. The result was a viewpoint-dependent temperature. When viewing the surface with the Sun at the robot's back, the surface appeared warmer. When viewing the surface with the Sun in front of the robot, the surface appeared cooler. As a result, the temperature did not follow the ideal curve exactly.

5.2.3 Estimating Thermal Inertia

Measured albedo, solar flux, and atmospheric flux were used to estimate thermal inertia for each sample. The measured albedo values varied between 0.11 and 0.13 for the granular samples. The bare rock had an albedo of 0.20. It is likely that the rock's albedo was actually significantly higher, and the measured albedo was strongly influenced by the surrounding terrain due to the small size

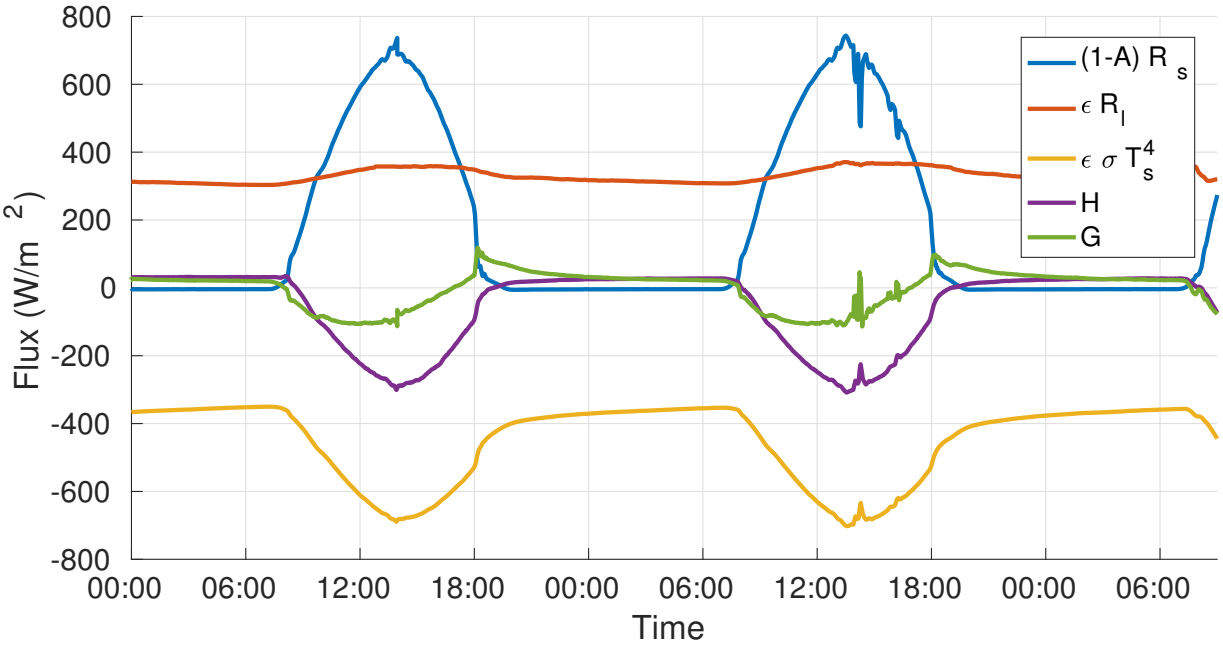

Figure 5.8: Heat fluxes from Equation 5.1 plotted over the course of the two day test. G refers to the heat flowing into the ground. Positive values of heat flux refer to heat being added to the surface. Negative values refer to heat either being radiated or conducted away from the surface.

of that sample. Flux values were measured over two days. Fluxes for up to 15 days before the test were estimated by repeated the fluxes measured during the test. Thermal inertia was estimated by minimizing the squared error between measured and model-predicted surface temperatures.

Figure 5.8 shows estimated values for the heat flux terms in Equation 5.1. G refers to the ground heat flux and is estimated by solving for G in Equation 5.1. The γ parameter for sensible heat flux was estimated to be 10.5 on day 1 and 11 on day 2. Assuming $C_T = 1.5 \times 10^{-3}$ [120] and nominal values for ρ_a and c_a of $1.2kg\,m^{-3}$ and $1.01kJ/(kg\,K)$, respectively, then these values of γ corresponds to average wind speeds of $5.8m/s$ and $6.1m/s$.

Measured gravimetric water content is given for each region (except the rocky areas) in Figure 5.9. In most cases, gravimetric water content increased overnight and decreased by 0.05 to 0.1 over the course of the day. A couple outliers did not decrease, which could be due to sampling error or the local geometry of terrain causing water to pool. The increase overnight was due to condensation from the atmosphere. The dew point during the test reached as low as 11°C overnight, and the air temperature reached as low as 9°C. This resulted in significant moisture being deposited on the surface overnight, which would then evaporate during the day. The changes in water content over the course of the day mean that latent heat flux was significant. It is likely that part of the effect of latent heat was accounted for in the sensible heat flux term and that the estimated γ parameters and wind speeds were higher than their true values.

Using ground-truth albedo values, thermal inertia was estimated by minimizing the squared error between model-predicted and measured temperatures. Figure 5.10 shows two example best-fit curves compared to the measured data points. Figure 5.11a shows estimated thermal inertia for each sample using all 48 hours of surface temperature data. There are a few outliers that

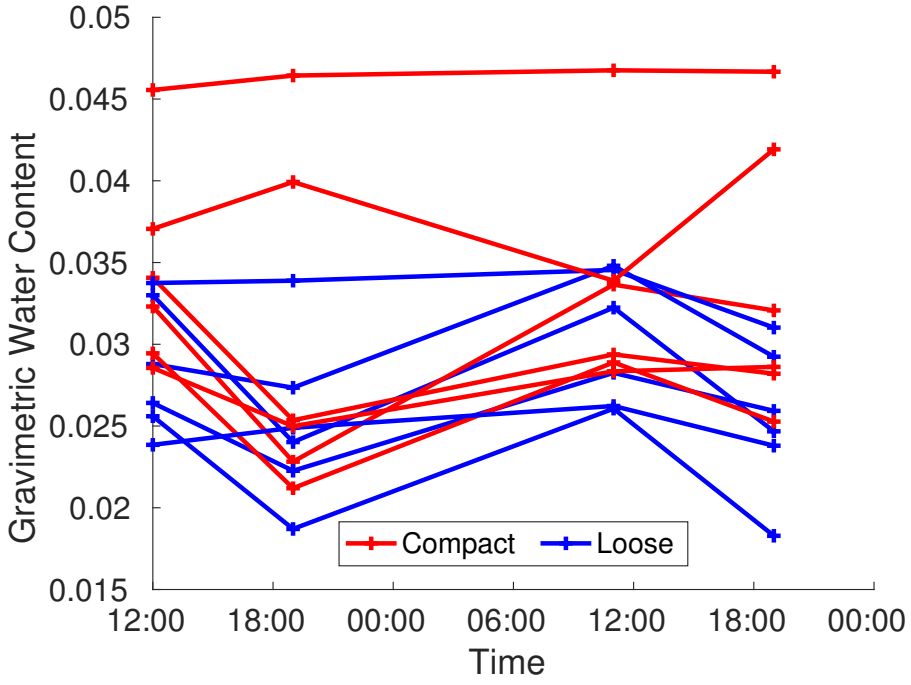

Figure 5.9: Gravimetric water content measured for each region over the course of the test.

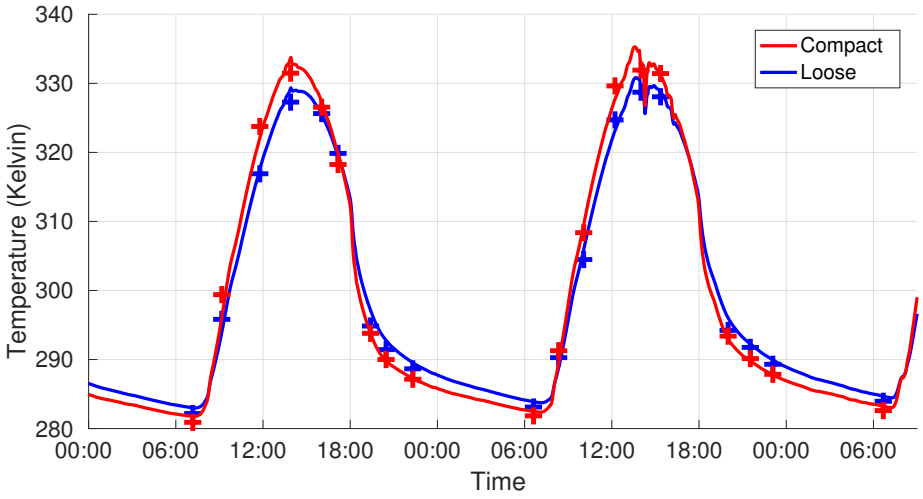

Figure 5.10: Comparison of measured data for a single sample (+'s) and analytically model output. The analytical model used ground-truth measured albedo and surface heat fluxes.

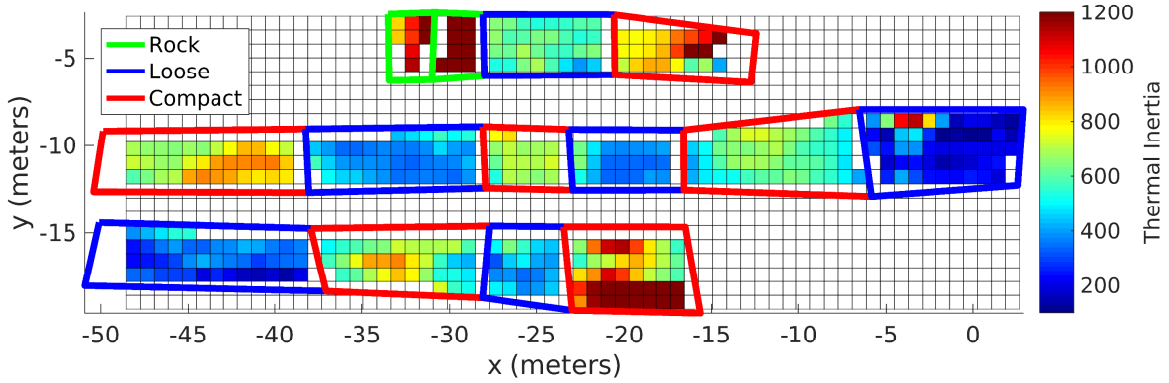

(a) Thermal inertia fit using all available temperature data at a given point.

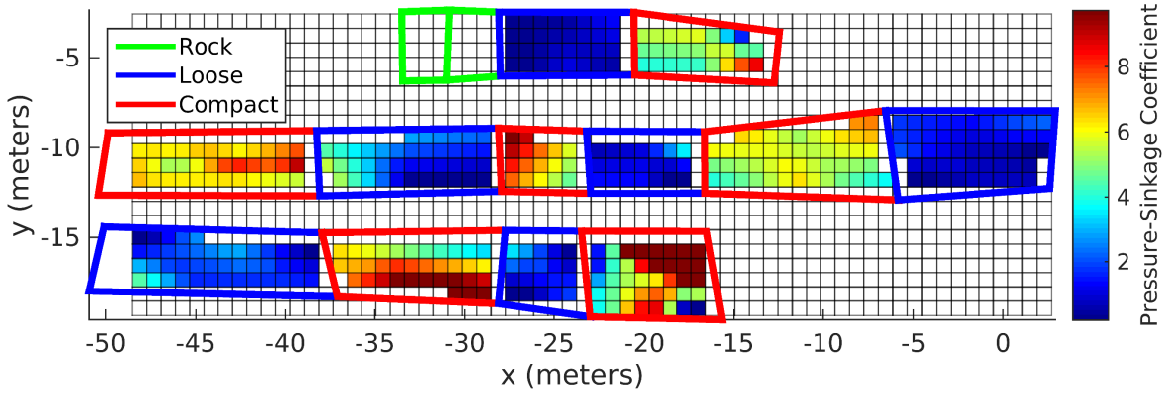

(b) The best-fit penetrometer coefficient interpolated over the surface and matched to each sample in the grid. Higher values indicate stronger materials that have greater resistance to sinkage.

Figure 5.11: Spatial plots of thermal inertia and pressure-sinkage coefficients.

were likely caused by mis-registration of thermal camera data. However, in most cases there is an obvious difference in thermal inertia between loose slag, compact slag, and rock. As expected, the thermal inertia of loose slag is the lowest, in compact slag it is slightly higher, and in rock it is significantly higher.

5.2.4 Pressure-Sinkage Measurements

Pressure-sinkage measurements were taken at 78 different locations in the site using a penetrometer with a 0.5 in diameter cone. Two measurements were taken at each location. For each measurement, the penetrometer was pushed into the surface manually at a constant rate. Pressure measurements were recorded at one inch increments up to 6 in deep. However, in many locations (mostly in the compacted regions), the maximum obtainable depth was shallower than 6 in. The pressure-sinkage measurement locations are shown on a map of the samples in Figure 5.12.

All of the pressure sinkage measurements are shown in Figure 5.13 and colorized by compaction. In almost all cases, the compact regions had higher pressure for a given depth than the loose regions. This indicates that, as expected, the compact materials were stronger than the loose materials. To provide a single metric for comparison, a linear pressure-sinkage model was

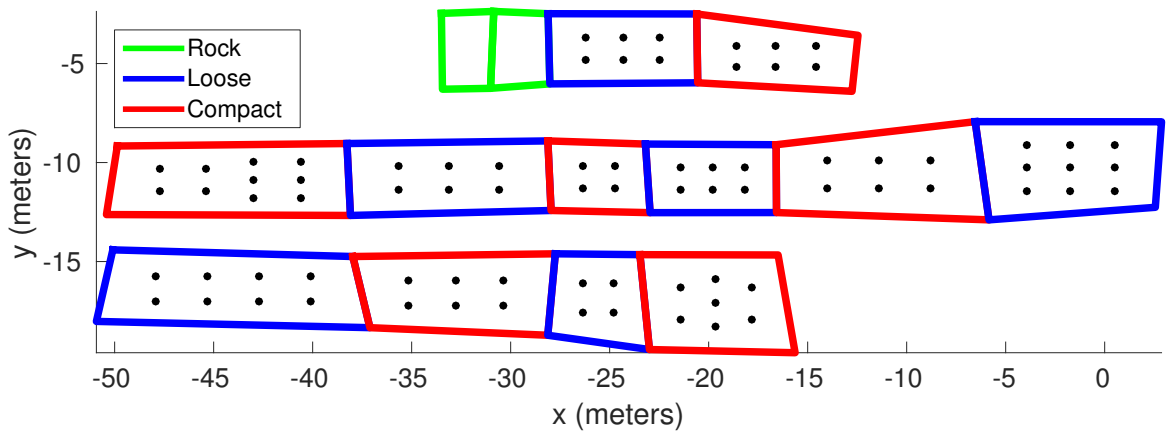

Figure 5.12: Black points indicate the locations of penetrometer measurements within each sample. Two measurements were taken at each point.

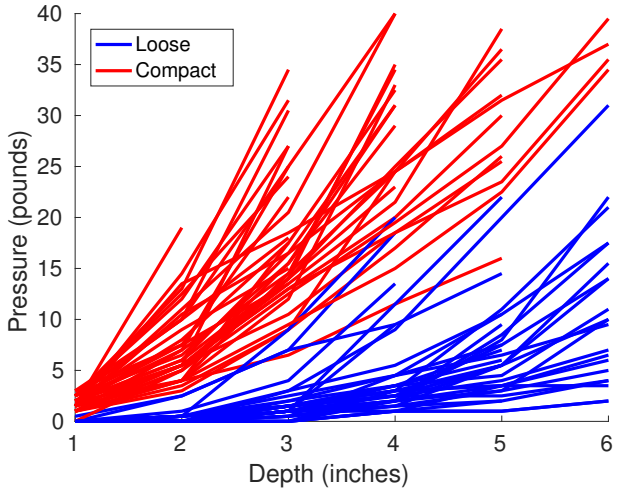

Figure 5.13: Measured pressure-sinkage curves in the granular slag for each point shown in Figure 5.12.

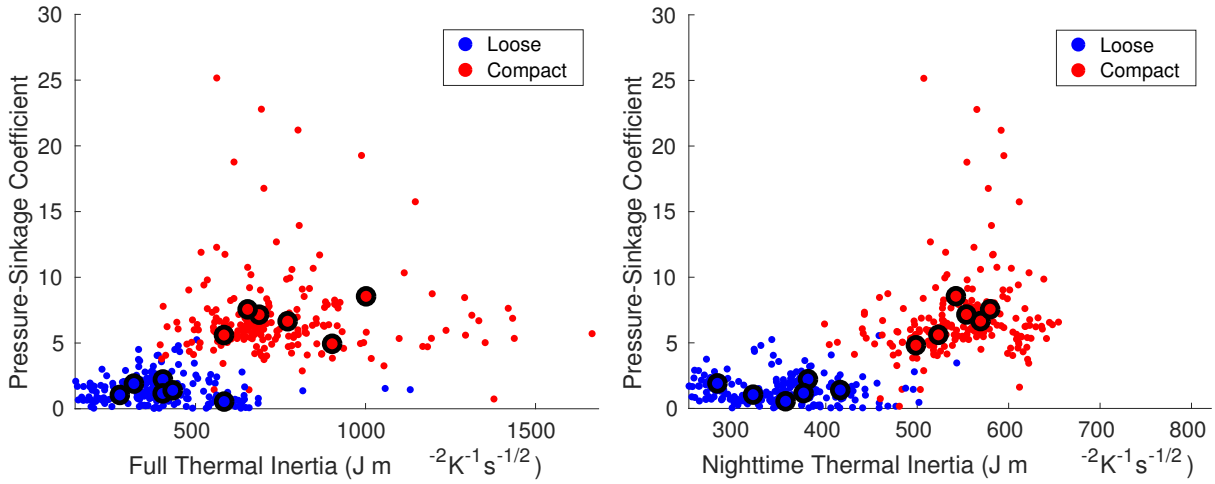

(a) Full data thermal inertia.

(b) Nighttime thermal inertia.

Figure 5.14: Estimated thermal inertia and apparent thermal inertia plotted against pressure-sinkage coefficient. The small points show the interpolated pressure-sinkage values and thermal inertia for each 0.8 by 0.8 m sample. The larger, outlined points show the average within each region.

fit for each measurement. This is equivalent to setting the sinkage exponent (n) in Equation 3.10 to 1. Comparisons are then made based on the pressure-sinkage coefficient (k_p). These pressure-sinkage coefficients were then interpolated for each sample and are presented in Figure 5.11b.

5.2.5 Predicting Compaction with Thermal Inertia

The thermal inertia of terrain was correlated to compaction and the measured pressure sinkage-curves. Figure 5.14 shows thermal inertia plotted against best-fit pressure-sinkage coefficients. Figure 5.14a uses data from all 48 hours and Figure 5.14b only uses temperature measurements made during the nighttime, which is expected to have lower error. The correlation coefficients for the interpolated pressure-sinkage coefficients and thermal inertia in each sample were 0.47 and 0.68 for thermal inertia estimates made using all the data and only nighttime data, respectively. P-values in both cases were negligibly small. A second comparison considers the average pressure-sinkage coefficients and thermal inertias within each of the 12 prepared granular regions. Using averages, the correlation coefficients were 0.85 and 0.83 for 48 thermal inertia measurements and nighttime measurements, respectively. The p-values were both less than 1×10^{-4}, indicating that the results are statistically significant. In both comparisons, there is a statistically significant, moderate-to-strong correlation between thermal inertia and the pressure-sinkage coefficient.

Nighttime temperatures better distinguish between the loose and compact terrain but have lower temperature differences. The average temperature difference between loose and compact regions ranges between only 1 and 1.5 K at night. However, with a 50 mK instrument sensitivity, this is easily detected. With both sources of thermal inertia, thermal inertia separates the two soil compaction levels reasonably well. Lower thermal inertia corresponds to lower pressure sinkage

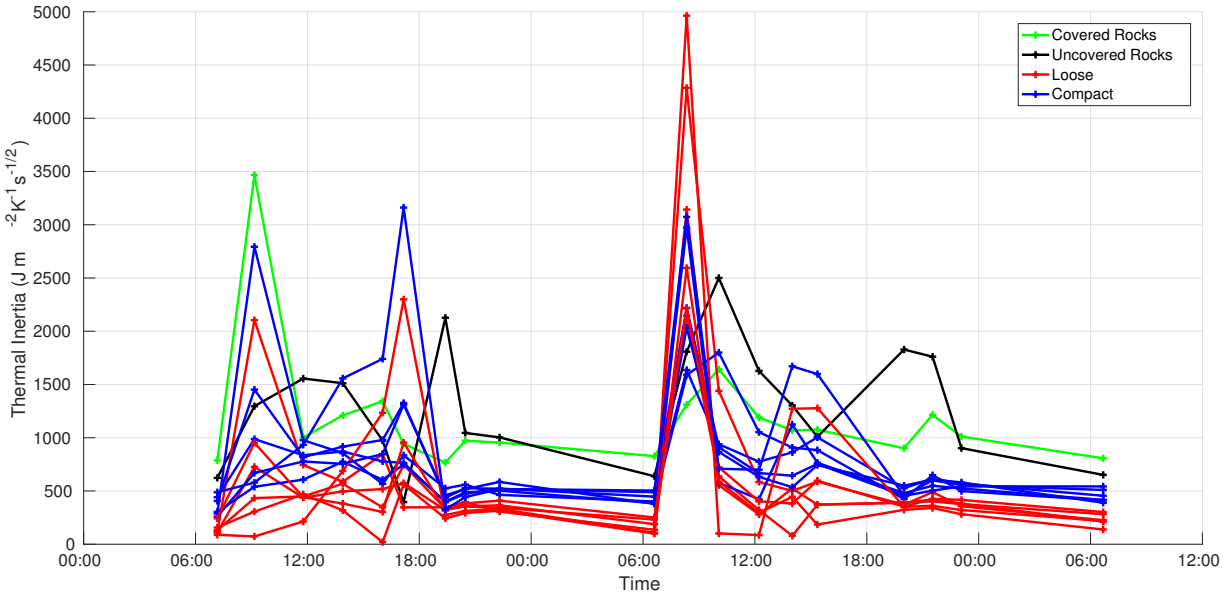

Figure 5.15: Average thermal inertia values for each of the 14 prepared regions plotted at the 19 measurement times over the two day period. Lines are colored by the type of terrain sample.

coefficients and less compaction. Higher thermal inertia corresponds to higher pressure-sinkage coefficients and more compaction.

Thermal inertia estimates varied over the course of the day due to errors in albedo estimation, reflections from solar radiation, and surface heat flux estimation. Average estimates of thermal inertia in each of the 14 prepared sample regions are plotted in Figure 5.15. Clearly at night there is lower variance in thermal inertia estimates than during the day. Loose and compact regions are better separated at night.

The goal of using thermal inertia in traversability prediction is to identify safe areas for the rover to travel. Two approaches are evaluated. The first approach is to identify traversable terrain using estimated thermal inertia. The second approach is to look at raw surface temperatures. When looking at surface temperatures, warmer terrain is considered more traversable at night and cooler terrain is considered traversable during the day. The boundaries between day and night are determined by identifying the intersection points of curves with thermal inertias of 200 and 600 $Jm^{-2}K^{-1}s^{-\frac{1}{2}}$.

The efficacy of both of these approaches at different times of day is evaluated using receiver operating characteristic (ROC) curves. Several example curves are shown in Figure 5.16. These show plots of the true positive rate versus the false positive rate for predicting a compact sample. Area under the ROC curve (AUC) is used to better quantify the accuracy of each method. The AUC is an estimate of the probability that a classifier ranks a randomly chosen compact sample higher than a randomly chosen loose sample [36]. The significance of each of these AUC values is easily obtained through a simple rescaling, which follows a Mann-Whitney U-distribution [14]. The Mann-Whitney U-test can be used to test the hypothesis that a randomly selected compact sample will have a higher thermal inertia than a randomly selected loose sample [100]. The null hypothesis is that a compact sample has equal or lower thermal inertia.

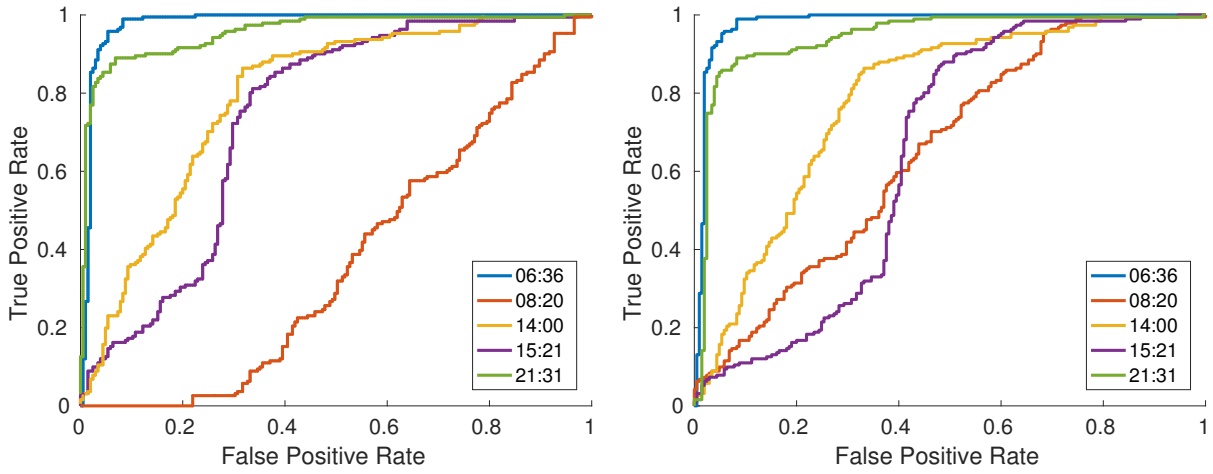

(a) Thermal inertia.

(b) Surface temperatures.

Figure 5.16: Example receiver operating characteristic (ROC) curves for different times of day. The positive and negative classes are compact and loose terrain, respectively. The two different ROC plots use thermal inertia and raw temperature.

The AUC for thermal inertia estimated using all of the data is 0.94 with a p-value of 1×10^{-53} indicating that the compact samples have higher thermal inertia than the loose samples with very high confidence. AUC is plotted at the 19 different measurement times for both methods in Figure 5.17. Figure 5.17a shows AUC for distinguishing compact slag from loose slag. A higher area under the curve corresponds to a better separation between loose and compact samples. P-values for both methods were much less than 0.01 in all cases except for thermal inertia at 8 a.m. on the second day.

The results are for thermal inertia and raw temperature similar. Both approaches identify compact samples most accurately after sunset and before dawn. In the middle of the day between about 10 a.m. and 4 p.m., both methods separate the classes; however, thermal inertia performs better. Errors in albedo measurement are expected to have the greatest effect during the day as shown in Figure 5.1. The benefit of using thermal inertia is that differences in albedo can be accounted for, resulting in more accurate thermal inertia measurements and correspondingly better separation between loose and compact terrain classes.

A second analysis was conducted to evaluate whether thermal inertia and temperature could distinguish rock from granular materials. The positive class was rock (either bare or covered in granular slag) and the negative class represented granular materials. Unfortunately, as explained earlier, there was likely significant error in the albedo measurement for bare rock due to the small size of the region. A third approach was evaluated to emphasize the importance of taking into account albedo and using it to estimate thermal inertia. Instead of using pyranometer-measured albedo, the best-fit albedo when fitting to the full two-day dataset was used. The mean albedo found by fitting to the data was 0.38 in contrast to the pyranometer-measured value of 0.20.

Figure 5.17b shows AUC for distinguishing either rock from slag plotted over the course of the test. During the day, all three techniques perform similarly. The error during the day came form the inability to distinguish between slag and slag-covered rock. At night, the use of best-fit

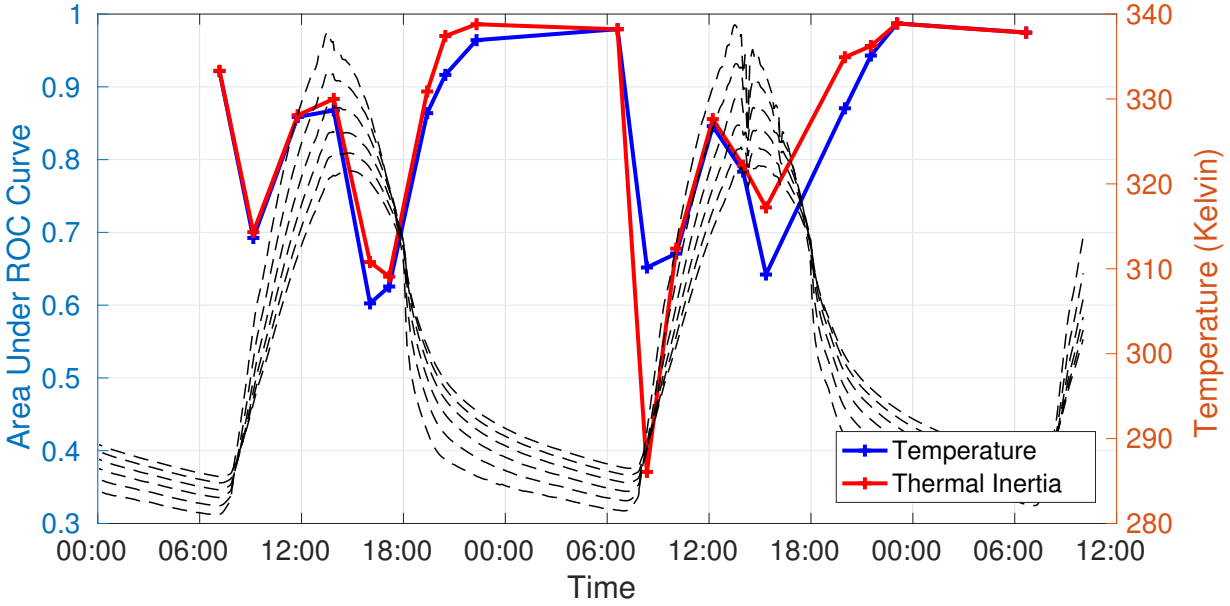

(a) Positive class - compact slag. Negative class - loose slag.

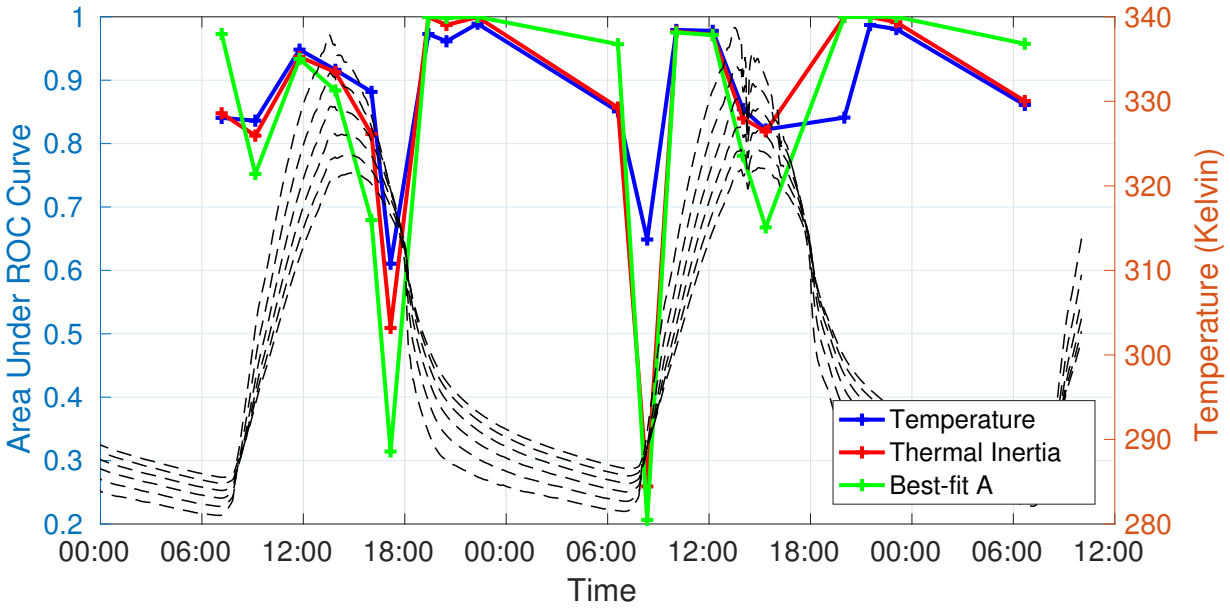

(b) Positive class - rock. Negative class - granular slag.

Figure 5.17: Area under the ROC curve (AUC) evaluated throughout the test. AUC is compared for thermal inertia and raw temperature. The dotted lines correspond to model-predicted temperatures for several different thermal inertias. “Best-fit A” refers to using thermal inertia with the best-fit albedo value from the full two-day dataset; whereas, “Thermal Inertia” uses pyranometer-measured albedos.

albedo enabled better separation between classes with AUCs of 1.0 before midnight and 0.96 pre-dawn. Using only temperature or thermal inertia with pyranometer-measured albedo have lower AUCs at night. This is because they are unable to distinguish the bare rock from slag. As shown in Figure 5.7, despite having much higher thermal inertia, the rock temperature is very similar to the temperature of compact slag after midnight until the sun comes up again. The rock absorbs less heat during the day due to its much higher albedo. This highlights the importance of having estimates of albedo and using thermal inertia rather than raw surface temperature. All three approaches have similar low AUC values at times thermal inertia temperature curves were crossing, which is expected and a limitation of the physics behind the approach. The p-values for all methods were much less than 0.01 except at 5 p.m. on the first day and 8 a.m. on the second day. In those cases the evidence was not enough to reject the null hypothesis that rock had the same or lower thermal inertia than slag.

Rock has significantly higher thermal inertia of any of the granular materials and it should have been easy to obtain an AUC of 1.0 before dawn (around 6 a.m.) using accurate estimates of albedo. The error at these times highlights a limitation of this approach on Earth. The sensible heat flux, H, was fit to all samples, which contained primarily granular materials. The best-fit flux was likely to have been significantly influenced by unmodeled latent heat flux. Latent heat would not have been nearly as significant in the rocks because granular materials can store water in between particles; whereas, rocks cannot. Consequently, the heat fluxes experienced by the rock were most likely unequal to the heat fluxes experienced by the granular slag, which led to errors in identifying rock.

Errors in albedo estimates and non-planar terrain surfaces are significant sources of error during the day. The largest, obvious errors came from non-planar surfaces and the resulting difference in temperature based on viewing direction. An example is shown in Figure 5.18. In this example, the same region is shown from two locations at almost the same time at approximately 180°different viewing angles. At around 3:30 p.m. sunlight was incident at a $\sim$30°angle from almost directly behind Figure 5.18a. Local slopes pointing towards the rover and sun were hotter than the slopes pointing away from the sun and toward the rover's position in Figure 5.18b. Consequently, the temperatures in Figure 5.18a appear warmer than in Figure 5.18b. Additional error could result from increased backscatter of infrared radiation into the thermal camera. Another potential contribution to the discrepancy in temperatures between the two figures could be drift in the radiometric calibration; however, it would not solely explain the magnitude of the difference. These temperature inconsistencies were significant when sun angles were lower in the morning and evening.

Both approaches (temperature and thermal inertia) performed poorly around 8 a.m. when the temperature curves of different thermal inertias are expected to cross. This is a known limitation of the physics behind this approach. It is difficult to distinguish materials since the temperatures are all very similar at that time. Errors in heat flux estimation are amplified at this time because the differences in temperature curves are so minute. A similar limitation exists in the evening. This resulted in decreased AUC between around 4 p.m. and 8 p.m. It is likely that performance would have dipped to similar levels as the morning, but the exact time when all of the ideal curves are crossing was not sampled on either day.

One potential source of bias in the results is the water content of the slag. Figure 5.19 shows the estimated thermal inertia plotted with the average water content over the course of the two-day

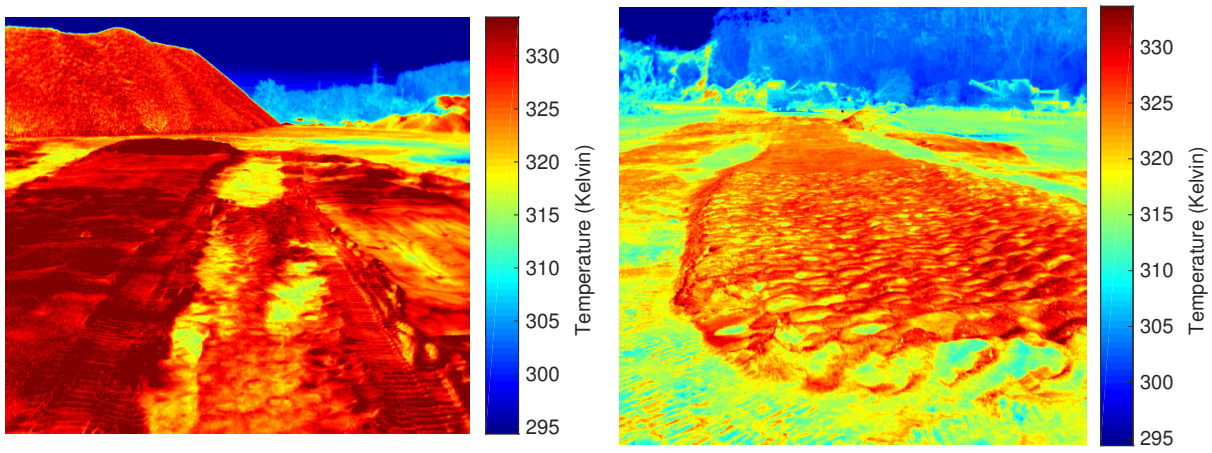

(a) Sun in front of the camera.

(b) Sun behind the camera.

Figure 5.18: Two images taken at around the same time from opposite perspectives showing the viewpoint dependence of temperatures with low sun angles (∼30°). The warm region furthest from the camera on the left corresponds to the region directly in front of the camera on the right. Images were taken at an approximately 180°difference in rover heading.

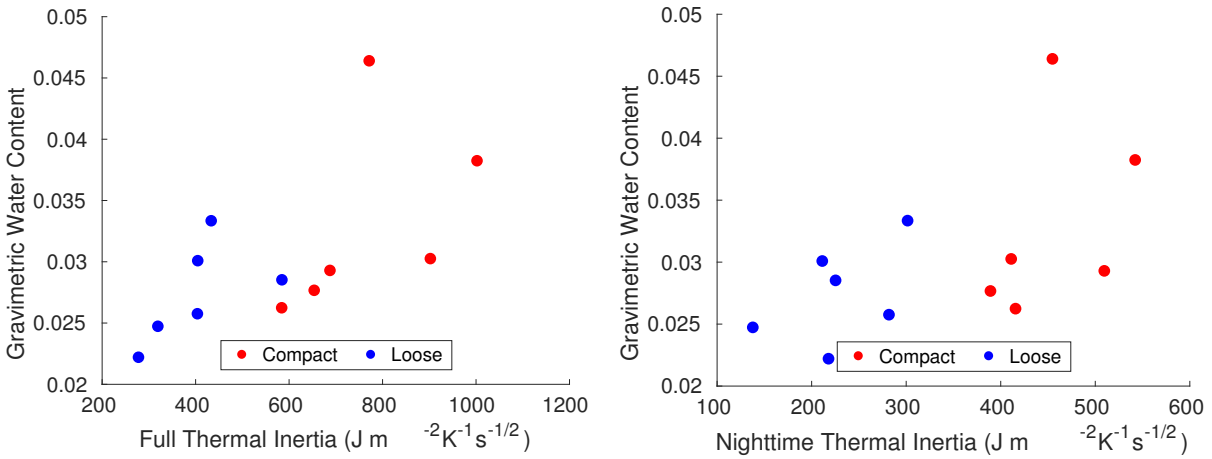

(a) Full data thermal inertia.

(b) Nighttime thermal inertia.

Figure 5.19: Estimated thermal inertia and nighttime thermal inertia plotted against average gravimetric water content for each of the 12 granular regions.

test for each of the 12 granular regions. All samples were prepared at the same time using the same slag source, which would have had approximately uniform water content. Thus, the difference in water content were either caused by the compaction or by the local geometry of the surface. Looser regions get warmer during the day, which could lead to more water escaping through evaporation. Looser regions also have more space between the grains for the water to escape. The highest water content region corresponded to a local depressions where water pooled and would have likely exhibited similarly high water content if it had been loose as well.

The correlation coefficients between water content and thermal inertia were 0.63 and 0.57 with p-values of 0.02 and 0.05 for thermal inertias estimated using all data and only nighttime data, respectively. Thus, with some confidence, it can be concluded that there was a moderate correlation between thermal inertia, compaction, and water content. More compact regions exhibited higher thermal inertias and water content than loose regions.

However, this moderate correlation does not fully explain the difference in thermal inertia between compact and loose regions. As previously discussed, the correlation coefficients between the average thermal inertia and average pressure-sinkage coefficients within each region were 0.85 and 0.83 for all data and nighttime data, respectively. Correlation of the average values is a more direct comparison to water content measurements than the more numerous interpolated pressure-sinkage coefficients. In summary, it is difficult to completely disambiguate the influence of water content from that of compaction. Both factors affected measured thermal inertia. Compact regions have higher thermal inertia than loose regions regardless of water content. However, the differences in temperature between the two densities appeared to be made greater by the differences in water content.

5.3 Continuous Data Collection in Sand

A second experiment was conducted to validate the correlation between the ability of thermal inertia to differentiate of different preparations of the same granular material. This experiment not only the effects of time of day but also the length of time observing terrain. This experiment also shows the ability of thermal inertia to differentiate soil compaction in a different material, silica sand.

5.3.1 Experimental Setup

For each experiment, 15 different samples were prepared in a grid pattern in a sand pit. 8 cells of the grid were compacted and 7 were loosened. The compact samples were prepared by removing the surface layer of the sand to reveal a more compact, cemented layer of sand underneath. The loose samples were prepared by manually loosening with a shovel. Both classes were leveled to provide a similar visual appearance for all cells.

The experiments were conducted in July in Pasadena, CA, which is a very dry climate. It had not rained for several weeks prior to the experiment. This experiment did not have the significant early-morning condensation that introduced water in the soil in the previous experiment. The dew point was -4°C and the temperature only reached as low as 18°C, so there was no morning condensation in this test. Water content measurements were not made as in the

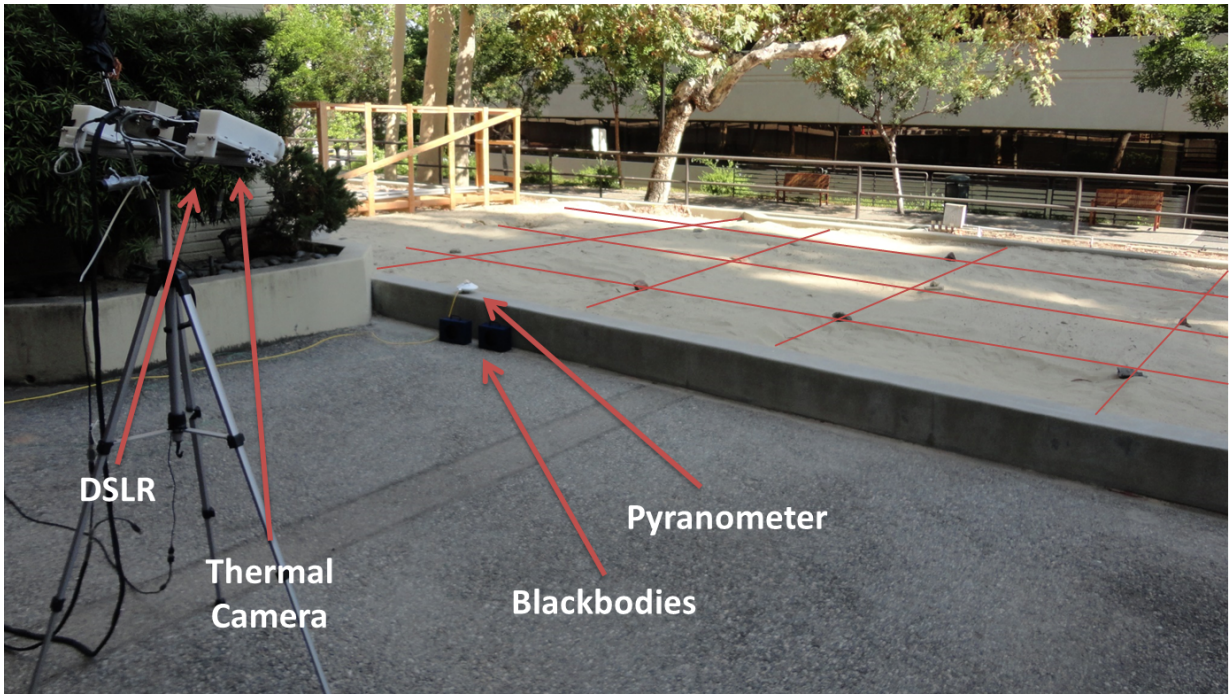

Figure 5.20: The experimental setup showing the thermal camera and DSLR viewing a grid of compact and loose sand.

previous experiment. However, based on the climate differences, the effect of variations in water content is expected to have been significantly lower.

The experimental setup is shown in Figure 5.20. A continuous, 48 hour dataset was collected. A pyranometer was placed next to the sand pit in order to get ground truth measurements for solar insolation. The sandpit was adjacent to buildings and trees, which caused changing shadows during the transit of the Sun. These shadows introduced significant error in the estimation of solar irradiance during the day. R_{lw} was estimated as a function of air temperature and dew point using a statistical model for atmospheric radiation under clear skies [73]. The weather was mostly clear; however, there were also short periods of transiting clouds, which are not accounted for in the model for R_{lw}. As in the prior experiment, the γ parameter for H was fit for each day using data from the other day.

Infrared imagery was collected using a Thermoteknix Miricle 110K thermal camera, which had a sensitivity of 60 mK. Because these cameras were not radiometrically calibrated and had high thermal drift, two blackbodies were placed in the field of view of the camera and held at different temperatures. Ground truth temperature of the blackbodies was measured throughout the day, with the exception of 11 p.m. to 7 a.m., to compensate for their fluctuating temperatures. By interpolating between the two temperature references in the thermal images, temperature was estimated across the scene. Temperatures for the samples over time where calculated by manually selecting the regions in the thermal imagery and averaging the temperature within each region. All instruments sampled at one minute intervals.

Two example thermal images are shown in Figure 5.21. The difference between different samples is easy do distinguish at night (8 p.m.) but more difficult at 11 a.m. Figure 5.21b shows

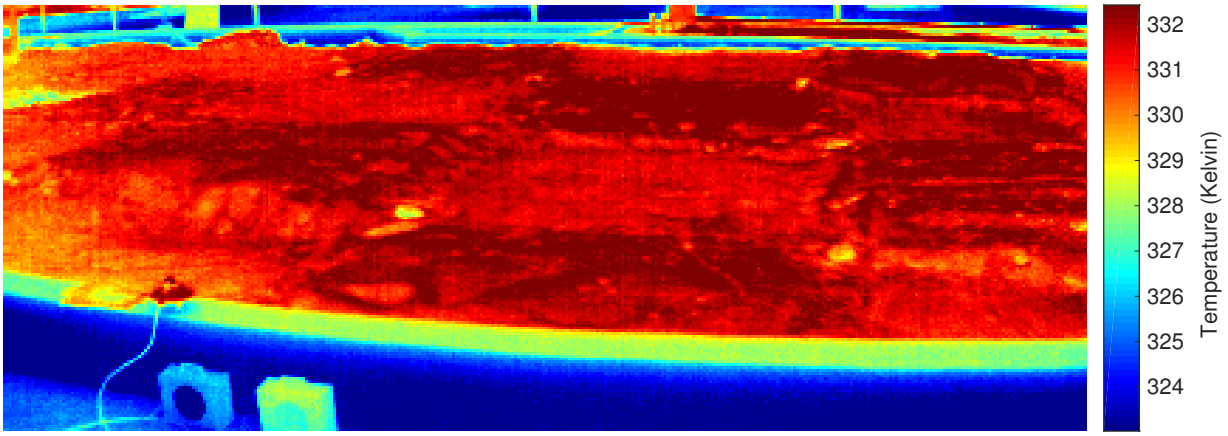

(a) 8 p.m.

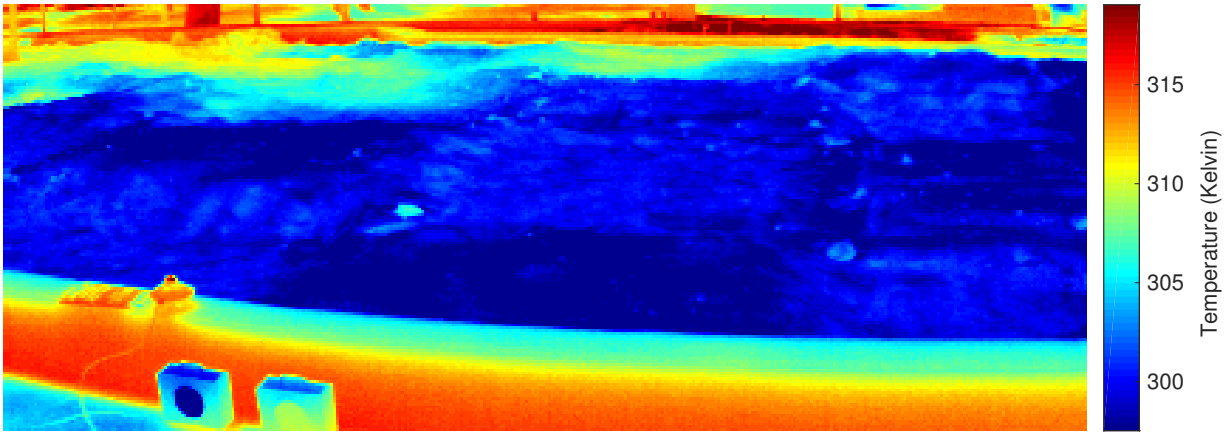

(b) 11 a.m.

Figure 5.21: Images of the sandpit showing the loose-compact grid at two different times of day.

one of the difficulties of predicting slip on Earth that was encountered in this test, shadowing by vegetation. Trees above the sand caused shadows in the sand that moved during the day (shown here in the top left of the image).

Traversability of each sample was estimated by measuring wheel slip under a constant drawbar pull. The robot used in these measurements was an iRobot ATRV-JR, which has a mass of 50 kg with pneumatic tires. For each test, it was commanded to drive forward at a constant velocity while a drag force of approximately 180 N was applied to the robot. A constant force was maintained manually by monitoring a spring scale. The velocity of the robot was measured by tracking three AprilTags on the side of the robot [111]. Wheel slip was calculated using difference between commanded and actual velocity divided by the commanded velocity, which was measured by driving on a flat, solid surface. However, there is some error in the slip measurements caused primarily by the variability in the robot's open-loop velocity control.

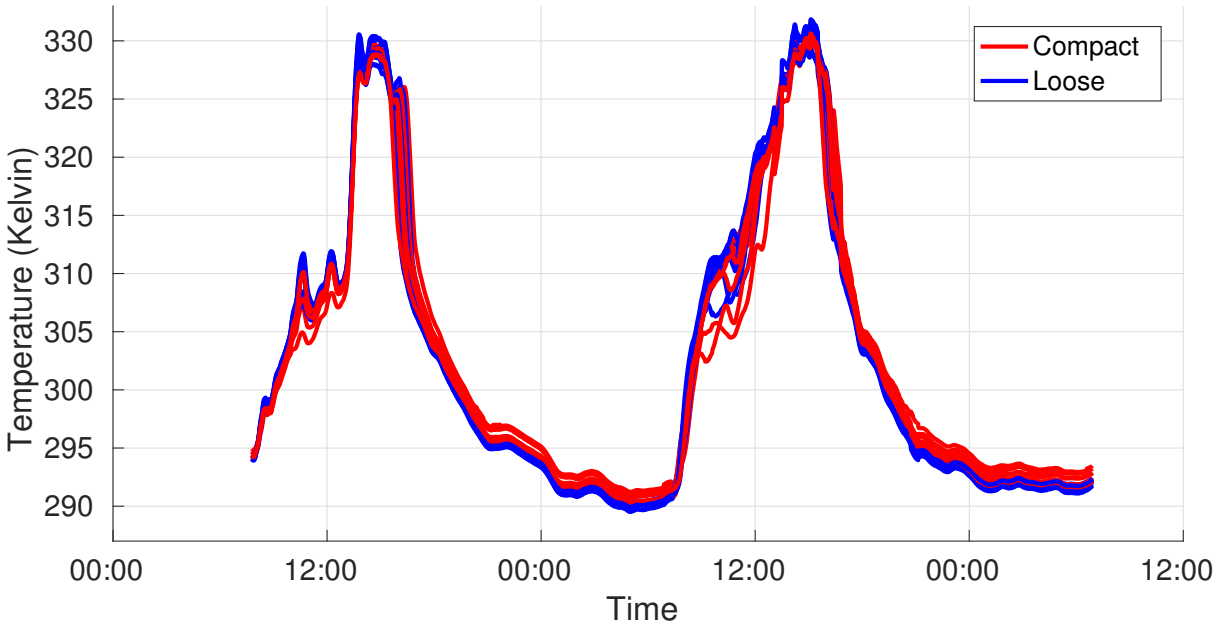

Figure 5.22: Temperatures of all 15 samples shown over the two-day measurement period. Temperatures were filtered with a 20 minute moving average filter.

5.3.2 Results

The temperature for each sample was found by averaging the temperature over the surface from the thermal imagery. Plots of temperatures over the course of the two day period are shown in Figure 5.22. The average compact sample was 0.8 K warmer than the average loose sample at night. During the day, the average compact sample was 0.6 K cooler. This temperature difference was very consistent at night but very erratic during the day. This non-ideal behavior during the day was caused by the shadows that transited over the surface. These temperature differences were small but still easily detected by the thermal camera with a 60 mK NETD.

The analytical model was fit to temperature and heat flux data to estimate thermal inertia for all 15 samples. When fitting to the full observation period of the sample, the average root mean squared error was 3.8 K with a maximum of 7.3 K and a minimum of 1.4 K. It was more difficult to estimate the surface heat flux in areas with shadows. Consequently, the model fit better to the samples that had fewer clouds and shadows.

The estimated values for thermal inertia are closely related to measured slip and compaction, but the relationship varies over the course of the day. Estimated thermal inertia is plotted against measured slip in Figure 5.23 for thermal inertia estimated at two different times per day. As in the previous experiment, AUC is used to compare the separability of loose and compact samples by thermal inertia and temperature. Figure 5.23a shows thermal inertia estimated using a temperature measurement at 8 p.m., which corresponded to an AUC of 1.0 with a p-value of 3×10^{-4}. With high confidence, thermal inertia perfectly separated the compact and loose samples. Since all of the compact regions had lower slip than all of the loose regions, higher thermal inertia also corresponded to higher traversability. This perfect separation is not the case at all times during the day. For example, Figure 5.23b shows the same plot but using temperature measurements at 11

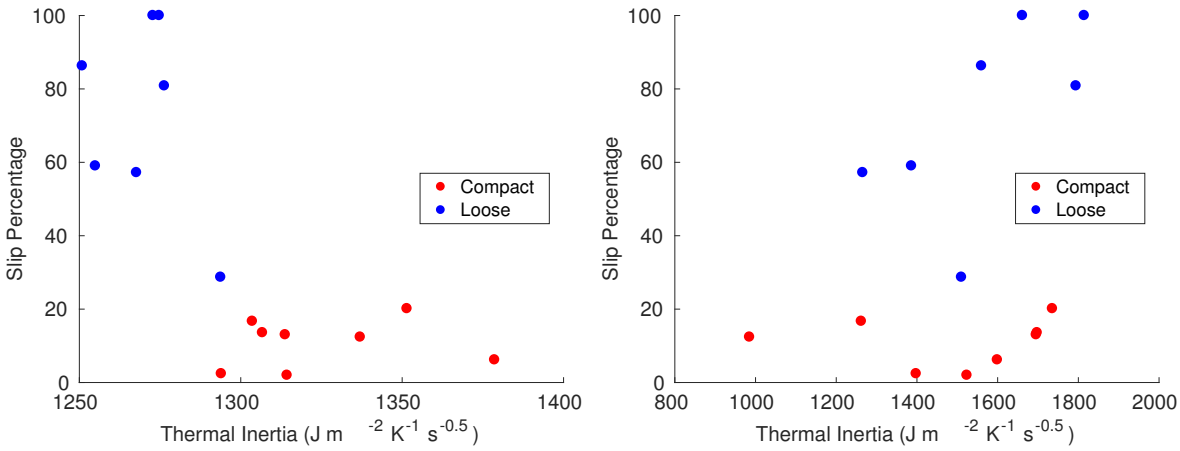

(a) AUC of 1.0 at 8 p.m.

(b) AUC of 0.43 at 11 a.m.

Figure 5.23: Slip plotted against thermal inertia at two different times per day. Samples were colorized by the prepared compaction level.

a.m. This resulted in an AUC of only 0.43, which is worse than random at selecting a compact sample. The p-value in this case was 0.69, so it is impossible to conclude that higher thermal inertia estimated at 11 a.m. corresponded to higher compaction. These errors were strongly influenced by the uneven illumination over the surface.

AUC was calculated every hour for the full 48 hours to understand how well thermal information separates compaction over the course of the day. As in the previous experiment, results using raw temperature are compared to results using estimated thermal inertia. Figure 5.24a shows AUCs at every point and Figure 5.24b shows p-values. Temperature and thermal inertia had similar AUCs and significance levels at most times during the day as would be expected since the albedo was treated as uniform. In this experiment, there is a much starker contrast between separability using nighttime day and daytime data than in the prior experiment. At night, thermal inertia almost perfectly separates compact and loose terrain with very high confidence levels. However, during the day, thermal inertia and temperature are both generally worse than random.

Additional analysis was performed to evaluate not only the effect of time of day but also the length of time observing the sample. The results from this analysis are shown in Figure 5.25. The highest AUCs were found with long observation periods that started between 12 p.m. and 3 p.m. and included data from the nighttime. This is supported by the albedo error analysis in 5.1, which shows that the lowest thermal inertia estimation error comes when sampling temperature at night and during the day. Based on this analysis, one would expect similarly low for measurements that start in the morning and end at night, which is not exhibited experimentally. This discrepancy is due to the fact that the highest prevalence of shadows was before noon during the day. Consequently, any measurements that include that data have higher error than those that do not. The lowest AUCs were found in samples that only included data from the middle of the day when the shadows caused uneven illumination. Another column of low AUCs occurs on both days between around 3 p.m. and 6 p.m. These errors are caused by a shadow as the sun falls behind a building for the evening.

In this experiment, thermal inertia was once again shown to provide near-perfect separation

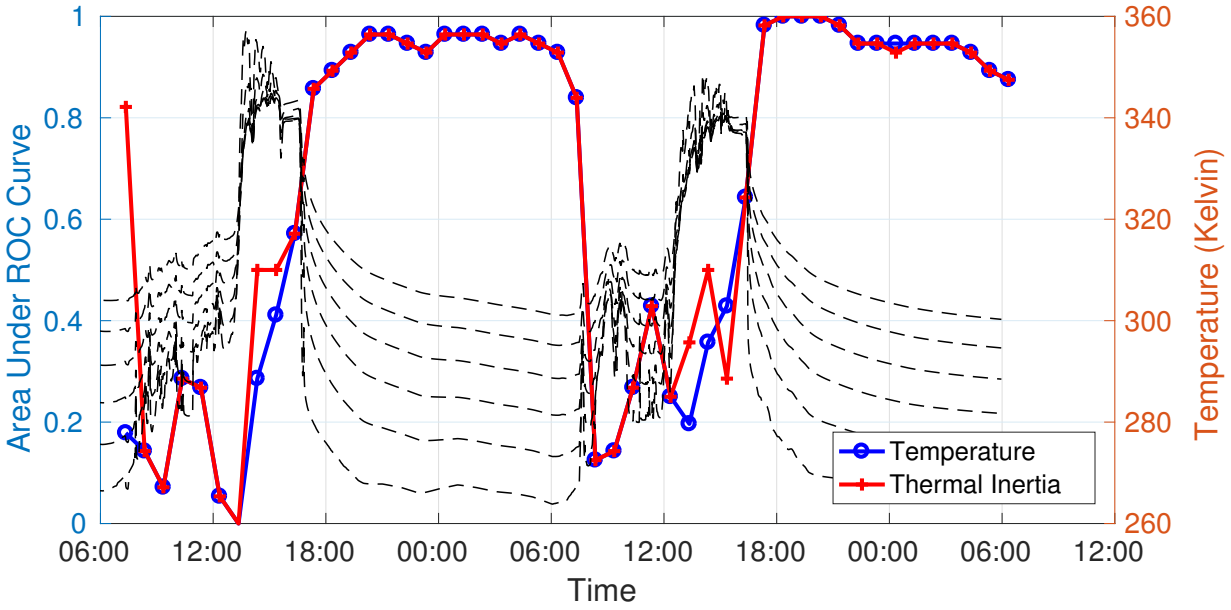

(a) Area under the ROC curve.

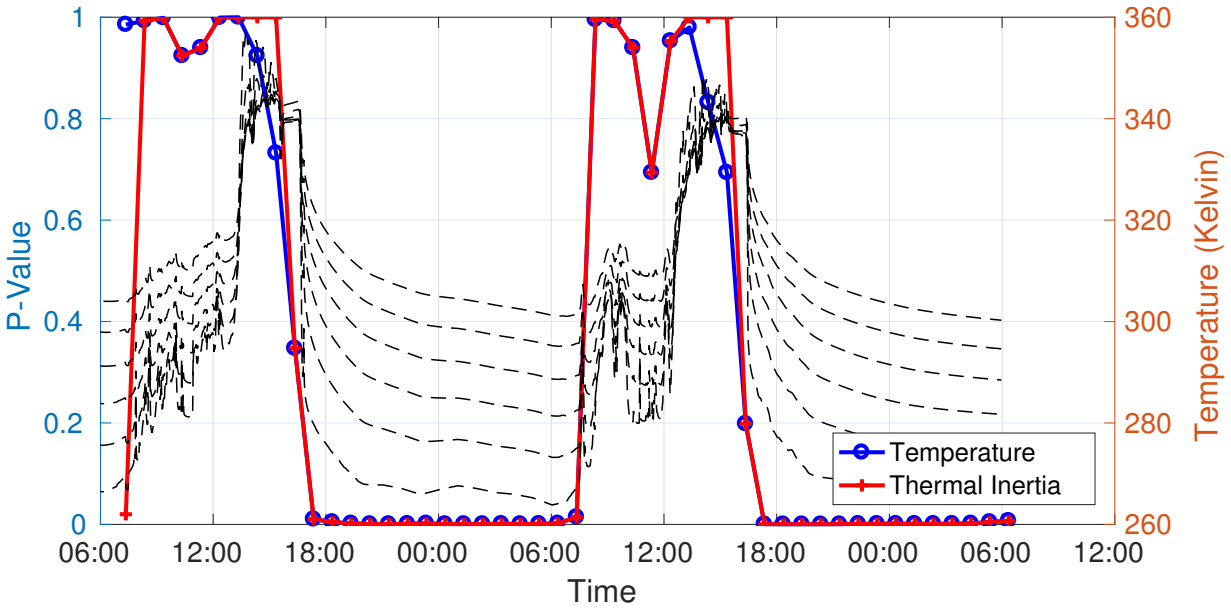

(b) P-value for statistical significance.

Figure 5.24: Area under the ROC curve (AUC) for evalauted throughout the test for predicting compact samples. AUC is compared for thermal inertia and raw temperature. The dotted lines correspond to model-predicted temperatures for several different thermal inertias.

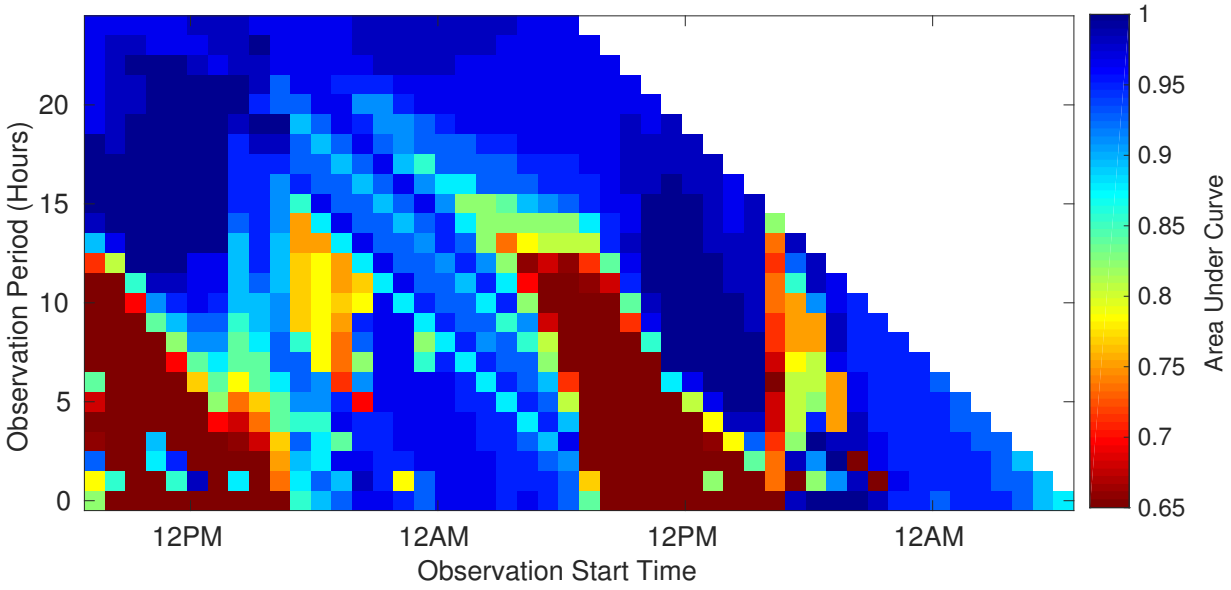

(a) Area under the ROC curve. Minimum value is limited to 0.65 to show contrast.

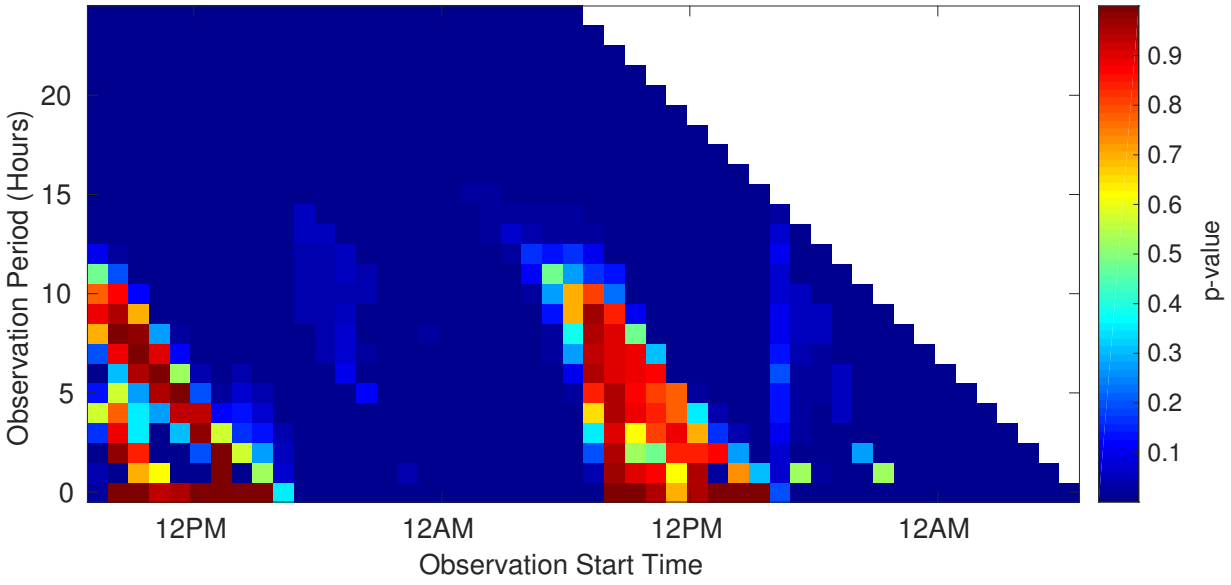

(b) P-value for statistical significance.

Figure 5.25: Area under the ROC curve (AUC) for evalauted throughout the test for predicting compact samples using thermal inertia. Results are shown for different the times of day and lengths of observation.

between loose and compact terrain at night. Compact terrain was confirmed to be more traversable through rover slip measurements. Observation times long enough to include data from both the day and night provided the best class separation. This experiment also illuminated the difficulties of applying this approach terrestrially. Uneven illumination caused by vegetation and man-made objects can cause significant errors during the day. These inaccuracies are less important at night.

5.4 Discussion

This chapter presented a method for determining relative differences in traversability in granular materials by estimating thermal inertia from infrared imagery. Both temperature and thermal inertia differentiated between different compaction levels of the same material despite similar surface appearance. In general, higher thermal inertia granular materials were more compact and traversable than lower thermal inertia granular materials. The quality of thermal inertia estimates and the resulting prediction of mobility is a function of both the length of time and the time of day the terrain is observed. Nighttime measurements provided accurate separation between loose and compact granular materials. Daytime measurements were more affected by shadows, flux errors, and albedo errors, which resulted in poor separation between terrain classes. Thermal inertia measurements were also shown to distinguish bedrock from granular materials even when the rock is below a thing layer of slag. At night, there was near-perfect separation between slag and rock. During the day, it became more difficult to distinguish between slag and rock covered with slag.

The rock experiments also showed the importance of estimating thermal inertia and how prediction of thermal inertia improves over raw temperature. Rock and slag were more easily separable at night when estimating thermal inertia with accurate albedo. In the experiments varying compaction, significant variations in slope and albedo were not explored. If these parameters had been varied, the performance or raw temperature measurements would have been significantly reduced. With accurate estimates of surface heat fluxes, the efficacy of thermal inertia should not be greatly affected by slope and albedo variations. This would rely on the ability to estimate albedo from a rover, which can be accomplished with visual cameras [48, 62] but was beyond the scope of this thesis.

Because of heat flux errors, absolute thermal inertia estimates varied throughout the day. However, relative differences in thermal inertia were shown to distinguish between compact and loose granular materials. A robot could leverage these measurements to detect changes in terrain properties and avoid potentially hazardous terrain. For example, assume a robot is driving down a compact, sandy road with high thermal inertia. If it detects a looser region with much lower thermal inertia ahead, it could choose to steer around rather than risk entrapment.

It should be noted that only differences in density were explored in these experiments and that the variations in density were extreme. Variations in density in natural terrain on Earth may be more subtle and produce smaller differences in temperature and thermal inertia. However, density was selected as a test case because it represents the hardest case. Materials are visual identical but differ in traversability. Actual differences in traversability in natural terrain are unlikely to be caused solely by density variations. Differences in particle sizes and cementation are also prevalent and can contribute towards significant differences in both thermal inertia and

traversability.

These experiments demonstrated the use of thermal inertia for distinguishing between loose and compact granular materials on Earth. However, the terrestrial environment is not ideal for this approach. Significant errors were caused by clouds, shadows from vegetation and buildings, water content, and atmospheric heat fluxes. This limits potential applicability on Earth to dry, desert environments that minimize the factors. Subsequent chapters will explore the Moon and Mars, where this approach is more appropriate.

Chapter 6

Predicting Slip in Sand on Mars

The most significant mobility challenges that rovers have encountered on Mars have been caused by loose, granular materials. Sandy regions cause wheels to slip and sink, which slows progress and risks entrapping a vehicle. However, terrain on Mars is very diverse. Both the macroscopic and microscopic characteristics of sand vary greatly over the surface. In most types of terrain, average terrain slope predicts slip with high accuracy. However, in sand, slope alone fails to fully account for the slip behavior [40, 132]. The inherent difficulty of predicting slip is exacerbated by the risk-averse nature of planetary rover missions that avoid sand regions whenever possible. This results in few training examples from which to learn a competent prediction model. Consequently feature-intensive, visual approaches that only consider surface appearance risk significant overfitting. Instead, this chapter uses thermal inertia as a single measurement that is highly correlated to the underlying granular properties that govern wheel-terrain interaction.

Previous chapters have used the relationship between thermal properties of terrain and wheel-terrain interaction to distinguish loose and compact granular materials experimentally on Earth. Unfortunately, due to differences in geology, gravity, and atmospheric pressure, showing a correlation between thermal inertia and mobility on Earth is not a guarantee that the same correlation exists on Mars. There is some evidence that thermal inertia is related to soil strength on Mars [116]; however, no study has deeply investigated its ability to improve rover mobility predictions. Simulation and laboratory experiments help but cannot exactly the capture either wheel-terrain interaction or thermal processes on Mars. The only way to confidently determine the extent to which thermal inertia is correlated with traversability is to show it empirically with in-situ data from the Mars rovers.

In prior terrestrial experiments, thermal inertia was used to show relative differences in compaction and traversability. On Mars, surface heat fluxes are easier to predict than on Earth and particle size differences cause significant variations in thermal inertia. This enables the use of absolute thermal inertia estimates to classify terrain as either safe or hazardous. Because this relies on accurate thermal inertia estimates, only high-confidence measurements that use data from the daytime and nighttime are included.

This chapter analyzes the capability of thermal inertia measurements to improve slip prediction in Martian sand using in-situ data from the Curiosity rover. For each wheel slip measurement in sand, thermal inertia is estimated using both Curiosity's onboard Ground Temperature Sensor (GTS) and the orbital Thermal Emission Imaging System (THEMIS). A mixture of experts (MoE)

approach is used to model slip behavior. This model assumes that slip cannot be explained by a single type of sand but is instead a combination of multiple independent models. A soft-max function assigns data to experts using thermal inertia as its input. Results from two-expert models are compared against one-expert model to show the ability of thermal inertia to identify high-slip sand regions using both ground-based and orbital observations.

6.1 Slip Prediction with Thermal Inertia Classes

This section describes an approach that uses thermal inertia to improve slip prediction. Thermal inertia is estimated for each slip measurement with Data from Curiosity's GTS. Slip models are then learned using a mixture of experts model that automatically separates terrain classes by thermal inertia.

6.1.1 Thermal Inertia Estimation

Thermal inertia is estimated for each slip measurement in sand. Curiosity is equipped with the Ground Temperature Sensor (GTS) that measures ground temperatures for scientific investigation of the geologic composition and atmospheric processes on Mars. The GTS is a set of thermopiles that are located on Curiosity's mast with a fixed pointing at 120°clockwise off azimuth and 22°down. It has a horizontal field of view of 60°and a vertical field of view of 40°. It measures one temperature value from an ellipse of nominally 100 m^2 at 4 o'clock relative to the rover's forward direction. This region is adjacent to and not in the path of the rover during straight drives. The baseline mode of operation is measuring temperature at 1 Hz for about 6 minutes at the beginning of every hour [136]. This is not an ideal sensor for mobility prediction because: (1) it only records one measurement from the entire ellipse and (2) it does not measure the terrain ahead of the rover. However, it still provides an unprecedented amount of data, which enables this investigation.

The KRC model was used to simulate surface temperatures [80]. Given a set of input parameters, it estimates the surface heat fluxes in Equation 3.4 and forward simulates the heat diffusion equation (Equation 3.6) to find the surface temperature at a desired time of day. Forward simulation of both surface and subsurface temperatures is accomplished using an iterative finite-differences approach. This model has been used extensively for orbital thermal analysis [48] and recently for GTS data [62]. For more detail see Kieffer [80].

The KRC model requires a number of input parameters to generate predicted surface temperatures. Thermal inertia and albedo are treated as free parameters. Slope, slope azimuth, dust opacity, solar longitude (season), latitude, and elevation were fixed inputs to the model. Slope and slope azimuth were estimated from Navcam imagery. Dust opacity was estimated by scaling Opportunity dust opacity measurements to match the elevation for Curiosity [91]. Opportunity data was used because it is a good approximation and dust opacity data for Curiosity is not yet published [90].

First the GTS data is filtered to remove measurements during which the rover is shadowing the measurement, the measurement falls out of calibration range, or the power supply is out of nominal operating range. Remaining GTS data points are low-pass filtered to reduce noise and then binned into 5 minute intervals throughout the day.

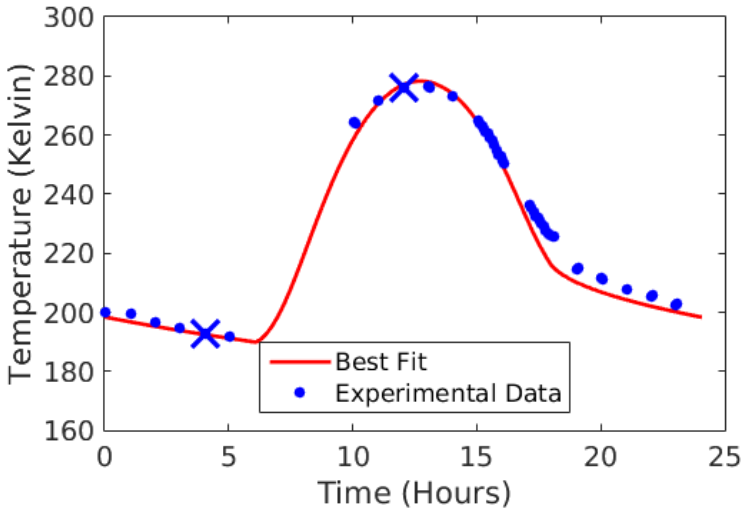

Figure 6.1: Example GTS data and best-fit model. The Xs indicate data points used to find the thermal inertia and albedo.

Both thermal inertia and albedo are unknown *a priori* and estimated following the example of Hamilton et al. [62] by minimizing the squared error between GTS-measured temperatures and the KRC analytical model. Albedo can be estimated from camera imagery but does not always match thermally-derived albedo [46]. Thus to avoid errors in thermal inertia estimates, albedo is also considered a free parameter. The optimization uses only GTS temperatures from pre-dawn and mid-day because the diurnal amplitude is strongly affected by thermal inertia and using only these measurements reduces error caused by slope and albedo. An example fit is shown in Figure 6.1. When fitting to only these points, the analytical model underestimates morning and afternoon temperatures, which is likely due to terrain heterogeneity [62]

6.1.2 Learning Slip Models

A two-expert MoE model is used to predict slip and separate low-slip sand from high-slip sand. A simple model with few hyperparameters is used to reduce overfitting due to the low availability of data. Here it is assumed that slip, y, in a given type of sandy terrain, T_i, is a function of the surface geometry, x. Let $\mathbf{x}$, $\mathbf{y}$, and $\mathbf{I}$ be $K \times 1$ vectors, where K is the number of data points. Additionally, it is assumed that each of $N = 2$ terrain classes can be separated using thermal inertia, I. This results in the following model for slip in sand:

$$p(\mathbf{y}|\mathbf{I}, \mathbf{x}, \Theta) = \sum_{i=1}^{N} \pi_i(\mathbf{I}, \nu_i) p(\mathbf{y}|\mathbf{x}, \theta_i) \tag{6.1}$$

where $\pi_i(\mathbf{I}, \nu_i)$ is the gating function for sand class T_i with parameters ν_i, $p(\mathbf{y}|\mathbf{x}, \theta_i)$ is the distribution of slip in a given class with parameters θ_i, and $\Theta = \{\{\nu_i\}_1^N, \{\theta_i\}_1^N\}$.

The gates are linear softmax functions:

$$\pi_i(\mathbf{I}, \nu_i) = \frac{\exp\left(\nu_i^T [\mathbf{I}, \mathbf{1}]\right)}{\sum_{j=1}^{N} \exp\left(\nu_j^T [\mathbf{I}, \mathbf{1}]\right)} \tag{6.2}$$

where each ν_i is a 2×1 weight vector. This simple softmax function was chosen to essentially provide a threshold on thermal inertia that separates low-slip and high-slip sand. Slip is modeled as an M^{th} degree polynomial of slope, $\mathbf{y} = \phi(\mathbf{x})\beta + \epsilon$. β is an $(M+1) \times 1$ weight vector, $\phi(\mathbf{x}) = [\mathbf{x}^n, \mathbf{x}^{n-1}, ..., \mathbf{x}^1, \mathbf{1}]$, and $\epsilon \sim \mathcal{N}(0, \sigma)$. If $\theta_i = \{\beta_i, \sigma_i\}$, it follows that

$$p(\mathbf{y}|\mathbf{x}, \theta_i) = p(\mathbf{y}|\mathbf{x}, \beta_i, \sigma_i) = \mathcal{N}\left(\phi(\mathbf{x})\beta_i, \sigma_i\right) \tag{6.3}$$

To reduce overfitting, slip is constrained to never decrease with increasing slope [40]. A linear model was chosen because conditioned on the model parameters, the data points are independent and identically distributed (i.i.d.), which makes fitting a model easier than with a nonparametric model [130]. Expectation Maximization is used to find the parameters Θ for the model following the approach in Yuksel et al. [171]:

(1) E-step. At iteration m, compute expected class assignments for each sample t given by $\{y_t, x_t, I_t\}$ [20]:

$$h_t^{(m)}\left(y_t|x_t, I_t\right) = \frac{p\left(y_t|x_t, I_t, \Theta_i^{(m)}\right)}{\sum_{j=1}^{N} p\left(y_t|x_t, I_t, \Theta_j^{(m)}\right)} \tag{6.4}$$

(2) M-step. Given the expected values for the latent class assignments, compute model parameters $\Theta^{(m+1)}$:

$$\nu^{(m+1)} = \underset{\nu'}{\operatorname{argmax}} \sum_{t=1}^{K} h_t^{(m)} \log \pi\left(I_t, \nu'\right) \tag{6.5}$$

$$\theta^{(m+1)} = \underset{\sigma', \beta'}{\operatorname{argmax}} \sum_{t=1}^{K} h_t^{(m)} \log p(y_t|x_t, \beta', \sigma') + \lambda \beta'^T \beta' \tag{6.6}$$

Where λ is a regularization parameter to prevent overfitting. Note that unlike in standard regression models, Equation 6.6 must be solved using constrained optimization due to the non-decreasing constraint. The E and M steps are alternated and repeated until convergence. The only design parameters are λ and M. λ was set to 1. M was set to 3 because a third degree polynomial was the simplest polynomial able to explain the data.

6.2 Testing Dataset from Curiosity

This section describes the data from Curiosity. Curiosity is a six wheeled rover with a rocker-bogie suspension system. It is 3 m long, 2.8 m wide, and has wheels 0.5 m in diameter [57]. It has been operating on Mars since August, 2012 and has driven over 15 km. Samples from sols 1-986 are

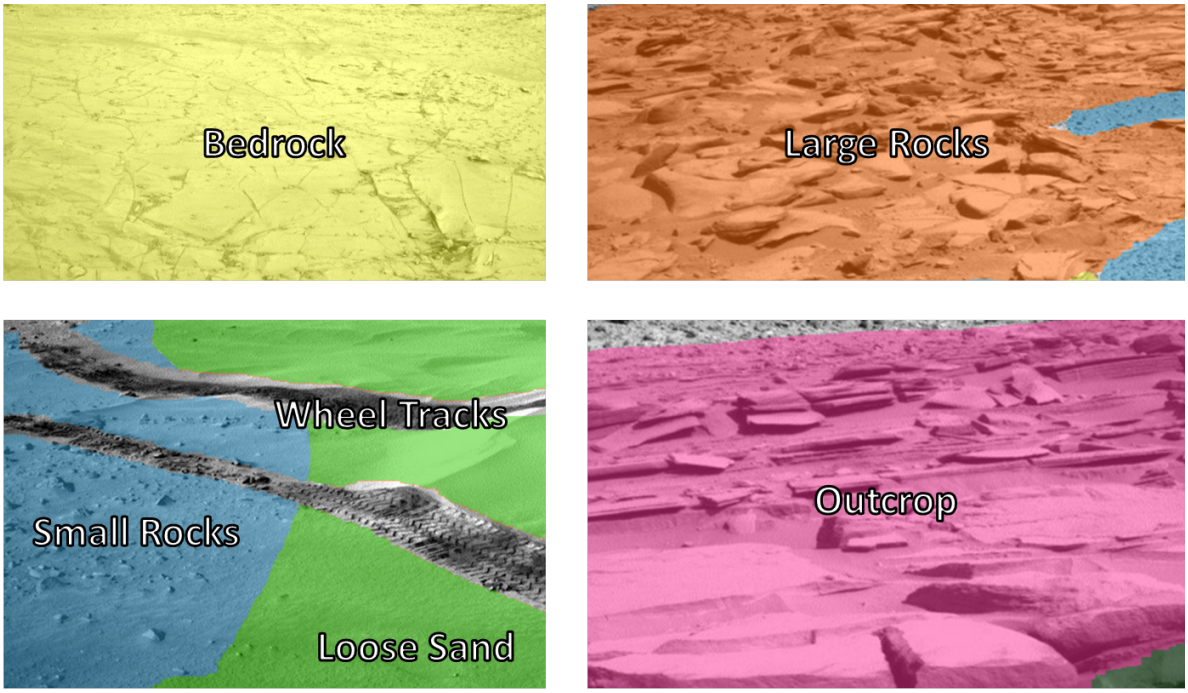

Figure 6.2: Six terrain classes identified by SPOC-G classifier [132]

considered here, where a sol refers to a day on Mars. Sand slip measurements are identified and matched to thermal inertia measurements. Resampling occurs to reduce data imbalance.

6.2.1 Finding Slip Measurements in Sand

To identify slip measurements in sand, a list of all VO slip measurements was collected. Almost all drives with VO enabled are between 0.5 and 1.25 m in length at 0.25 increments. Only drives greater than or equal to 0.5 m in length are considered here. Position error for VO is expected to be less 2.5% of the drive distance [97]. The slip for a given drive is calculated as the average of all individual wheel slips. This slip magnitude includes both longitudinal and lateral slip. Slope is the magnitude of rover tilt averaged over the drive as calculated by the IMU. Positive slope corresponds to driving up the slope and negative slope corresponds to driving down the slope regardless of driving direction (i.e. forward versus reverse). Slip and slope magnitude were used instead of decomposing both into longitudinal and lateral components to reduce the risk of overfitting. Both slip and slope were predominantly in the longitudinal direction [40].

Instead, drives through sand were automatically identified using a terrain classifier and false positives are manually removed. Terrain classes are identified by applying the SPOC-G [132] terrain classifier to Navcam imagery. Figure 6.2 shows the six terrain classes SPOC-G identifies. Sand is identified when there is a smooth surface without any rocks. It can either evenly sloped or rippled.

$\sim$2500 Navcam images were classified. The terrain class for each slip measurement was estimated as the mode class of all predictions from all images viewing that location. Using the combination of multiple labeled images for a given location tends to correctly identify more of

the drives in sand; however, it also leads to more false positives. This is in contrast to identifying class from only one "best" image as in Rothrock et al. [132], which has fewer false positives but identifies fewer of the actual drives in sand. For example, in Figure 6.3a, wheel tracks in deep sand were predicted to be outcrops in the closest images to the site. However, it is identified as sand using multiple viewpoints.

Once all sandy regions were automatically identified, false positives were manually eliminated. Measurements where fewer than four of the wheels were on sandy terrain were removed. Examples of correctly identified drives in sand are shown in Figures 6.3a–6.3d. Examples of false positives that were manually removed are shown in Figures 6.3e and 6.3f. At times it can be difficult to determine exactly what "sand" is. For example, in Figure 6.3f, all of the wheels were on sand. However, under four of the wheels were also rocks on top of the sand, which was classified as *Small Rocks*, so these samples were removed.

6.2.2 Matching Thermal Inertia

To reduce bias for geologic investigation, Curiosity's GTS points off to the side of the rover towards a region that the rover will never drive over without turning. Thus, slip measurements rarely directly overlap with GTS thermal inertia measurements. Instead, thermal inertia for a given slip sample was estimated by taking the closest sample that contains part of the same terrain class as the slip sample (i.e. the closest thermal inertia measurement classified as sand).

The terrain class of each thermal inertia measurement was estimated by first finding the region that the sensor was viewing. Then the terrain class was found using the same approach as described in Section 6.2.1 for slip data. Example matches are shown in Figure 6.4. In some cases, there is very clear overlap between the slip and thermal inertia measurements (e.g. Figures 6.4e and 6.4c). In other cases, there is no clear measurement in that same sand region. This was the case in Moonlight Valley (on the left of Figure 6.4a). Moonlight Valley was considered to be part of Dingo Gap. This likely introduces some error as Arvidson et al. have estimated that the sand Dingo Gap is more traversable than in Moonlight Valley [8]. Hence, the thermal inertia in Moonlight valley would likely have been measured lower.

Similar problems exist in Figures 6.4d,6.4g, and 6.4i, where the measured thermal inertia for that site is higher than it would have been had the sand been measured alone. In Logan's Pass (Figure 6.4i), there was no matching GTS measurement in the *Sand* class. However, the matched measurement included mostly sand that only had small rocks on top, so the thermal inertia was most likely not greatly increased.

For each slip measurement, an orbital estimate of thermal inertia is also identified using THEMIS data. THEMIS is a thermal emission spectrometer orbiting Mars that measures surface temperature at a resolution of 100 m per pixel [32]. Thermal inertia estimates were taken directly from data products produced by the THEMIS team [31]. Thermal inertia for each sample is identified by finding the corresponding pixel in the thermal inertia map. An example is shown in Figure 6.5.

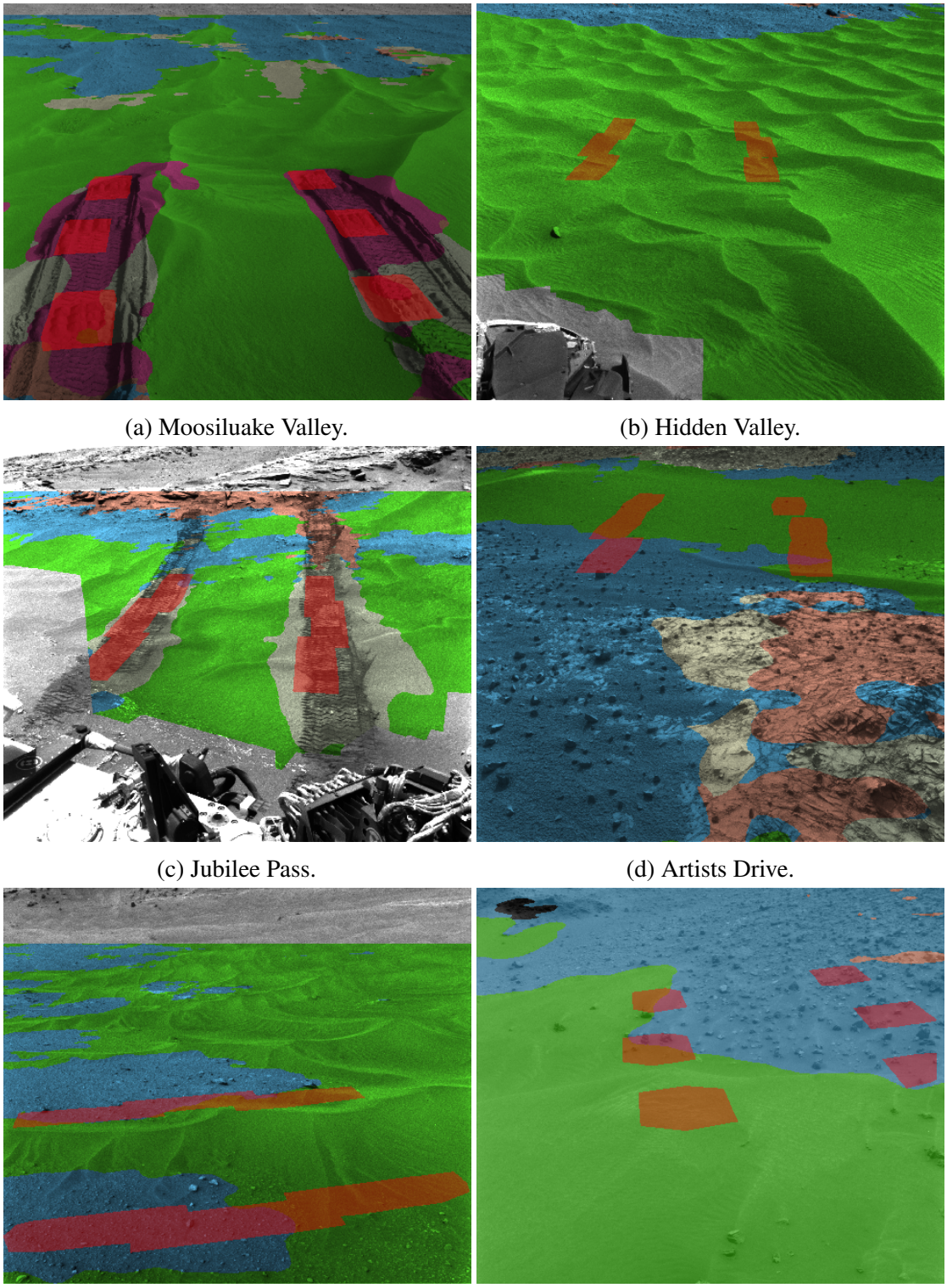

(a) Moosiluake Valley.

(b) Hidden Valley.

(c) Jubilee Pass.

(d) Artists Drive.

(e) Sol 799 sand.

(f) Logan's Pass.

Figure 6.3: Example images of slip measurements in sand colorized by predicted terrain class. (a)–(d) were used in the data set, (e) and (f) are examples of measurements that were eliminated due to heterogeneous terrain. The red regions indicate the location of the rover's wheels during its drive.

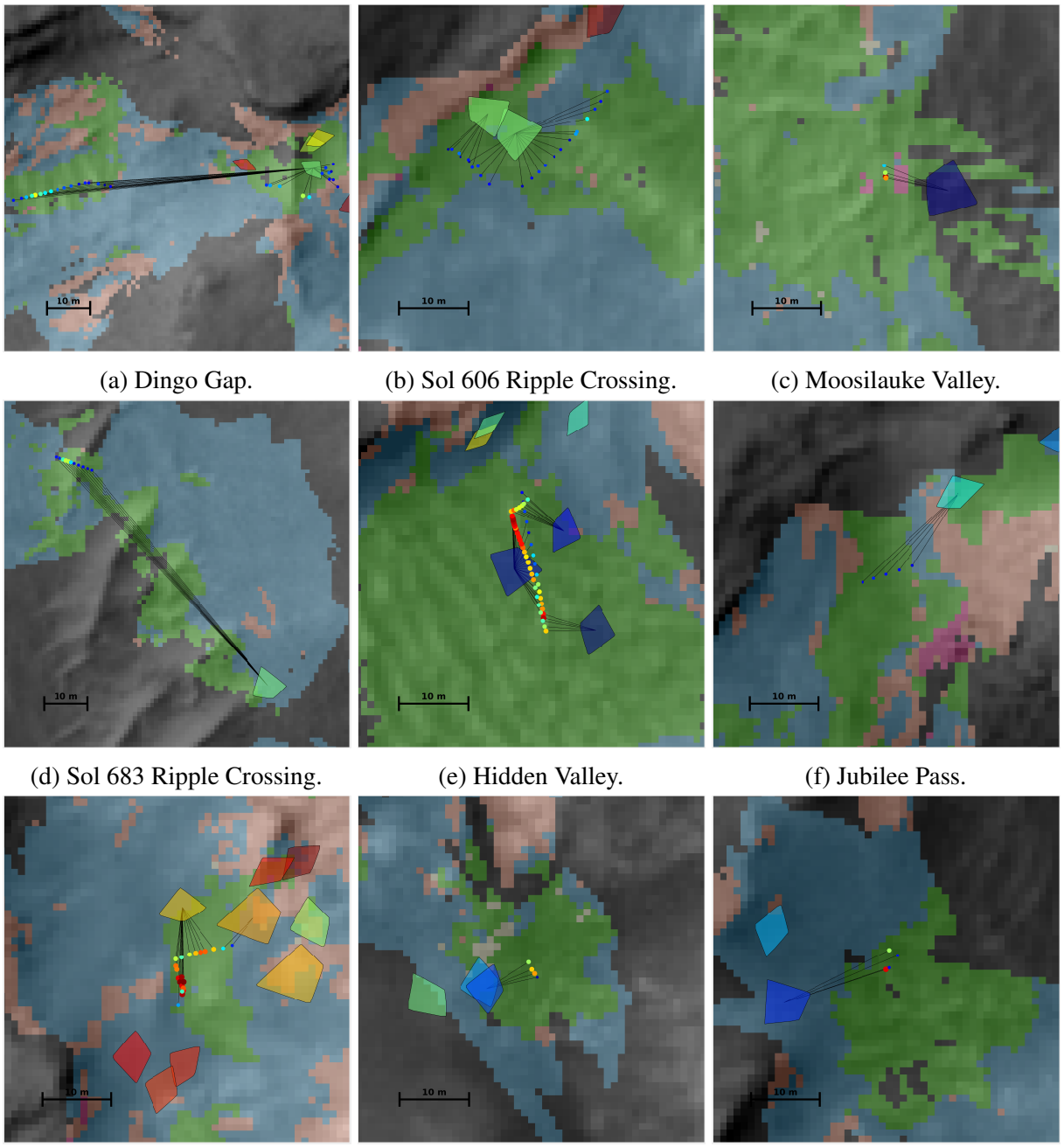

(a) Dingo Gap. (b) Sol 606 Ripple Crossing. (c) Moosilauke Valley.

(d) Sol 683 Ripple Crossing. (e) Hidden Valley. (f) Jubilee Pass.

(g) Artists Drive. (h) Sol 978 Logans Pass. (i) Sol 983 Logans Pass.

Figure 6.4: Matches between GTS data and slip data for all 9 sites. Slip data points are shown as circular data points at the location of the center of the rover. Data points are sized and colored by slip. Larger redder data points correspond to more slip. Smaller, bluer data points are less slip. GTS measurements are the kite-shaped regions and are colored by thermal inertia. Bluer is lower thermal inertia, redder is higher thermal inertia. Plots are overlaid on Hirise orbital imagery with estimated terrain classes from Navcam imagery. Black lines show each slip measurements matched to the best GTS measurements.

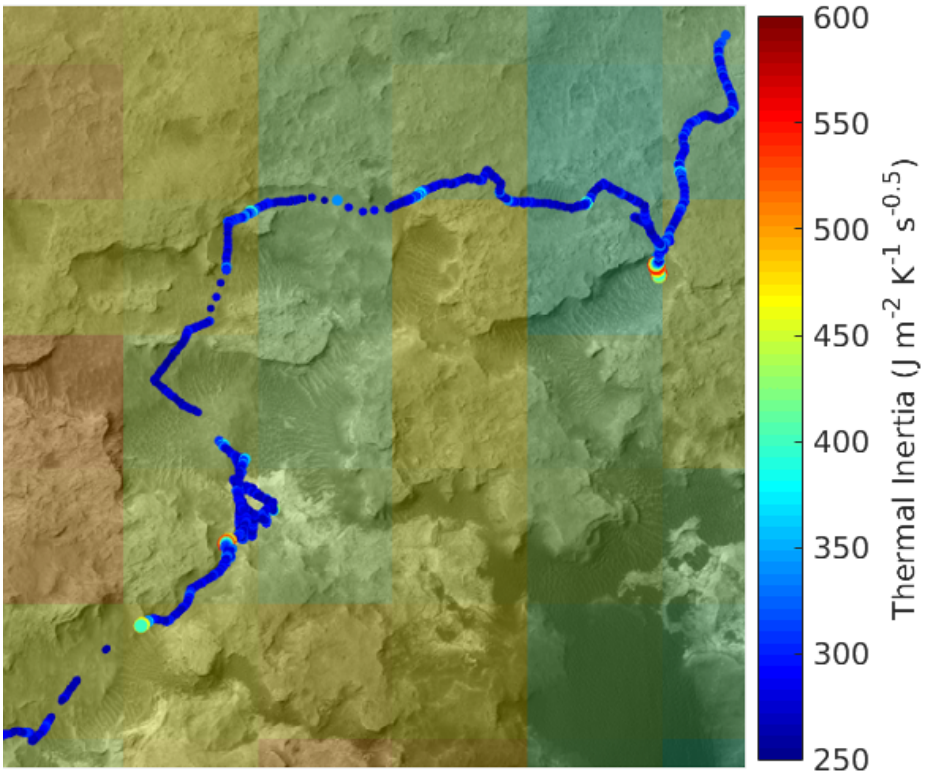

Figure 6.5: Orbital THEMIS thermal inertia image overlaid on Hirise camera image. Plotted points show Curiosity's path and are sized and colored by slip. Bluer, smaller points have lower slip. Redder, larger points have higher slip. The colormap corresponds to the overlaid THEMIS image.

Table 6.1: Drives in sand listed by name of the site, the first sol, the number of samples, maximum slope x_{max} (degrees), maximum slip y_{max} (percentage), average GTS thermal inertia I_{GTS}, and average THEMIS thermal inertia I_{THEMIS}. Units of I are $\frac{J}{m^2 K \sqrt{s}}$. Note the correlation between I_{GTS} and y_{max}. Sites are sorted by I_{GTS}.

Site Name	**Sol**	**Num.**	$\mathbf{x_{max}}$	$\mathbf{y_{max}}$	$\mathbf{I_{GTS}}$	$\mathbf{I_{THEMIS}}$
Moosilauke Valley	672	4	3.5	79.7	20	451
Hidden Valley	709	49	7.4	80.7	29	413
Sol 983 Logans Pass	983	5	9.6	75.2	47	438
Sol 978 Logans Pass	978	4	8.2	59.8	51	400
Jubilee Pass	747	5	8.4	15.4	88	467
Sol 683 Ripple Crossing	683	11	8.4	47.9	107	456
Dingo Gap	528	30	13.9	51.5	108	479
Sol 606 Ripple Crossing	606	23	8.1	33.3	109	483
Artists Drive	923	17	16.4	83.4	141	456
Total: 9 sites		148				

6.2.3 Resampling

All of the identified measurements of slip in sand are summarized in Table 6.1. This table illustrates the small amount of independent samples available and the imbalance of the data. There are two main problems: (1) there are only 9 independent regions of sand that Curiosity has driven through and (2) slip measurements are not evenly distributed between sites. This data distribution works if it is assumed that each slip measurement is i.i.d. This is clearly not true since many of these samples are closely related to samples in the same site. A more reasonable assumption is that sand characteristics and resulting slip behavior is i.i.d. across the surface. Thus each site should be treated as a sample and not the slip measurement. Oversampling is used to account for this. Underrepresented sites are oversampled so that each of the sites listed in Table 6.1 has the same number of samples.

Because there were few samples at high slopes, four synthetic samples were also added for training from the Earth-calibrated model [67]. Samples were added at the minimum slope with 100% slip, x_{max}, and $-x_{max}1$ for -100%. For Curiosity, $x_{max} = 15^\circ$. These were repeated at both the maximum and minimum thermal inertia (for the given instrument). These constraining points help reduce overfitting to moderate slopes.

6.3 Results and Discussion

Slip samples are plotted in Figure 6.6 and colorized by thermal inertia for GTS estimates and THEMIS. The range of thermal inertia estimates are very different between the two sources; however, this is not considered problematic since only within-model comparisons are made [62, 80, 128]. This discrepancy is likely influenced by the use of MER dust opacity estimates and the significantly greater spatial averaging in the orbital data. Qualitatively, both thermal inertia

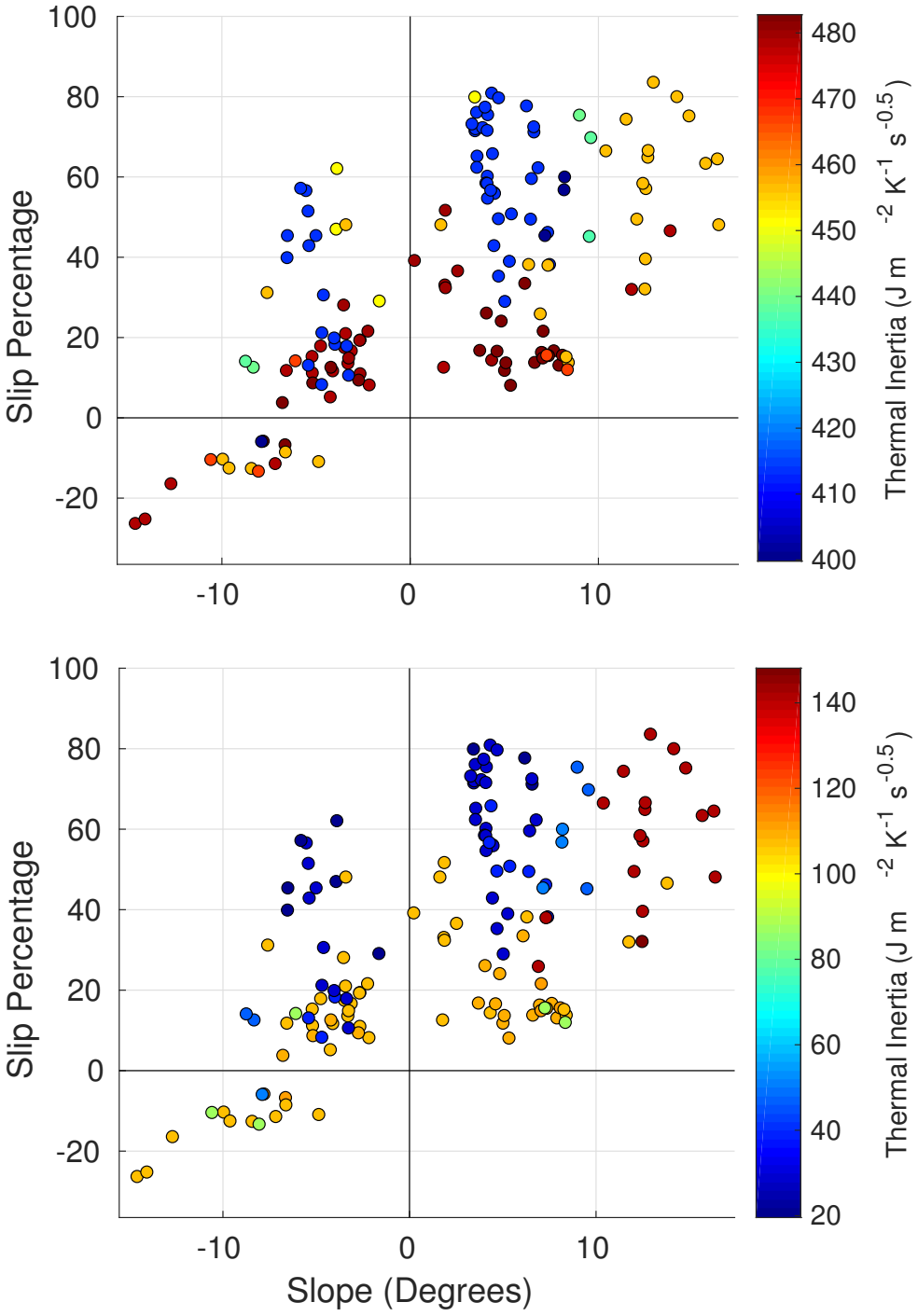

Figure 6.6: Slip versus slope data and models for sand colorized by thermal inertia for THEMIS (top) and GTS (bottom).

Table 6.2: Root mean squared error (RMSE) for the best-fit model using all data and leave-one-out cross validation (CV) for all models both with and without resampling. Standard deviations from 10 trials are shown for the metrics calculated for the re-sampling cases.

	No Resampling		**Resampling**	
Model	Best-fit	CV	Best-fit	CV
Single Expert	20.9	24.0	20.5 ± 0.04	23.1 ± 0.06
Two-Expert THEMIS	15.1	17.6	14.9 ± 0.03	17.5 ± 0.09
Two-Expert GTS	15.1	17.5	14.9 ± 0.03	16.9 ± 1.06

sources distinguish between higher-slip sand and lower-slip sand at a given slope value. In particular, the highest slip data points either occurred at high slope ($\sim$15°) and high thermal inertia or at lower slope ($\sim$5°) but low thermal inertia. The low slope samples with the highest-slip occurred at Moosilauke Valley, Hidden Valley, and both Logan's Pass sites. These four regions also correspond to the GTS lowest thermal inertia.

To quantify the benefit of thermal inertia in slip prediction, three models were compared: (1) a single expert model, (2) a two-expert model using GTS measurements, and (3) a two-expert model using THEMIS measurements. The models are compared based on their root mean squared error (RMSE) for the best-fit model on all of the data and using leave-one-out cross validation. In this context, "leaving one out" means training on data from $N-1$ sites and testing on the remaining site during each iteration of cross validation. Performance was compared for using both the original and resampled data.

Slip models for the single expert and two-expert models are shown in Figure 6.7. Correspondence between predicted terrain class, slip, slope, and site name is shown in Figure 6.8. In all of the two-expert models shown, a very clear trend was learned. Low thermal inertia resulted in higher slip at t a given slope. Both with and without resampling, the GTS and THEMIS models are very similar to each other. In most cases, resampling has the effect that the fewer, high-slip measurements are more heavily weighted. This results in the low-thermal inertia (blue) model shifting to higher slip.

Overall quantitative results are shown in Table 6.2. In all metrics, the two-expert models had lower error than the single-expert model. This supports the hypothesis that thermal inertia improves slip prediction on Mars. The rover slips more as thermal inertia decreases. With resampling, learned thresholds were 69 and $453\frac{J}{m^2K\sqrt{s}}$ for GTS and THEMIS, respectively.

The degraded performance in the cross validation metrics from the best-fit RMSE suggests that the models are overfitting the data somewhat. However, this is expected given that there are only 9 unique sites. In cross validation the two-expert models have lower error than the single-expert model showing that models including slip prediction have higher predictive performance. The reduction in RMSE with resampling in the best-fit is expected, more samples are clustered around fewer points. There is a corresponding reduction in cross validation error for all three models that suggests that the resampled data decreases overfitting to sites with more slip measurements. However, the reduction in error is very slight. This could indicate that the data distribution was not a significant, at least with a simple third degree polynomial model.

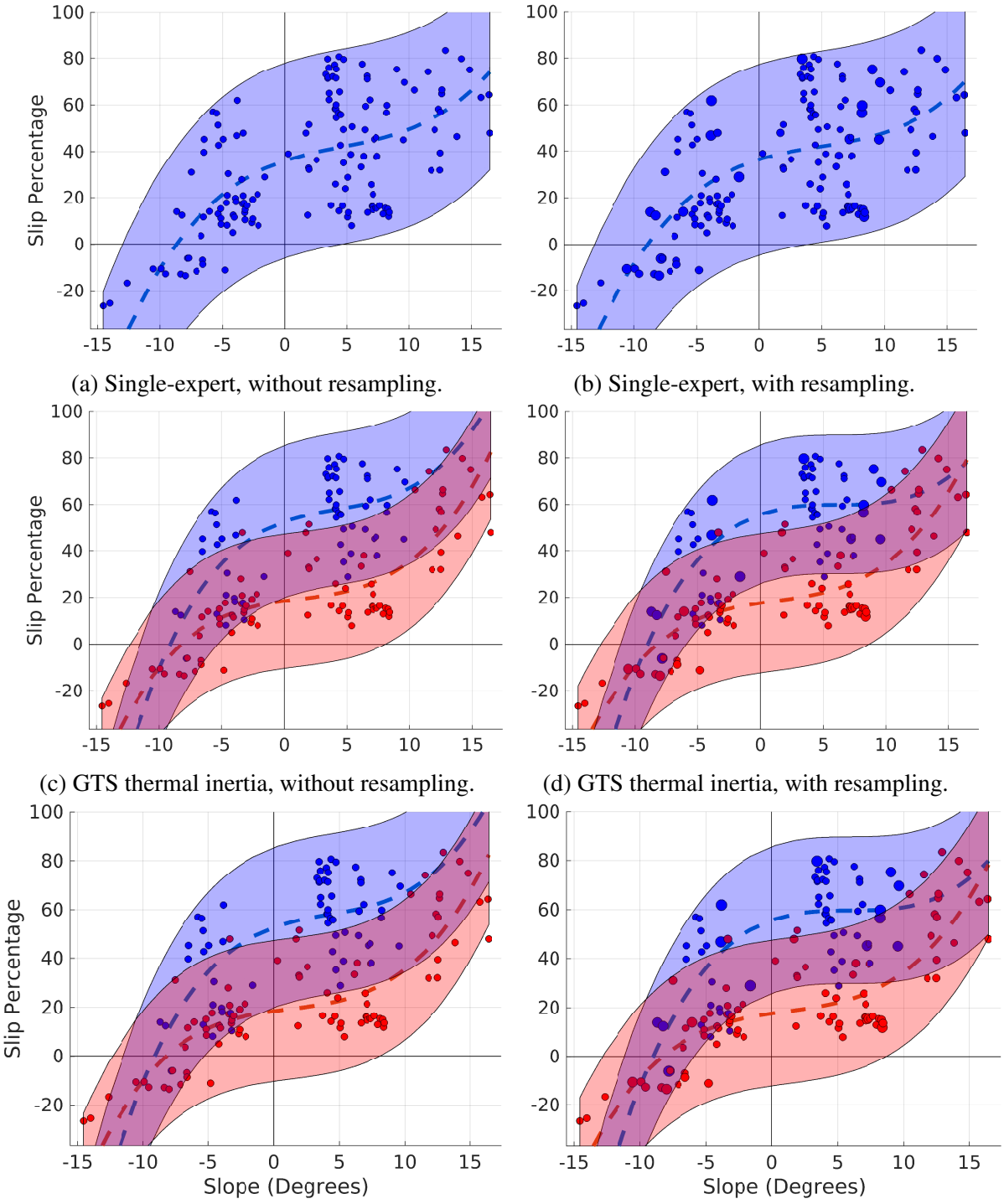

(a) Single-expert, without resampling.

(b) Single-expert, with resampling.

(c) GTS thermal inertia, without resampling.

(d) GTS thermal inertia, with resampling.

(e) THEMIS thermal inertia, without resampling.

(f) THEMIS thermal inertia, with resampling.

Figure 6.7: Slip models for loose sand. Curves for the best-fit two-expert model using GTS data are plotted in red and blue. With two experts, the blue model corresponds to lower thermal inertia than the red model. Mean and two-sigma bounds are plotted for both. Samples are colorized by the most likely expert and sized by relative weight after resampling. The mean of the single-expert model is plotted in black. Models learned from resampled data.

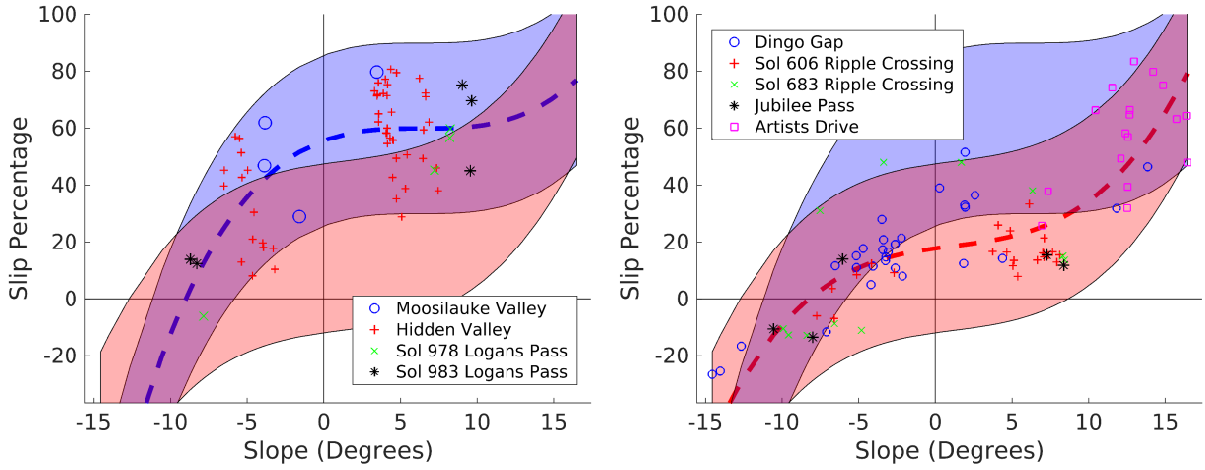

(a) High thermal inertia samples.

(b) Low thermal inertia samples.

Figure 6.8: Slip models for loose sand. Curves for the best-fit two-expert model using GTS data are plotted in red and blue. With two experts, the blue model corresponds to lower thermal inertia than the red model. Mean and two-sigma bounds are plotted for both. Samples are colorized by the site from which they were gathered and sized by relative weight after resampling. Models learned from resampled data.

The higher cross-validation error for the THEMIS model with resampling is mostly caused by misclassifying Moosilauke valley. The THEMIS thermal inertia estimate is higher (relatively) than the GTS estimate (see Table 6.1). Moosilauke valley is in a small ripple field surrounded by high thermal inertia terrain. When THEMIS averages at 100 m resolution, the result is a higher observed thermal inertia than likely corresponds to the sand alone. Thus, the GTS and THEMIS models agreed more closely for larger areas of sand. This shows the benefit of ground-based sampling. It can identify smaller hazardous regions than lower-resolution orbital instruments. The variance in the cross validation estimate with resampling for the GTS model is caused by mis-classification of Jubilee Pass. In 3 of 10 trials, the two-expert GTS model classified Jubilee Pass as high-slip because it has the lowest thermal inertia of the sites identified as low-slip when using all of the data.

One significant problem with the GTS measurements is that it is not always measuring where the rover is driving, and the terrain is very heterogeneous. GTS measurements do not always correspond to sand directly under the rover. Heterogeneity also makes it difficult to interpret terrain as a single "type". Despite these imprecise measurements, thermal inertia still improved slip prediction significantly.

There are several factors that affect traversability in sand: rover configuration, sand properties, and surface geometry. The apparent thermal inertia is affected by the physical properties of the sand grains and depth of the surface layer. Without ground truth (e.g. for sand depth), it is difficult to determine exactly how much each factor affected either the thermal inertia measurements or wheel-terrain interaction. However, evidence suggests both depth and physical properties were important. For example, Arvidson et al. [8] estimate that the properties of the sand at Dingo Gap were more traversable than at Hidden Valley. Higher GTS thermal inertia at Dingo Gap

supports this claim. In addition, on visual inspection, sand depth is related to both traversability and thermal inertia. For example, sand at Artist's Drive (Figure 6.3d) appears shallower than other areas such as Hidden Valley (Figure 6.3b). It had correspondingly higher thermal inertia and the rover slipped at higher slopes.

6.4 Summary and Conclusions

This chapter presented experimental results showing the feasibility of improving slip prediction on Mars by classifying sand using absolute measurements of thermal inertia. Slip prediction accuracy was compared among a single-expert model and two-expert models using both GTS- and THEMIS-based thermal inertia measurements. Results showed that separating low-slip, high thermal inertia sand from high-slip, low thermal inertia sand significantly reduced cross-validation error. Slip predictions from orbital and ground-based data were similar. However, GTS measurements more reliably detected smaller regions of hazardous sand. Resampling data by assuming that regions of sand rather than slip measurements were i.i.d. also improved prediction accuracy.

Given this encouraging empirical evidence and the theoretical connection, there is little doubt a correlation exists between thermal inertia and mobility for rovers operating in granular materials on Mars. However, the terrain on Mars is very diverse and Curiosity's data thus far is limited to measurements in sand from one region of Mars. More data is accumulating as the mission proceeds. Data must be gathered to determine whether the models hold true in other types of terrain (e.g. duricrust over sand). Before considering implementation, it is necessary to fully understand what types of hazards can and can't be detected, at what times of day, how many of those hazards couldn't be detected visually, and how rover operations would have to be adjusted to account for thermal inertia measurements. Further analysis should also include effects of heterogeneous terrain and ripples in sand, which were likely causes of intraclass variance.

Chapter 7

Density Variations in Lunar Polar Craters

The thermal properties of lunar regolith and, therefore, surface temperatures are strongly influenced by particle size and density [49, 50]. Previous studies have fit density models to the lunar surface using observations from orbital instruments [151]. Other studies have specifically analyzed the thermal environment of polar craters [113, 152]. Some regions have been discovered on the surface that are indistinguishable in visual imagery but surface temperatures reveal regolith that is likely very loosely packed and caused by fresh crater impacts [15, 16].

This chapter analyzes the ability of a rover to detect changes in temperature caused by differences in regolith density both on the surface and in shaded craters on the poles of the Moon that never receive direct sunlight. These craters are of great scientific interest because of the presence of water but are hypothesized to have much looser regolith than in equatorial regions because the lack of a freeze-thaw cycle that slowly settles terrain [149]. Surface temperatures were calculated for a range of lunar regolith densities by simulating the thermal environment of a lunar polar crater using experimentally determined regolith thermal properties. These temperature differences were then analyzed to determine the likelihood that they are detectable by sensors on lunar rover by comparing to the capabilities of DIVINER, a state-of-the-art radiometer aboard the Lunar Reconnaissance Orbiter (LRO).

This chapter is published in [41].

7.1 Crater Temperature Simulations

A series of simulations was conducted to estimate the temperature differences that changes in regolith density cause. A generalized lunar crater model was used to simulate the geometry of craters as a triangular mesh at different latitudes the lunar poles. Surface heat fluxes on each mesh element were calculated using ray tracing from the Sun and from emitted and reflected radiation from the rest of the crater. Surface temperatures were calculated for each crater element using a finite differences approximation to the solution of the one-dimensional heat diffusion equation with an upper boundary condition given by a balance between incident and emitted heat fluxes on surface.

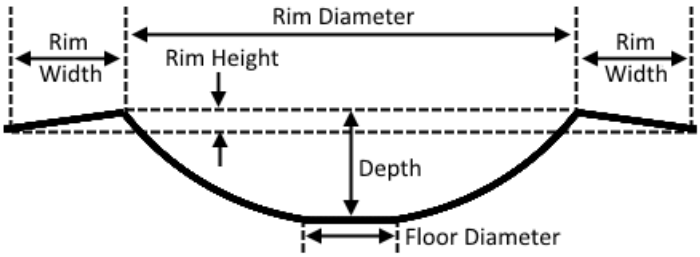

Figure 7.1: Diagram showing crater cross-section and parameters associated with a generalized lunar crater.

Table 7.1: Coefficients for idealized crater model with rim diameter <10 km [64]

Crater Parameter (y)	**Exponent** (b)	**Coefficient** (a)
Depth	1.010	0.196
Rim height	1.014	0.036
Rim width	1.011	0.257
Floor diameter	1.765	0.031

7.1.1 Idealized Lunar Crater Model

To show general applicability, all simulations used an idealized crater model. Lunar craters have morphologies that vary with their size. Only craters with a diameter of 10 km or less were considered in this paper. These craters generally have simple craterforms without central peaks that often occur in larger craters [64].

Figure 7.1 shows a cross-section of the crater model used in this work. Rim width, rim height, depth, and floor diameter are all functions of the rim diameter of the form where is a crater parameter, is the rim diameter, and a and b are coefficients. This function and its coefficients have been determined through analysis of lunar craters from orbital imagery. These values were taken from Heiken et al. [64] and are reproduced in Table 1.

Given the dimensions of a crater, a crater cross-section was constructed using straight lines for the rims and the floor. The crater walls were constructed by fitting a circle to the inner endpoints of each side of the crater rim and the endpoints of the crater floor. A point cloud for the full crater was then generated by rotating the cross-section about its central axis. A triangular mesh was created from the point cloud. An example crater mesh with a diameter of 10 km is shown in Figure 7.2.

7.1.2 Lunar Thermal Model

The temperature at any point in the crater is a balance between incident and reflected solar radiation, emitted radiation, incident infrared radiation emitted from surrounding terrain, and heat conduction into the ground. The equation representing this surface boundary condition on the

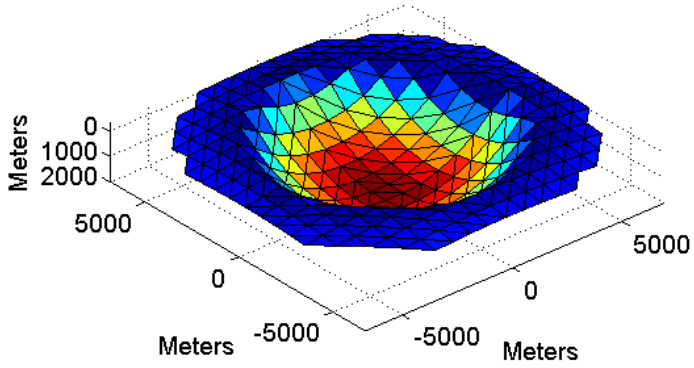

Figure 7.2: Example triangular mesh of a 10km crater colored by height.

Moon is:

$$(1-A)R_S + \epsilon R_e - \epsilon\sigma T_S^4 = k\frac{\partial T}{\partial Z}\bigg|_{Z=0} \tag{7.1}$$

where A is albedo, ϵ is emissivity, σ is the Stefan–Boltzmann constant, R_S is solar radiation, R_e is incident radiation emitted from surrounding terrain, T_S is the temperature of the surface, k is thermal conductivity, T is temperature, Z is depth, and $\frac{\partial T}{\partial Z}\Big|_{Z=0}$ is the derivative of temperature in the ground evaluated at the surface. The Albedo for lunar regolith was estimated to be 0.12 [17] and emissivity was assumed to be 0.98 in this work [151]. Given values for all other variables, T was calculated over time by solving the 1D heat diffusion equation:

$$\frac{\partial T}{\partial t} = \frac{k}{\rho c}\frac{\partial^2 T}{\partial Z^2} \tag{7.2}$$

where ρ is the material density and c is the specific heat. A two layer model is used to represent the subsurface density profile. The surface layer is nominally 2 cm deep and the bottom layer extends from 2 cm to 2 m. At the poles the surface layer may be thicker, but 2 cm thick was used in this paper based on prior work on thermal modeling. In reality, the density is also a continuous function of depth; however, to keep the problem tractable, two-layer models are often used for analysis [104]. The surface boundary condition at Z=0 is given by Equation (7.1). The boundary condition at the bottom, 2 m below the surface, is a geothermal heat flux of 0.033 W/m^2 [152]. The heat equation was solved using a finite differences approach. Time was evenly discretized, but depth was not. The size of each discrete element increased geometrically with depth from the surface [80].

The heat capacity for lunar regolith was determined using returned samples from the Apollo mission. Specific heat capacity is a function of temperature and is shown in Figure 7.3. It is determined by the following equation [66]:

$$\begin{aligned} c\,(T) = &-2.3173 \times 10^{-2} + 2.1270 \times 10^{-3}T + 1.5009 \times 10^{-5}T^2 \\ &- 7.3699 \times 10^{-8}T^3 + 9.6552 \times 10^{-11}T^4 \quad \frac{J}{kg\,K} \end{aligned} \tag{7.3}$$

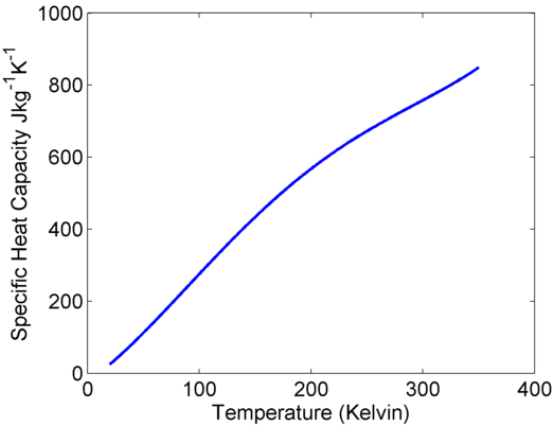

Figure 7.3: Plot showing heat capacity vs. temperature for lunar regolith using Equation 7.3.

Table 7.2: Coefficients for thermal conductivity model [38]

Sample	$\mathbf{b_0}$ (æ)	$10^{-3}\frac{W}{m\,K}$	$\mathbf{b_3}$ (æ)	$10^{-11}\frac{W}{m\,K^4}$
1300 $\frac{kg}{m^3}$		0.922		3.19
1640 $\frac{kg}{m^3}$		0.985		2.06
1970 $\frac{kg}{m^3}$		1.25		1.59

Likewise, the thermal conductivity for lunar regolith was treated as a temperature and density dependent function [17]:

$$k\left(\rho,T\right)=b_0\left(\rho\right)+b_3\left(\rho\right)T^3 \quad \frac{W}{m\,K} \tag{7.4}$$

where $b_0\left(\rho\right)$ $b_3\left(\rho\right)$ were determined from samples from Apollo 12 and summarized in Table 7.2 [38]. The coefficients for specific samples were determined by interpolating between experimentally calculated values.

For lunar rock, Equation 7.4 was still used for heat capacity. However, thermal conductivity was found by first finding temperature and density dependent thermal diffusivity and then solving for conductivity given density and heat capacity. Thermal diffusivity of lunar rocks under vacuum was found using returned Apollo rocks. The equation is given as follows:

$$\alpha_{rock}\left(T\right)=c_0+\frac{c_1}{T} \quad \frac{m^2}{s} \tag{7.5}$$

where α_{rock} is the thermal diffusivity of rock, and c_0 and c_1 are experimentally determined parameters. $c_0=3.05 \quad \frac{m^2}{s}$ and $c_0=0.040 \quad \frac{m^2\,K}{s}$. The density of rock was assumed to be $3070 \quad \frac{kg}{m^3}$ [51].

All of the parameters for both lunar regolith and rock have been determined for certain density and temperature ranges. When the temperature or density falls outside that range, the accuracy is lower. Despite lower certainty for some samples, these are the still best available estimates and are used in this work.

7.1.3 Temperature and Flux Calculations

Incident fluxes and resulting surface temperatures were calculated for each crater mesh element by simulating a separate thermal model for each element forward in time and periodically recalculating the fluxes and surface boundary conditions. In this work, boundary conditions were recomputed every four hours. In between calculations of boundary conductions, the surface and subsurface temperatures of each crater element were stepped forward in time using finite differences as described above.

To calculate incident solar flux, the crater model was rotated and translated along the surface of the Moon to evaluate craters at different latitudes. Then the path of the sun with respect to the crater was found using DE421 ephemeris data [165]. The Sun was modeled as a 2D circular mesh that was always rotated to point directly at the center of the Moon. The intensity of each mesh element was found using a solar limb darkening model. This accounts for the fact that the brightness distribution of the Sun is circularly symmetric but varies along the radius. To an observer, the center of the Sun appears brighter than the rim. This work used the limb darkening model of [109]. Reflected solar radiation was estimated using a scatter-gather approach assuming a Lambertian bi-directional reflectance function [113]. The amount of radiation transferred from mesh element i to mesh element j as a fraction of energy leaving element i was precomputed as

$$a_{ij} = \frac{1}{\pi} \frac{\cos\theta_i \cos\theta_j dS_j}{d_{ij}^2} \tag{7.6}$$

where θ_i and θ_j are the angles between the normal vectors of elements i and j and the line between the centers, d_{ij} is the distance between i and j, and dS_j is the surface area of element j [152]. Three bounces were computed for solar radiation. With an albedo of 0.12, reflected radiation becomes negligible after three bounces.

Each time fluxes are recalculated, the influence of emitted radiation from the rest of the crater on each individual crater element was also computed. The amount of flux incident on element j from element i is $a_{ij}\epsilon\sigma T_S^4$. Bounces are not considered because the amount of radiation reflected in the infrared spectrum is so low due to the high emissivity of regolith. The influence of terrain outside of the crater was also not considered in this work.

7.2 Experiments

A series of simulations was conducted to evaluate the magnitude of temperature differences that changes in regolith density profiles are predicted to cause. Simulations were run for 10 km-diameter craters with latitudes between -80°and -90°at 2°increments. The craters were discretized into 502 triangular mesh elements. Each simulation ran for 4 years with ephemeris data from January 1, 2016 to January 1, 2020. Three years were used to spin up the model and establish subsurface temperature profiles in the craters. Using greater than three years for spin-up time showed no significant effect on surface temperatures. Results were generated using the final year of data.

At each latitude, a first simulation was run with a nominal density profile characteristic of equatorial regions of the Moon. In this case, the top layer was 2 cm deep and contained 1300

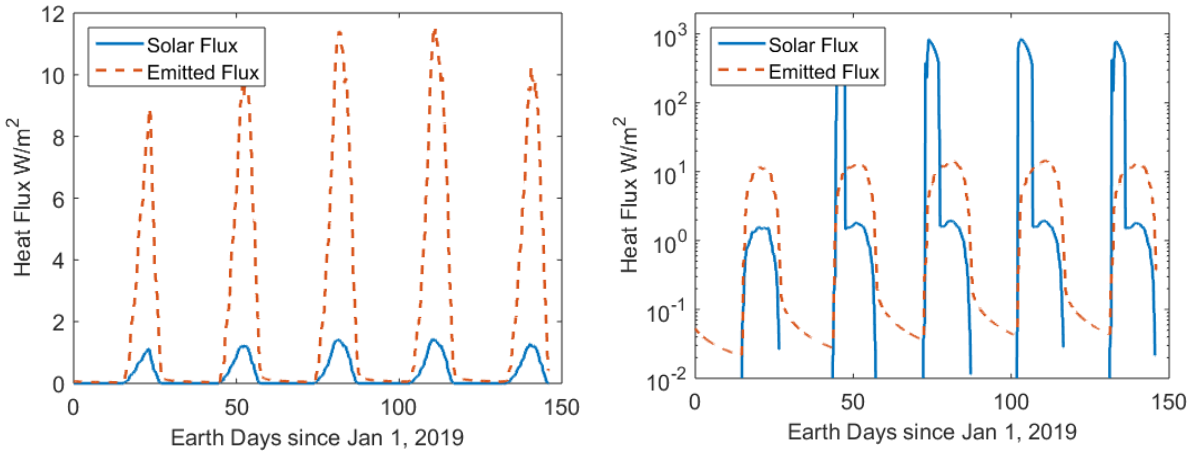

(a) Crater floor.

(b) Near the top of the crater wall (semi-log scale).

Figure 7.4: Plots comparing incident direct and reflected solar energy against energy emitted from the surrounding crater at -86°latitude shown for several lunar days. Different colored lines correspond to different degrees of latitude.

kg/m^3 regolith. The bottom layer contained 1800 kg/m^3 regolith [151]. During these simulations, the incident fluxes on each crater element from the Sun and the surrounding crater were collected and saved. Examples of solar and emitted heat fluxes incident on crater elements are shown in Figure 7.4. Note that for the region on the floor of the crater, the emitted heat flux from the surrounding area is more important than solar, while for a region on the crater wall, the opposite is true.

The density values considered ranged from approximately the lowest reported in situ lunar density from Luna 13 (800 kg/m^3) to the highest reported in situ lunar density from Apollo 17 (2000 kg/m^3) [25, 29]. Density profiles were required to have a top layer with lower or equal density to the bottom layer. For simplicity in presentation of results, a density profile of 1300 kg/m^3 over regolith 1800 kg/m^3 will be referred to as nominal regolith, and density profile of 800 kg/m^3 over regolith 1100 kg/m^3 will be referred to as loose regolith. Nominal regolith values were the equatorial best fit from [151] and loose regolith values are estimates based on minimum measured lunar regolith densities. It was assumed in this work that all samples have the same particle size. This is a reasonable assumption since the particle size distribution does not vary much over most of the Moon's surface [64]. It is speculated that particles may be smaller at the poles of the Moon [149]. However, that was not taken into account in these simulations. These simulations also did not take into account any effect of accumulated volatiles in the regolith may have on the thermal properties.

Using the saved heat fluxes from the nominal case, another set of simulations was conducted at each latitude over a set different subsurface regolith density profiles. In effect, this estimates the temperature at each crater element as if its density was changed but the rest of the crater remained at the nominal case. This represents the difference in temperature a rover would see for an off-nominal density region in a crater where the rest of the terrain is the nominal case. A detectable temperature difference indicates that the rover could detect a variation in density. Thus the important quantity is the difference in temperature between these simulations and the

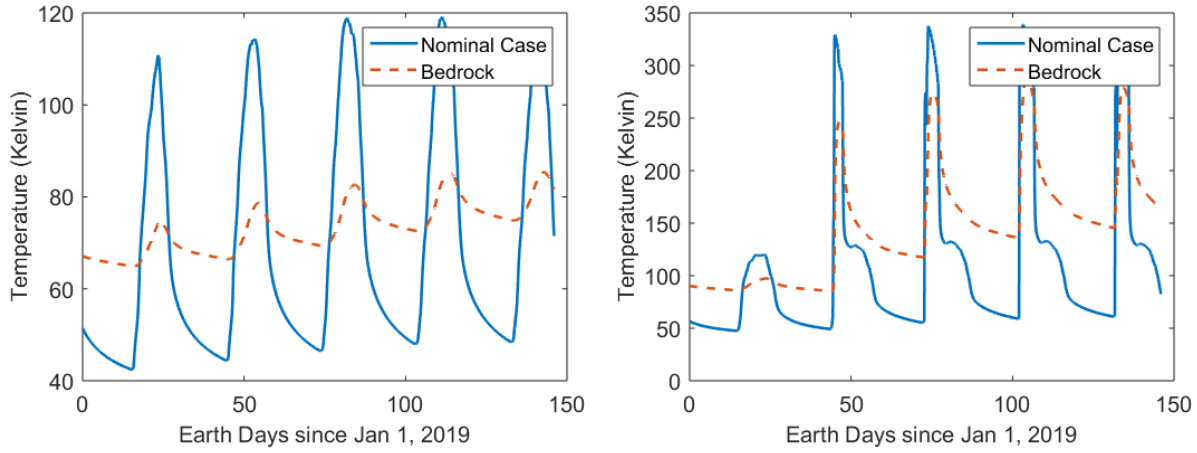

(a) Crater floor.

(b) Near the top of the crater wall.

Figure 7.5: Simulated temperatures of nominal regolith (1300 $\frac{kg}{m^3}$ over 1800 $\frac{kg}{m^3}$) and rock at -86°latitude shown for several lunar days.

nominal case. If the density of a specific crater element is altered, it changes the temperature and thus the radiation emitting from the surface. This will have a small effect on the temperature of the surrounding crater elements and the radiation they emit. That small temperature change will slightly alter the incident radiation on the original crater element. It was assumed, however, that this effect is negligible.

Figure 7.5 shows resulting temperature curves for the nominal case and for bedrock over a one year period for a crater at -86°latitude both on the floor of the crater and on the rim. There was a significant temperature difference (> 20 K) at almost all times of the year for distinguishing between rock and regolith. When comparing different regolith density profiles, the difference was not as large. Figure 7.6 shows the difference between nominal and loose regolith for craters at different latitudes. At most of the times during the day, there was a difference in temperature between nominal and loose regolith. The difference was greatest at night, generally between 2 K and 3 K. This change in temperature is well above the 0.94 K standard deviation of lunar regolith temperatures, which implies that it is detectable [112]. Referring to Figure 7.5, these differences occur at an absolute temperature of approximately 50 K. A crater exactly on the pole at -90°latitude exhibits unique behavior due to very oblique angle of the Sun. This also made it more prone to discretization errors of both the crater mesh and the Sun mesh.

Nighttime temperatures are generally better for detecting density changes because density effects on surface temperature become more pronounced and the effects of slope and albedo are minimized [48]. Figure 7.7a analyzes nighttime temperature differences for several regolith density profiles. These results show that the bottom regolith layer had the largest influence on nighttime temperatures. The surface layer did have a mild effect, especially right after the sun sets. The greater the difference in density, the more pronounced the surface temperature difference was.

Figures 7.7b and 7.8 show that the location in the crater and the crater's latitude have influence as well. In general, samples further up the crater wall and with more equatorial latitudes had greater swings in surface heat flux and temperature. This increased the temperature differences between density profiles. These generalizations were true for the idealized crater model; however,

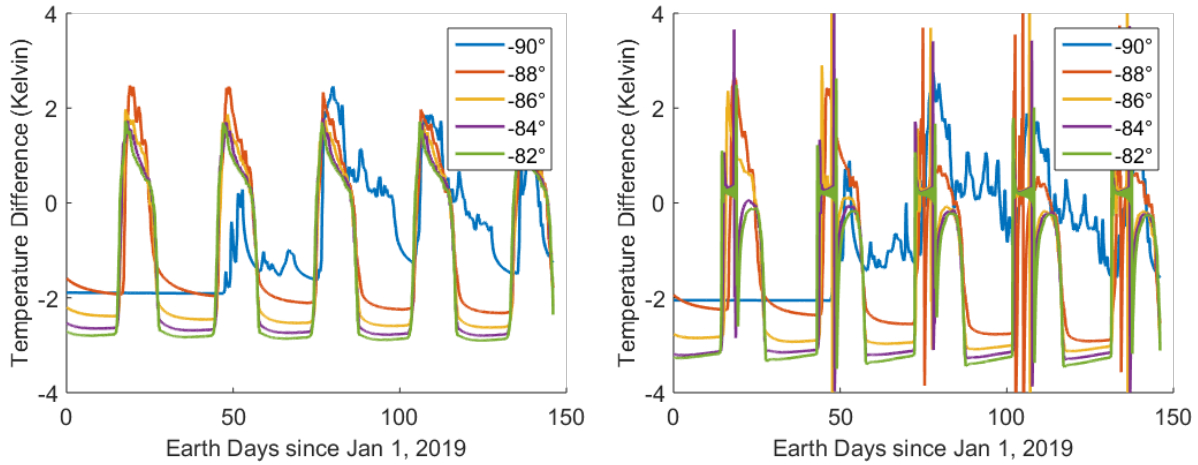

(a) Crater floor.

(b) Near the top of the crater wall.

Figure 7.6: Loose regolith (800 $\frac{kg}{m^3}$ over 1100 $\frac{kg}{m^3}$) surface temperatures minus nominal regolith (1300 $\frac{kg}{m^3}$ over 1800 $\frac{kg}{m^3}$) surface temperatures shown for several lunar days and latitudes.

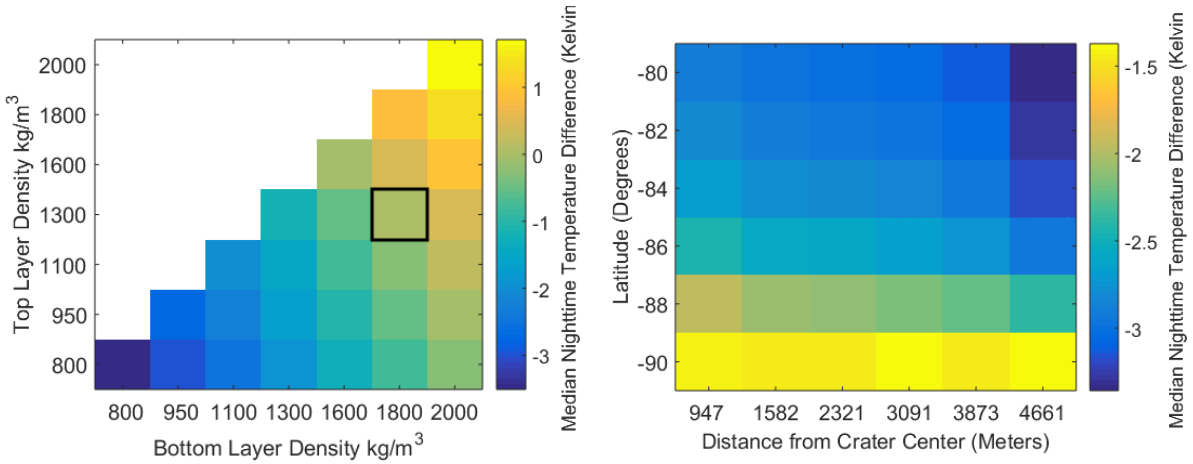

(a) Median nighttime temperatures differences for different density profiles minus nominal regolith (1300 kg/m^3 over 1800 kg/m^3, outlined in black) at 86°latitude on the crater floor.

(b) Median nighttime temperatures differences for loose regolith (800 kg/m^3 over 1100 kg/m^3) minus nominal regolith (1300 kg/m^3 over 1800 kg/m^3) at different latitudes and crater. locations.

Figure 7.7: Comparisons of temperature differences as functions of density and crater location.

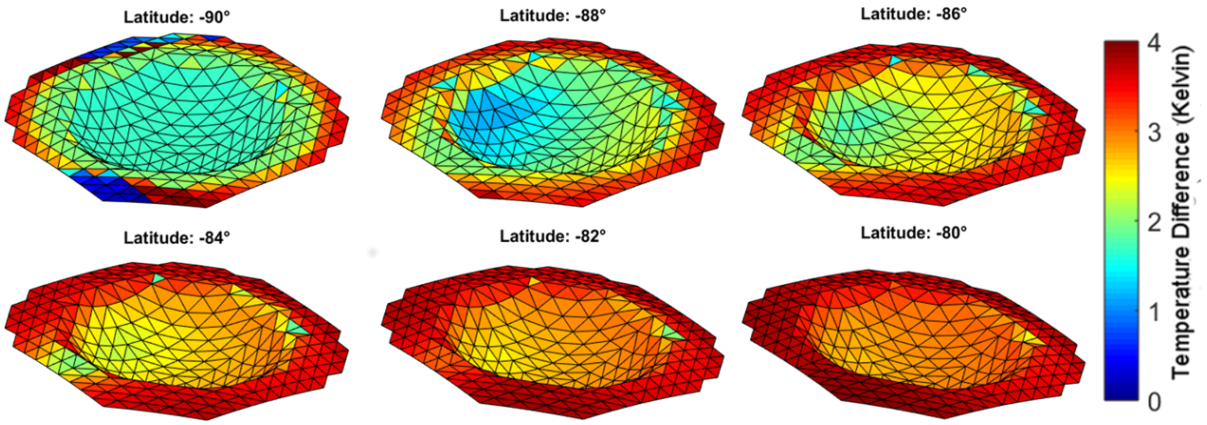

Figure 7.8: Estimated nighttime absolute temperature differences between nominal (1300 kg/m^3 over 1800 kg/m^3) and loose (800 kg/m^3 over 1100 kg/m^3) regolith in a lunar crater at different latitudes.

every crater is different. The unique geometry of a crater and the surrounding terrain will cause deviations from the general case.

A final experiment was conducted to determine how temperature differences vary with latitude on the surface of the Moon without considering crater effects. At lower latitudes, crater geometry becomes less important because the illumination angles are higher and the whole crater receives direct sunlight during the day. Figure 7.9 shows first quartile, median, and third quartile nighttime temperature differences. At very high $\sim$90°latitudes, illumination is very glancing and seasonal variations are more important than diurnal variations. As latitudes become more equatorial, seasonal variations become less important and diurnal variations take over. This results in the local minimum in temperature difference around $\sim$80°. However, at all latitudes, there is a significant difference in nighttime temperature during the night between loose and nominal regolith. Figure 7.9b shows there is not a corresponding, significant daytime temperature difference. Consequently, confident separations of loose and compact regolith can only be made on the Moon at night.

7.3 Measurability of Temperature Differences

Despite the fact that density variation causes differences in temperature, these temperature differences are generally small and can occur at very low temperatures. There are inherent, practical difficulties in measuring these small differences because of the low signal-to-noise ratios and absolute radiometric calibration accuracies that detectors can attain at these temperatures.

The best infrared detector for comparison is the DIVINER instrument on the LRO. DIVINER is a radiometer specifically designed to measure lunar surface temperatures in both warm equatorial regions and cold, permanently shadowed regions on the poles. DIVINER can detect temperatures as low as 20 K [112], which implies that regolith temperatures predicted in simulation are detectable.

It is also likely that a detector could be developed that detects low relative temperature differences at these absolute temperatures. For comparison, at 50 K the Noise Equivalent Temperature

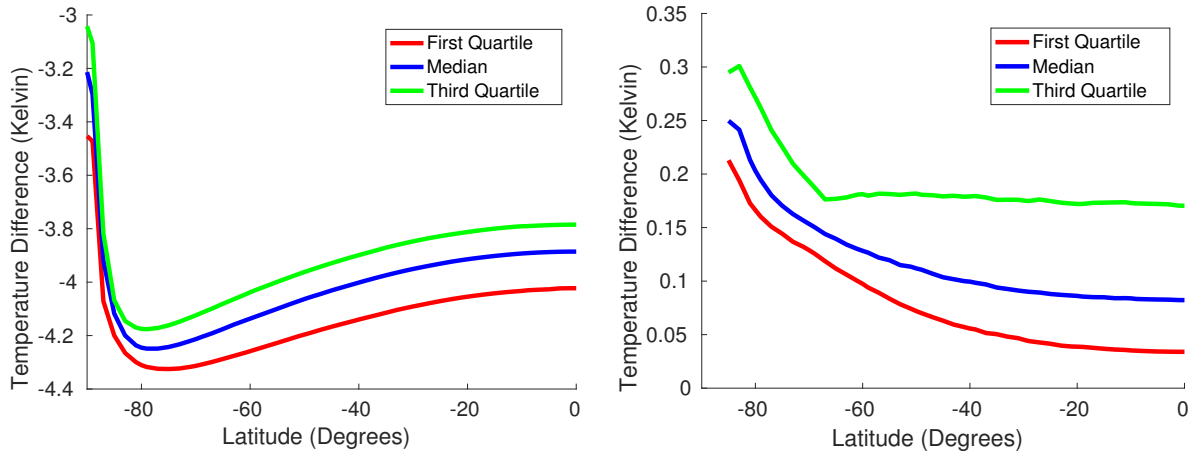

(a) Nighttime

(b) Daytime

Figure 7.9: Estimated absolute temperature differences between nominal (1300 kg/m^3 over 1800 kg/m^3) and loose (800 kg/m^3 over 1100 kg/m^3) regolith on the lunar surface (not in a crater) at different latitudes. The median as well as the first and second quartile are shown for both nighttime and daytime data.

Difference (NETD) for DIVINER is approximately 2 K. This implies that the minimum measurable temperature difference is 2 K, which is near the median surface temperature difference between nominal and loose regolith for most polar crater latitudes. However, each pixel on the DIVINER detector only has an instantaneous field of view of approximately 10 mrad, a size of 240 m x 480 m, and an integration time of 128 ms [112]. Increasing the amount of averaging both temporally and spatially could increase the accuracy, which would enable a detector to resolve temperature differences needed to detect differences in density in permanently shadowed craters [9].

The integration time on DIVINER is short in order to prevent smearing given the high velocity of LRO [112]. A rover does not suffer that problem and could remain stationary for short periods of time to greatly increase the signal-to-noise ratio by a factor of $\sqrt{n}$, where n is the number of measurements. For example, sitting still and averaging the signal over a period of one minute would increase the signal-to-noise ratio by more than a factor of 20.

More difficulty arises in radiometric calibration for determining the absolute temperature of the terrain. When looking at a 50 K scene, DIVINER has a calibration accuracy of about 5 K. This error is primarily due to calibration offset uncertainty [112]. While the radiometric accuracy could be increased in future instrument developments, it is unlikely to be eliminated entirely as a source of error. Thus, to estimate traversability, a rover can and must use relative temperature differences, which are more reliable than radiometric calibration at these temperatures.

From these results, it is clear that a difference in regolith density causes a change in surface temperature. In many situations, the nighttime temperature difference between nominal and loose regolith is expected to be between 2 K and 3 K, which is 2-3 times higher than the standard deviation of rock-free lunar regolith surface temperatures (0.94 K) [16, 112]. In addition, there is a significant temperature difference (> 20 K) between exposed rock and regolith under almost

all conditions, which could be leveraged to enable rovers to avoid hazardous, rocky areas. These effects exist at all latitudes studies with more prominent disparities occurring at lower latitudes. Based on an analysis of the capabilities of DIVINER, it is likely that a sensor could be developed that would enable a robot to sense relative temperature differences between loose and compact regolith even at night when temperatures reach 50 K and below. However, at lower temperatures absolute radiometric accuracy will be difficult to achieve.

7.4 Summary and Conclusions

Results of surface temperature simulations suggests that a difference in regolith density causes a significant, detectable change in surface temperature. In many situations, the nighttime temperature difference between nominal and loose regolith is expected to be between 2 K and 3 K. In addition, there is a significant temperature difference (>20 K) between exposed rock and regolith under almost all conditions, which could be leveraged to enable rovers to avoid hazardous, rocky areas as well. These effects exist at all latitudes studied with more prominent disparities occurring at lower latitudes. Based on an analysis of the capabilities of DIVINER, it is likely that a sensor could be developed that would enable a robot to sense relative temperature differences between loose and compact regolith even at night when temperatures reach 50 K and below. However, at lower temperatures absolute radiometric accuracy will be difficult to achieve.

Future work should focus on techniques for estimating regolith density from temperature measurements, an in-depth sensor investigation, and analysis of potential polar mission destinations. Current thermal property estimation techniques from infrared imagery are mostly strict optimizations that treat all samples in a scene independently. To overcome the low radiometric accuracy of sensors operating in cold conditions, new statistical algorithms will need to be developed that leverage relative differences in terrain temperature to predict both density and traversability. To truly determine the viability of this technique, a more in depth study is required on hardware capabilities of thermal sensors that could be integrated into a lunar rover mission. A specific analysis of potential lunar polar landing sites would also be invaluable for determining the efficacy of this technique since each unique crater geometry causes unique behavior. In addition, effects of differing particle size distributions and ice content in regolith were not considered in the thermal model. These effects must be explored to understand how they affect this technique.

The results of this study relied on best-available estimates predicted lunar regolith density distributions and the effects that those have on the thermal properties of terrain. The predicted density distributions were estimated from minimum and maximum in-situ measured density from lunar surface missions. Estimating thermal properties for these distributions at times meant extrapolating from values measured on a narrower range of densities from Apollo samples. This also assumed that lunar polar regolith had the same particle size distribution as the Apollo samples. Unfortunately the accuracy of these assumptions cannot be known before a robot visits the poles and measures the surface properties.

Chapter 8

Relevance on Planetary Bodies

Thermal inertia is a single measurable quantity that is correlated to wheel-terrain interaction. This is in contrast to vision-based approaches that require many texture- and color-based features that are not clearly correlated to traversability. Thermal inertia observations can distinguish traversable from hazardous granular terrain.

The effectiveness of thermal methods to classify traversability of terrain is strongly influenced by time of day and the properties of the planetary body of interest, including atmospheric properties, terrain properties, and illumination period. In general, nighttime observations and longer times lead to better separation between loose and compact sand; whereas, daytime observations and shorter times are less reliable. This chapter draws together results and analysis from prior chapters to discuss how thermal inertia is best applied to predict mobility, and how well and in what situations this approach can apply to Mars, the Moon, and Earth. Analysis is also conducted to evaluate what type of sensor is needed to passively estimate thermal inertia for traversability prediction using natural illumination.

8.1 Predicting Traversability with Thermal Inertia

A rover could use thermal inertia to improve mobility prediction by either: (1) using absolute thermal inertia estimates to classify terrain or (2) using relative difference in thermal inertia to detect potentially hazardous changes in terrain properties. Absolute thermal inertia estimates enable comparisons of terrain across days and seasons but have higher errors because of variations in thermal camera calibration and surface flux conditions. Relative comparisons between thermal inertia measurements taken near the same time are more likely to ensure that higher estimated thermal inertia in fact corresponds to a higher traversability material because calibration and flux errors are constant.

The absolute approach uses measurements of thermal inertia to classify terrain into either hazardous or safe. This is the approach for Mars that was taken in Chapter 6. A softmax classifier used thermal inertia to identify whether sand was high- or low-slip. This approach requires accurate estimates of thermal inertia. In the Curiosity analysis, only high-confidence measurements of thermal inertia were used that had data from both pre-dawn and mid-day, which is expected to result in uncertainties of $\sim$20%[62]. However, it is not always practical to

dwell for an entire daylight period to evaluate terrain for traversability. Due to differences in mobility systems, using an absolute approach would require some calibration for a specific rover to determine the "degree" of a particular hazard; however, generally higher thermal inertia regions would be preferred.

To expedite driving, a rover could instead only wait and observe the terrain for a high confidence thermal inertia measurement periodically or when it identifies potentially hazardous terrain. Terrain can be evaluated in several ways. First, it could use visual data to identify potentially hazardous regions (i.e. sand), which is the approach taken in Chapter 6. This would avoid unnecessary time spent measuring terrain temperatures when the rover is only driving over bedrock. Second, it could use priors from orbital thermal data. If a rover is traveling in an area with very low thermal inertia measured from orbit, then it is more likely that it will encounter hazardous, low-thermal inertia terrain along its drive than the orbital thermal inertia was high. Lastly, it could evaluate the distribution of potential thermal inertias as it drives. If it detects an area with a high probability of being hazardous, it could wait and obtain a more confident measurement. For example, if a rover detected that duricrust ahead was warmer than the model-predicted temperature for duricrust, it could wait for a few hours to observe more of the temperature curve. This would help it determine whether it was thick duricrust or thin duricrust hiding a dangerous sand trap.

The relative approach for using thermal inertia in mobility prediction is to detect changes in thermal inertia that could correspond to hazardous terrain. This method has the benefit that relative differences in thermal inertia are more accurate than absolute estimates of thermal inertia because radiometric calibration and heat flux errors are independent of terrain. This is the approach evaluated in Chapter 5. For example, assume a rover is driving on high thermal inertia, warm, compact sand at night, and it sees a sharp drop in temperature and thermal inertia ahead of it. The rover should evaluate that as potentially hazardous. It could then either circumvent the obstacle, cautiously enter to test whether the sand is safe, or wait to collect a longer observation of surface temperatures. An implementation of this approach could learn a cost function on-line that penalizes entering an area with significantly lower thermal inertia than a region on which a rover is currently driving. The result is that the rover prefer more compact, safer routes. It would not have an absolute measure of "safeness" but rather would make relative comparisons.

8.2 Mars

Mars has near-ideal conditions for estimating thermal inertia to identify hazardous terrain. At Martian atmospheric pressure, variations in granular properties that affect mechanical properties also cause large differences in thermal properties. Thermal inertia is very strongly affected by particle size and moderately affected by density. More compact materials with larger particles have higher thermal inertia and are easier for a robot to traverse. These variations in thermal properties manifest themselves as clear differences in temperature during the day and at night on Mars.

Mars also has a very thin atmosphere so that sensible and latent heat fluxes are negligible when considering the surface energy balance [98]. The cloud-free atmosphere of Mars precludes the shadow transients that make the method generally less practical on Earth. The result is even

and predictable heat fluxes on Mars (when considering km scale distances). These predictable heat fluxes enable accurate estimation of thermal inertia from diurnal illumination. With accurate thermal inertia estimates, terrains can be compared across seasons, at different locations, and with different atmospheric conditions (dust opacity levels). Thermal inertia can even more confidently separate hazardous from benign terrain when observations are taken at the same time.

8.2.1 Simulations

Empirical evidence in Chapter 6 supports the hypothesis that thermal inertia measurements distinguish low-slip from high-slip sand on Mars. However, the ground truth sand properties are not known and the data set is limited. To better understand the situations in which thermal inertia is useful, thermal simulations are used. A set of three tests were conducted that evaluate how well thermal inertia can separate: (1) sand sizes, (2) sand depths, and (3) duricrust depths. In each test, the ability of thermal inertia to separate terrain types was evaluated at different times during the day and for different lengths of time observing surface temperatures.

As in Section 6.1.1, Kieffer's KRC model [80] was used to simulate surface temperatures. Nominal surface temperature values were computed for each terrain type over a range of slopes, dust opacities, and albedos. The ranges used are shown in Table 8.1. Nominal values based on Curiosity's location on Mars were used for latitude, elevation, solar longitude, and slope azimuth.

Elevation and solar longitude are only expected to have small effects on the ability of thermal imaging to differentiate materials and were not explicitly tested. Elevation primarily affects surface atmospheric pressure and heat fluxes, which can be measured on the rover. Consequently, uncertainty is assumed to be negligible. Errors in slope azimuth estimates will certainly have an effect on traversability prediction, but it was not explicitly studied here. The effect is expected to be similar to that of slope. At equatorial and mid-latitudes, latitude is not expected to have a significant effect. However, at higher latitudes, frost is present, which could reduce the ability of thermal inertia to differentiate terrains. The effect of frost, however, is not addressed here.

After computing the nominal temperatures for each terrain test case, Monte-Carlo simulations were conducted. A set of 50 simulations were run over a range of times of day and lengths of time observing the surface. In each simulation, thermal inertia was estimated with noise introduced into both surface temperature "measurements" and terrain parameter estimates. This emulates a rover estimating thermal inertia on Mars with measurement errors. Uncertainties were adapted from those estimated for the MER Mini-TES instruments [46].

Each of the 50 simulations first sampled errors in dust opacity and temperature measurement bias caused by radiometric calibration error. These errors are independent of individual terrain regions, so they are applied equally to each case. Next, terrain-dependent errors were sampled. These errors included surface temperature measurement noise (shot noise), slope error, and albedo error. Finally, given the noisy estimates of surface temperatures and the noisy parameter estimates, thermal inertia was estimated for each terrain case. In these tests, albedo was fixed to the noisy estimate, and thermal inertia was the only free variable.

Different terrain types were simulated in this analysis using measured and empirical models of Martian thermal properties. Thermal conductivities for different particle size sands were computed using the empirical relationship derived by Presley and Christensen for Martian atmospheric pressures [122]:

Table 8.1: List of parameters needed for the KRC model [80]. The bottom parameters are assumed to be known with high accuracy. The top parameters are not known accurately, so the uncertainty values are also given. Temperature bias and noise refer to error in measuring the surface temperatures.

Thermal Model Parameters	**Value**	**Uncertainty**
Temperature Bias	Computed	$\pm$ 0.5 K
Temperature Noise	Computed	$\pm$ 0.1 K
Atmospheric Dust Opacity	0.1–1	$\pm$ 0.02
Terrain Slope	0–2°	$\pm$ 0.1°
Albedo	0.15–0.35	$\pm$ 0.01
Latitude	4.7°S	
Elevation	-3 km	
Solar Longitude (Season)	0°	
Terrain Slope Azimuth	0°	

Table 8.2: Material properties of terrain types used in simulation. Thermal inertia is in $Jm^{-2}K^{-1}s^{-\frac{1}{2}}$, condutivity is in $Wm^{-1}K^{-1}$, density is in $kg\,m^{-1}3$, heat capacity is $JK^{-1}kg^{-1}$, and skin depth is in cm. Thermal properties adapted from [62, 122, 127].

Material Type	**Thermal Inertia**	**Conductivity**	**Density**	**Heat Capacity**	**Skin Depth**
35 μm Sand	136	0.020	1375	837	2.0
150 μm Sand	191	0.039	1467	837	2.6
450 μm Sand	247	0.065	1558	837	3.2
1000 μm Sand	298	0.094	1650	837	3.6
Duricrust	889	0.494	1875	854	9.3
Bedrock	2506	3.001	2500	837	20.1

$$k = \left(C\,P^{0.6}\right) d^{\left(-0.11 \log P/K\right)} \tag{8.1}$$

where P is pressure, d is particle size diameter in μm, $C \approx 0.0015$, and $K \approx 8.1^{-4}$ Torr. Martian atmospheric pressure averages around 4.5 Torr. Specific heat capacity was assumed to be 630 $JK^{-1}kg^{-1}$ regardless of particle size [62]. Density was varied between 1375 kg/m^3 and 1875 kg/m^3 [127]. Thermal inertia is computed for each particle size using Equation 3.5. The thermal properties for rock and duricrust were taken from estimates in Putzig and Mellon [127]. All thermal properties used for this test are summarized in Table 8.2. Also listed are the diurnal skin depths, which indicate the depths at which a heat wave is attenuated by e^{-1} beneath the surface.

The variations in skin depth demonstrate that higher thermal inertia leads to greater measurement depth. In sand, diurnal surface temperature variations are only going to be strongly affected by materials a few centimeters below the surface. The skin depths in duricrust and bedrock are significantly higher. The high skin depth in duricrust is important because it enables detection of

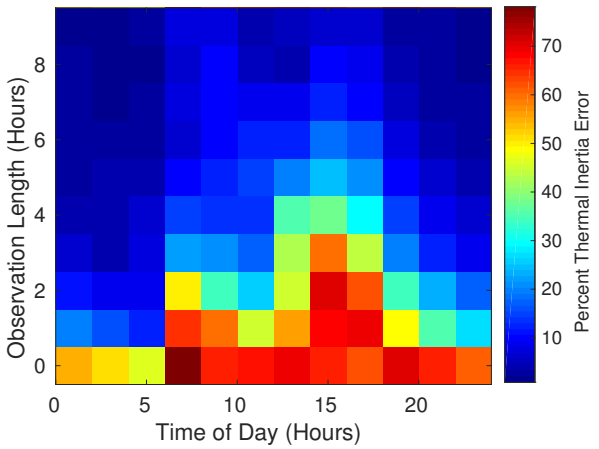

Figure 8.1: Root mean squared percent error for estimating thermal inertia using expected measurement errors from Table 8.1. Percent error is defined as (actual-estimated)/actual.

subsurface sand below duricrust.

Figure 8.1 shows the root mean squared percent error for estimating thermal inertia over a range of observation periods and start times for the homogeneous terrain types shown in Table 8.2. As is expected, longer observation times produce the lowest measurement errors. In addition, nighttime measurements, have better results because the effects of albedo are less significant. Measurements taken during the middle of the day when the Sun is up are more sensitive to errors in albedo and slope.

The following three experiments evaluate how well a robot can distinguish between different types of terrain hazards on Mars, at what times of day, and how long it must observe the terrain to make a confident prediction.

Particle Size

The first of three experiments evaluated the ability of thermal inertia to separate different particle size sands. Three cases were evaluated for distinguishing: (1) 35 μm from 150 μm, (2) 150 μm from 450 μm, and (3) 450 μm from 1000 μm. Example raw temperature curves are shown in Figure 8.2a. Larger variations in particle size cause greater differences in temperature.

Area under the ROC curve (AUC) was evaluated for each of the 50 samples to determine separability. The positive class is the larger particle size in each case. Figure 8.3 shows the mean and standard deviation for AUC for separating 35 μm from 150 μm sand. Results were almost identical for the other two test cases, so they are not shown. In each test, the same behavior is evident. It is easier to distinguish fine particles from coarser particles at night and with longer observations times. Longer observations times also significantly reduce the variance in AUC. At almost all times during the day, an observation period of only 1 or 2 hours results in a high AUC.

Mean AUC is very close to or equal to 1 in many cases even when the error in absolute thermal inertia is 10–20%. This is because relative comparisons are higher confidence. When making relative comparisons between measurements of different terrains taken at the same time, errors in radiometric calibration of the sensor and atmospheric conditions are equal. Only temperature

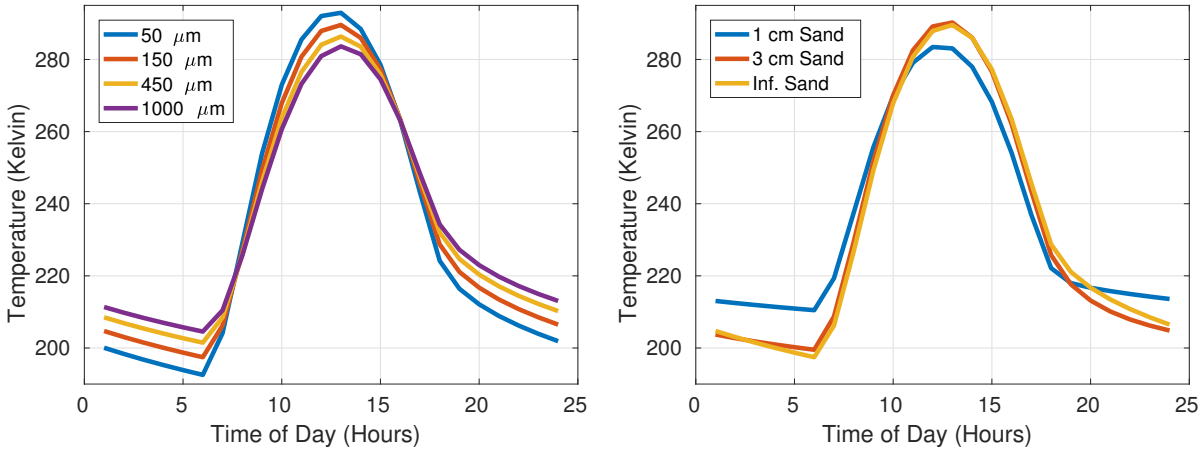

(a) Sand particle sizes.

(b) Depths of sand over rock.

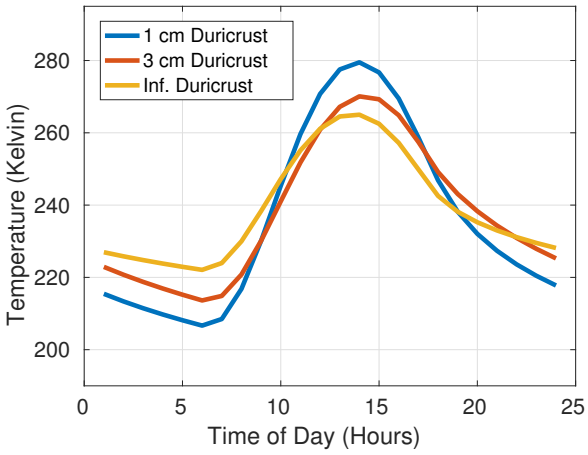

(c) Thickness of duricrust over sand.

Figure 8.2: Example simulated temperature curves for the different cases evaluated in each experiment.

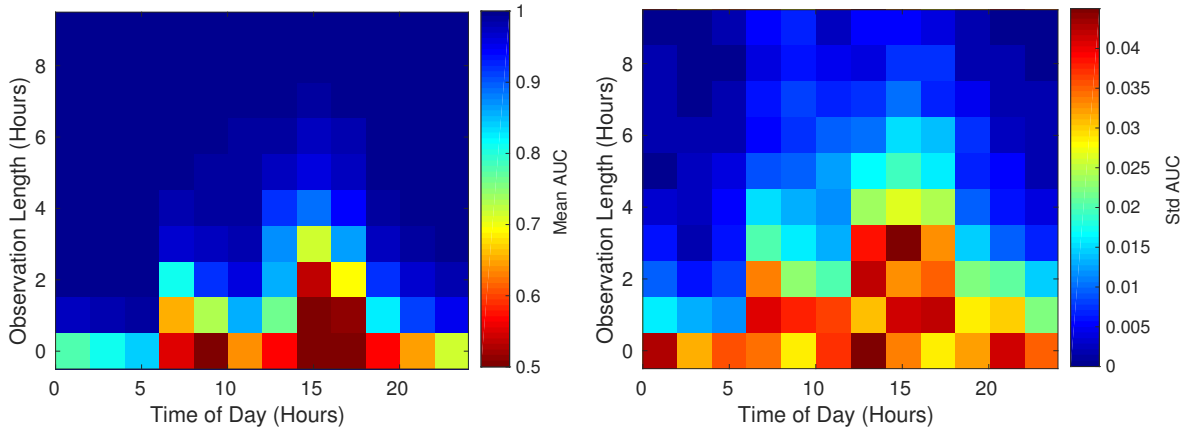

(a) Mean.

(b) Standard deviation.

Figure 8.3: AUC evaluated at different start times and for different lengths of time observing surface temperatures. The positive class is 150 μm and the negative class was 35 μm evaluated over 50 samples.

noise, slope, and albedo estimates can be different. The result is that comparisons between measurements of terrain taken at the same time with the same instrument have lower relative error than measurements of terrain taken at different times or with different instruments. Consequently, there is higher confidence when thermal inertia is used to detect relative differences in traversability than when it is used to make an absolute mapping from thermal inertia to traversability.

Surface Layer Sand Depth

The second experiment evaluated the ability of thermal inertia estimates to distinguish between different depths of sand. Deep sand can embed wheels and should be avoided when possible. The experiment compared different depths of a surface layer of 150 μm sand over bedrock. The tests evaluated the ability of thermal inertia to distinguish between surface layers of: (1) 1 cm and 3 cm and (2) 3 cm and homogeneous sand. In the inhomogeneous cases, it is an approximation to treat the materials as homogeneous and find a single best-fit thermal inertia.

The mean and standard deviation of the AUC for both cases are shown in Figure 8.4. In test (1), there is a clear difference between 1 cm sand and 3 cm sand at most times per day. At night, especially near dawn, instantaneous observations can distinguish between the two depths in most cases. At all times per day, observation periods of 1 to 8 hours produce AUCs of 1.0. This separability is expected since the diurnal skin depth in the sand is $\sim$4 cm. The surface is strongly influenced by materials between 1 and 3 cm.

However, distinguishing between a 3 cm layer of sand over bedrock and infinitely deep homogeneous sand is not as easy. This is expected becuase 3 cm is near the sand's diurnal skin depth. Not much information from below the skin depth reaches the surface. The only successful time period is immediately predawn. In fact, at most times of the day, thermal inertia confidently picks the infinitively deep sand as more traversable. Except immediately predawn, the 3 cm sand behaves like a lower thermal inertia material. 3 cm below the surface of sand, there is very little

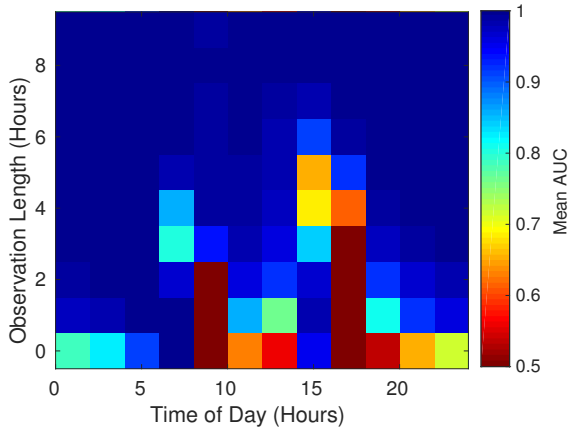

(a) Mean - 1 cm sand vs. 3 cm sand.

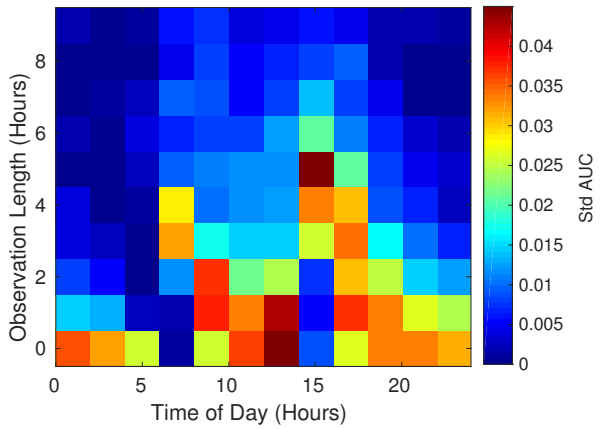

(b) Standard deviation - 1 cm sand vs. 3 cm sand.

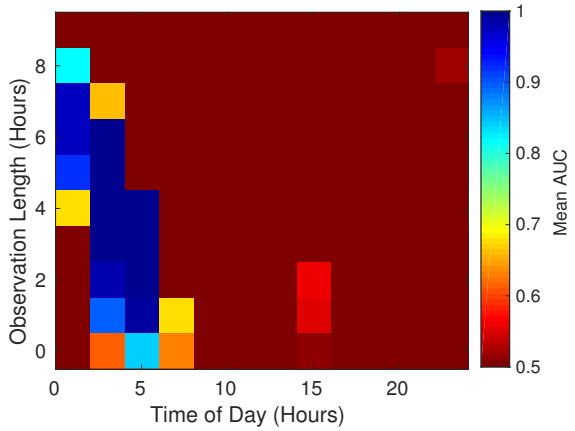

(c) Mean - 3 cm sand vs. Inf. sand.

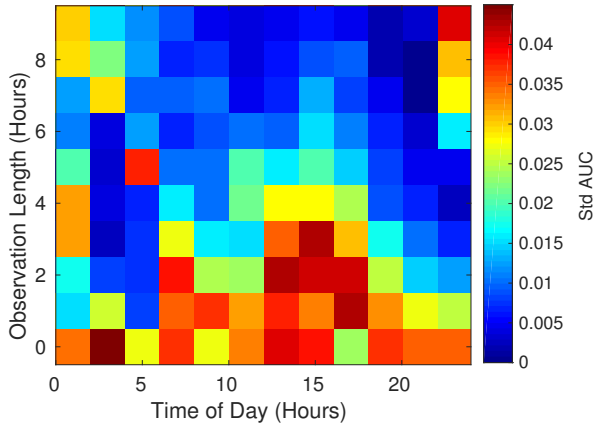

(d) Standard deviation - 3 cm sand vs. Inf. sand.

Figure 8.4: AUC for predicting surface sand depth evaluated at different start times and for different lengths of time observing surface temperatures. The positive class is the thinner layer of sand over rock. All cases were evaluated over 50 samples.

heat transfered to or from the subsurface rock. This is shown in Figure 8.2b. This result suggest that a rover might need to consider a two layer model when predicting terrain characteristics and traversability. Though even with a two layer model, there are limitations to the depth sensed by this approach.

Duricrust Layer Depth

The third and final experiment addresses distinguishing different thickness of duricrust over loose sand. This experiment emulates the failure case for the Spirit rover, which fell through a thin layer ($\sim$ 1 cm) of duricrust into a deep layer of sand underneath [6]. Similar to the previous experiment, two different cases are evaluated: (1) distinguishing 1 cm duricrust over sand from 3 cm duricrust over sand and (2) distinguishing 3 cm duricrust from infinitely deep duricrust. In both cases, 150 μm sand was used. Comparison of the temperature curves of each type of terrain during the day are shown in Figure 8.2c.

The mean and standard deviation of the AUC are shown in Figure 8.5. There is a very clear difference between 1 cm thick duricrust and 3 cm thick duricrust at night. At most times per day, a short 1 hour observation period enables near perfect separation between the two classes. It is also possible to tell the difference between 3 cm thick duricrust and infinitely thick, homogeneous duricrust. AUCs are lower for instantaneous measurements and longer observation periods are required to obtain perfect separation. The effective sensing depth in duricrust is significantly greater than in sand because of the increased thermal skin depth. These results demonstrate that thermal inertia can differentiate between different thicknesses of duricrust over loose sand. A rover equipped with a thermal sensor could have successfully identified the duricrust-covered sand that trapped Spirit as a hazard.

8.2.2 Discussion

These simulations, along with the empirical results from the Mars rovers, demonstrate that thermal inertia can identify differences in terrain to improve mobility prediction. Thermal inertia detects differences in particle size, density, and depth of surface sand and duricrust layers that are either difficult or, in some cases, impossible for visual techniques to predict.

While driving, the most basic approach is to apply thermal inertia to identify potentially hazardous changes by observing relative differences in thermal inertia, which is more reliable than absolute thermal inertia measurements. For example, the sand that entrapped spirit was 25 cm deep and had collected in a 8 m wide crater that was covered by duricrust (Figure 8.6a). Spirit's left three wheels fell into that crater while its right three wheels remained on what appeared to be more solid terrain [6]. If the rover had a thermal sensor, it could have detected that, despite similar appearance, the crater had lower thermal inertia than the surrounding terrain. This would have only required a single nighttime measurement or a short, $\sim$ 1 hour, observation during the day. Since surface albedo was exactly the same, the simulation results in Figure 8.5a underestimate the ability of thermal inertia to differentiate the terrain, and a shorter observation could have sufficed.

The other approach is to use thermal inertia as an absolute measurement to classify terrain as hazardous or safe. Based on Figure 8.1, it is clear that a single temperature measurement is rarely enough to generate an accurate estimate of thermal inertia. Hence, absolute measurements might

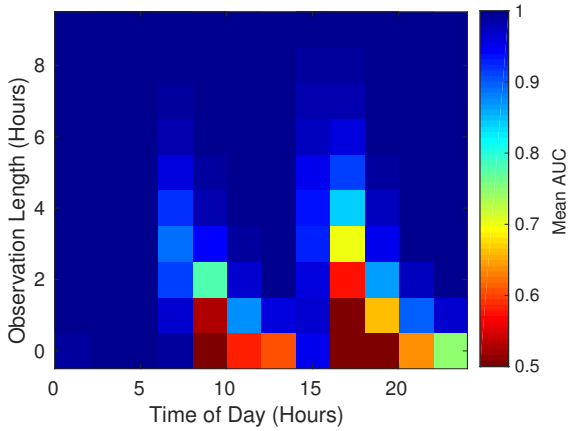

(a) Mean - 1 cm crust vs. 3 cm crust.

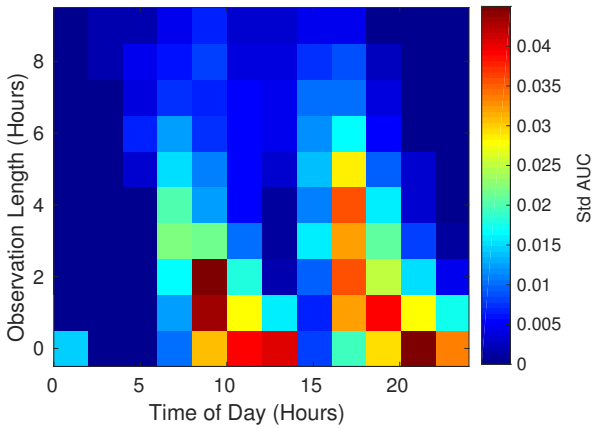

(b) Standard deviation - 1 cm crust vs. 3 cm crust.

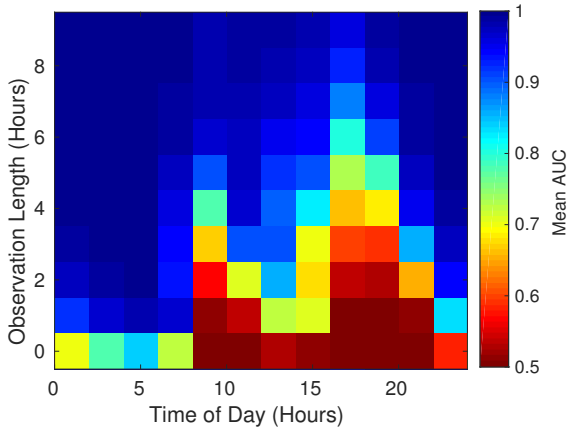

(c) Mean - 3 cm crust vs. Inf. crust.

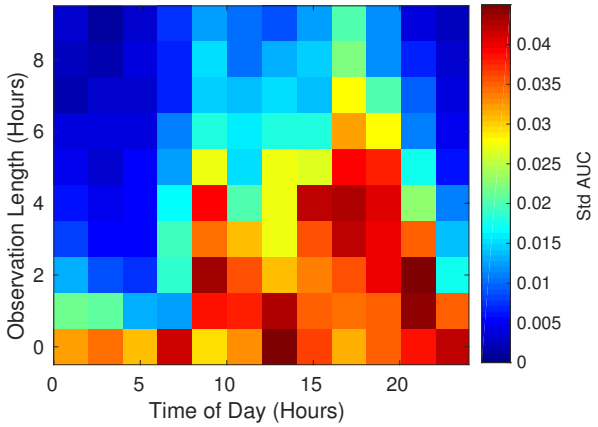

(d) Standard deviation - 3 cm crust vs. Inf. crust.

Figure 8.5: AUC for predicting duricrust thickness evaluated at different start times and for different lengths of time observing surface temperatures. The positive class is the thicker layer of duricrust over sand. All cases were evaluated over 50 samples.

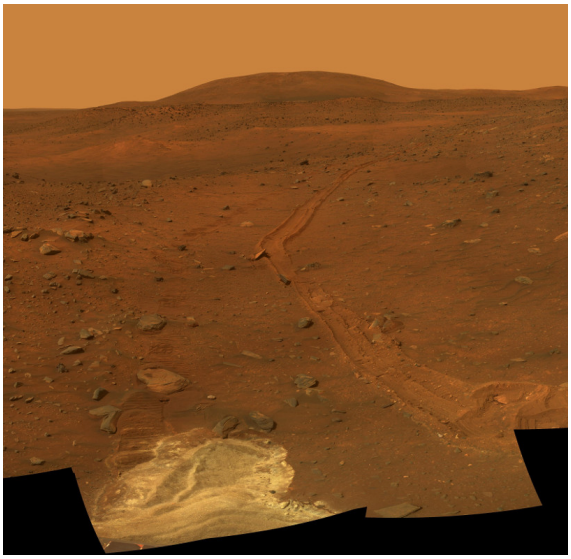

(a) Spirit's tracks leading up to it's entrapment. The bottom left of the image shows the light loose sand beneath the redish duricrust layer.

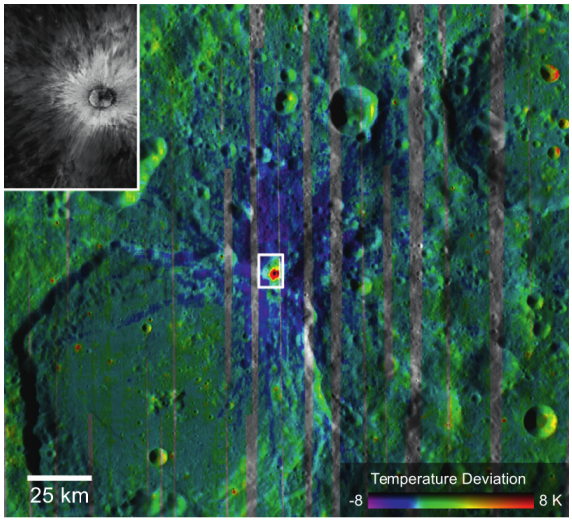

(b) Image of a crater showing a comparison of Lunar regolith nighttime temperature and closeup visual imagery (inset). Colder temperatures show looser regolith. Image credit: [16].

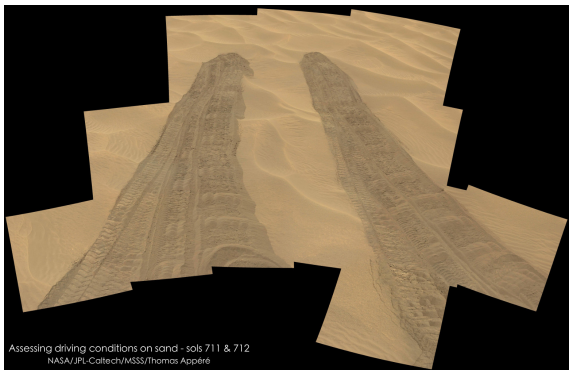

(c) Curiousity's tracks in Hidden Valley, 80% slip.

(d) Dingo Gap dune after Curiosity traverse.

Figure 8.6: Examples of situations where thermal inertia could aid traversability prediction. Credit to NASA/JPL for (a), (c), and (d).

only need to be used in areas where terrain is evaluated to be potentially hazardous. This is the approach used in Chapter 6. Terrain was first evaluated to be potentially hazardous sand. Then, thermal inertia was used to identify which regions were more or less traversable.

Observations also do not have to be continuous. A rover could look at the path ahead, collect science data, and then look at the path ahead again an hour later. However, even continuous observations would not significantly slow a planetary rover because thermal sensors have look-ahead distance that could measure the terrain while driving. A rover that detects temperatures 30 m ahead has a 50 min observation time at an average speed speed of 1 cm/s (average speed of MER rovers). In many cases, 50 min is enough time to evaluate terrain for hazards using thermal inertia.

Two critical, unanswered questions remain. First, in what situations would thermal inertia successfully identify hazardous terrain that the best possible visual prediction algorithm would fail? Second, how abundant are these situations? This thesis has shown experimentally that the use of thermal inertia enabled higher accuracy slip prediction in visually-identified sand than the use of terrain slope alone for Curiosity's traverse. The first generation of the SPOC-G terrain classifier was used to identify sand [132]. However, this is not necessarily the best classifier for mobility purposes. For example, all of the regions classified as high-slip by thermal inertia also had large polygonal ripples. The lower-slip, higher-thermal inertia sand generally had smaller ripples. A better visual classifier might instead characterize *Sand* as two classes, rippled sand and smooth sand. The great challenges encountered to date are on rippled sand.

It is possible that by avoiding sand with polygonal ripples, a rover could avoid all sand hazards. However, both sand properties and local geometries are important. If Curiosity had encountered sand with the granular properties of Dingo Gap (Figure 8.6d) but the ripples of Hidden Valley (Figure 8.6c), simulations indicate that it would have successfully traversed instead of becoming entrapped as it did [8]. There is no known correspondence between ripple geometry and material properties. Ripples form based on wind direction and local topography[1]. In theory, there can be loose sand with significant ripples and loose sand with few ripples. Using vision alone could avoid the rippled loose sand but would still be caught in the smooth loose sand. There are also situations involving vertically layered materials where thermal data could identify what vision cannot. Examples include detecting differences in surface sand depth and duricrust thickness as explored in simulation above.

There are clearly situations in which thermal can detect hazardous terrain where vision would fail. The more difficult question remains. How often do these situations occur on Mars? Are they so rare that a rover mission would not expect to encounter one, or are they sufficiently abundant that a thermal sensor is necessary to prevent entrapment? Chapter 6 demonstrated improved slip prediction in sand on Mars. However, this was a small sample from one region of Mars, and it is difficult to either prove or disprove that the best possible visual classifier could not have equaled its performance. The only provable situation any rover on Mars has experienced in which thermal imaging could have prevented entrapment but vision could not is Spirit's entrapment beneath duricrust (Figure 8.6a). Based on the analysis in Figure 8.5a, there should have been a noticeable thermal inertia difference despite identical visual appearance. Spirit, Opportunity, and Curiosity have collectively driven over 66 km on Mars. Even if these mission-ending situations that are

[1]Ray Arvidson, personal correspondence

undetectable by vision are only expected to occur once every 100 km, it can still be argued that a thermal sensor would be beneficial. Preventing just one mission failure could justify the additional cost and complexity of a thermal sensor given the billion dollar pricetags of Mars missions.

8.3 The Moon

Using thermal information to predict traversability on the Moon is a very different problem than on Mars. One of the most significant factors is the Moon's much slower diurnal cycle. The illumination period on Mars is just over 1 Earth day but is 28 Earth days on the Moon. The benefit of waiting longer to observe the terrain is seeing more of the diurnal curve. While a rover might only need to wait a few hours to see enough of the diurnal temperature curve to evaluate terrain on Mars, it could require days to do the same thing on the Moon. Consequently, a rover cannot be expected to measure anything more than essentially a single instance in time.

As on Earth and Mars, time of day also has a significant effect on the effectiveness of this approach. Nighttime temperatures separate loose and compact terrain; whereas, daytime data is less reliable. Because illumination changes so slowly on the Moon, terrain temperatures quickly reach steady states and there are not significant temperature differences between different types of terrain. A rover can expect less than a 0.2 K difference in temperature between loose and compact regolith during the day. Thus, the rover is limited to essentially only single-point measurements during the night.

The nighttime and single-point limitations mean that thermal inertia measurements might only be useful for mobility prediction on the lunar poles. In lower latitude regions, it is expected that rovers would drive during the day, when this is not useful, and hibernate through the cold temperatures at night. However, at the poles, rovers may takes brief forays into permanently dark, shadowed regions. In these shadowed regions, as shown in Figure 7.6, more significant temperature differences are expected. On the floor of a crater, temperature differences between loose and compact terrain are expected to be $\sim$2 K both at night and during the day.

At the low temperatures in lunar craters, absolute radiometric calibration is difficult. Hence, the most reliable mobility prediction approach is to look for differences in thermal inertia, rather than finding a mapping between absolute thermal inertia values and mobility. For example, if a rover saw a thermal inertia differences like in Figure 8.6b, then it should suspect the lower thermal inertia region is more dangerous. Fortunately, the Moon does have some characteristics that benefit this approach. The lack of atmosphere makes heat fluxes even across the surface and more predictable, though there are still difficulties with estimating reflected and emitted radiation from the environment. In addition, within a given region, the surface is fairly homogeneous, so relative errors in albedo estimation are not significant [64].

The same question posed for Mars also applies to the Moon: does a rover expect to encounter situations where thermal mobility prediction can identify hazards that vision cannot? It is already known that lunar cold spots exist that are impossible to distinguish visually but straightforward to identify thermally. These cold spots are hypothesized to correspond to very loose regolith. They have been identified from orbit at latitudes less than $\sim 50^\circ$, but not yet on the poles because the greater temperature variations at higher latitudes makes identifying these regions more difficult [16]. It is also theorized that the regolith in permanently dark craters is much looser

than elsewhere on the Moon [149]. However, it is not yet known precisely what these regolith properties may be. While there is strong evidence and theory to suggest that there are regions of loose regolith on the lunar poles that would be hard to identify visually, the exact properties and abundance of these regions remains unknown.

In summary, overall applicability of thermal sensing for mobility prediction on the Moon is significantly more limited than on Mars. Simulations indicate that thermal imaging could identify loose regolith in permanently shadowed lunar craters. It could also improve traversability prediction at night anywhere on the Moon; however, rovers are unlikely to drive at night.

8.4 Earth

Though the goal of this research has been predicting traversability in extraterrestrial environments, field testing necessarily took place on Earth. This provided insight into how and when thermal inertia could improve mobility prediction. Earth is unique because of its atmosphere, clouds, moisture, and vegetation. Thermal inertia is best applied to mobility prediction when illumination is even over the surface of terrain. However, on Earth, clouds, vegetation, and man-made structures cast shadows on the terrain that move throughout the day. This results in uneven illumination, which makes relative difference in thermal inertia and traversability extremely difficult to predict, especially during the day.

Even when solar illumination is uniform across the terrain, atmospheric effects add uncertainty to thermal inertia measurements. It is difficult to estimate latent and sensible heat fluxes, which adds error to absolute thermal inertia. However, relative thermal differences can at times still distinguish between mechanical properties of granular materials.

Hence, the applicability of thermal inertia to traversability prediction on Earth is very limited. Very dry deserts are the only potential environments where thermal inertia could make a significant impact on traversability prediction. The lack of moisture and vegetation as well as fewer clouds make it more straightforward to identify differences in material properties. Aside from beaches, desert environments are also the only real locations where loose, aeolian sand exists and must be avoided.

An example use case is shown in Figure 8.7. Consider a robot driving down a desert road evident by the tire tracks in Figure 8.7a. The sand on the road is much more compact that the sand off of the road despite very similar visual appearance. However, there is a clear temperature difference evident in Figure 8.7b. In the thermal image, the loose sand is up to 15 K warmer than the compact sand. A rover equipped with a thermal camera could detect a significant difference in thermal inertia and be cautious about entering the very warm regions. This could be implemented by giving higher cost to lower thermal inertia regions. In this example, the images were taken during the day and show a clear temperature difference. However, the field experiments in Chapter 5 demonstrated that the best application of this approach is during the night. At night, errors caused by uneven illumination and albedo errors are less significant.

Because the primary target of this thesis was dry planetary environments, moisture content did not pertain. On Earth, moisture was addressed but not in depth. Some experimental results showed a moderate correlation between water content and thermal inertia. This agrees with the results from González et al, who found that dry sand had much lower thermal inertia than wet sand. They

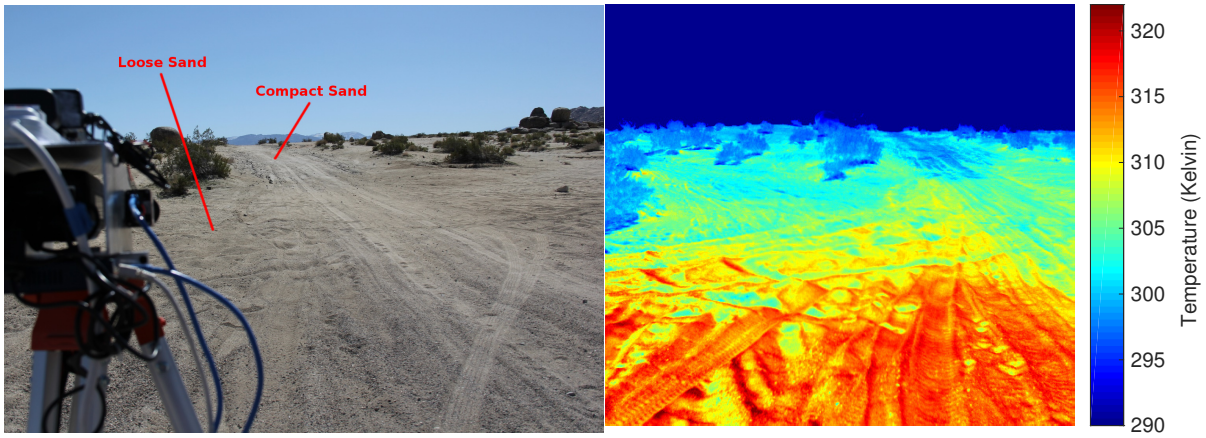

(a) Visual image.

(b) Thermal image.

Figure 8.7: Example situation where thermal inertia could be used to distinguish compact from looser sand in a desert environment on Earth. Images are taken at Johnson Valley in California.

also found a corresponding increase in traversability as water content increased. There is certainly a limit to that correlation, since over-saturated, muddy soils show a decrease in traversability. It is possible that future work could use thermal information to improve predictions of traversability in vegetated and wet environments on Earth; however, analysis of those situations is beyond the scope of this thesis.

Leveraging thermal inertia for mobility prediction on Earth is made very difficult by clouds, vegetation, water content, and atmospheric effects. Deserts are perhaps the only environments where this could have an impact, particularly on driving at night.

8.5 Sensor Requirements

One key consideration is the sensing required to measure the thermal properties of terrain from a rover. Curiosity's GTS is not ideal for traversability prediction because it is too low resolution, unable to be pointed, and not aimed at the rover's general path. An ideal sensor would be aimed at the rover's path. It would have high enough resolution so that each pixel is measuring a homogeneous region of terrain. It also needs to have low noise. Less integration time necessary to collect a low-noise thermal image is better because the rover can keep driving. On Earth, this is not a significant problem. Thermal cameras already exist with high enough resolution and low enough noise to adequately predict slip. For example, the thermal camera used in Section 5.2 had a of 640 x 480, NETD of 50 mK at 60 Hz, and radiometric accuracy of ± 2 K. It is more difficult to develop a similar instrument for space applications that meets the resolution and accuracy requirements because of the need for radiation-hardened electronics. In addition, lower temperatures on other planetary bodies result in less blackbody radiation, which decreases the signal to noise ratio.

To illustrate why high resolution is needed, another simulation was conducted using the KRC thermal model for Mars [80]. Consider the situation where 150 μm sand is surrounded by bedrock.

This sand may be too fine and loose to drive through, but if the region is small it could be hard to measure. A high resolution thermal sensor can isolate the sandy region in a pixel of its own, but a lower resolution (or orbital) camera would include some of the bedrock in its measurement of the sand. The resulting, measured temperature is no longer going to be the actual temperature of either the rock or the sand but instead somewhere in between. Assuming unit emissivity, the resulting temperature is:

$$T_b = \left(C_s T_{sand}^4 + (1 - C_s)\, T_{rock}^4\right)^{\frac{1}{4}} \tag{8.2}$$

where T_b is the measured temperature, T_{sand} is the actual sand temperature, T_{rock} is the actual rock temperature, and C_s is the fraction of the pixel containing sand.

Thermal properties for 150 μm sand and bedrock are given in Table 8.1. First, surface temperatures for both materials were simulated over the course of a day using an albedo of 0.25, a slope of 0, and an atmospheric dust opacity of 0.5. Next, a range of C_s values were used to evaluate temperatures, T_b, for the rock sand mixture. Finally, for each T_b, thermal inertia and effective particle size were estimated. Effective particle size was estimated using Equation 8.1.

Results from this simulation are shown in Figure 8.8. Figure 8.8a shows the measured temperature minus the actual sand temperature. As less sand and more rock is measured in a given pixel, the temperature during the day goes down and goes up at night. The estimated thermal inertia using T_b is shown in Figure 8.8b. Thermal inertia steadily increases as the percentage of sand is decreased. This affect varies over the course of the day, however. When illumination begins to change rapidly in the evening or at night, it briefly becomes easier to identify the sand. Unfortunately, the overall accuracy at these times of day is very low as shown previously. Finally, Figures 8.8c and 8.8d show the estimated particle sizes derived from the thermal inertia in Figure 8.8b. After only a 80% mixing at most times during the night, the estimated particle size will be more than twice the actual particle size. This helps to explain the disparity in thermal inertia range between the GTS ($\sim$10 m resolution) and THEMIS (100 m resolution) in Chapter 6. THEMIS was measuring much more than just sand in most pixels. This analysis shows the importance of measuring a homogeneous material. A robot could be misled into predicting a region of sand is safe if its measurement also includes a more compact or rocky area the rover does not intend to drive on.

The obvious conclusion is that higher resolution is always better. However, on the Moon or Mars, radiation-hardened, high-resolution instruments might be a challenge. Instead, a reasonable minimum resolution is one that enables isolation of a region on the ground the size of the rover's wheels. Assuming a rover wants to evaluate the terrain under its 0.2 m wide wheels accurately at a distance of 10 m away, this would require an angular resolution of $\sim$1.1°. This is comparable to the 1.15°resolution of the MER Mini-TES instruments on Mars [33]. The ideal solution would be an instrument with a pixel array; however, it could also be possible to put a simpler, single-pixel sensor on the rover's mast that could be pointed at regions of interest. This is how the Mini-TES instrument was used. An example image showing an array of Mini-TES temperature measurements is shown in Figure 8.9.

As resolution gets finer, integration time required to reach a sufficient signal to noise ratio (SNR) becomes longer. For example, Mini-TES required integration times of 4 and 160 seconds to achieve an SNR of 400 at resolutions of 20 and 8 mrad, respectively [33]. Signal to noise ratio

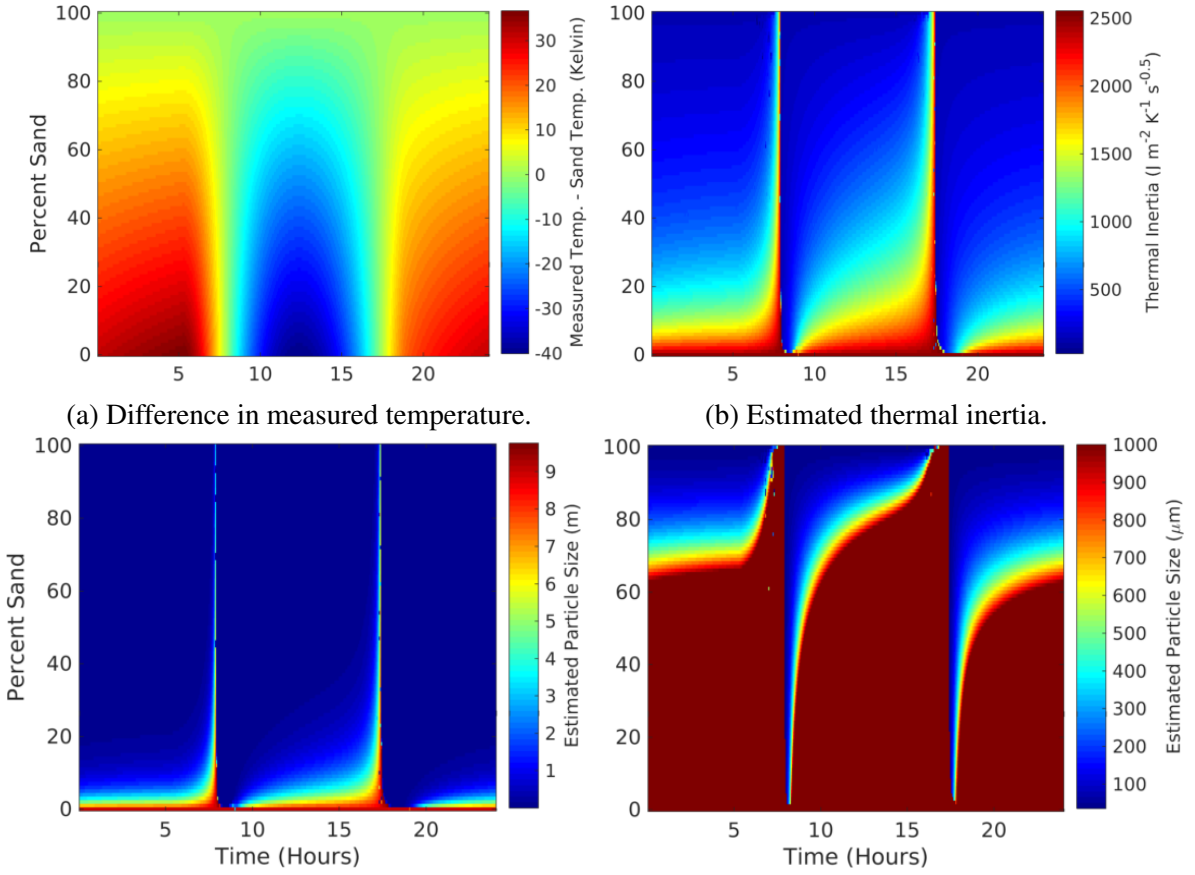

(a) Difference in measured temperature.

(b) Estimated thermal inertia.

(c) Estimated sand particle size.

(d) Estimated sand particle size (color map limited).

Figure 8.8: Simulation results showing the effects of averaging the temperature from 150 μm sand and bedrock within one pixel. Effects are shown for different percentages of the pixel containing sand.

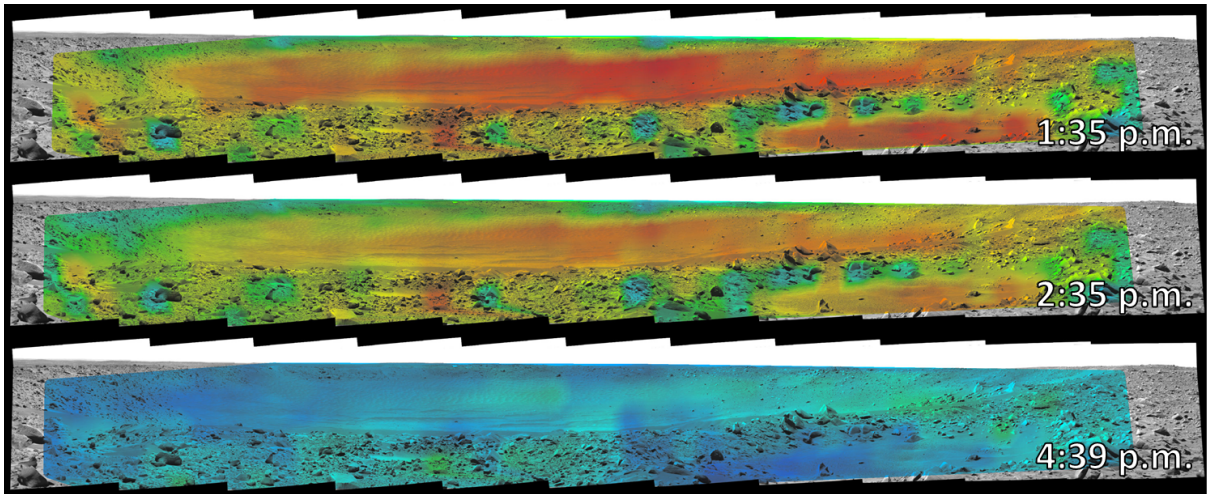

Figure 8.9: Interpolated Mini-TES measured temperatures of Bonneville Crater on Mars interpolated overlaid on Spirit Navcam imagery. Warmer temperatures are shown in red, cooler temperatures in blue. Image credit: NASA/JPL

also decreases as temperature decreases because less radiation is emitted from the surface. As discussed earlier, this means that longer integration times are required in cold situations, such as permanently shadowed craters on the Moon. Shorter integration times are necessary in warmer regions on Earth and Mars. Clearly, a sensor with lower noise is better for mobility prediction. However, on the Moon and Mars, periodically stopping for $\sim$1 minute or so to take a high SNR image will not significantly affect a rover's average traverse speed since planetary rovers already travel very slowly.

The keys to good thermal data for traversability prediction are fine resolution, wide spatial coverage, and high temporal coverage. These are not characteristics that are necessarily unique to ground-based sensors and could apply to an orbital sensor as well. A suitable orbital sensor should have fine enough resolution to detect rover-scale hazards. This is more difficult to achieve from orbit because atmospheric effects limit the achievable resolution of a sensor, especially at longer wavelengths. However, this is not as significant of an issue on Mars as on Earth because Mars has a much thinner atmosphere. An orbital sensor also needs enough data to cover the region the rover intends to drive with samples at multiple times during the day. This desire is at odds with the need for fine resolution. Fine resolution requires a narrow field of view and high coverage needs a wide field of view. An orbital instrument with low spatial coverage will be limited in the number of times it can observe a region, which will likely result in sampling fewer times during the day. Samples would likely occur across seasons, which may make it more difficult to accurately infer and compare thermal inertias. Finally, localization can be difficult. As relative localization errors accumulate, it is less likely that a rover knows its exact location within an orbital map. However, if these engineering challenges can be overcome, an orbital sensor could likely perform as well as a ground-based sensor. It could even have the advantage of obtaining measurements from a much wider area at a single point in time which enables more direct comparisons between different terrains.

Chapter 9

Conclusions

This thesis demonstrates that thermal inertia is a single measurement that is correlated to the physical parameters that govern traversability. Moreover, it discerns that thermal inertia provides insight into the granular properties of terrain both at and below the surface. This is in contrast to visual techniques that require more complicated texture- and color-based feature representations that are not necessarily correlated to bulk mechanical properties below the surface. This thesis analyzed how, where, and when a thermal approach applies. Most importantly, it demonstrated the feasibility of using thermal inertia to improve slip prediction using in-situ Mars rover data by reducing cross-validation slip prediction error by 27%. Even with an imperfect sensor that only takes one measurement from a 10 by 10 m region and cannot be pointed ahead of the robot, classification of terrain using thermal inertia correctly identified all four of the low-slope ($< 10^{\circ}$) drive secessions as hazardous.

This thesis instead establishes the correlation between wheel-terrain interaction and bulk thermal properties. It concludes that rover-scale measurements of the thermal properties of terrain improve traversability prediction in planetary environments by enabling differentiation between compact and loose granular materials.

9.1 Summary

For a granular material, both thermal inertia and wheel-terrain interaction are strongly effected by density, particle size distribution, layering, and cementation. As these parameters are varied, in general, increases in thermal inertia correlate to increases in traversability. It is for this reason that thermal inertia can be used to improve traversability. While this relationship held in all experiments in this thesis, the correlation is not necessarily one-to-one in all cases. For example, particle shape also effects wheel-terrain interaction but does not have a clear connection to thermal inertia. In other cases, it is possible that materials could have different combinations densities and particle sizes, such that the relationship between thermal inertia and traversability does not hold. Though it is likely that these edge cases exist, they were not encountered in the experiments in this thesis.

The thermal properties of terrain were estimated by measuring surface temperatures caused by either: (1) natural atmospheric and solar heat fluxes or (2) impingement by a rover-born

Table 9.1: Summary of differences between solar and laser heat fluxes. Summarizes differences in the length of time heating the surface, the type of subsurface heat diffusion (3D or 1D), dependence on time of day, and effective sensing depth.

Source	Heating Period	Diffusion	Time of Day Dependence	Sensing Depth
Laser	$\sim$ 1 s	3D	Minimal	$\sim$2 mm
Natural	1 diurnal period	1D	Strong	$\sim$4 cm

laser. Transient temperature curves were fit to physics-based analytical models to find the best-fit thermal inertia and diffusivity, respectively. Both thermal inertia and diffusivity were shown to distinguish between loose and compact states of the same granular material.

The use of natural illumination is superior to a laser because it has vastly greater flux and coverage and provides information at range beyond a rover. Table 9.1 summarizes the differences between the two approaches. When using a laser, measurements are limited a single point in front of the rover. When leveraging natural heat fluxes, the whole environment can be incorporated into the thermal solution. Surface temperature variations caused by natural heat fluxes are influenced by terrain much deeper below the surface than those caused by a robot's laser. Uniform illumination over the surface results in no lateral heat flow, so heat can only diffuse in one dimension. When using a laser, the surface illumination is a point, so heat diffuses in three dimensions, which attenuates heat waves below the surface. Natural heat fluxes also have a significantly longer period, which enables heat to reach much deeper below the surface. Surface temperatures controlled by diurnal illumination include information from several centimeters below the surface, depending on the thermal skin depth of the material[1]. A short pulse of light from a point laser is limited to only probing the top $\sim$1–2 mm of terrain [2]. Hence, the best way to measure the thermal properties of terrain is to use natural heat fluxes rather than a laser to heat the surface.

When using natural heat fluxes like solar and atmospheric radiation, the ability of thermal inertia to identify hazardous terrain depends greatly on time of day, length of time observing the surface, and characteristics of the environment. Longer observation times enable a rover to collect data from more of the diurnal temperature curve, resulting in more accurate thermal inertia estimates. Nighttime measurements result in significantly lower error than daytime measurements because inaccuracies in slope, albedo, and heat flux estimates are less significant.

The ideal environment has: (1) uniform and predictable illumination over the surface, (2) no vegetation or water, (3) warm surface temperatures, (4) an atmospheric pressure of $\sim$1–100 Torr, and (5) a moderate-length diurnal period. Uniform heat-fluxes enable direct comparisons between different regions of terrain because the entire surface receives the same heat flux. Predictable fluxes enable accurate absolute measurements of thermal inertia for comparisons that span days and seasons. Vegetation and water content influence the thermal properties, making it more difficult to isolate differences in granular characteristics. Significant vegetation also casts shadows on terrain, which makes it nearly impossible to conclude anything about the terrain properties.

[1]The thermal skin depth (effective sensing depth) for lunar regolith at 150 K is $\sim$4.1 cm.

[2]Assuming a NETD of 0.5 K and a 1 second pulse, measurement depths on the Moon are estimated to be 1.6 mm and 2.2 mm for surface heat fluxes of 2 and 5 kW/m^2, respectively.

Table 9.2: Overview of the characteristics of an environment that are conducive to thermal imaging for traversability prediction. Check marks indicate that whether each characteristic applies to either Mars, the Moon, craters on the poles of the Moon, or Earth.

Characteristic	Mars	Moon	Moon–Polar Craters	Earth
Uniform Illumination	✓	✓		✓
Predictable Illumination	✓	✓		
Negligible Water Content	✓	✓	✓	
Warm Temperatures	✓	✓		✓
Low Atmospheric Pressure ($\sim$1–100 Torr)	✓			
Moderate Diurnal Period	✓			✓

Warmer surface temperatures make measurement of surface temperatures both more precise and more accurate. More radiation results in a higher signal-to-noise ratio, and absolute temperature calibration becomes easier. Atmospheric pressures of $\sim$1–100 Torr are also ideal because it is within this range that differences in particle sizes have the most significant affect on thermal conductivity. The presence of any atmosphere also increases thermal conductivities and skin depths, which means the surface temperature is influenced by terrain further beneath the surface when any atmosphere is present. Finally, the ideal diurnal period is long enough to facilitate large thermal skin depths and, thus, is a function of the thermal properties of terrain (see Equation 3.3). However, a period that is too long (e.g. the Moon) has illumination that changes too slowly and materials can become indistinguishable during the day. Table 9.2 summaries how these characteristics apply to the environments studied in this thesis.

Thermal inertia can either be used as an absolute measurement or a relative measurement. Absolute measurements of thermal inertia are noisier but enable classification of terrain across entire traverses. This approach is more susceptible to variations in radiometric calibration accuracy and surface heat flux estimates. Consequently, it is best suited to environments with predictable heat fluxes and warm temperatures (i.e. Mars). Relative estimates of thermal inertia more reliably separate safe from hazardous terrain because calibration and heat flux errors are independent of the terrain measured. However, this restricts comparisons between terrains to short time scales rather than across days and seasons. This thesis analyzed Mars, the Moon, and Earth, which are the most likely environments where these approaches could be applied.

Mars

Mars is the best environment in the solar system to apply thermal inertia for mobility prediction. It is close enough to the Sun for viable solar flux. It is mostly dry, surface illumination is uniform (i.e. no clouds or trees), its surface temperatures are warm enough for accurate radiometric calibration, and its atmospheric pressure is near-ideal. The 4.5 Torr atmosphere enables clear differentiation between particle sizes and densities of materials [121, 122]. The existence of an atmosphere also increases thermal conductivities and consequently thermal skin depths. This helps to provide information from several centimeters beneath the surface.

Experimental data from the Curiosity rover's Ground Temperature Sensor (GTS) showed

that classifying sand based on absolute thermal inertia measurements reduced cross-validation slip prediction error from 23.1 to 16.9. As expected, high thermal inertia sand was classified as low slip and low thermal inertia sand was classified as high slip (Chapter 6). The use of GTS measurements slightly outperformed orbital THEMIS measurements in cross validation error. This result and the analysis of instrument resolution effects in Section 8.5 demonstrate that ground-based, high-resolution measurements enable higher accuracy predictions of thermal inertia and traversability.

Simulations demonstrated that thermal inertia can differentiate between particle sizes of sand, different depths of sand (up to $\sim$3 cm), and different depths of duricrust (up to $\sim$9 cm). Most importantly, thermal inertia can distinguish between a solid, thick crust and a thin crust that hides deep sand underneath. This was the situation that trapped the Spirit rover, and these materials are indistinguishable using only visual approaches.

In most cases, hazards can be identified using nighttime measurements or by observing the surface over the course of an hour. This does not significantly slow down rover operations since planetary rovers are slow and observations can be made while driving. At certain times during the day or for certain types of hazards, longer observation times will be needed. A rover should pause for longer observations during these times or when significant hazards are more likely. Future Mars missions may drive throughout the night, and thermal imaging provides an unequaled ability to not only navigate around geometric hazards but simultaneously evaluate the granular terrain for traversability.

The Moon

Thermal methods for predicting traversability on the Moon are disadvantaged by the lack of an atmosphere, a 29.5 day diurnal period, and fairly homogeneous terrain. The vacuum of the Moon reduces thermal conductivities and inertias in granular materials, making it difficult to obtain information quickly from deep beneath the surface. The very slowly changing illumination causes temperatures to quickly reach steady state during the day, resulting in very small differences in temperature between loose and compact materials. There are more significant temperature variations during the night ($\sim$4 K); however, these occur at very low temperatures ($<$ 100 K), which makes absolute radiometric calibration difficult. In addition, it is likely that a rover will not travel through the night at all but instead hibernate to survive the cold and lack of solar power. This suggests that at most places on the Moon, measurements of thermal inertia would not have a significant practical effect on traversability prediction.

The exceptions to this are the permanently dark craters on the lunar poles that are important science targets due to the existence of ice in the regolith. It is hypothesized that regolith in these craters could be much looser than in other areas due to the lack of a freeze-thaw cycle that helps to compact materials over time [149]. Chapter 7 demonstrated in simulation that temperature differences between loose and nominal regolith in permanently shadowed craters are expected to be between 2 and 3 K despite the lack of direct sunlight. This temperature difference occurs at very low temperatures ($<$ 50 K), which makes absolute radiometric temperature accuracy difficult to achieve. Instead, a rover could use relative differences in temperature to prefer driving on higher thermal inertia materials, which would reduce the probability of encountering hazardous regolith. The simulation results relied on estimates of the physical and thermal properties of regolith in

permanently shadowed lunar craters derived from samples taken during lunar surface missions. Unfortunately, before a mission actually investigates the poles, it is impossible to determine the accuracy of these assumptions.

Earth

Earth is uniquely disadvantaged by moisture, clouds, vegetation, and atmosphere. The combination of these characteristics limit the applicability of this approach only to dry, desert environments on cloud-free days where no vegetation or man-made structures cast uneven shadows. Even in dry desert environments, absolute measurement of thermal inertia is still difficult due to atmospheric effects that make accurate estimation of surface heat fluxes nearly impossible. In addition, terrestrial vehicles are much faster than planetary rovers, and thus it is unreasonable to expect a robot to measure surface temperatures at more than one instance in time. Consequently, relative measurements of thermal inertia provide the only way to identify hazardous terrain.

Chapter 5 presented two terrestrial experiments showing that relative differences in thermal inertia distinguish between loose and compact states of granular terrain, which are visually similar. Relative measurements of thermal inertia enabled near-perfect separation of loose and compact terrain at night. Errors caused by reflected radiation, slopes, albedos, and shadows reduced classification accuracy during the day. While evidence suggests that daytime data is still useful in dry, barren environments, the most probable and reliable application of this approach is mobility prediction at night. Even in dry, cloudless environments, estimation of heat fluxes is still difficult due to atmospheric effects, which makes absolute thermal inertia measurements difficult, especially during the day.

9.2 Contributions

This thesis contributes analysis of how a rover could use terrain thermal measurements to improve traversability prediction on Mars and the Moon. Specifically, the contributions of this thesis are:

1. An approach for differentiating between loose and compact terrain using a laser to induce a transient temperature response. Experimental validation used different compaction levels of three different lunar regolith simulants.
2. An approach for using relative difference in rover-measured thermal inertia to distinguish between loose and compact terrain. Terrestrial validation showed near-perfect separation of loose and compact terrain at night and high error during the day.
3. A method for classifying sand as either safe or hazardous using absolute measurements of thermal inertia and a mixture of experts approach.
4. Tests conducted on Curiosity data provided the first quantitative feasibility analysis that demonstrated 27% improvement in accuracy when using thermal inertia to predict slip on Mars.
5. Simulation-based analysis showing that at most times during the Martian day, thermal inertia can differentiate between particles sizes of sand, depths of surface sand, and depths of duricrust. Results demonstrated that at most times during the day only 1 to 2 hour-long

observations are necessary to find relative differences in thermal inertia that can distinguish between safe and hazardous terrain.

6. Analysis showing that even in permanently shadowed lunar polar craters with no direct sunlight, there is a measurable temperature difference between loose and compact regolith.

9.3 Future Work

Future work must address the development of both the algorithm and the sensor that would enable a robot to autonomously predict traversability. Rovers must identify both hazards that are obviously immediately and regions that it should observe for longer to better evaluate. A suitable algorithm must both predict the most likely terrain properties and understand the uncertainty. One potential approach would be to discretize the set of terrain types that a rover is expected to encounter and update the likelihood of each terrain as new measurements come in. A discretized set of terrain types could be similar to the terrains used in Section 8.2, including different depths of sand over rock, different thickness of duricrust over sand, and sands with different thermal inertias. This offers a direct path for inclusion of visual data. For example, a classifier could identify the surface class as sand, which rules out other potential terrain types that have rock or duricrust as the surface layer.

To fully evaluate these techniques, a long duration field test in a large natural, planetary analog environment is necessary. Testing should emulate Martian operations and occur over the course of several diurnal cycles. A large, natural environment is necessary because of the practical constraints of field testing this approach. Terrain cannot be immediately tested upon after being manually prepared. At least a day must pass to allow the subsurface temperatures to revert to the natural distribution. Hence, large, natural environments are much more conducive to field testing than smaller, controlled settings. The ideal test environment has significant windblown sand with variations in particle size distribution, density, and rock. It would be dry with low humidity and have minimal clouds and vegetation. Ideal terrestrial test environments include Dumont Dunes as well as regions near aeolian sand in the Atacama Desert and the Sahara Desert.

Experimental results showed an improvement in slip prediction on Mars when using thermal inertia. However, the in-situ dataset from the Curiosity rover was limited to one region on Mars. To strengthen the argument for implementation of this approach on future Mars rovers, more data should be analyzed. Fortunately, Curiosity will continue to drive and collect more data. In addition, the planned Mars 2020 rover will contain the MEDA instrument, which will collect very similar data to the Curiosity's GTS [131]. Neither instrument is appropriate for the implementation of traversability prediction on-line because of the low resolution and fixed pointing angle. However, they will both provide an unprecedented amount of data that could strengthen the case for inclusion of a higher resolution thermal camera on a pan-tilt mount on future Mars rovers.

On the Moon, the promising application domains are permanently shadowed craters on the poles. Simulations in this thesis demonstrated a measurable temperature difference between loose and compact regolith in these craters but relied on best-available assumptions of polar regolith properties. The accuracy of these assumptions can be verified during missions that visit these craters. Once the range of regolith characteristics is better understood, future research

should refine the analysis in thesis with experimentally measured regolith properties. Then a more confident conclusion can be made to determine whether or not future mining and in-situ resource utilization robots should be equipped with thermal cameras for traversability prediction in permanently shadowed lunar craters.

Because of vegetation, clouds, and water content, it is unlikely that this approach will improve traversability prediction in most environments on Earth. However, in dry, desert environments there is still promise, especially for nighttime driving. Terrestrial experiments addressed variations in density without exploring differences in particle sizes and cementation, which are likely to contribute to greater temperature differences. To more confidently evaluate whether thermal inertia could improve traversability prediction on Earth, more data collection is required in the actual environments where this might apply.

9.4 Closing Remarks

This thesis has demonstrated that measurements of thermal inertia have great potential to improve traversability prediction for rovers operating on Mars. Future rovers will aim to travel further and with less input from operators. Thermal inertia can enable a robot to autonomously identify hazards that are undetectable by vision alone, such as deep sand beneath thin duricrust. Avoidance of even one mission-ending hazard could justify incorporation of the thermal methods to predict traversability developed in this thesis.

Bibliography

[1] Andrade, J., R. Lindemann, K. Iagnemma, B. Trease, I. Vlahinic, and C. Senatore (2012). XTerramechanics: Integrated Simulation of Planetary Surface Missions. Technical report. 3.4.1

[2] Angelova, A., L. Matthies, D. Helmick, and P. Pernoa (2007). Learning and Prediction of Slip from Visual Information. *Journal of Field Robotics 24*(3), 205–231. 2.2a, 2.2

[3] Angelova, A., L. Matthies, D. Helmick, and P. Perona (2006). Slip Prediction Using Visual Information. In *Proceedings of Robotics: Science and Systems*, Philadelphia. 2.2

[4] Anthony, J. L. and C. Marone (2005). Influence of particle characteristics on granular friction. *Journal of Geophysical Research: Solid Earth 110*(8), 1–14. 3.4.2, 3.5

[5] Arvidson, R. E., J. W. Ashley, J. F. Bell, M. Chojnacki, J. Cohen, T. E. Economou, W. H. Farrand, R. Fergason, I. Fleischer, P. Geissler, R. Gellert, M. P. Golombek, J. P. Grotzinger, E. Guinness, R. M. Haberle, K. E. Herkenhoff, J. Herman, K. D. Iagnemma, B. L. Jolliff, J. R. Johnson, G. Klingelhöfer, A. H. Knoll, A. T. Knudson, R. Li, S. M. McLennan, D. W. Mittlefehldt, R. V. Morris, T. J. Parker, M. S. Rice, C. Schröder, L. A. Soderblom, S. W. Squyres, R. J. Sullivan, and M. J. Wolff (2011). Opportunity Mars Rover Mission: Overview and Selected Results From Purgatory Ripple to Traverses to Endeavour Crater. *Journal of Geophysical Research: Planets 116*(2), 1–33. 1.1.1, 3.4

[6] Arvidson, R. E., J. F. Bell, P. Bellutta, N. A. Cabrol, J. G. Catalano, J. Cohen, L. S. Crumpler, D. J. Des Marais, T. A. Estlin, W. H. Farrand, R. Gellert, J. A. Grant, R. N. Greenberger, E. A. Guinness, K. E. Herkenhoff, J. A. Herman, K. D. Iagnemma, J. R. Johnson, G. Klingelhöfer, R. Li, K. A. Lichtenberg, S. A. Maxwell, D. W. Ming, R. V. Morris, M. S. Rice, S. W. Ruff, A. Shaw, K. L. Siebach, P. A. De Souza, A. W. Stroupe, S. W. Squyres, R. J. Sullivan, K. P. Talley, J. A. Townsend, A. Wang, J. R. Wright, and A. S. Yen (2010). Spirit Mars Rover Mission: Overview and Selected Results from the Northern Home Plate Winter Haven to the Side of Scamander Crater. *Journal of Geophysical Research: Planets 115*, 1–19. 1.1, 1.1.1, 8.2.1, 8.2.2

[7] Arvidson, R. E., P. Bellutta, F. Calef, A. A. Fraeman, J. Garvin, O. Gasnault, J. Grant, J. Grotzinger, V. Hamilton, M. Heverly, K. A. Iagnemma, J. Johnson, N. Lanza, S. Le Mouelic, N. Mangold, D. Ming, M. Mehta, R. V. Morris, H. Newsom, N. Renno, D. Rubin, J. Schieber, R. Sletten, N. T. Stein, F. Thuillier, A. R. Vasavada, J. Vizcaino, and R. C. Wiens (2014, may). Terrain Physical Properties Derived From Orbital Data and the First 360 Sols of Mars Science Laboratory Curiosity Rover Observations in Gale Crater. *Journal of Geophysical Research: Planets*. 2.1.1

[8] Arvidson, R. E., M. C. Heverly, K. D. Iagnemma, P. Bellutta, M. Maimone, D. Rubin, A. A. Fraeman, N. T. Stein, F. Zhou, J. P. Grotzinger, and A. R. Vasavada (2016). Mars Science Laboratory Curiosity Rover Megaripple Crossings up to Sol 710 in Gale Crater. *Journal of Field Robotics*. 1.1.1, 1.1.1, 1.2, 2.2, 6.2.2, 6.3, 8.2.2

[9] Aye, K. M., D. A. Paige, M. A. Siegler, E. Sefton-Nash, and B. T. Greenhagen (2014). Diviner Monitoring of Coldest Lunar Polar Regions. *45th Lunar and Planetary Science Conference*, 2893. 7.3

[10] Bagnell, J., D. Bradley, D. Silver, B. Sofman, and A. Stentz (2010). Learning for Autonomous Navigation. *IEEE Robotics Automation Magazine 17*(2), 74–84. 2.2

[11] Bahrami, M., M. M. Yovanovich, and J. R. Culham (2006). Effective thermal conductivity of rough spherical packed beds. *International Journal of Heat and Mass Transfer 49*(19-20), 3691–3701. 3.3.1

[12] Bajracharya, M., A. Howard, L. H. Matthies, B. Tang, and M. Turmon (2009). Autonomous Off-Road Navigation with End-to-End Learning for the LAGR Program. *Journal of Field Robotics 26*(1), 3–25. 2.2

[13] Bajracharya, M., B. Tang, A. Howard, M. Turmon, and L. Matthies (2008). Learning Long-Range Terrain Classification for Autonomous Navigation. In *IEEE International Conference on Robotics and Automation*, pp. 4018–4024. 2.2

[14] Bamber, D. (1975). The Area Above the Ordinal Dominance Graph and the Area Below the Receiver Operating Characteristic Graph. *Journal of Mathematical Psychology 12*(4), 387–415. 5.2.5

[15] Bandfield, J. L., R. R. Ghent, A. R. Vasavada, D. A. Paige, S. J. Lawrence, and M. S. Robinson (2011). Lunar Surface Rock Abundance and Regolith Fines Temperatures Derived from LRO Diviner Radiometer Data. *Journal of Geophysical Research 116*. 1.1.2, 7

[16] Bandfield, J. L., E. Song, P. O. Hayne, B. D. Brand, R. R. Ghent, A. R. Vasavada, and D. A. Paige (2014). Lunar Cold Spots: Granular Flow Features and Extensive Insulating Materials Surrounding Young Craters. *Icarus 231*, 221–231. 1.1.2, 1.3a, 2.3, 7, 7.3, 8.6b, 8.3

[17] Bauch, K. E., H. Hiesinger, J. Helbert, M. S. Robinson, and F. Scholten (2014). Estimation of Lunar Surface Temperatures and Thermophysical Properties: Test of a Thermal Model in Preparation of the MERTIS Experiment Onboard BepiColombo. *Planetary and Space Science 101*, 27–36. 7.1.2, 7.1.2

[18] Bekker, M. G. *Introduction to Terrain-Vehicle Systems*. 3.4, 3.4.1

[19] Berczi, L.-P., I. Posner, and T. D. Barfoot (2015). Learning to Assess Terrain from Human Demonstration Using an Introspective Gaussian-Process Classifier. In *IEEE Conference on Robotics and Automation*. 2.2

[20] Bishop, C. M. (2006). *Pattern Recognition and Machine Learning*. 6.1.2

[21] Brooks, C. (2009). *Learning to Visually Predict Terrain Properties for Planetary Rovers*. Ph. D. thesis. 2.2b, 2.2

[22] Brooks, C. A. (2012). Self-Supervised Terrain Classification for Planetary Surface Exploration Rovers. *Journal of Field Robotics 29*(3), 445–468. 2.2

[23] Caillas, C. (1990). Thermal Imaging for Robotic Applications in Outdoor Scenes. Technical report. 2.3

[24] Carrier, D. (2005). The Four Things You Need to Know About the Geotechnical Properties of Lunar Soil. *Lunar Geotechnical Institute*, 23. 1.2, 3.1, 3.1

[25] Carrier, W. (1974). Apollo Drill Core Depth Relationships. *Earth, Moon, and Planets 10*, 183–194. 1.1.2, 7.2

[26] Carrier, W. D., J. K. Mitchell, and A. Mahmood (1973). The Relative Density of Lunar Soil. In *Lunar and Planetary Science Conference*, pp. 2403–2411. 3.1

[27] Carslaw, H. and J. C. Jaeger (1959). *Conduction of Heat in Solids*. Oxford: Oxford University Press. 4.1.1

[28] Chen, I. and S. Lee (1983). Transient temperature profiles in solids heated with scanning laser. *Journal of Applied Physics 54*(2), 1062–1066. 4.1.1

[29] Cherkasov, I. I., V. V. Gromov, N. M. Zobachev, A. A. Musatov, V. V. Mikheev, V. Petrukhim, and V. V. Shvarev (1968). Soil-Density Meter-Penetrometer of the Automatic Lunar Station Luna-13. *Soviet Physics Doklady 13*, 336. 1.1.2, 7.2

[30] Cho, A. G.-C., J. Dodds, and J. C. Santamarina (2006). Particle Shape Effects on Packing Density , Stiffness and Strength Natural and Crushed Sands. *Journal of Geotechnical and Geoenvironmental Engineering 132*(May), 591–602. 3.1, 3.1, 3.4.2, 3.5

[31] Christensen, P. R., R. L. Fergason, C. S. Edwards, and J. Hill (2013). THEMIS-Derived Thermal Inertia Mosaic of Mars: Product Description and Science Results. *44th Lunar and Planetary Science Conference*, Abstract #2822. 6.2.2

[32] Christensen, P. R., B. M. Jakosky, H. H. Kieffer, M. C. Malin, H. Y. Mcsween, K. Nealson, G. L. Mehall, S. H. Silverman, S. Ferry, M. Caplinger, and M. Ravine (2002). The Thermal Emission Imaging System (THEMIS) for the Mars 2001 Odyssey Mission. *Space Science Reviews 110*, 85–130. 2.3, 6.2.2

[33] Christensen, P. R., G. L. Mehall, S. H. Silverman, S. Anwar, G. Cannon, N. Gorelick, R. Kheen, T. Tourville, D. Bates, S. Ferry, T. Fortuna, J. Jeffryes, W. O'Donnell, R. Peralta, T. Wolverton, D. Blaney, R. Denise, J. Rademacher, R. V. Morris, and S. Squyres (2003). Miniature Thermal Emission Spectrometer for the Mars Exploration Rovers. *Journal of Geophysical Research-Planets 108*(E12), –. 8.5, 8.5

[34] Cline, H. and T. Anthony (1977). Heat Treating and Melting Material with a Scanning Laser or Electron Beam. *Journal of Applied Physics 48*(9), 3895. 4.1.1, 4.1.2

[35] Colaprete, A., P. Schultz, J. Heldmann, D. Wooden, M. Shirley, K. Ennico, B. Hermalyn, W. Marshall, A. Ricco, R. C. Elphic, D. Goldstein, D. Summy, G. D. Bart, E. Asphaug, D. Korycansky, D. Landis, and L. Sollitt (2010). Detection of Water in the LCROSS Ejecta Plume. *Science 330*(6003), 463–8. 1.1.2

[36] Cortes, C. and M. Mohri (2005). Confidence intervals for the area under the ROC curve. *Advances in Neural Information Processing Systems 17*, 305–312. 5.2.5

[37] Costes, N. C., J. E. Farmer, and E. B. George (1972). Mobility Performance of the Lunar Roving Vehicle: Terrestrial Studies Apollo 15 Results. Technical report. 1.1.2

[38] Cremers, C. J. (1973). Thermophysical Properties of Apollo 12 Fines. *Icarus 18*, 294–303. (document), 3.3.2, 7.2, 7.1.2

[39] Cunningham, C., I. Nesnas, and W. L. Whittaker (2015). Terrain Traversability Prediction by Imaging Thermal Transients. In *IEEE Conference on Robotics and Automation*, Seattle. 5

[40] Cunningham, C., M. Ono, I. Nesnas, J. Yen, and W. L. Whittaker (2017). Locally-Adaptive Slip Prediction for Planetary Rovers Using Gaussian Processes. In *IEEE Conference on Robotics and Automation*. (document), 2.1, 2.3, 2.2, 6, 6.1.2, 6.2.1

[41] Cunningham, C., W. L. Whittaker, and I. Nesnas (2016). Detecting Loose Regolith in Lunar Craters Using Thermal Imaging. In *ASCE Conference on Earth and Space*. 7

[42] Cunningham, C., U. Wong, K. M. Peterson, and W. L. R. Whittaker (2013). Predicting Terrain Traversability from Thermal Diffusivity. In *Field and Service Robotics*, Brisbane, Australia. 4

[43] Engel, J., T. Schöps, and D. Cremers (2014). Lsd-slam: Large-scale direct monocular slam. In *European Conference on Computer Vision*, pp. 834–849. Springer. 5.2.2

[44] Estlin, T., D. Gaines, B. Bornstein, S. Schaffer, V. Tompkins, D. R. Thompson, A. Altinok, R. C. Anderson, M. Burl, R. Castaño, D. Blaney, L. D. Flores, T. Nelson, R. Wiens, O. Grove, P. O. Box, and L. Alamos (2010). Automated Targeting for the MSL Rover ChemCam Spectrometer. In *Internaitonal Symposium on Artificial Intelligence, Robotics and Automation in Space (i-SAIRAS)*. 2.1

[45] Estlin, T. A., B. J. Bornstein, D. M. Gaines, R. C. Anderson, D. R. Thompson, M. Burl, R. Castaño, and M. Judd (2012, may). AEGIS Automated Science Targeting for the MER Opportunity Rover. In *ACM Transactions on Intelligent Systems and Technology*, Volume 3, pp. 1–19. 2.1

[46] Fergason, R. L., P. R. Christensen, J. F. Bell, M. P. Golombek, K. E. Herkenhoff, and H. H. Kieffer (2006). Physical Properties of the Mars Exploration Rover Landing Sites as Inferred from Mini-TES-Derived Thermal Inertia. *Journal of Geophysical Research: Planets 111*(2). 2.3, 5.1.2, 6.1.1, 8.2.1

[47] Fergason, R. L., P. R. Christensen, M. P. Golombek, and T. J. Parker (2012, may). Surface Properties of the Mars Science Laboratory Candidate Landing Sites: Characterization from Orbit and Predictions. *Space Science Reviews 170*(1-4), 739–773. 2.3

[48] Fergason, R. L., P. R. Christensen, and H. H. Kieffer (2006). High-resolution Thermal Inertia Derived from the Thermal Emission Imaging System (THEMIS): Thermal Model and Applications. *Journal of Geophysical Research: Planets 111*(12), 1–22. 2.3, 3.2.2, 5.4, 6.1.1, 7.2

[49] Fountain, J. and E. West (1970). Thermal Conductivity of Particulate Basalt as A function of Density in Simulated Lunar and Martian Environments. *Journal of Geophysical Research 75*(20). 3.3.2, 3.5, 7

[50] Fountain, J. and E. West (1976). Thermal Diffusivity of Lunar Fines: Temperature and Particle Size Effects. *Lunar and Planetary Science Conference*. 7

[51] Fujii, N. and M. Osako (1973). Thermal Diffusivity of Lunar Rocks Under Atmospheric

and Vacuum Conditions. *Earth and Planetary Science Letters 18*(4817), 65–71. 7.1.2

[52] Gamsky, J. N. and P. T. Metzger (2010). The Physical State of Lunar Soil in the Permanently Shadowed Craters on the Moon. In *ASCE Conference on Earth and Space*, pp. 14–17. 1.1.2

[53] Goldberg, S. B., M. W. Maimone, and L. Matthies (2002). Stereo Vision and Rover Navigation Software for Planetary Exploration. In *IEEE Aerospace Conference*, Volume 5, pp. 2025–2036. 2.1

[54] Golombek, M., J. Grant, D. Kipp, A. Vasavada, R. Kirk, R. Fergason, P. Bellutta, F. Calef, K. Larsen, Y. Katayama, A. Huertas, R. Beyer, A. Chen, T. Parker, B. Pollard, S. Lee, Y. Sun, R. Hoover, H. Sladek, J. Grotzinger, R. Welch, E. Noe Dobrea, J. Michalski, and M. Watkins (2012). Selection of the Mars Science Laboratory Landing Site. *Space Science Reviews 170*(1-4), 641–737. 2.3

[55] González, R., A. López, and K. Iagnemma (2017). Thermal Vision, Moisture Content, and Vegetation in the Context of Off-Road Mobile Robots. *Journal of Terramechanics 70*, 35–48. 2.3

[56] Greenwood, W. R., R. L. Jones, G. H. Heiken, M. J. Bender, and R. O. Hill (1971). Lunar-Surface Closeup Stereoscopic Photography on the Sea of Tranquility. Technical report. 1.1.2

[57] Grotzinger, J. P., J. Crisp, A. R. Vasavada, R. C. Anderson, C. J. Baker, R. Barry, D. F. Blake, P. Conrad, K. S. Edgett, B. Ferdowski, R. Gellert, J. B. Gilbert, M. Golombek, J. Gómez-Elvira, D. M. Hassler, L. Jandura, M. Litvak, P. Mahaffy, J. Maki, M. Meyer, M. C. Malin, I. Mitrofanov, J. J. Simmonds, D. Vaniman, R. V. Welch, and R. C. Wiens (2012). Mars Science Laboratory Mission and Science Investigation. *Space Science Reviews 170*(1-4), 5–56. 6.2

[58] Haberman, R. (1987). *Elementary applied partial differential equations: with Fourier series and boundary value problems*. Prentice-Hall Englewood Cliffs, NJ. 4.1.1

[59] Hadsell, R., P. Sermanet, J. Ben, A. Erkan, M. Scoffier, K. Kavukcuoglu, U. Muller, and Y. LeCun (2009). Learning Long-Range Vision for Autonomous Off-Road Driving. *Journal of Field Robotics 26*(2), 120–144. 2.2

[60] Hadsell, R., P. Sermanet, A. Erkan, J. Ben, J. Han, B. Flepp, U. Muller, and Y. LeCun (2007). Online Learning for Offroad Robots : Using Spatial Label Propagation to Learn. In *Robotics: Science and Systems*. 2.2

[61] Halatci, I., C. A. Brooks, and K. Iagnemma (2007). Terrain Classification and Classifier Fusion for Planetary Exploration Rovers. In *IEEE Aerospace Conference*, pp. 1–11. IEEE. 2.2

[62] Hamilton, V. E., A. R. Vasavada, E. Sebastián, M. De La Torre Juárez, M. Ramos, C. Armiens, R. E. Arvidson, I. Carrasco, P. R. Christensen, M. A. De Pablo, W. Goetz, J. Gõmez-Elvira, M. T. Lemmon, M. B. Madsen, F. J. Martín-Torres, J. Martínez-Frías, A. Molina, M. C. Palucis, S. C. R. Rafkin, M. I. Richardson, R. A. Yingst, and M.-P. Zorzano (2014). Observations and Preliminary Science Results from the First 100 Sols of MSL Rover Environmental Monitoring Station Ground Temperature Sensor Measurements at Gale Crater. *Journal of Geophysical Research: Planets 119*, 745–770. (document), 2.3, 3.2.2, 5.4, 6.1.1, 6.3, 8.1, 8.2, 8.2.1

[63] Happold, M., M. Ollis, and N. Johnson (2006). Enhancing Supervised Terrain Classification with Predictive Unsupervised Learning. In *Robotics: Science and Systems*. 2.2

[64] Heiken, G., D. Vaniman, and B. M. French (1991). *Lunar Sourcebook: a User's Guide to the Moon*. CUP Archive. (document), 1.1.2, 3.1, 7.1, 7.1.1, 7.1.1, 7.2, 8.3

[65] Helmick, D., A. Angelova, and L. Matthies (2009). Terrain Adaptive Navigation for Planetary Rovers. *Journal of Field Robotics 26*(4), 391–410. 2.2

[66] Hemingway, B. (1973). Specific Heats of Lunar Soils, Basalt, and Breccias from the Apollo 14, 15, and 16 Landing Sites, Between 90 and 350 K. In *Lunar and Planetary Science Conference*, Volume 3, pp. 2481–2487. 7.1.2

[67] Heverly, M., J. Matthews, J. Lin, D. Fuller, M. Maimone, J. Baesaidecki, and J. Leichty (2013). Traverse Performance Characterization for the Mars Science Laboratory Rover. *Journal of Field Robotics 30*(6), 835–846. 2.1, 2.1.1, 6.2.3

[68] Ho, K., T. Peynot, and S. Sukkarieh (2013). A Near-to-Far Non-Parametric Learning Approach for Estimating Traversability in Deformable Terrain. *IEEE International Conference on Intelligent Robots and Systems*, 2827–2833. 2.2

[69] Ho, K., T. Peynot, and S. Sukkarieh (2016). Nonparametric Traversability Estimation in Partially Occluded and Deformable Terrain. *Journal of Field Robotics*. 2.2

[70] Horai, K.-I. (1981). The Effect of Interstitial Gaseous Pressure on the Thermal Conductivity of a Simulated Apollo 12 Lunar Soil Sample. *Physics of the Earth and Planetary Interiors 27*(1), 60–71. 3.3.2

[71] Howard, A., M. Turmon, L. Matthies, B. Tang, A. Angelova, and E. Mjolsness (2007). Towards Learned Traversability for Robot Navigation: From Underfoot to the Far Field. *Journal of Field Robotics 23*(11/12), 1005–1017. 2.2

[72] Iagnemma, K., C. Senatore, and B. Trease (2011). Terramechanics Modeling of Mars Surface Exploration Rovers for Simulation and Parameter Estimation. *IDETC/CIE 2011 ASME International Design Engineering Technical Conferences & Computers and Information in Engineering Conference*, 1–8. 2.1.1, 3.4, 3.4.2

[73] Idso, S. B. (1981). A Set of Equations for Full Spectrum and 8- to 14- um and 10.5- to 12.5-um Thermal Radiation From Cloudless Skies. *Water Resources Research 17*(2), 295–304. 5.3.1

[74] Igwe, O., H. Fukuoka, and K. Sassa (2012). The Effect of Relative Density and Confining Stress on Shear Properties of Sands with Varying Grading. *Geotechnical and Geological Engineering 30*(5), 1207–1229. 3.4.2, 3.4.2, 3.5

[75] Igwe, O., K. Sassa, and F. Wang (2007). The Influence of Grading on the Shear Strength of Loose Sands in Stress-Controlled Ring Shear Tests. *Landslides 4*(1), 43–51. 1.2, 3.4.2, 3.5

[76] Jackel, L., E. Krotkov, M. Perschbacher, J. Pippine, and C. Sullivan (2007). The DARPA LAGR Program: Goals, Challenges, Methodology, and Phase I Results. *Journal of Field Robotics 23*(11-12), 945–973. 2.2

[77] Jakosky, B. M. and P. R. Christensen (1986). Global Duricrust on Mars: Analysis of Remote-Sensing Data. *Journal of Geophysical Research: Solid Earth 91*(B3), 3547–3559. 1.2, 3.1, 3.3.1, 3.3.2, 3.3.2

[78] Johnson, J. B., A. V. Kulchitsky, P. Duvoy, K. Iagnemma, C. Senatore, R. E. Arvidson, and

J. Moore (2015). Discrete Element Method Simulations of Mars Exploration Rover Wheel Performance. *Journal of Terramechanics 62*, 31–40. 2.1.1

[79] Kasparek, G. and D. Vortmeyer (1976). Radiative Heat Transfer in Packed Beds of Spheres with Negligible Heat Resistance. *Heat and Mass Transfer 9*, 117–128. 3.3.1

[80] Kieffer, H. H. (2013). Thermal Model for Analysis of Mars Infrared Mapping. *Journal of Geophysical Research: Planets 118*(3), 451–470. (document), 3.2.1, 3.2.2, 6.1.1, 6.3, 7.1.2, 8.2.1, 8.1, 8.5

[81] Kim, D., J. Sun, S. M. Oh, J. M. Rehg, and A. F. Bobick (2006). Traversability Classification Using Unsupervised On-Line Visual Learning for Outdoor Robot Navigation. In *IEEE International Conference on Robotics and Automation*, pp. 518–525. 2.2

[82] Kloss, C. and C. Goniva (2011). LIGGGHTS - Open Source Discrete Element Simulations of Granular Materials Based on Lammps. In *Supplemental Proceedings: Materials Fabrication, Properties, Characterization, and Modeling*, Volume 2, pp. 781–788. 2.1.1

[83] Knuth, M. A., J. B. Johnson, M. A. Hopkins, R. J. Sullivan, and J. M. Moore (2012). Discrete Element Modeling of a Mars Exploration Rover Wheel in Granular Material. *Journal of Terramechanics 49*(1), 27–36. 2.1.1

[84] Krebs, A., C. Pradalier, and R. Siegwart (2010). Adaptive Rover Behavior Based on Online Empirical Evaluation: Rover Terrain Interaction and Near to Far Learning. *Journal of Field Robotics 27*(2), 158–180. 2.2

[85] Krenn, R. and G. Hirzinger (2009). SCM – a Soil Contact Model for Multi-Body System Simulations. In *European Regional Conference of the International Society for Terrain-Vehicle Systems*. 2.1.1

[86] Kring, D. (2006). Lunar Mobility Review. In *Lunar Exploration Initiative*. 1.1.2

[87] Labuz, J. F. and A. Zang (2012). Mohr–coulomb failure criterion. In *The ISRM Suggested Methods for Rock Characterization, Testing and Monitoring: 2007-2014*, pp. 227–231. Springer. 3.4.1, 3.4.1

[88] Lade, P. V. and D. D. Overton (1989). Cementation Effects in Frictional Materials. *Journal of Geotechnical Engineering 115*(10), 1373–1387. 1.2, 3.4.2

[89] Lambe, T. W. (1960). A Mechanistic Picture of Shear Strength in Clay. In *Research Conference on Shear Strength of Cohesive Soils*. 3.4.2, 3.5

[90] Lemmon, M. T. (2014). The Mars Science Laboratory Optical Depth Record. In *LPI Contributions*, pp. 1–2. 6.1.1

[91] Lemmon, M. T., M. J. Wolff, J. F. Bell, M. D. Smith, B. A. Cantor, and P. H. Smith (2015). Dust Aerosol, Clouds, and the Atmospheric Optical Depth Record Over 5 Mars Years of the Mars Exploration Rover Mission. *Icarus 251*, 96–111. 6.1.1

[92] Leung, W. and A. Tam (1984). Techniques of Flash Radiometry. *Journal of Applied Physics 56*(1), 153. 4, 4.1.1

[93] Li, W., Y. Huang, Y. Cui, S. Dong, and J. Wang (2010). Trafficability Analysis of Lunar Mare Terrain by Means of the Discrete Element Method for Wheeled Rover Locomotion.

Journal of Terramechanics 47(3), 161–172. 2.1.1

[94] Lichtenberg, K. and D. Fike (2010). *Remote Sensing and Terramechanics Study of Mars using Orbital and Rover Data Sets*. Ph. D. thesis. 1.1.1

[95] Liu, J. M. (1982, May). Simple Technique for Measurements of Pulsed Gaussian-Beam Spot Sizes. *Opt. Lett. 7*(5), 196–198. 4.1.2

[96] Maimone, M. (2016). A martian vision: Impact of jpl robotics vision and mobility research on the mars rovers. In *JPL Robotics Section Senior Lecture Series*. (document), 2.1

[97] Maimone, M., Y. Cheng, and L. Matthies (2007). Two Years of Visual Odometry on the Mars Exploration Rovers. *Journal of Field Robotics 24*(3), 169–186. 2.1, 6.2.1

[98] Martínez, G. M., N. Rennó, E. Fischer, C. S. Borlina, B. Hallet, M. T. Juárez, A. R. Vasavada, M. Ramos, V. Hamilton, and R. M. Haberle (2014). Surface Energy Budget and Thermal Inertia at Gale Crater: Calculations from Ground-Based Measurements. *Journal of Geophysical Research: Planets 119*, 1822–1838. 2.3, 5.1.1, 8.2

[99] Masamune, S. and J. M. Smith (1963). Thermal Conductivity of Beds of Spherical Particles. *Industrial & Engineering Chemistry Fundamentals 2*(2), 136–143. (document), 3.6, 3.3.1, 3.3.2

[100] Mason, S. J. and N. E. Graham (2002). Areas Beneath the Relative Operating Characteristics (ROC) and Relative Operating Levels (ROL) Curves: Statistical Significance and Interpretation. *Quarterly Journal of the Royal Meteorological Society 128*(584), 2145–2166. 5.2.5

[101] Matthies, L. and A. Rankin (2003). Negative Obstacle Detection by Thermal Signature. *Proceedings 2003 IEEE/RSJ International Conference on Intelligent Robots and Systems (IROS 2003) 1*(818). 2.3

[102] Mazhar, H., T. Heyn, A. Pazouki, D. Melanz, A. Seidl, A. Bartholomew, A. Tasora, and D. Negrut (2013). CHRONO: A Parallel Multi-Physics Library for Rigid-Body, Flexible-Body, and Fluid Dynamics. *Mechanical Sciences 4*(1), 49–64. 2.1.1

[103] Mellon, M., B. M. Jackosky, H. H. Kieffer, and P. R. Christensen (2000, Dec). High-Resolution Thermal Inertia Mapping from the Mars Global Surveyor Thermal Emission Spectrometer. *Icarus 148*(2), 437–455. 2.3, 3.2.1

[104] Mitchell, D. L. and I. De Pater (1994). Microwave Imaging of Mercury's Thermal Emission at Wavelengths from .3 to 20.5 cm. *Icarus 110*, 2–32. 7.1.2

[105] Moody, J. and R. Hendel (1982). Temperature Profiles Induced by a Scanning CW Laser Beam. *Journal of Applied Physics 53*(6), 4364. 4.1.2

[106] Moreland, S. (2013). *Traction Processes of Wheels in Loose, Granular Soil*. Ph. D. thesis, Carnegie Mellon University. 3.4.1, 3.4.1

[107] Morgan, J. K. (1999). Numerical Simulations of Granular Shear Zones Using the Distinct Element Method 2 . Effects of Particle Size Distribution and Interparticle Friction on Mechanical Behavior. *Journal of Geophysical Research 104*(B2), 2721–2732. 1.2, 3.4.2, 3.4.2, 3.5

[108] Nakashima, H., H. Fujii, A. Oida, M. Momozu, H. Kanamori, S. Aoki, T. Yokoyama, H. Shimizu, J. Miyasaka, and K. Ohdoi (2010). Discrete Element Method Analysis of Single Wheel Performance for a Small Lunar Rover on Sloped Terrain. *Journal of Terramechanics 47*(5), 307–321. 2.1.1

[109] Negi, B. S., N. C. Bhowmik, S. S. Mathur, and T. C. Kandpal (1985). Solar Limb Darkening and Ray Trace Evaluation of Solar Concentrators. *Applied Optics 24*(2), 296. 7.1.3

[110] Neugebauer, G., G. Münch, H. H. Kieffer, S. C. Case Jr., and E. Miner (1971). Mariner 1969 Infrared Radiometer Results: Temperatures and Thermal Properties of the Martian Surface. *The Astronomical Journal 76*(8), 719–749. 3.3.1

[111] Olson, E. (2011). AprilTag: A Robust and Flexible Visual Fiducial System. In *2011 IEEE International Conference on Robotics and Automation*, pp. 3400–3407. 5.3.1

[112] Paige, D. A., M. C. Foote, B. T. Greenhagen, J. T. Schofield, S. Calcutt, A. R. Vasavada, D. J. Preston, F. W. Taylor, C. C. Allen, K. J. Snook, B. M. Jakosky, B. C. Murray, L. A. Soderblom, B. Jau, S. Loring, J. Bulharowski, N. E. Bowles, I. R. Thomas, M. T. Sullivan, C. Avis, E. M. De Jong, W. Hartford, and D. J. McCleese (2010). The Lunar Reconnaissance Orbiter Diviner Lunar Radiometer Experiment. *Space Science Reviews 150*(1-4), 125–160. 7.2, 7.3

[113] Paige, D. A., M. A. Siegler, J. A. Zhang, P. O. Hayne, E. J. Foote, K. A. Bennett, A. R. Vasavada, B. T. Greenhagen, J. T. Schofield, D. J. McCleese, M. C. Foote, E. DeJong, B. G. Bills, W. Hartford, B. C. Murray, C. C. Allen, K. Snook, L. A. Soderblom, S. Calcutt, F. W. Taylor, N. E. Bowles, J. L. Bandfield, R. Elphic, R. Ghent, T. D. Glotch, M. B. Wyatt, and P. G. Lucey (2010, Oct). Diviner Lunar Radiometer Observations of Cold Traps in the Moon's South Polar Region. *Science 330*(6003), 479–482. 1.1.2, 1.2, 7, 7.1.3

[114] Parker, W. J., R. J. Jenkins, C. P. Butler, and G. L. Abbott (1961). Flash Method of Determining Thermal Diffusivity, Heat Capacity, and Thermal Conductivity. *Journal of Applied Physics 32*(9), 1679. 4

[115] Parsons, A. J. and A. D. Abrahams (2009). *Geomorphology of desert environments*. 3.1

[116] Perko, H. a., J. D. Nelson, and J. R. Green (2006). Mars Soil Mechanical Properties and Suitability of Mars Soil Simulants. *Journal of Aerospace Engineering 19*(3), 169–176. 6

[117] Peynot, T., S.-T. Lui, R. McCallister, R. Fitch, and S. Sukkarieh (2014). Learned Stochastic Mobility Prediction for Planning with Control Uncertainty on Unstructured Terrain. *Journal of Field Robotics 31*(6), 969–995. 2.2

[118] Piqueux, S. and P. R. Christensen (2009a). A Model of Thermal Conductivity for Planetary Soils: 1. Theory for Unconsolidated Soils. *Journal of Geophysical Research 114*, 1–20. 3.3.1, 3.3.1, 3.3.1

[119] Piqueux, S. and P. R. Christensen (2009b). A Model of Thermal Conductivity for Planetary Soils: 2. Theory for Unconsolidated Soils. *Journal of Geophysical Research 114*, 1–20. 3.3.2, 3.5

[120] Pond, S., D. B. Fissel, and C. A. Paulson (1974). A Note on Bulk Aerodynamic Coefficients for Sensible Heat and Moisture Fluxes. *Boundary-Layer Meteorology 6*(1-2), 333–339. 5.1.1,

5.1.1, 5.2.3

[121] Presley, M. and P. Christensen (1997a). The Effect of Bulk Density and Particle Size Sorting on the Thermal Conductivity of Particulate Materials Under martian Atmospheric Pressures. *Journal of Geophysical Research 102*, 9221–9229. 3.3.2, 3.3.2, 3.3.2, 3.5, 3.5, 9.1

[122] Presley, M. A. and P. R. Christensen (1997b). Thermal Conductivity Measurements of Particulate Materials 2. Results. *Journal of Geophysical Research: Planets 102*(E3), 6551–6566. (document), 3.3.1, 3.3.2, 3.5, 8.2.1, 8.2, 9.1

[123] Presley, M. A. and P. R. Christensen (2010, Jul). Thermal Conductivity Measurements of Particulate Materials: 5. Effect of Bulk density and Particle Shape. *Journal of Geophysical Research: Planets 115*(E7), 13. 3.3.2, 3.3.2, 3.5, 3.5

[124] Presley, M. A., R. A. Craddock, and N. Zolotova (2009). The Effect of Salt Crust on the Thermal Conductivity of One Sample of Fluvial Particulate Materials Under Martian Atmospheric Pressures. *Journal of Geophysical Research: Planets 114*(11), 1–8. 3.3.2, 3.5

[125] Price, J. C. (1977). Thermal Inertia Mapping: A New View of the Earth. *Journal of Geophysical Research 82*(18), 2582–2590. 2.3, 5.1.1

[126] Price, J. C. (1985). On the Analysis of Thermal Infrared Imagery: The Limited Utility of Apparent Thermal Inertia. *Remote Sensing of Environment 18*(1), 59–73. 5.1.1, 5.1.1

[127] Putzig, N. and M. Mellon (2007). Apparent Thermal Inertia and the Surface Heterogeneity of Mars. *Icarus 191*(1), 68–94. (document), 2.3, 3.3.2, 3.3.2, 3.5, 8.2, 8.2.1

[128] Putzig, N., M. Mellon, B. Jakosky, S. Pelkey, S. Martínez-Alonso, B. Hynek, and N. Murphy (2004). Mars Thermal Inertia from THEMIS Data. *Lunar and Planetary Science Conference 35*, 1863. 6.3

[129] Putzig, N. E. (2006). *Thermal Inertia and Surface Heterogeneity on Mars*. Ph. D. thesis, University of Colorado. 1.1.1, 1.2, 3.2.1, 3.2.1, 3.2.1, 3.2.1, 3.3.1, 3.3.1, 3.3.1

[130] Rasmussen, C. E. and Z. Ghahramani (2002). Infinite Mixtures of Gaussian Process Experts. *Advances in Neural Information Processing Systems 2*, 881–888. 6.1.2

[131] Rodriguez-Manfredi, J., F. Gomez-Gomez, J. Gomez-Elvira, S. Navarro, O. Prieto-Ballesteros, E. Sebastian, M. de la Torre, J. Schofield, L. Tamppari, N. Bridges, et al. (2017). Atmospheric science with the mars 2020 rover. In *The Sixth International Workshop on the Mars Atmosphere*, pp. 4408. 9.3

[132] Rothrock, B., J. Papon, R. Kennedy, M. Ono, M. Heverly, and C. Cunningham (2016). SPOC : Deep Learning-based Terrain Classification for Mars Rover Missions. In *AIAA: Space*. (document), 2.1, 6, 6.2, 6.2.1, 6.2.1, 8.2.2

[133] Sanders, D. (1984). Temperature Distributions Produced by Scanning Gaussian Laser Beams. *Applied Optics*. 4.1.2

[134] Schaal, S. and C. G. Atkeson (1998). Constructive Incremental Learning from Only Local Information. *Neural Computation 10*(8), 2047–2084. 2.2

[135] Schultz, P. H., B. Hermalyn, A. Colaprete, K. Ennico, M. Shirley, and W. Marshall (2010). The LCROSS Cratering Experiment. *Science 330*, 468–472. 1.1.2

[136] Sebastián, E., C. Armiens, J. Gómez-Elvira, M. P. Zorzano, J. Martinez-Frias, B. Esteban, and M. Ramos (2010). The Rover Environmental Monitoring Station Ground Temperature Sensor: A Pyrometer for Measuring Ground Temperature on Mars. *Sensors 10*(10), 9211–9231. 6.1.1

[137] Senatore, C. and K. Iagnemma (2014). Analysis of Stress Distributions Under Lightweight Wheeled Vehicles. *Journal of Terramechanics 51*(1), 1–17. 3.4.1

[138] Shen, C. (2005). *Rarefied Gas Dynamics: Fundamentals, Simulations and Micro Flows*, Volume 22. 3.3.1

[139] Shinohara, K., M. Oida, and B. Golman (2000). Effect of Particle Shape on Angle of Internal Friction by Triaxial Compression Test. *Powder Technology 107*(1-2), 131–136. 3.4.2, 3.5

[140] Simmons, R. and L. Henriksen (1996). Obstacle Avoidance and Safeguarding for a Lunar Rover. In *AIAA Forum on Advanced Developments in Space Robotics*. 2.1

[141] Singh, S., R. Simmons, T. Smith, A. Stentz, V. Verma, A. Yahja, and K. Schwehr (2000). Recent Progress in Local and Global Traversability for Planetary Rovers. *IEEE International Conference on Robotics and Automation*, 1194–1200. 2.1

[142] Skonieczny, K. (2013). *Lightweight Robotic Excavation*. Ph. D. thesis, Carnegie Mellon University Pittsburgh, PA. 4.3

[143] Smith, W., D. Melanz, C. Senatore, K. Iagnemma, and H. Peng (2014). Comparison of Discrete Element Method and Traditional Modeling Methods for Steady-State Wheel-Terrain Interaction of Small Vehicles. *Journal of Terramechanics 56*, 61–75. 2.1.1

[144] Sofman, B., E. Lin, J. A. Bagnesll, J. Cole, N. Vandapel, and A. Stentz (2006). Improving Robot Navigatino through Self-Supervised Online Learning. *Journal of Field Robotics 23*, 1059–1075. 2.2

[145] Souza, A. D. (2005). Incremental Online Learning in High Dimensions. *Neural Computation*, 2602–2634. 2.2

[146] Squyres, S. W., R. E. Arvidson, D. Bollen, J. F. Bell, J. Brückner, N. A. Cabrol, W. M. Calvin, M. H. Carr, P. R. Christensen, B. C. Clark, L. Crumpler, D. J. Des Marais, C. D'Uston, T. Economou, J. Farmer, W. H. Farrand, W. Folkner, R. Gellert, T. D. Glotch, M. P. Golombek, S. Gorevan, J. A. Grant, R. Greeley, J. Grotzinger, K. E. Herkenhoff, S. Hviid, J. R. Johnson, G. Klingelhöfer, A. H. Knoll, G. Landis, M. T. Lemmon, R. Li, M. B. Madsen, M. C. Malin, S. M. McLennan, H. Y. McSween, D. W. Ming, J. Moersch, R. V. Morris, T. Parker, J. W. Rice, L. Richter, R. Rieder, C. Schröder, M. Sims, M. Smith, P. Smith, L. A. Soderblom, R. J. Sullivan, N. J. Tosca, H. Wänke, T. Wdowiak, M. J. Wolff, and A. S. Yen (2006). Overview of the Opportunity Mars Exploration Rover Mission to Meridiani Planum: Eagle Crater to Purgatory Ripple. *Journal of Geophysical Research: Planets 111*(12), 1–19. 1.1.1

[147] Stavens, D. and S. Thrun (2006). A Self-Supervised Terrain Roughness Estimator for Off-Road Autonomous Driving. In *Conference on Uncertainty in Artificial Intelligence (UAI-06)*, pp. 469–476. 2.2

[148] Tam, A. and B. Sullivan (1983). Remote Sensing Applications of Pulsed Photothermal

Radiometry. *Applied Physics Letters 43*(4), 333–335. 4

[149] Taylor, G., J. Neubert, P. Lucey, and E. McCullough (2004). The Uncertain Nature of Polar Lunar Regolith. *Space Resources Roundtable VI*. 1.1.2, 7, 7.2, 8.3, 9.1

[150] Trease, B., R. E. Arvidson, R. Lindemann, K. Bennett, F. Zhou, K. Iagnemma, C. Senatore, and L. V. Dyke (2011). Dynamic Modeling and Soil Mechanics for Path Planning of the Mars Exploration Rovers. *ASME 2011 International Design Engineering Technical Conference & Computers and Information in Engineering Conference IDETC/CIE*, 1–11. 2.1.1

[151] Vasavada, A. R., J. L. Bandfield, B. T. Greenhagen, P. O. Hayne, M. A. Siegler, J. P. Williams, and D. A. Paige (2012, Dec). Lunar Equatorial Surface Temperatures and Regolith Properties from the Diviner Lunar Radiometer Experiment. *Journal of Geophysical Research: Planets 117*(4), 1–12. 1.1.2, 2.3, 7, 7.1.2, 7.2, 7.2

[152] Vasavada, A. R., D. A. Paige, and S. E. Wood (1999). Near-Surface Temperatures on Mercury and the Moon and the Stability of Polar Ice Deposits. *Icarus 141*, 179–193. 7, 7.1.2, 7.1.3

[153] Vasavada, A.R., Grotzinger, J.P., Arvidson, R.E., Calef, F.J., Crisp, J.A., Gupta, S., Hurowitz, J., Mangold, N., Maurice, S., Schmid, M.E., Wiens, R.C., Williams, R.M.E., Yingst, R. (2014). Overview of the Mars Science Laboratory mission: Bradbury Landing to Yellowknife Bay and beyond. *Journal of Geophysical Research: Planets 119*, 1134–1161. 2.1

[154] Vernaza, P., B. Taskar, and D. D. Lee (2008). Online, Self-Supervised Terrain Classification via Discriminatively Trained Submodular Markov Random Fields. *IEEE International Conference on Robotics and Automation*, 2750–2757. 2.2

[155] Wagstaff, K. L., D. R. Thompson, A. Allwood, D. L. Bekker, N. A. Cabrol, T. Fuchs, K. Ortega, and W. Abbey (2013, Aug). Smart, Texture-Sensitive Instrument Classification for in situ Rock and Layer Analysis. *Geophysical Research Letters 40*(1). 2.1

[156] Wang, L. C., W. Long, and S. J. Gao (2014). Effect of Moisture Content, Void Ratio and Compacted Sand Content on the Shear Strength of Remolded Unsaturated Clay. *Electronic Journal of Geotechnical Engineering 19*(Q), 4413–4426. 1.2, 3.4.2, 3.5

[157] Wang, Y.-H. and S.-C. Leung (2008). A Particulate-Scale Investigation of Cemented Sand Behavior. *Canadian Geotechnical Journal 45*(1), 29–44. 3.4.2, 3.5

[158] Watson, K. (1964). *I. The Thermal Conductivity Measurements of Selected Silicate Powders in Vacuum from 150–350 K. II. An Interpretation of the Moons Eclipse and Lunation Cooling as Observed through the Earths Atmosphere from 8–14 Microns*. Ph. D. thesis. 3.3.1

[159] Webster, G. (2014). Curiosity Mars Rover Checking Possible Smoother Route. 1.1.1

[160] Webster, G., D. Brow, and L. Cantillo (2015). NASA Mars Rover Curiosity Reaches Sand Dunes. 1.1.1

[161] Webster, G. and D. Brown (2015). NASA's Curiosity Rover Adjusts Route Up Martian Mountain. 1.1.1

[162] Wellington, C., A. Courville, and A. T. Stentz (2005). Interacting Markov Random Fields for Simultaneous Terrain Modeling and Obstacle Detection. In *Robotics: Science and Systems*. 2.2

[163] Wellington, C. and A. Stentz (2004). Online Adaptive Rough-Terrain Navigation Vegetation. In *IEEE International Conference on Robotics and Automation*. 2.2

[164] Wellington, C. and A. T. Stentz (2003). Learning Predictions of the Load-Bearing Surface for Autonomous Rough-Terrain Navigation in Vegetation. In *Field and Service Robotics*. 2.2

[165] Williams, J. G., D. H. Boggs, and W. M. Folkner (2008). DE421 Lunar Orbit, Physical Liberations, and Surface Coordinates. 7.1.3

[166] Wissa, A. E., C. C. Ladd, and T. W. Lambe (1964). Effetive Stress Strength Parameters of Stabilized Soils. In *MIT Department of Civil Engineering*. 1.2, 3.4.2, 3.5

[167] Wong (2009). *Terramechanics and Off-Road Vehicle Engineering: Terrain Behaviour, Off-Road Vehicle Performance and Design.* Butterworth-Heinemann. 3.4

[168] Wong, J. Y. (2001). *Theory of Ground Vehices*. John Wiley & Sons. 2.1, 2.1.1, 3.4, 3.4.1, 3.4.1, 4.3

[169] Wong, U., B. Garney, W. Whittaker, and R. Whittaker (2010). Camera and LIDAR Fusion for Mapping of Actively Illuminated Subterranean Voids. *Field and Service Robotics*. 3.4.1

[170] Wong, U. Y. (2012). Lumenhancement : Exploiting Appearance for Planetary Modeling. (April). 1.2, 3.4.2, 3.5.1

[171] Yuksel, S. E., J. N. Wilson, and P. D. Gader (2012). Twenty Years of Mixture of Experts. *IEEE Transactions on Neural Networks and Learning Systems 23*(8), 1177–1193. 6.1.2

[172] Zhou, F., R. E. Arvidson, K. Bennett, B. Trease, R. Lindemann, P. Bellutta, K. Iagnemma, and C. Senatore (2014). Simulations of Mars Rover Traverses. *Journal of Field Robotics 31*(1), 141–160. 2.1.1, 3.4.1